

# **Sunlight-driven generation of singlet oxygen via porphyrin-coated membranes**

Zur Erlangung des akademischen Grades eines  
DOKTORS DER INGENIEURWISSENSCHAFTEN (DR.-ING.)

von der KIT-Fakultät für Chemieingenieurwesen und Verfahrenstechnik des  
Karlsruher Instituts für Technologie (KIT)  
genehmigte

DISSERTATION

von

M. Sc. Roman Lyubimenko  
aus Nischni Nowgorod, Russland

Tag der mündlichen Prüfung: 29.11.2022

Erstgutachterin: Prof. Dr.-Ing. Andrea Iris Schäfer (IAMT, KIT)

Zweitgutachter: Prof. Dr. Frank-Dieter Kopinke (UFZ)



„Damit das Mögliche entsteht, muss immer wieder das Unmögliche versucht werden.“ (To make the possible happen, one must attempt the impossible)

Quelle: *Mein Hermann Hesse – Ein Lesebuch Hrsg.*  
(Udo Lindenberg, 2008, Suhrkamp Verlag, S.26)





# Contents

<b>Kurzfassung</b> .....	<b>v</b>
<b>Abstract</b> .....	<b>vii</b>
<b>Acknowledgments</b> .....	<b>ix</b>
<b>List of Acronyms</b> .....	<b>xi</b>
<b>List of Symbols</b> .....	<b>xii</b>
<b>List of Publications</b> .....	<b>xv</b>
<b>1 Introduction</b> .....	<b>1</b>
1.1 Motivation .....	1
1.2 Objectives and Outline of the Thesis .....	5
<b>2 Theoretical Background</b> .....	<b>7</b>
2.1 Organic Micropollutants .....	8
2.1.1 Macro- and Micropollutants .....	8
2.1.2 Steroid Hormone Micropollutants in Water Bodies .....	9
2.1.3 Summary .....	14
2.2 Introduction to Photocatalytic Water Treatment .....	15
2.2.1 Current Limitations of Semiconductor Photocatalysis .....	16
2.3 Photosensitizer Selection .....	16
2.3.1 Definition and Examples of Photosensitizers .....	17
2.3.2 Singlet Oxygen for Water Remediation .....	18
2.3.3 Tetrapyrrole-Based PSs for Photocatalytic Water Treatment .....	18
2.3.4 The Mechanism of ROS Generation by Photosensitizers .....	20
2.3.5 Limited Photostability and Possible Solutions .....	22
2.4 Challenges of Heterogeneous Photocatalysis .....	23
2.4.1 Mass Transfer Limitation .....	23
2.4.2 Recovery of Suspended Particles from the Aqueous Phase .....	24
2.4.3 Light Attenuation and Low Quantum Efficiency .....	25
2.4.4 Dissolved Oxygen Deficiency .....	27
2.5 Photocatalytic Membranes .....	28
2.5.1 Different Configurations of Photocatalytic Membrane Reactors .....	28

2.5.3	Fundamentals of Solute Mass Transfer through a Membrane. . . . .	29
2.5.3	Selection of Membrane Material . . . . .	31
2.5.4	Fabrication Strategies of Photocatalytic Membranes . . . . .	33
2.5.5	Photosensitizer-Coated Membranes for Water Remediation . . . . .	34
2.5.6	Cost Analysis of Water Treatment Using Photocatalytic Membranes . . . . .	35
2.5.6	Mechanisms of Contaminant Removal by Photocatalytic Membranes . . . . .	37
2.6	Studies of Reaction Kinetics of PS-assisted Oxidation . . . . .	40
2.6.1	Studies of Operating Parameters. . . . .	40
2.6.2	Water Quality Parameters . . . . .	43
2.7	Summary . . . . .	46
<b>3</b>	<b>Materials and Methods. . . . .</b>	<b>47</b>
3.1	Chemicals and Solvents . . . . .	48
3.2	Preparation of Photocatalytic Membranes . . . . .	49
3.2.1	Types and Characteristics of PVDF Used Membranes . . . . .	49
3.2.2	Experimental Procedure . . . . .	51
3.2.3	Evaluation of Photosensitizer Loading. . . . .	52
3.3	Experimental Systems for Photocatalytic Membranes . . . . .	53
3.3.1	Description of the Photocatalytic Membrane Filtration Set-up . . . . .	53
3.3.2	Light Sources . . . . .	56
3.3.3	Light Soaking Chamber for Accelerated Aging of Membranes . . . . .	60
3.4	Analytical Methods. . . . .	61
3.4.1	Total Organic Carbon Analysis . . . . .	61
3.4.2	UV-Vis Analysis of Permeate Outlet . . . . .	61
3.4.3	Identification of Degradation By-products with Mass Spectrometry . . . . .	62
3.4.4	Ultra-High Pressure Liquid Chromatography Coupled with Flow Scintillation Analyzer . . . . .	63
3.4.5	Liquid Scintillation Counting . . . . .	67
3.5	Characterization Methods . . . . .	67
3.5.1	Optical Characterization of Photosensitizers. . . . .	67
3.5.2	Surface Characterization of Pristine and Photocatalytic Membranes . . . . .	70
3.5.3	Characterization of Membrane Structure . . . . .	71
3.6	Experimental Protocols. . . . .	72
3.6.1	Operating and Water Quality Parameters . . . . .	72
3.6.2	Photocatalytic Degradation of Organic Pollutants . . . . .	75

---

3.6.3	Figure-of-Merits of Photocatalytic Membranes Performance . . . . .	78
3.6.4	Error Analysis . . . . .	80
3.6.5	Accelerated Aging of Pristine and Photocatalytic Membranes . . . . .	85
<b>4</b>	<b>Pd-Porphyrin-Loaded Membranes for MB Removal . . . . .</b>	<b>87</b>
4.1	Introduction . . . . .	88
4.2	Characterization of Pd-TFPP/PVDF Membranes . . . . .	88
4.2.1	Adsorption Studies . . . . .	88
4.2.2	Optical Characterization of Porphyrin-Coated Membranes . . . . .	90
4.3	Evaluation of Photocatalytic Performance . . . . .	93
4.3.1	Probing Singlet Oxygen Generation with Uric Acid . . . . .	93
4.3.2	Methylene Blue as a Model Pollutant in Photocatalytic Experiments . . . . .	94
4.3.3	Influence of Process Parameters on the MB . . . . .	97
4.4	Stability of Pd-TFPP/PVDF Membranes . . . . .	100
4.5	Summary . . . . .	102
<b>5</b>	<b>Pd-Porphyrin-Loaded Membranes for SH Removal . . . . .</b>	<b>103</b>
5.1	Introduction . . . . .	104
5.2	The Effect of Process Parameters on SH Degradation . . . . .	105
5.2.1	Change in 17 $\beta$ -estradiol Degradation during a Prolonged Run . . . . .	105
5.2.2	Influence of Water flux on the Degradation Performance . . . . .	105
5.2.3	Implications of Studies of 17 $\beta$ -Estradiol Concentration in the Feed . . . . .	107
5.2.4	Calculation of the Bimolecular Rate Constant . . . . .	108
5.2.5	Influence of Light Intensity . . . . .	110
5.2.6	Influence of Feed Solution pH on the 17 $\beta$ -Estradiol Removal . . . . .	111
5.3	Photocatalytic Degradation of Multiple Steroids . . . . .	113
5.3.1	Oxidation of Steroid Hormones in Mono-Component Solutions . . . . .	113
5.3.2	Oxidation of Steroid Hormones in Multi-Component Mixtures . . . . .	115
5.3.2	Suggested Mechanism of 17 $\beta$ -estradiol Oxidation . . . . .	117
5.4	Summary . . . . .	118
<b>6</b>	<b>Palladium- vs Noble-Metal-Free Porphyrin Complexes . . . . .</b>	<b>119</b>
6.1	Introduction . . . . .	120
6.2	Characterization of Noble-Metal-Free PCM . . . . .	121
6.3	The Effect of Process Parameters on SH . . . . .	123
6.3.1	Effect on Porphyrin Loading on Photocatalytic Removal of 17 $\beta$ -estradiol . . . . .	123

6.3.2	Photocatalytic Degradation of Steroid Hormones . . . . .	126
6.4	Limiting Factors of Photocatalytic Oxidation using Noble-Metal Free PS . . . . .	127
6.4.1	Generation of <sup>102</sup> as a Limiting Factor of Noble-Metal-Free Porphyrins . . . . .	127
6.4.2	Photophysical Studies of Porphyrins with and without Noble Metals . . . . .	129
6.5	Changes Caused by Accelerated Aging of PCM . . . . .	131
6.6	Summary . . . . .	133
<b>7</b>	<b>Contact of Reactants with Fixed Photosensitizer and Reaction Kinetics . . . . .</b>	<b>135</b>
7.1	Introduction . . . . .	136
7.2	Mass Transport Limitation in PCMs . . . . .	136
7.3	Influence of Membrane Type on PCM Characteristics . . . . .	126
7.3.1	Small-Pore Size Membranes Provide the Large Surface Area. . . . .	138
7.3.2	Impact of the Membrane Type on 17 $\beta$ -estradiol Degradation . . . . .	142
7.4	Role of Contact Time in the 17 $\beta$ -estradiol . . . . .	143
7.4.1	Porphyrin Depth Distribution in Single and Stacked PCMs. . . . .	143
7.4.2	Extended Contact Time in Stacked PCMs for 17 $\beta$ -estradiol Elimination. . . . .	144
7.5	Studies of NM20 Membranes under Optimized Conditions for SH . . . . .	147
7.6	Summary . . . . .	148
<b>8</b>	<b>Conclusion . . . . .</b>	<b>149</b>
8.1	Summary and Discussion. . . . .	149
8.2	Future Outlook . . . . .	152
8.2.1	Degradation Performance . . . . .	152
8.2.2	Photosensitizer Stability. . . . .	152
8.2.3	Reaction Modelling and PCM Optimization . . . . .	153
	<b>Appendix: Supporting Graphs . . . . .</b>	<b>154</b>
	<b>Bibliography. . . . .</b>	<b>158</b>

# Kurzfassung

Eines der größten Probleme der Menschheit ist die rasch abnehmende Verfügbarkeit von sauberem Trinkwasser. Die starke Verunreinigung von Gewässern mit gefährlichen und langlebigen Stoffen, die in Spurenkonzentrationen vorkommen – Mikroverunreinigungen – ist ein ernstes Umweltproblem. Ein Paradebeispiel für solche Mikroverunreinigungen sind Steroidhormone, bei denen es sich um starke endokrin wirkende Chemikalien handelt, die auch mit verschiedenen Krebsarten in Verbindung gebracht werden. Die herkömmliche Aufbereitung hat sich als unzureichend erwiesen, um Mikroverunreinigungen (einschließlich Steroidhormone) zu reduzieren, die ohne angemessene Aufbereitung in die zur Trinkwasseraufbereitung genutzten Gewässer gelangen. Der Einsatz zahlreicher Verfahren zur fortgeschrittenen Wasseraufbereitung ist aufgrund mehrerer üblicher Nachteile begrenzt: i) Einsatz giftiger Chemikalien; ii) Anfallen hochkonzentrierter fester oder flüssiger Abfälle; iii) hoher Energiebedarfs, und iv) intensiver Chemikalienverbrauch. Daher fehlt es an nachhaltigen und wirksamen Methoden für den Abbau von Mikroschadstoffen.

Ziel dieser Arbeit ist es, die oben genannten Einschränkungen zu überwinden, indem photokatalytische Membranen (PCM) für die photokatalytische Oxidation von Steroidhormonen in Wasser entwickelt werden. Dieses hybride Verfahren kombiniert die Zerstörung von Schadstoffen mit einer Membranfiltration, die sowohl ökologische als auch wirtschaftliche Risiken verringern kann. Darüber hinaus besteht die entscheidende Rolle der PCM darin, die Schadstoffmoleküle in engen Kontakt mit den organischen Photokatalysatormolekülen (Porphyrin) zu bringen und dadurch die Abbaugeschwindigkeit zu beschleunigen.

Die PCMs wurden aus polyvinylidenfluorid (PVDF)-Membranen durch Imprägnierung mit Porphyrinmolekülen hergestellt. Es wurden in dieser Arbeit i) photophysikalische (durch Absorptions- und Photolumineszenzspektroskopie), ii) morphologische (Porosimetrie, Rasterelektronenmikroskopie, Flugzeit-Sekundärionen-Massenspektrometrie), iii) Filtrations- (Wasserdurchlässigkeit) und iv) photokatalytische Eigenschaften der verwendeten PCMs untersucht. Die Porosität der modifizierten Membran sowie die Wasserdurchlässigkeit blieben nach der Porphyrinadsorption gleich. Die photophysikalischen Eigenschaften von membranbeladenen Palladium-Porphyrinen – i) die starke Lichtabsorption, ii) die lange Lebensdauer des angeregten Triplett-Zustands, und iii) das effiziente strahlungslose Übergang (Intersystem Crossing) – wurden nicht wesentlich verändert. Die immobilisierten Pd-Porphyrine wandelten die Moleküle des gelösten Sauerstoffs effizient in Singulett-Sauerstoff um. Der Lebensdauer des angeregten Triplett-Zustands wurde von  $\langle \tau \rangle = 0,74$  ms in entgastem Wasser auf  $\langle \tau \rangle = 0,13$  ms in luftgesättigtem Wasser reduziert.

Die experimentellen Untersuchungen des Schadstoffabbaus (Methylenblau-Farbstoff und Steroidhormon-Mikroverunreinigungen) wurden in einem photokatalytischen Durchfluss-Membranreaktor untersucht. Die Beleuchtung der eingebauten Membran wurde in einer Edelstahlzelle mit einem inkrustierten Quarzfenster verwirklicht. Die Analyse von Steroidhormonen in Konzentrationen von Nanogramm pro Liter erfolgte durch flüssigchromatographische Methoden in Kombination mit einem Durchfluss-Szintillationsanalysator. Sowohl organische Farbstoffe als auch Steroidhormone wurden bei Verwendung von photokatalytische PVDF-Mikrofiltrationsmembranen (mittlere Porengröße  $0,2 \mu\text{m}$ ) effizient abgebaut. Bis zu 82 % Methylenblau (bei einer Verweilzeit von 8,6 s und einer Konzentration von  $1 \text{ mg L}^{-1}$ ) und bis zu 98 %  $17\beta$ -Östradiol (bei einer Verweilzeit von 4,3 s und einer Konzentration von  $100 \text{ ng L}^{-1}$ ) wurden in einem Durchgang abgebaut.

Es wurde festgestellt, dass die Geschwindigkeit des photokatalytischen Prozesses einer kinetischen Limitierung (bei niedriger Bestrahlungsstärke) oder einer Stofftransportkontrolle (bei hoher Bestrahlungsstärke) unterliegt. Die Lichtintensität und der Permeatfluss sind für die Reaktion geschwindigkeitsbestimmend und miteinander verknüpft. Bei Lichtintensitäten, die dem Sonnenlicht entsprechen ( $80,5 \text{ mW cm}^{-2}$  im Wellenlängenbereich von 350–1150 nm), erreichten PCMs auf Basis von Porphyrinen mit (Palladium) und ohne Edelmetallionen (Zink, freie Base) im aktiven Zentrum von Porphyrinen einen vergleichbaren Abbau von 17 $\beta$ -Estradiol. Bei niedrigen Lichtintensitäten zeigten die drei Arten von porphyrinbeschichteten Membranen eine unterschiedliche photokatalytische Aktivität, die auf die unterschiedliche Quantenausbeute von Singulett-Sauerstoff zurückgeführt wurde.

Die begrenzte Photostabilität bei längerer Beleuchtung – inhärente bei organischen Photosensibilisatoren – hängt mit der Umwandlung der Porphyrine in ihre nahen Homologen (Chlorine und Bakteriochlorine) zusammen. Diese Verbindungen behalten ihre photokatalytische Aktivität bei (nachgewiesen durch den Methyleneblau-Abbau) und bleiben an der Oberfläche der PVDF-Membran adsorbiert. Eine weitere Bestrahlung führt schrittweise zum vollständigen Photobleaching. Die Kinetik dieses Prozesses hängt von der Lichtintensität und dem Vorhandensein eines Quenchers von Singulett-Sauerstoff ab. Die beschleunigten Alterungstests zeigten, dass Zn-Porphyrin einer 3–4 mal längeren Bestrahlung (entspricht 222 Tagen Sonnenlicht) standhalten kann als Free-Base oder Pd-Porphyrin, bevor die Halbwertszeit erreicht war (der Abbau der Hälfte der PCM-beladenen Porphyrinmoleküle). Ein weiterer, stark limitierender Faktor – ein Mangel an Kontaktfläche und Kontaktzeit – wurde durch i) die Verwendung einer PVDF-Ultrafiltrationsmembran mit einer größeren Oberfläche und ii) die Optimierung der Dicke der porphyrinbeschichteten Membran oder des Wasserflusses angegangen. Als Folge davon sank die 17 $\beta$ -Estradiol-Konzentration unter den Richtwert für Trinkwasser ( $1 \text{ ng L}^{-1}$ ). Dieser Ansatz ermöglichte auch den Abbau von niedrig reagierenden Schadstoffen, wie den von Testosteron (bis zu 54% bei einer Verweilzeit von 4,3 s und einer Konzentration von  $100 \text{ ng L}^{-1}$ ).

Bevor porphyrinbeschichtete PVDF-Membranen in der Praxis eingesetzt werden können, müssen noch einige offene Fragen geklärt werden. Die wichtigsten Hindernisse sind: i) die Vielseitigkeit des organischen Photokatalysators durch den Nachweis des Abbaus persistenter Steroidhormone (Testosteron, Progesteron) und neuartiger Schadstoffklassen; ii) die Photostabilität des organischen Photokatalysators; und iii) die Rolle der Wassermatrix für die Abbaueffizienz. Insgesamt erweisen sich die auf Porphyrin-Photosensibilisatoren basierenden PCM als vielversprechendes System für die Eliminierung von Mikroverunreinigungen.

**Schlagwörter:**

Photokatalyse; Membranen, Photosensibilisator; Reaktionstechnik; Mikroschadstoffe; Wasseraufbereitung

# Abstract

One of humanity's greatest problems is the rapidly decreasing availability of clean drinking water. Severe contamination of water bodies with hazardous and persistent substances found in trace concentrations – micropollutants – is a serious environmental problem. A prime example of such micropollutants is steroid hormones, which are potent endocrine-disrupting chemicals and are also associated with various types of cancer. Conventional treatment has proven limited in reducing micropollutants (including steroid hormones) that, without proper treatment, enter the water bodies used to prepare drinking water. The use of numerous processes for advanced water treatment is limited because of several common drawbacks: i) the use or formation of toxic chemicals; ii) the accumulation of highly concentrated solid or liquid waste; iii) high energy demand, and iv) intensive chemical consumption. Hence, sustainable and effective methods for degradation of micropollutants are lacking.

The goal of this thesis is to overcome the aforementioned limitations by developing photocatalytic membranes (PCM) for photocatalytic oxidation of water-borne steroid hormones. This hybrid process combines the destruction of contaminants with membrane filtration that can reduce both environmental and economic risks. Additionally, the critical role of PCMs is to bring pollutant molecules into close contact with organic photocatalyst (porphyrin) molecules, thereby accelerating the degradation rates.

The PCMs have been prepared from poly(vinylidene fluoride) (PVDF) membranes by impregnation with porphyrin molecules. The thesis reveals i) photophysical (via absorption and photoluminescence spectroscopy); ii) morphological (porosimetry, scanning electron microscopy, time-of-flight-secondary ion mass spectrometry); iii) filtration (water permeability); and iv) photocatalytic properties of the employed PCMs. The photophysical properties of membrane-loaded palladium porphyrins – i) strong light absorption, ii) the long lifetime of the excited triplet state, and iii) efficient radiationless transition (intersystem crossing) – were not significantly altered. The lifetime of the excited triplet state was reduced from  $\langle\tau\rangle = 0.74$  ms in degassed water to  $\langle\tau\rangle = 0.13$  ms in air-saturated water. Similarly, the porosity of the modified membrane and the water permeability remained unchanged after porphyrin adsorption.

Experimental studies of contaminant degradation (methylene blue dye and steroid hormone micropollutants) were investigated in a photocatalytic flow-through membrane reactor. Illumination of mounted membrane was realized in a stainless steel cell with an incrustated quartz window. Analysis of steroid hormones at concentrations of nanograms per liter was performed by liquid chromatographic methods in combination with a flow-through scintillation analyzer. Both organic dyes and steroid hormones undergo efficient degradation when using PVDF microfiltration membranes (mean pore size  $0.2\ \mu\text{m}$ ) impregnated with Pd-porphyrin. Up to 82% methylene blue (at a residence time of 8.6 s and a concentration of  $1\ \text{mg L}^{-1}$ ) and up to 98% 17 $\beta$ -estradiol (at a residence time of 4.3 s and a concentration of  $100\ \text{ng L}^{-1}$ ) were degraded in one pass.

It has been established that the rate of the photocatalytic process is subject to kinetic control (at low irradiance) or mass transfer control (at high irradiance). The light intensity and the permeate flux are rate-determining for the reaction and are linked to each other. At light intensities equivalent to sunlight ( $80.5\ \text{mW cm}^{-2}$  in the wavelength region of 350–1150 nm), PCMs based on porphyrins with (palladium) and without noble metal ions (zinc, free base) in the active center of porphyrins can achieve comparable degradation of 17 $\beta$ -estradiol. At low light intensities, the three types of porphyrin-coated membranes exhibit different photocatalytic activity, which is attributed to the different quantum yield of singlet oxygen production.

Limited photostability under prolonged illumination – inherent to organic photosensitizers – is linked to the transformation of porphyrins to their close homologs (chlorins and bacteriochlorins). These compounds preserve the photocatalytic activity and are retained on the PVDF membrane. Further irradiation eventually leads to complete photobleaching. The kinetics of this process depends on the light intensity and the presence of singlet oxygen quencher. The accelerated aging tests show that Zn-porphyrin can withstand 3–4 times longer exposure (an equivalent of 222 days of sunlight) than free-base or Pd-porphyrin, before half of their molecules loaded on the PVDF membrane degrade. Another potent limiting factor – a lack of contact area and contact time – has been addressed by: i) using ultrafiltration PVDF membrane with a greater surface area; and ii) optimizing the thickness of the porphyrin-coated membrane or water flux. As a result, the 17 $\beta$ -estradiol concentration decreased below the guideline value for drinking water (1 ng L<sup>-1</sup>). This approach also enabled the degradation of low-reacting contaminants, such as that of testosterone (up to 54% at a residence time of 4.3 s and the feed concentration of 100 ng L<sup>-1</sup>).

Before porphyrin-coated PVDF membranes meet their practical application, several open challenges must be resolved. The most critical roadblocks are: i) the versatility of organic photocatalyst by demonstrating the degradation of persistent steroid hormones (testosterone, progesterone) and novel contaminant classes; ii) the photostability of organic photocatalyst; and iii) the role of water matrix in the degradation efficiency. Overall, the PCMs based on porphyrin photosensitizer are found to be a promising system for micropollutant elimination.

**Keywords:**

photocatalysis, membranes; photosensitizers, reaction kinetics, micropollutants, water treatment



# Acknowledgments

Financial support for the research in this dissertation was provided from the following funding sources: i) Helmholtz Association, including (a) a professorial recruitment initiative, (b) the Helmholtz Energy Materials Foundry (HEMF) for Prof. Bryce S. Richards, and Dr. Andrey Turshatov, (c) Helmholtz ERC Recognition Award NAMEPORED for Prof. Bryce S. Richards, Dr. Andrey Turshatov and Prof. Andrea I. Schäfer; ii) the NanoMembrane strategic initiative of the Science and Technology of Nanosystems (STN) program; iii) the support of the Karlsruhe Nano Micro Facility (KNMF); and iv) Research Field Energy – Program Materials and Technologies for the Energy Transition – Topic 1 Photovoltaics.

When I reflect on the path I have paved over the past five years, I consider myself fortunate for all the people I have met on this scientific journey. Before I close this life chapter, I would like to acknowledge explicitly the help of the following people and organizations.

Firstly, I would like to thank my main supervisors Prof. Bryce S. Richards and Dr. Andrey Turshatov. They always gave me a fair and thorough evaluation of my work. The elaborate sense of humor of Prof. Richards, his expertise in photonics, his scientific and argumentation skills always created the positive environment and made our private and group meetings enjoyable. I am extremely grateful to Dr. Andrey Turshatov for being a “living synapse” in the neural work of the two research institutes to which I belonged. His continuous support, immense help in many aspects of work and life together with our shared Russian sense of humor dragged me through the many tough aspects of the doctorate journey, in particular during the development of the liquid chromatography method. His enormous patience and unconditional faith in me are what kept me going. My doctoral dissertation would not have been possible without my second supervisor, Prof. Dr. Ing. Andrea I. Schäfer, who believed in me and allowed me to pursue my Ph.D. in a very ambitious and well-equipped scientific group. Our scientific discussions and communication – at times harsh – helped me on the way to learning the scientific method, turning a disciple into a novice expert.

This dissertation is indebted to my dear friends and fellow mates from the IMT institute: Natalia Kiseleva, Dr. Michael Oldenburg, Dr. Vitor Vlnieska, Emil Mamleyev, Andrey Mikhaylov, Margarita Zakharova. Our trips to Köln, Amsterdam, far Indonesia, and the famous Russian tour were the highlights of the year. Special thanks to Natalia Kiseleva for being the cheerful and insightful office neighbor and helping me with the preparation and performance of photoluminescence studies; Emil Mamleyev and Andrey Mikhaylov for agreeing to my spontaneous requests for scanning electron microscopy (SEM) sessions and sharing their well-thought view on scientific method; Dr. Michael Oldenburg and Margarita Zakharova for their valuable help in structuring any wild ideas and having a good amount of laugh together. I want to thank Dr. Dmitry Busko who helped design and conduct the experiments for measurements of singlet oxygen luminescence, the steady-state and time-resolved phosphorescence studies reported in Chapter 4 and Chapter 6. Overall, our Russian-gang meet-ups helped me to keep some semblance of sanity, for which I am eternally grateful.

The following IMT members are greatly acknowledged: Dr. Michael Adams for his cheerful spirit, welcoming birthday and Halloween parties, and help with thesis proofreading; Stephan Dottermusch for sharing his knowledge in operating an ultraviolet-visible spectrophotometer and for assistance in collecting the SEM images of poly(vinylidene fluoride) (PVDF) membranes; Dr. Malte Langehörst and Dr. Marius Jakoby for helping with our IMT group retreats and being the part of our multi-cultural party gang; Eduard Madirov (Kazan University, now at IMT, KIT) for the help with setting up the solar simulator and fluorescence measurements; Milian Kaiser for the streak camera measurements; Dr. Aditya Chauhan for his help with SEM images of PVDF membranes reported in Chapter 7 and always giving a valuable

feedback on my work; Dr. Ian Howard for valuable comments on results of photoluminescence studies; Dr. Damien Hudry for his absolute helpfulness, strict but fair leadership of the lab.

I would like to thank the groupmates in my second home at the IAMT Institute. Our very first conference (Euromembrane 2018) with Matteo Tagliavini, Prantik Samanta, Tobias Berger, and Minh Nguyen feels like a motivational starter pack on the road to a Ph.D., especially when I recall our wild dances in the Spanish club. Special thanks to Tobias Berger and Shabnam Lotfi – my partners in crime, happiness, and sorrow – with whom we paved together this thorny path of photocatalytic water treatment.

I greatly acknowledge Tobias Berger for his help in writing the LabView controlling software, tinkering around in the lab, using your invaluable 3D printer skills (cuvette holder design for the integrating sphere), and most importantly diluting our non-German community with beer and barbeque sessions. Minh Nguyen – a sort of local superhuman at the IAMT – has been a net savior for the entire IT infrastructure and repeatedly kept the liquid chromatography instrument software running smoothly. The countless fruitful discussions we had on adsorption, reaction kinetics, and scientific writing gave me lots of valuable insights and improved the quality of the discussion sections. Also, I would like to acknowledge Shabnam Lotfi for handling the management of the lab, the consumable and gas storage rooms – responsibilities that were often overlooked by others; Mehran Aliaskari, Yang-Hui Cai, James Joseph for their extreme helpfulness in lab issue solving, and specifically Yang-Hui Cai for his constant assistance in analyzing total organic carbon samples; Matteo Tagliavini and Dr. Alessandra Imbrogno for preparation of stock solutions of radiolabeled steroid hormones (including radiotracer management and waste disposal, error propagation analysis and your Italian spirit and sweets.

I greatly appreciate the Millipore company (Merck group) for donating the polyvinylidene fluoride membrane roll that gave a head start to this work; to the Institute of Nanotechnology (INT, KIT) for providing the laboratory space, where the results of the experimental Chapter 4 were produced; to the Institute for Micro Process Engineering (IMVT, KIT), in particular to Dr. Heinz Lambach (IMVT, KIT), for designing and manufacturing the membrane cell for the photocatalytic membrane set-up.

The following people helped tremendously during the development of the analytical method: Dr. Frank Kirschhöfer (IFG, KIT) for the guidance with setting up the liquid chromatography instrument and guidance on the way to developing the method for steroid hormone detection; Thomas Becker, Martin Schömer (Perkin Elmer, Germany) for assistance in the maintenance of a UHPLC instrument and troubleshooting, Steve Zimmerli (Long Island Scientific Services, U.S.A.) for the continuous guidance and help in troubleshooting of the radiodetector; Jürgen Wendel (ITEP) for providing the tritiated water standard; Jürgen Benz (IMT) for the assistance in the utilization of radioactive hormones. I would like to mark the utmost expertise of the following people, who have conducted critical research that has enriched this thesis: Dr. Alexander Welle (IFG, KIT) for the ToF-SIMS measurement of the porphyrin-coated membranes and in-depth discussion of the results presented in Chapters 4 and 7; Dr. Peter G. Weidler for recording the argon adsorption/desorption isotherms and their analysis, which provided the specific surface area of studied membranes; Dr. Thomas Luxbacher (Anton Paar, Austria) for zeta potential analysis of fresh and aged porphyrin-coated membranes; Margarete Offermann (IAM-ESS, KIT) and Dr. Joachim Binder (IAM-ESS, KIT) for measurements of the membrane porosity and pore size distribution using mercury intrusion porosimetry.

Last but not least, my deepest gratitude goes to my family and friends in Russia for their waves of encouragement and being a part of the roller-coaster ride. Despite the distance, I felt the constant support of my dear friends Sveta and Denis, Nikita and Yana, and the hearth of their homes, where I was always welcome. To my mum and dad, Sveta and Mikhail, I owe my curiosity about the world, passion for reading, and mental strength. Our Skype calls, though sometimes sporadic and loud, were a burst of unconditional love that, to paraphrase Nietzsche, reminded me of the “why” such that I could bear any “how”. Люблю.

# List of Acronyms

AOP	Advanced oxidation processes	21H,23H-porphine palladium(II)
	Attenuated total reflectance	pH <sub>IEP</sub>
ATR-FTIR	Fourier transform infrared spectroscopy	PL
DAQ	Data acquisition card	PMR
EPA	Environmental Protection Agency	PNEC
FSA	Flow scintillation analysis	PS
	5,10,15,20-	PVDF
H <sub>2</sub> -TFPP	tetrakis(pentafluoro-phenyl)–21H,23H-porphine	PWT
ISC	Intersystem crossing	RO
GC-MS/MS	Gas chromatography coupled with tandem mass spectrometry	ROS
LC-MS/MS	Liquid chromatography coupled with tandem mass spectrometry	SEM
LED	Light-emitting diode	SH
LOD	Limit of detection	SolSim
LSC	Liquid scintillation counter	TOF-SIMS
MB	Methylene Blue	TRL
MF	Microfiltration	UA
	5,10,15,20-	UHPLC
MnCl-TFPP	tetrakis(pentafluoro-phenyl)–21H,23H-porphine manganese (III)chloride	UF
MP	Micropollutants	UV
NF	Nanofiltration	Vis
<sup>1</sup> O <sub>2</sub>	Singlet form of molecular oxygen	(W)WTP
PCM	Photocatalytic membrane	
Pd-TFPP	5,10,15,20-tetrakis(pentafluoro-phenyl)–	
		5,10,15,20-tetrakis(pentafluoro-phenyl)–21H,23H-porphine zinc (II)

# List of Symbols

Greek letters	Description	Unit
$\bar{\alpha}$	Integral absorptance	%
$\alpha_\lambda$	Spectral absorptance	–
$\beta$	Exponent showing the relationship to irradiance	–
$\beta_{LS}, \beta_{PS}$	Matching coefficients for a light source or porphyrin type	–
$\gamma_{Hg}$	Surface tension of mercury	N m <sup>-1</sup>
$\epsilon_\lambda$	Molar extinction coefficient at a wavelength $\lambda$	M <sup>-1</sup> cm <sup>-1</sup>
$\epsilon$	Constant of proportionality of the irradiance relationship	mol L <sup>-1</sup> s
$\zeta$	Zeta potential	mV
$\eta$	Conversion coefficient between the depth profile distribution of Pd <sup>+</sup> ions and PS molecules in PCMs	–
$\theta_{PS}$	Surface coverage by porphyrin molecules	–
$\theta_c$	Contact angle	°
$\kappa_p, \kappa_f$	Electrical conductivity in the permeate and feed streams	μS cm <sup>-1</sup>
$\lambda_{exc}$	Excitation wavelength(s)	nm
$\mu$	Light attenuation coefficient	m <sup>-1</sup>
$\xi$	Photonic efficiency	–
$\nu$	Light intensity matching factor	W m <sup>-2</sup> nm <sup>-1</sup>
$\sigma_{NC}, \sigma_{BG}, \sigma_b$	Standard deviation of net, background, blank count rates	Counts min <sup>-1</sup>
$\langle \tau_T^0 \rangle, \langle \tau_T \rangle, \langle \tau_{T,MB}^0 \rangle$	Average triplet-state lifetime in degassed, air-saturated water, and degassed solution of methylene blue in water	s
$\Phi_\Delta$	Quantum yield of singlet oxygen generation	–
$\Phi_T$	Quantum yield of population of triplet excited states	–
$\varphi_{abs}$	Absorbed photon flux	s <sup>-1</sup> m <sup>-2</sup>
$\varphi_{abs,\lambda}, \varphi_{inc,\lambda}$	Spectral distribution of absorbed and incident photon flux	s <sup>-1</sup> m <sup>-2</sup> nm <sup>-1</sup>
$\varphi_{abs,V}$	Volumetric absorbed photon flux	mol <sub>ph</sub> m <sup>-2</sup> L <sup>-1</sup>
$\varphi'_{inc,\lambda}$	Spectral distribution of incident photon flux	–
$\psi_m$	Membrane porosity	–
Symbols	Description	Unit
$A_{\Delta_s}, A_{\Delta,ref}$	Integrated area of PL spectra of the reference and studied PS	a.u.
$A_m$	Membrane filtration area	m <sup>2</sup>
$A_s$	Surface area of a membrane	m <sup>2</sup>
$a_s$	Specific surface area	m <sup>2</sup> g <sup>-1</sup>
$a_V$	Surface-to-volume ratio	m <sup>2</sup> m <sup>-3</sup>
$a'_V$	Active surface-to-volume ratio	m <sup>2</sup> m <sup>-3</sup>
$C_p, C_f$	Molarity in feed or permeate	mol L <sup>-1</sup>

Symbols	Description	Unit
$C_f, C_p, C_{p,ss}$	Solute (mass) concentration in feed, permeate and steady-state concentration in permeate	$\text{g L}^{-1}$
$C_{BL}$	Concentration of pollutant in the boundary layer	$\text{g L}^{-1}$
$C^1_{O_2,ss}$	Steady-state concentration of singlet oxygen	$\text{mol L}^{-1}$
$D_i$	Molecular diffusion coefficient of solute $i$ in bulk solution	$\text{m}^2 \text{s}^{-1}$
$\bar{d}_{por}$	Average pore size diameter	m
$d_{solut}$	Solute diameter	m
$E$	Energy	$\text{kJ mol}^{-1}$
$E_{EO}$	Specific electrical consumption per removal order	$\text{kWh m}^{-3} \text{ order}^{-1}$
$E_{S,T}$	Energy of singlet and triplet excited states of a PS molecule	$\text{kJ mol}^{-1}$
$E^{T*}_{ox}$	Excited state oxidation potential	V (vs. NHE)
$E^0$	Redox potential of electrochemical couple	V (vs. NHE)
$F$	Faraday constant	$\text{kcal V}^{-1} \text{ mol}^{-1}$
$f_{T,\Delta}^{O_2}$	Ratio of the quenched porphyrin triplet states to the produced $^1\text{O}_2$ molecules	–
$\Delta G_{PET}$	Gibbs energy for electron transfer	$\text{kcal mol}^{-1}$
$H_{abs}$	Cumulative dose of absorbed radiation	$\text{kWh m}^{-2}$
$H^{sol}_{abs,av}$	Daily average dose of absorbed solar light radiation	$\text{kWh m}^{-2} \text{ day}^{-1}$
$H^{sol}_{abs,an}$	Annual global solar irradiation on a horizontal surface	$\text{kWh m}^{-2} \text{ y}^{-1}$
$h$	Planck's constant	J s
$h_m$	Membrane thickness	cm
$I_{inc}$	Incident light intensity	$\text{mW cm}^{-2}$
$I_{inc,\lambda}$	Experimental spectral irradiance	$\text{W m}^{-2} \text{ nm}^{-1}$
$I'_{inc,\lambda}$	Spectral irradiance obtained from the incident photon flux	norm.
$I''_{inc,\lambda}$	Normalized spectral irradiance	–
$I_{ref}, I_s$	Intensity of absorbed light of a reference and sample PS	a.u.
$J_w$	Water flux	$\text{L m}^{-2} \text{ h}^{-1}$
$J_s$	Solute molar flux	$\text{mol m}^{-2} \text{ s}^{-1}$
$K_{ads}$	Adsorption equilibrium constant	–
$k_{\Delta}$	Rate constant of $^1\text{O}_2$ deactivation	$\text{s}^{-1}$
$k_i$	Intrinsic (bimolecular) rate constant of $i$ disappearance	$\text{L mol}^{-1} \text{ s}^{-1}$
$k_{obs}$	Observed rate constant of $i$ disappearance	$\text{s}^{-1}$
$k_m$	Reactant-to-surface mass transfer coefficient	$\text{m s}^{-1}$
$k_{pb}$	Rate constant of porphyrin photobleaching	$\text{h}^{-1}$
$k_q$	Rate constant of excited-state quenching of porphyrins	$\text{L mol}^{-1} \text{ s}^{-1}$
$l$	Characteristic length	m
$l_{3D}$	Three-dimensional mean squared displacement (diffusion path)	m
$l_{opt}$	Optical pathlength	m

Symbols	Description	Unit
$M_i$	Molar mass of a solute	$\text{g mol}^{-1}$
$m_m$	Mass of a membrane	g
$N_i$	Amount of substance $i$	mol
$N_A$	Avogadro's constant	$\text{mol}^{-1}$
$N_{ML}$	Theoretical monolayer capacity	mol
$n_D$	Refractive index	–
$P_{el}$	Electric power	W
$P_{\text{eq},1(2)}, P_{\text{ref},1(2)}$	Equilibrium and reference pressures in a pycnometer device	bar
$\Delta P$	Transmembrane pressure	bar
$P_T^{O_2}$	The probability of PS quenching by oxygen	–
$Q_{f,p}$	Feed/permeate flow rate	$\text{L h}^{-1}$
$q_e$	Mass adsorbed per surface area of a membrane	$\text{ng cm}^{-2}$
$\bar{q}_{PS}, \bar{q}_{PS}^{opt}$	Experimental and optimized photosensitizer loading	$\mu\text{mol cm}^{-2}$
$\bar{q}_{PS,z}$	Depth profile distribution of porphyrin molecules in a PCM	$\mu\text{mol cm}^{-2} \mu\text{m}^{-1}$
$q_{Pd^+,z}$	Depth profile distribution of $\text{Pd}^+$ ions in a PCM	norm.
$R_i$	Removal of $i$ pollutant	%
$R_S$	Chromatographic peak resolution	–
$\bar{r}''_i$	Rate of $i$ disappearance per membrane area	$\text{mol m}^{-2} \text{s}^{-1}$
$\bar{r}_i$	Volumetric rate of $i$ disappearance	$\text{mol L}^{-1} \text{s}^{-1}$
$S$	Slope of a calibration curve	a.u.
$\bar{T}$	Integral transmittance	%
$T_\lambda$	Spectral transmittance	–
$t_{1/2,eq}$	Number of days equivalent to photobleaching of the half of loaded porphyrin molecules	days
$t_\Delta$	Lifetime of singlet oxygen	s
$\bar{t}_{con}, \bar{t}_r$	Mean contact time and hydraulic residence time within a PCM	s
$t_{mix}$	Mixing time of a solute in the membrane pore volume	s
$t_{op}$	Operation (illumination) time	h
$t_{ret}$	Chromatographic retention time	min
$u_L$	Speed of light	$\text{m s}^{-1}$
$u_s, u_r$	Superficial velocity in the feed line and in the radial direction	$\text{m s}^{-1}$
$V_p$	Volume of passed permeate	L
$V_{por}$	Pore volume of a membrane	L
$V_R$	Photoreactor volume	L
$V_{solv}$	Volume of solvent for preparation of a solution	L
$w_{1,2}$	Width(s) of a peak at half-height	min
$x_i$	Amplitude of the $i$ -th component of the PL decay	–
$\bar{y}_b, y_{LOD}, y_{LOQ}$	Response of the FSA detector at blank, LOD, LOQ level	$\text{Counts min}^{-1}$

# List of Publications

## Peer-Reviewed Journals

The dissertation consists of four core publications (in bold) published in peer-reviewed scientific journals:

- (1) **Lyubimenko, R., Busko, D., Schäfer, A. I., Richards, B. S., Turshatov, A. (2019). Efficient photocatalytic removal of methylene blue using a metalloporphyrin–poly(vinylidene fluoride) hybrid membrane in a flow-through reactor. ACS Appl. Mater. Interfaces, 11 (35), 31763–31776.**
- (2) Lyubimenko, R., Richards, B. S., Turshatov, A., Schäfer, A. I. (2020). Separation and degradation detection of nanogram-per-litre concentrations of radiolabelled steroid hormones using combined liquid chromatography and flow scintillation analysis. *Sci. Rep.* 10, 7095.
- (3) **Lyubimenko, R., Gutierrez Cardenas, O. I., Richards, B. S., Turshatov, A., Schäfer, A. I. (2021). Photodegradation of steroid-hormone micropollutants in a flow-through membrane reactor coated with Pd(II)-porphyrin. Appl. Catal. B: Environ. 291, 120097.**
- (4) **Lyubimenko, R.; Richards, B. S.; Schäfer, A. I.; Turshatov, A. (2022). Noble-metal-free photosensitizers for continuous-flow photochemical oxidation of steroid hormone micropollutants under sunlight. J. Membr. Sci., 642, 119981.**
- (5) **Lyubimenko, R., Welle, A., Weidler, P., Turshatov, A., Richards, B. S., Schäfer, A. I. (2022). Enhanced photocatalytic efficiency via improved contact in a solar-driven membrane reactor for steroid hormone removal. Chem. Eng. J., 451, 138449.**
- (6) Raota, C.S., Lotfi, S., Lyubimenko, R., Richards, B. S., Schäfer, A. I. Determination of photostability of polymer-based photocatalytic membranes using accelerated ageing (submitted).

## Scientific Contribution at Conferences

The parts of the thesis have been presented at international scientific conferences:

1. Keynote lecture. 12/2020, International Congress on Membranes & Membrane Processes 2020 (online).
2. Oral presentation. 10/2020, 16th Annual workshop on emerging high-resolution mass spectrometry (HRMS) and LC-MS/MS applications in environmental analysis and food safety (online).
3. Oral & Poster presentation. 07/2018, Euromembrane 2018, Valencia, Spain





# 1 Introduction

## 1.1 Motivation

### Water Scarcity and Micropollutant Issue

The value of water, an embodiment of life on Earth, are beyond measure. While water is considered to be an abundant natural resource, clean water scarcity significantly affects humanity. Over 2 billion people worldwide have insufficient access to water. The demand increases annually by 1%, and is expected to grow by one-third by 2050.<sup>1</sup> These estimates cast bleak projections for population diseases, primarily because of poor sanitary conditions in developing countries.<sup>2</sup> Additionally, water-related diseases are a primary cause of child mortality.<sup>3</sup> Population growth has increased demands for freshwater (by a factor of six over the last century),<sup>1</sup> and for chemical goods used in the agricultural, energy and private sectors.<sup>4</sup> This increased level of water consumption to produce energy and food (known as the water–food–energy–nexus<sup>5</sup>) has inevitably strained treatment facilities, resulting in water quality deterioration. Consequently, countless pollutants (known and emerging) are released to the environment because of incomplete removal. Handling a broad spectrum of pollutants and pathways into the environment (agricultural, hospital runoff, or sewers) can be overwhelming for local treatment facilities.

Despite the relatively high water costs, the developed countries, including Germany (\$2.80 m<sup>-3</sup>), the United Kingdom (\$2.30 m<sup>-3</sup>), the United States (\$1.6 m<sup>-3</sup>), and Japan (\$1.04 m<sup>-3</sup>), are considered water-secured.<sup>6</sup> Seasonal water shortage might still have global effects on citizens within major cities in the future as a result of climate change and expanding urbanisation.<sup>7</sup> However, the economic or socio-economic reasons for water scarcity still prevail in regions with stressed economies, such those in central Africa, South Asia, and South America. Clean water, or indeed water of adequate quality, cannot simply be afforded due to the lack of infrastructure; in particular, for disinfection and decontamination of fresh water.

The main water quality-related challenge is reduction of emerging pollutants in trace (picogram to microgram) concentrations denoted as micropollutants (MP).<sup>8,9</sup> Among them, steroid hormones (SH) exhibit long-term effects of endocrine disruption, thus jeopardizing natural flora and fauna at nanogram-per-liter (ng L<sup>-1</sup>) concentrations.<sup>10–12</sup> The natural SHs (e.g., estrone, 17 $\beta$ -estradiol, and synthetic 17 $\alpha$ -ethynylestradiol, found in contraceptive pills) have been detected in municipal wastewaters and surface waters.<sup>13, 14</sup> In response to heightened awareness of SH effects, European Union (EU) legislation on water quality has become more stringent. Already, the risks posed by 17 $\beta$ -estradiol (one of the most active SHs) have been acknowledged by Directive (EU) 2020/2184 of the European Parliament.<sup>15</sup> The document recommends: i) monitoring and remedial operations for 17 $\beta$ -estradiol; and ii) establishing a target concentration of 1 ng L<sup>-1</sup> in drinking water. The conventional water treatment processes operating in centralised scheme do not always meet such a stringent guideline value for SH micropollutants.

### Conventional Water Treatment Plant Train

Both industrial and municipal water is conventionally processed in centralized treatment facilities using a multistep strategy, which relies on the principles of partitioning, filtration, and (bio)chemical transformation. The schematics of conventional wastewater treatment plants (WWTP) is depicted in Figure

1.1a: ① pre-treatment (mechanical screening, grit removal); ② primary steps (removal of sediments in clarifiers); ③ secondary steps (activated sludge treatment, trickling filter, rotating biological contactors); ④ tertiary steps to remove nutrients and pathogens; and ⑤ chlorination, ultraviolet light disinfection steps. Figure 1.1b illustrates the steps of conventional treatment at water treatment plants (WTP): ⑥ primary (flocculation/coagulation); ⑦ secondary (sand, powder (PAC) or granulated activated carbon (GAC) filtration), and ⑧ tertiary (oxidation, disinfection) treatment.

While conventional WTP is not designed to remove MP to levels not exhibiting effect on biota (below predicted no-effect concentration, PNEC), partial removal is achieved via mechanisms of i) sorption, ii) biological transformation, iii) volatilization, and iv) abiotic degradation (photolysis). Incomplete removal of SH (see also Chapter 2) suggests that neither secondary nor tertiary treatment in conventional WWTP can offer an effective barrier to these persistent harmful substances, which are then discharged into surface water.<sup>16</sup> A large range of SH removal values at different WWTP/WTPs<sup>13, 17</sup> additionally suggest that efficiency of treatment is dependent on pollutant type and process organization. While the process can be improved by varying operating parameters (for example, hydraulic residence time), the introduction of additional steps of tertiary treatment (denoted as step ⑨, see also Figure 1.1b) is occasionally the only viable solution to combat the appearance of MP in the WTP effluent.

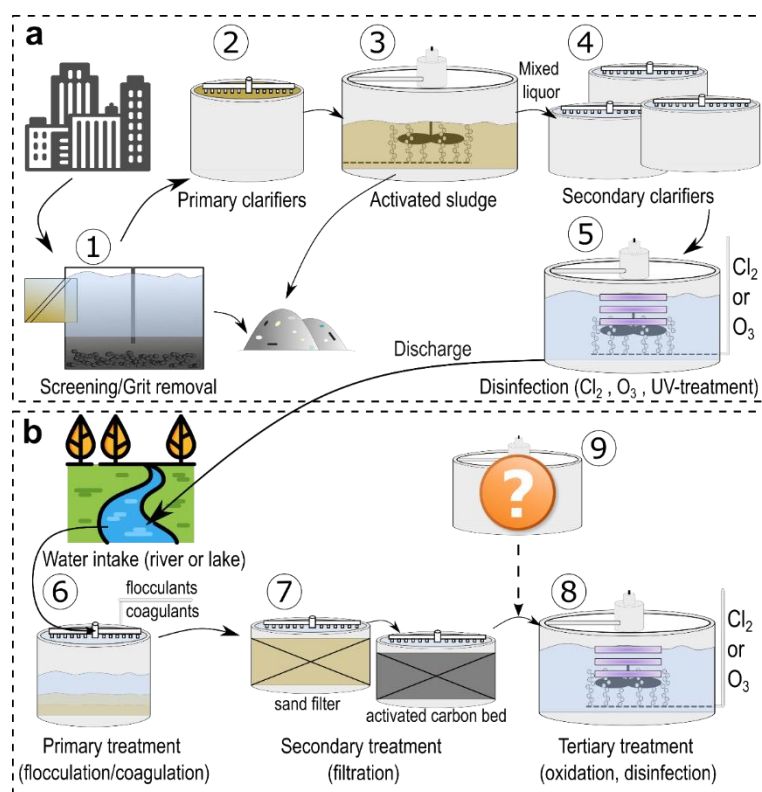


Figure 1.1: Schematic flow of conventional **a** wastewater and **b** water treatment plants.

## Advanced Water Treatment Technologies

Over the past century, WWTPs have been continually upgraded using innovative remediation technologies to handle occurring water-related environmental issues.<sup>18</sup> Similarly, modern challenges of water decontamination, including removal of emerging MP and limited resiliency to growing water and energy

input demand,<sup>19</sup> can be solved via new control strategies.<sup>20</sup> The lack of legislation inhibits local authorities from replacing conventional WTP/WWTP trains with those using advanced water treatment technologies. Except for a few countries, regulations on MP release into the environment are underdeveloped.

In 2014, Switzerland employed Water Protection Act setting the goal for selected WWTP to mitigate MP by 80% by 2040 via implementing state-of-the-art technologies.<sup>21</sup> Among measures of MP reduction in water bodies, the German federal authorities (Umweltbundesamt/UBA) propose the installation of a fourth treatment stage due to its effectiveness, a broad spectrum of affected contaminants, and moderate costs for implementation.<sup>22</sup> Although there are concerns regarding the need for the proposed actions,<sup>23</sup> advanced water remediation methods can be integrated into existing centralized (instead of step ④⑤) or decentralized modular systems, and can help meet water guidelines.

### *Membrane-Based Processes*

The rapid development of membrane-based processes and distinct reduction of costs for membrane fabrication over the last decades have turned pressure-driven membrane filtration into the durable, widespread water treatment technology.<sup>24</sup> Driven by the increasingly stringent regulatory norms of water quality, the emergence of membrane filtration has represented the entire paradigm shift in water treatment relying conventionally on the coagulation methods.<sup>25</sup> To date, membrane filters are categorized by the pore diameter thus: porous microfiltration (MF), ultrafiltration (UF), nanofiltration (NF), and dense reverse osmosis (RO) membranes.

Unlike the comparatively high energy costs of RO for water reuse (1.5–2.5 kWh m<sup>-3</sup>), NF membranes are operated at moderate pressure (3.5–5.5 bar) and for this reason less energy demanding (0.6–1.2 kWh m<sup>-3</sup>).<sup>26</sup> Both NF and RO membranes have been successfully used for the treatment of surface water and showed high removal of a broad span of MP classes,<sup>17, 27</sup> including SH.<sup>28</sup> Relatively coarse filters, such as UF and MF membranes, have been successfully implemented in hybrid technology realized in membrane bioreactors.<sup>29</sup> The combination of activated sludge treatment with membrane filtration enables the separation of sludge flocs and particulate matter in addition to ensuring higher sludge retention time (>15 days) and thus improved removal efficiency than using conventional sludge treatment.<sup>30</sup> Notably, the effectiveness of membrane bioreactors for removal of MP has been confirmed as well for SH (64–99%), such as estrone, 17 $\beta$ -estradiol, testosterone, and 17 $\alpha$ -ethynylestradiol.<sup>27, 31</sup> Integration of UF with PAC/GAC adsorption presents a safe strategy for preparation of drinking water due to disinfection, absence of any by-products, and total adsorbent retention.<sup>32</sup> The adsorption technology has proven effective, low-cost (0.16–0.18€ m<sup>-3</sup>, if coupled with sand filter) removal of hydrophobic SH and other non-polar pollutants from synthetic and municipal water.<sup>32, 33</sup> The problem of poor removal of hydrophilic and negatively charged MPs however remains.

### *Advanced Oxidation Processes*

The disadvantage of the technologies explained above is that all of them generate liquid/solid residuals (sludge, highly concentrated and toxic streams, spent adsorbent). This newly formed waste requires further utilization (for example via incineration) to preclude a secondary pollution.<sup>34, 35</sup> Moreover, waste management is troublesome in remote areas that have little infrastructure and depend on decentralized water treatment systems, which apply a closed-loop or on-site waste disposal. Rather than diverting the MP from water, advanced oxidation processes (AOPs) can transform them by producing in situ (on-site) highly reactive oxygen species (ROS), for example hydroxyl radicals or singlet oxygen. What makes AOPs appealing for eliminating the water pollutants, is that: i) no hazardous chemicals are theoretically introduced; and ii) partial mineralization and disinfection are attained. The individual or cluster AOP-based systems are well integrated into small-scale production of potable and non-potable water on-site (point-of-use or point-of-entry) or within a neighborhood area. Additionally, the focus on the quality of in- and

outflow water specified by the consumer may enable the use of less labor-intensive and less energy-intensive technologies, hence decreasing maintenance and operating costs.<sup>19</sup>

The major challenges inherent to all AOPs remain: i) formation and toxicity assessment of products; ii) ROS scavenging by organic and inorganic matrix components undermining the performance;<sup>19, 36</sup> iii) system design allowing the scale-up of the process; and iv) high energy demand.<sup>37</sup> Additionally, not all AOPs achieve efficient disinfection and some may even produce hazardous by-products.<sup>37</sup> For instance, ozonation – one of the most implemented AOP techniques – can result in the formation of toxic non-biodegradable bromates, which are known to be carcinogenic.<sup>38</sup> This problem has been partially circumvented by i) maintaining O<sub>3</sub> concentration very low,<sup>39</sup> ii) implementing ozone membrane contactors,<sup>40</sup> iii) providing RO or NF pre-treatment for bromide removal.<sup>41</sup> Although ozone treatment is effective for removing SHs and other MP,<sup>42</sup> dealing with toxic ozone necessitates extensive training of personnel that limits its use in low-maintenance water treatment systems.

To avoid dosing and storing ROS precursors (O<sub>3</sub> or H<sub>2</sub>O<sub>2</sub>), ROS generation can be realized by using catalytic materials. These can be activated with various stimuli, such as electricity (electrochemical oxidation),<sup>43</sup> light (photocatalysis),<sup>44</sup> magnetic fields (magnetoelectric effect-induced catalysis),<sup>45</sup> mechanical stress (piezoelectrochemical oxidation).<sup>46</sup> A strong advantage is the ability for these technologies to be successfully integrated into modular systems,<sup>19</sup> wherein the (decentralized) oxidative treatment is customized to the water quality parameters and the existing infrastructure.<sup>47</sup> Reducing the energy demand to the level of the benchmarked processes (chlorination, ozonation) appears to be the main roadblock on the avenue towards the industrialization of catalytic AOPs.<sup>37</sup> Accordingly, renewable (solar, wind, geothermal) energy sources to drive the oxidation process will have a head-start in the future threatened with depletion of non-renewable recourses.<sup>48</sup>

In a broad span of AOPs, photocatalytic water treatment (PWT) has acquired more “scientific hype” than any other process.<sup>49</sup> One benefit of photocatalysis is that the energy of (sun)light is supplied for chemical transformation of pollutants into potentially safe oxidation products (and ultimately to carbon dioxide and water) under mild conditions.<sup>44</sup> Also, the technology lacks intensive use of chemical reagents (or even toxic ones; e.g., ozone) strongly relying on photocatalyst, oxygen and dissolved species. The available information on MP removal with photocatalysis is often based on studies carried out using aqueous solutions with target pollutants added at concentrations ( $\mu\text{g L}^{-1}$ – $\text{mg L}^{-1}$ ) not appropriate to the environment. The mechanism and efficiency of photocatalytic oxidation of MP at realistic levels ( $\text{ng L}^{-1}$ ) remain still underdeveloped.

## Photocatalytic Membranes in Water Treatment

Considerable advances in abatement of water-borne micropollutants (e.g., SHs) were shown via the combination of membrane filtration with photocatalytic oxidation.<sup>50, 51</sup> Photocatalytic membranes (PCMs) are distinct from the other photoreactor designs for two reasons: i) the photocatalyst sits firmly on the membrane that excludes catalyst recovery (which is energy-consuming) causing membrane fouling; and ii) forced convective mass transfer through the membrane can resolve the resistance of external diffusion of reactants to the catalyst surface.<sup>52</sup> The latter point is particularly appealing, because inefficient application of produced reactive oxygen species (ROS) remains a key technological hurdle for heterogeneous photocatalysis.<sup>36, 53</sup>

While semiconductor-coated membranes (e.g., titanium oxide) are effective in removing micropollutants from waste- and surface waters, they lack the attribute of visible-light response, preventing them from harvesting solar energy.<sup>54</sup> When it comes to using sunlight energy to produce chemical energy, nature knows better. The process of photosynthesis, whereby plants produce chemical energy, relies on porphyrin

molecules (among other components). These are critical elements of chlorophyll pigments in photosystems I and II. Regardless of the appeal of mimicking nature, implementation of porphyrins and other photosensitisers in PWT remains challenging. For photosensitiser-coated membranes to develop competitiveness in water treatment, they must: i) reduce micropollutants to a level set by regulatory agencies; ii) be economically viable (using abundant materials); and iii) resist prolonged exposure to UV–visible light. It is vital to acknowledge and comprehend the underlying limiting factors and materials involved in the photocatalytic process.

## 1.2 Objectives and Outline of the Thesis

This thesis will demonstrate that a palladium-porphyrin-coated polyvinylidene fluoride membrane can achieve efficient single-pass (without recirculation of the treated water) elimination of SHs at nanogram-per-liter concentrations (removal up to 98%) under visible light excitation, including sunlight generated via an accurate solar simulator. Hence, such visible light-responsive systems should be interesting for photocatalytic water treatment applications. Using the facile method of adsorption, membranes of various areas can be easily coated with good control over the amount of loaded porphyrin that leaves room for scaling up of the process. Note that the studies showing the performance of decontamination process under real conditions (sunlight, cloudiness, water containing natural organic matter) have not been undertaken by the author.

In summary, the following objectives are set in this thesis:

1. Demonstrate the degree of degradation both for real (steroid hormones) and model pollutants (organic dyes) in single-pass continuous-flow experiments;
2. Determine the influence of membrane support, porphyrin type (nature of coordinated metal), the photosensitizer loading, operational parameters (water flux, light intensity), and solution chemistry (pH, pollutant concentration, background electrolyte) on degree of removal and kinetics of the process;
3. Undertake photostability studies of membrane-loaded photosensitizer to determine the material longevity and thus practical feasibility of prolonged sunlight exposure;
4. Develop a technique to separate and quantify the steroid hormones at environmental concentrations.

The flow chart of the thesis structure is illustrated in Figure 1.2.

The theoretical background of the work is established in **Chapter 2**. The chapter encompasses: i) the current state of SH micropollutants found in aquatic environments (origin, fate and the adverse effects on human and wildlife health); ii) the fundamentals of the photocatalytic water treatment using organic photosensitizers. Based on a survey of existing literature on photocatalytic membranes, scientific gaps in current knowledge of PWT using porphyrin-coated membranes have been identified.

**Chapter 3** describes in detail the materials, experimental system, techniques used for preparation, characterization, and evaluation of photocatalytic performance. **Chapter 4** introduces the fabrication of Pd(II)-porphyrin-coated membranes and details the characterization of optical and photophysical properties. Furthermore, the photocatalytic activity of PCM has been successfully demonstrated in degradation experiments using a model contaminant (methylene blue dye). **Chapter 4** also covers the effect of extended illumination on the chemical stability of porphyrin-coated membranes and reveals the transformation products of methylene blue degradation and porphyrin photobleaching.

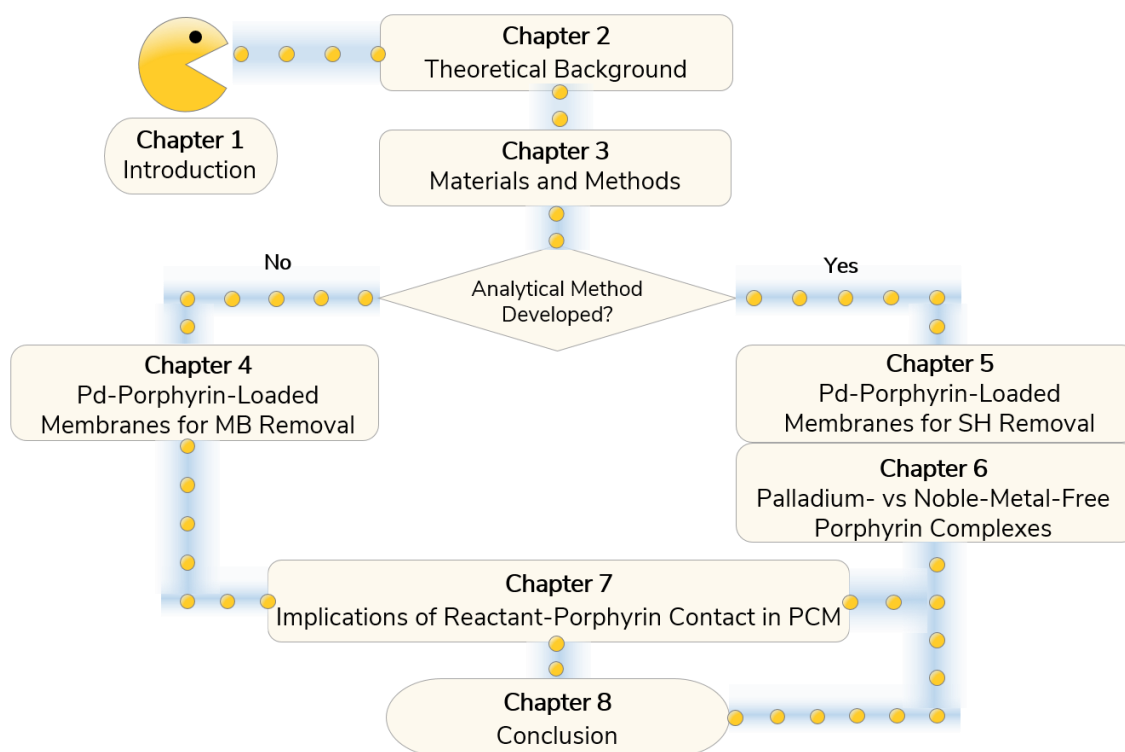


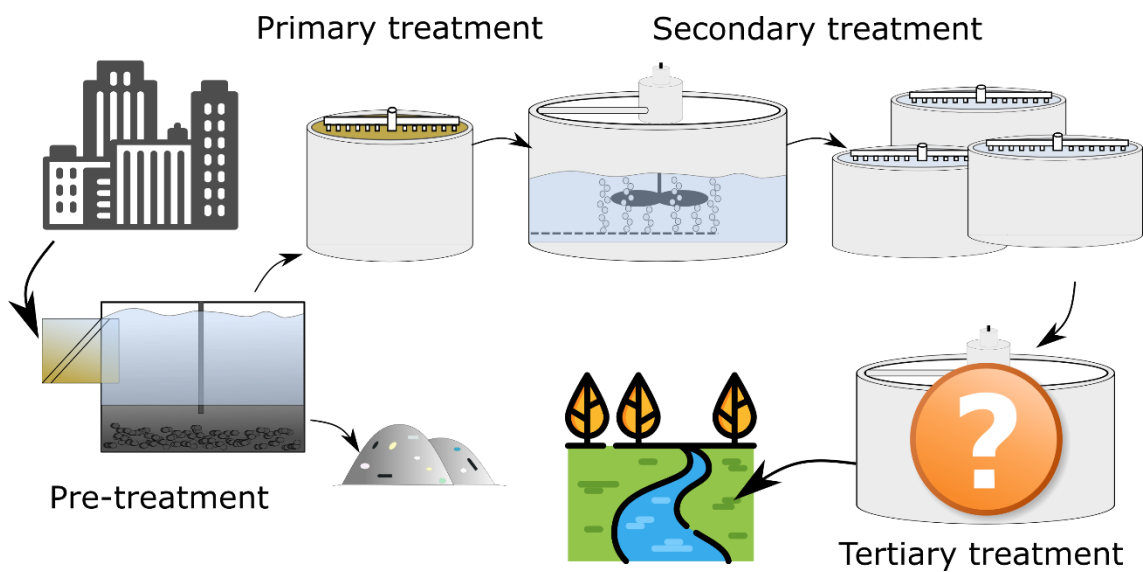
Figure 1.2 Illustration of the structure and topics covered in the thesis

**Chapter 5** presents the results of experiments that exploit the previously developed Pd(II)-porphyrin-coated membranes for the removal of steroid hormones at nanogram-per-liter concentrations. For this, a new analytical method based on liquid chromatography and flow scintillation analysis (UHPLC-FSA) has been developed. This analytical tool allows direct analysis without preconcentrating trace amounts of analytes and therefore accurate examination of the effects of process parameters and limiting factors of degradation kinetics.

The effect of exchanging Pd-containing porphyrin with more abundant noble metal-free counterparts is revealed in **Chapter 6**. The presence or absence of a coordinated metal ion in the central cavity of porphyrin molecules strongly affects the photophysical properties, photostability, and overall photocatalytic activity of photosensitizer-coated membranes (singlet oxygen quantum yield). Given one of the key discoveries of Chapter 5 (mass transfer-limited regime), **Chapter 7** examines how the morphology of the porphyrin-loaded membrane affects the  $17\beta$ -estradiol photodegradation process. This chapter reveals the interplay of surface area, mass transfer of reactants, and reaction kinetics using six PVDF membranes distinct by the pore size and thickness.

**Chapter 8** summarizes the results of the experimental chapters and provides a conclusion on this thesis, as well as the recommendations for future research. Chapter 8 is followed by an appendix that presents the raw data from the photocatalytic experiments not presented in the main chapters. The bibliography is placed at the end of the thesis.

# 2 Theoretical Background



The chapter gives a brief literature review on the origin, occurrence, physical and toxicological properties of steroid hormone micropollutants in water bodies. The instrumentation for analysis of steroid hormones in natural and synthetic (laboratory) water at the part-per-trillion level has been thoroughly examined.

This chapter also provides the key fundamentals of photocatalysis and defines the limitations of photosensitizers and photocatalytic membranes for application in water treatment. The process parameters, their influence on oxidation kinetics and the metrics of treatment efficiency have been described. Overall, this chapter creates the theoretical framework for the ideas and concepts tested in the empirical chapters.

## 2.1 Organic Micropollutants

Owing to the slump in mortality rates, exponential population growth has dealt humanity an ultimate challenge: supply of food and clean water in times of ever-increasing demand. Industrialisation has helped somewhat mitigate hunger, yet brought up the requirement for energy, which threatens to cut natural water supplies. Notably, food and energy production require fresh water, which in turn consumes energy for the decontamination/remediation process. This relationship is commonly referred to as the water-food-energy-nexus.<sup>5</sup> In other words, the dependence of activities of water-intensive agricultural and energy sectors on extensive use of natural and synthetic chemical compounds leads to water pollution, which to date echoes in all parts of the world.<sup>8</sup> For clean water to be assured, frequent monitoring and effective methods of water remediation needs to be implemented starting from the treatment of natural water.

### 2.1.1 Macro- and Micropollutants

Natural water is, by definition, not safe for drinking, because it contains metals, salts, acids, nutrients, natural organic matter. Both water treatment plants and scientific laboratories are well established for monitoring and controlling the chemical compounds present in water bodies at microgram to milligram concentrations and thus referred to as macropollutants. The origin, impact on the aquatic environment, mechanisms, and methods of macropollutant removal are comparatively well established.<sup>55, 56</sup>

To that end, challenges still exist with other organic trace pollutants of natural or synthetic origin. These carbon-containing compounds – revealed in the environment at low ( $\text{ng L}^{-1}$ ) to ultra-low ( $\text{pg L}^{-1}$ ) concentrations – are collectively known as micropollutants (MP).<sup>57, 58</sup> To the classes of MP belong industrial chemicals,<sup>59</sup> consumer products,<sup>60</sup> pesticides,<sup>16</sup> pharmaceuticals,<sup>61</sup> SH,<sup>62</sup> transformation products.<sup>63</sup> Many of the chemicals are persistent and tend to accumulate in the aquatic environment, triggering adverse biological effects to the living organisms.<sup>13</sup> During recent decades, monitoring and toxicology studies have given rise to public concern regarding MP in surface waters due to potential contamination of drinking water. The origin, major sources, and negative effects of MP are summarised in Table 2.1.

In this thesis, the class of SH was selected as target pollutants from a wide variety of MPs, due to the broad spectrum of exposure effects at extremely low concentrations ( $\text{ng L}^{-1}$  range). This presents a problem both for the analysis and the treatment of steroid hormone-polluted water as mentioned in the following sections.



Table 2.1 Overview of main micropollutant classes, the major sources and toxicity effects

Class of MP	Origin/field of use	Source (Route)	Exposure effects
Biocides	Bactericides, Fungicides Herbicides Insecticides Rodenticides Pesticides	Domestic effluents (from cleaning, gardening, household pest control) Agricultural run-off	Microbial toxicity Growth of pesticide resistance Endocrine system disruption (in mammals)
Consumer products	Cosmetics Detergents Disinfectants Fragrances Preservatives UV-filters	Domestic effluents (from bathing, washing)	Bioaccumulation Long environmental half-lives Acute toxicity Endocrine system disruption
Industrial products	Flame retardants Lubricants Plasticizers Solvents Perfluoroalkyl substances	Industrial wastewater Domestic effluents (from leaching and migration) Rainwater (from evaporation)	Bioaccumulation Acute toxicity Endocrine system disruption Cause of different types of cancer
Pharmaceuticals	Antibiotics Antidepressants Painkillers Beta-blockers	Domestic effluents (from excretion) Hospital effluents	Growth of antibiotic resistance Endocrine system disruption
Steroid hormones	Natural hormones Growth promoters Human and veterinary therapy Oral contraceptives	Domestic effluents (from excretion) Agricultural run-off (from animal farms)	Endocrine, immune, and reproduction system disruption (in fish, mammals); Cause of different types of cancer
Transformation products	MP metabolites Disinfection and biooxidation by- products	Wastewater (due to natural or chlorination ozonation-induced transformation)	Cause of different types of cancer Mutagenic effects

### 2.1.2 Steroid Hormone Micropollutants in Water Bodies

All steroid hormones (SH) share the tetracyclic steroid skeleton, as shown in Figure 2.1. Naturally produced steroid hormones modulate multiple physiological processes in humans and other vertebrates.<sup>64</sup> In contrast, synthetic SHs are artificially devised to result in therapeutic effects (such as those in contraceptive pills).<sup>65</sup> Both natural and synthetic SH are released through excretion into sewers or the environment mainly in a conjugated, less biologically active form (with glucuronide and sulfate groups).<sup>66</sup>

However, as a result of enzyme-induced hydrolysis, conjugated SH can be transformed in the environment or during the water treatment process to their corresponding free forms thus resulting in underestimation of removal efficiency.<sup>14</sup>

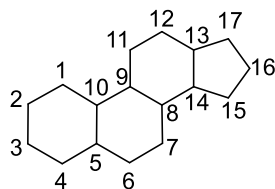


Figure 2.1: General chemical structure of steroid class of hormones. The atom numbering (including the tritium isotopes) is in accordance with the International Union of Pure and Applied Chemistry (IUPAC) nomenclature

### Occurrence

The primary route of SHs entering the environment is anthropogenic: use of birth control pills, hormonal therapy, agricultural wastes from animal manure, livestock feedlots. For instance, the release of estrogen hormones, including estrone and  $17\beta$ -estradiol, from animal farms (poultry, cow, and horse manures) in the UK has reached 1,315 and 570 kg per year, respectively.<sup>67</sup> This amount ( $1.6 \cdot 10^6$  mg/day of  $17\beta$ -estradiol) is by far more than the average excretion by humans (0.0077 mg/day)<sup>68</sup> even during the pregnancy (0.28–0.6 mg/day).<sup>69</sup> An additional route for SH to enter the aquatic environment is via improper disposal of contraceptive pills or medicaments flushed to the sewers or as solid waste. Municipal and hospital effluents processed on treatment plants can additionally contribute to estrogen pollution due to incomplete removal. Overview of the organisation and challenges of the modern water treatment process is given in **Chapter 1**.

Table 2.2 summarizes the occurrence of  $17\beta$ -estradiol in addition to other selected SH, such as estrone, testosterone, and progesterone in wastewater influents/effluents and surface water.<sup>70</sup> Discovery of SH in surface, groundwater<sup>13</sup> and even drinking water<sup>70-72</sup> has come to be a huge public concern because of the potential for these to interfere with the normal functioning of flora and fauna.<sup>12</sup> Despite the scarce studies confirming the SH concentrations above PNEC in drinking water, the sustainable use of surface waters as a preventive measure is recommended.<sup>73</sup> Considering the relatively low PNEC (shown as well in Table 2.2), SH are highly biologically potent substances. At  $\mu\text{g L}^{-1}$ – $\text{ng L}^{-1}$  concentration, these chemicals are reported to result in abnormal sexual development<sup>10</sup> and cause different cancer variants.<sup>74</sup> The reports indicate that exposure to endocrine-disrupting chemicals, such as SH, may impair semen quality and male fertility. Yet, there is no to date solid evidence of such effects in humans.<sup>75, 76</sup>

Table 2.2 The occurrence of SH in wastewater influents/effluents and surface water in comparison to the predictive no-effect concentration

Steroid hormone	Concentration <sup>a</sup> , ng L <sup>-1</sup>			PNEC <sup>b</sup> , <sup>18</sup> ng L <sup>-1</sup>	Ref.
	Wastewater influent	Wastewater effluent	Surface water		
17 $\beta$ -estradiol	<0.1–285	0.1–96	<0.2–134	0.04	14, 77, 78
Estriol	<0.1–517	<0.2–100	0.03–4.5 10 <sup>4</sup>	67	14, 78, 79
Estrone	<0.2–500	<0.2–80	0.5–1.5 10 <sup>3</sup>	3.6	9, 14, 78
Ethinyl-estradiol	<1–78.4	<0.6–12.3	0.1–460	0.004	78, 80, 81
Testosterone	<0.3–258	<0.1–10	<0.5–35	1000	77, 78, 82–84
Progesterone	<0.8–342	<0.4–8	<0.06–300	200	77, 78, 84, 85

<sup>a</sup> the concentration range is reported on the basis of the limit-of-quantification of the analytical method and the highest reported concentration

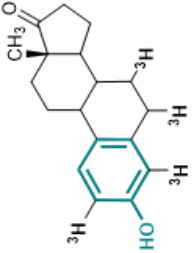
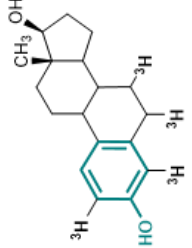
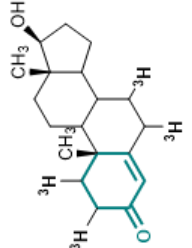
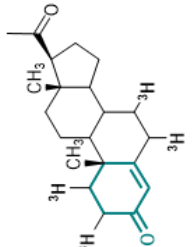
<sup>b</sup> Predicted No Effect Concentration

### Toxicology

The especially apparent deviations in reproductive behaviour, central nervous system, and gender differentiation have been observed in fish, birds, reptiles, and mammals exposed to elevated concentrations of SH and other endocrine disruptors.<sup>12, 86–88</sup> Moreover, the SHs are prone to accumulate and biomagnify in tissues, resulting in increased concentrations in animals of higher trophic (food chain) level.<sup>89</sup> The effect of estrogens in surface water on the fish population is controversial. A study by Kidd et al. revealed the reduced reproductive success of fathead minnow fish in addition to feminization of males after exposure to 5–6 ng L<sup>-1</sup> of ethinylestradiol.<sup>90</sup> Interestingly, the same research group conducted a seven-year field study on the lake that exhibited the recovery of the fish population after its original decline in presence of 5–6 ng L<sup>-1</sup> of ethinylestradiol.<sup>91</sup> A study by Schubert et al. informed no difference in the reproductive capability of brown trout after 150 days of exposure to water containing estrone (14 ng L<sup>-1</sup>) and 17 $\beta$ -estradiol (2 ng L<sup>-1</sup>).<sup>92</sup> Overall, drawing parallels between human and animal exposure is not practical or meaningful, as often the studies have little consistency due to different light doses (in kWh). The effect of SH on growth and photosynthesis in plants is ambiguous and must be further examined.<sup>12</sup>

In this thesis, four natural SHs were selected due to the growing occurrence in an aquatic environment and its strong impact on humans and wildlife. Table 2.3 demonstrates the selected physicochemical properties and the relative estrogenic potency of the SHs. Estrone and 17 $\beta$ -estradiol are important natural estrogens, which dissociate around pK<sub>a</sub> = 10.2–10.8 due to the presence of a phenolic functional group. Testosterone (from the group of androgen SH) and progesterone (precursor to estrogen) molecules lack phenol groups and thus remain neutral in the pH range from 3 to 12. This difference in chemical structures will influence the efficiency of photocatalytic removal, as described in Chapters 5–7. Hydrophobicity and quantity of hydrogen bond donors/acceptors affect the interaction of SH with hydrophobic surfaces that will be covered in Chapters 5 and 6 as well.

Table 2.3 Physicochemical attributes of steroid hormones employed in this thesis.

Characteristic	Estrone	17 $\beta$ -estradiol	Testosterone	Progesterone	Ref.
Molecular weight, g mol <sup>-1</sup>	270.4	272.4	288.4	314.5	
Solubility: in water, mg L <sup>-1</sup>	0.8–1.5 (22–25 °C)	1.7–3.9 (at 20–25 °C)	22.8–70.1 (at 20 °C)	6.9–10.1 (at 20 °C)	93-97
Solubility: in methanol, mg L <sup>-1</sup>	5.2·10 <sup>3</sup>	2.6·10 <sup>4</sup>	---	5.4·10 <sup>4</sup>	98–100
Solubility: in ethanol, mg L <sup>-1</sup>	6.8·10 <sup>3</sup>	2.9·10 <sup>4</sup>	2.2·10 <sup>5</sup>	---	98, 99, 101
Relative <sup>a</sup> estrogenic activity (-)	0.02–0.45	1	10 <sup>-4</sup> –10 <sup>-2</sup>	2·10 <sup>-2</sup>	102, 103
pK <sub>a</sub> (-)	10.3–10.8	10.2–10.7	not defined	not defined	94, 104, 105
Hydrogen bond donor (acceptor)	1 (2)	2 (2)	1 (2)	0 (2)	
Structure					106–109

<sup>a</sup> based on PNEC levels, using 17 $\beta$ -estradiol as the reference compound;

### *Regulation and Detection of Steroid Hormones*

Considering the strong endocrine-disrupting effect and bioaccumulation of SH, legislative control over these substances has intensified over the years. The initial act of acknowledgment issued by the European Union was the Directive 2008/105/EC, adding 17 $\beta$ -estradiol and ethinylestradiol to the list of compounds requiring close monitoring in drinking water. The European Commission Scientific Committee on Health and Environmental Risks then suggested the environmental quality standard for 17 $\beta$ -estradiol in surface water at 0.4 ng L<sup>-1</sup>.<sup>110</sup> In 2012, the US Environmental Protection Agency (EPA) introduced a regulation in the safe drinking water act that forced water suppliers to monitor among other pollutants one synthetic (ethinylestradiol) and six endogenous (originating from organisms) steroid hormones, including estrone and 17 $\beta$ -estradiol, testosterone and estriol.<sup>111</sup>

The Directive 2020/2184 secured the status of 17 $\beta$ -estradiol in the watch list and established the guideline concentration at 1 ng L<sup>-1</sup> in water intended for human consumption.<sup>15</sup> The first watch list including the benchmark value for 17 $\beta$ -estradiol was finally adopted on January 2022. To meet such a stringent quality standard and toxicology thresholds (PNEC), the monitoring relying on ultrasensitive analytical tools need to be conducted. Table 2.4 provides a comparison of contemporary analytical methods for SH analysis. One of the most powerful and frequently used analytical methods – also recommended by US EPA and Directive 2008/105/EC – is ultra-high-performance liquid chromatography (UHPLC) coupled with tandem mass spectrometry (LC-MS/MS). However, the state-of-the-art LC-MS/MS instruments struggle to offer a sufficient limit-of-quantification (LOQ < 1 ng L<sup>-1</sup>) without enrichment of analytes.<sup>112</sup> Notably, conventional electrospray ionization mode provides low ionization of non-polar SH at low concentrations.<sup>113</sup>

One workable solution to the lack of sensitivity is the extraction (for example, solid-phase extraction) of analytes. To that end, this procedure introduces another error due to variable or incomplete recovery.<sup>114</sup> The rising errors can compromise the finding and thus the overall efficiency of treatment. Secondly, ultra-low (pg L<sup>-1</sup>) concentrations require enrichment factors of 10 to 1,000 and consequently large volumes of water (250 to 4,000 mL).<sup>115-117</sup> However, large sample volumes are not always available for laboratory experiments when it comes to developing new methods of water purification and studying process kinetics.

Gas chromatography coupled with tandem mass spectrometry (GC-MS/MS) is comparable to LC-MS/MS relating to sensitivity (0.17 ng L<sup>-1</sup> for 17 $\beta$ -estradiol)<sup>70</sup> after pre-concentration of SH and provides exceptional peak resolution. The analysis of non-volatile SH is feasible only after the derivatization procedure, whereby analytes are transformed into the compounds with an additional moiety improving the volatility, thermal stability, and ionization of overall molecule.<sup>118</sup> Similar to the off-line extraction step, derivatization is a labor-intensive procedure that strongly restricts the sample throughput and can be a source of error.<sup>119</sup>

An alternative method is implemented using the liquid scintillation counting (LSC) method. While LSC is not suitable for real water samples, the method does not require sample preparation steps and is apt for routine measurement of radiolabelled SHs at sub-ng L<sup>-1</sup> concentration concentration (see Table 2.4). The LSC principle is based on the scintillation effect, that is, the emission that occurs when a scintillator (scintillation liquid) comes into contact with ionizing radiation from the decay of a radionuclide.<sup>120</sup> The LSC method is unable to separate analytes prior to detection that limits its use by non-destructive water treatment methods (membrane filtration, adsorption) and single-compound studies. Exact feeding of the scintillation liquid into the flow cell enables in-line scintillation counting, often referred to as flow scintillation analysis (FSA).

Table 2.4: The comparison of GC-MS/MS, LC-MS/MS, and scintillation methods for analysis of SH micropollutants

	LOQ <sup>a</sup> , ng L <sup>-1</sup>	Advantages	Disadvantages
GC-MS/MS	0.04–4.0 <sup>121</sup> (after derivatization)	Excellent sensitivity and chromatographic resolution Apt for target and non-target analysis	Derivatization required for non-volatile or thermally unstable analytes Extraction required to achieve low LOQ levels
LC-MS/MS	1.0–5.0 (direct injection) <sup>112</sup> 0.1–4.0 (after extraction) <sup>114</sup>	Excellent sensitivity Excellent chromatographic resolution	Extraction required to achieve low LOQ levels Signal suppression by matrix interference
LSC	0.1–0.9 <sup>122</sup>	Apt for low-concentration and low-volume samples (no sample preparation) Rapid single-component analysis	Not suited to natural water No analyte or by-product separation Identification of non-target analytes is not possible
LC-FSA	1.7–2.4 <sup>123</sup>	Apt for low-concentration and low volume samples Analysis of single- and multi-component mixtures	Not suited to natural water Identification of non-target analytes only possible with in-line connected MS

<sup>a</sup> provided for estrone and 17 $\beta$ -estradiol

Both LSC and FSA are widespread methods for metabolite and drug discovery/analysis in biosciences dealing with many low-concentrated samples.<sup>124, 125</sup> For a wider variety of applications, an FSA device can be coupled as an in-line detector to an LC instrument. The LC-FSA instrument allows the analysis of gradually eluted multi-component radiochemical mixtures without compromising sample throughput. Although there exist studies using the LC-FSA method for quantification of certain SH at  $\mu\text{g L}^{-1}$  concentrations,<sup>126–128</sup> there have been no reports on the FSA method applied for measurement of selected steroid hormones at  $\text{ng L}^{-1}$  concentration. Additionally, the rapid growth of small particle-size LC columns has ushered in the era of UHPLC operating at high pressure, improved resolution, and decreased runtime.<sup>129</sup>

Besides the work being part of this thesis,<sup>123</sup> the studies reporting the UHPLC-FSA for SH analysis are missing. Lack of studies may suggest limited compatibility between UHPLC and FSA instruments. Strong peak dispersion was observed when trying to resolve narrow analyte peaks in a large flow cell of FSA-detectors (40–1000  $\mu\text{L}$ ).<sup>130</sup> Despite the given challenge, this approach appears promising for the separation and quantification of SH and degradation products at minimal LOQ. Therefore, it is desirable to develop the UHPLC-FSA method for analysis of individual radiolabeled SHs and their mixtures. The operation of the FSA detector and its coupling with the UHPLC instrument is described in detail in **Chapter 3**.

### 2.1.3 Summary

Organic micropollutants, specifically SHs, slowly transition from the category of emerging pollutants to regulated contaminants. Given their mostly anthropogenic origin, elevated concentrations have been

observed in wastewater streams and surface water. The detection of steroid hormones breaching the PNEC level have potentially serious consequences on aquatic wildlife. The effects of high 17 $\beta$ -estradiol and ethinylestradiol concentrations on the animal population are controversial, yet the physiological or even morphological changes upon long-term exposure to SH cannot be ignored. To that end, a group of four SHs was selected as target contaminants, which encompass the classes of endogenous SH, such as estrogens (estrone, 17 $\beta$ -estradiol), androgens (testosterone), and progestogens (progesterone). Their analysis at an environmentally relevant level (ng L<sup>-1</sup>) would require a sensitive analytical instrument capable of tackling low-volume, low-concentration samples (e.g., FSA). Given the occasionally high levels of SH in influents and effluents of water treatment plant (WTP), there must be careful examination of the water treatment process to assess and remove the risk of accumulation of pollutants due to incomplete removal. In this context, oxidative technologies for water purification may be more useful than those that merely divert hazardous chemicals. The key fundamentals to using AOPs in water treatment are given in the next section.

## 2.2 Introduction to Photocatalytic Water Treatment

In 1987, Glaze et al. formally defined AOPs as techniques able to produce hydroxyl (HO<sup>•</sup>) radicals for oxidation of persistent water-borne contaminants.<sup>131</sup> Currently, a plethora of techniques fit the definition of AOPs, including Fenton-like processes, photolytic hydrogen peroxide- and ozone-based treatment, persulfate activation, photocatalysis, wet air oxidation, whereas the list of ROS has been expanded (see Table 2.5). High standard reduction potentials indicate the thermodynamic favorability of oxidation reactions of most organic compounds. However, oxidation efficiency is a function of i) kinetics, ii) stoichiometry, iii) water matrix, and iv) contact between the generated ROS and the pollutant molecules.<sup>132</sup>

Table 2.5: Types and properties of ROS involved in photochemical processes

	Half-equation	Standard potential, V vs. NHE (pH 7.0)	Lifetime in water, (pH 7.0)	Ref.
Sulfate radical	SO <sub>4</sub> <sup>•-</sup> /SO <sub>4</sub> <sup>2-</sup>	+2.60 – +3.10	30–40 $\mu$ s	133
Hydroxyl radical	HO <sup>•</sup> , H <sup>+</sup> /H <sub>2</sub> O	+2.3 (acidic)	<0.01 $\mu$ s	134
	HO <sup>•</sup> /HO <sup>-</sup>	+1.8 (neutral)		135
Ozone	O <sub>3</sub> , H <sup>+</sup> /O <sub>2</sub> , H <sub>2</sub> O	+2.08	1–10 <sup>3</sup> s	136
Hydrogen peroxide	H <sub>2</sub> O <sub>2</sub> , H <sup>+</sup> /H <sub>2</sub> O	+1.78	~10 h	137
	H <sub>2</sub> O <sub>2</sub> , H <sup>+</sup> /HO <sup>•</sup> , H <sub>2</sub> O	+0.46		
Carbonate radical	CO <sub>3</sub> <sup>•-</sup> /CO <sub>3</sub> <sup>2-</sup>	+1.59	<8,000 $\mu$ s	137
Superoxide anion	O <sub>2</sub> <sup>•-</sup> /H <sup>+</sup> , H <sub>2</sub> O <sub>2</sub>	+0.94	1–3,000 min	137
Singlet oxygen	<sup>1</sup> O <sub>2</sub> /O <sub>2</sub> <sup>•-</sup>	+0.65	(3.3 $\pm$ 0.5) $\mu$ s	138

### 2.2.1 Current Limitations of Semiconductor Photocatalysis

The first photochemical transformations using semiconductors date back to 1955.<sup>139</sup> Fujishima and Honda's report from 1978 on the electrochemical photolysis of water<sup>140</sup> sparked a scientific gold rush. The fact that the discovery of hydrogen production from water using titanium oxide (TiO<sub>2</sub>) came at the right time (after the oil crisis) resulted in the opening of a vast research niche promising cheap access to clean energy. The parental nature of this paper for the field of photocatalysis brought countless studies that discovered new appealing properties (low toxicity, affordable price, and strong oxidative power), fundamental mechanisms, and even new applications for TiO<sub>2</sub>.<sup>44, 141, 142</sup>

Despite an abundance of literature on photocatalytic water treatment and even pilot-scale efforts, a gap is widening between academic research and industrial needs.<sup>53</sup> A handful of commercially successful systems with a focus on water decontamination can be found, including Photo-Cat reactor from Purifics (Canada),<sup>143</sup> Puralytics process with portable SolarBag and Shield products (United States of America),<sup>144</sup> Titanium AOP reactor from Brightwater Environmental (United Kingdom).<sup>145</sup> Predictably, the technology readiness level (TRL) of heterogeneous photocatalysis for treatment of pharmaceutical and urban wastewater is estimated to be TRL2 (technology concept formulated) and TRL4 (technology validation in the lab), respectively.<sup>146</sup> More compelling appears the on-site treatment of agricultural wastewater (reached TRL6) because the vast areas necessary for harvesting solar illumination are not an issue in this industrial sector.<sup>146</sup>

The water regulations on the release of MPs in surface water that could promote the design and testing of pilot-scale reactors in the appropriate environment are still lacking. More importantly, the roadblock on the way to widespread commercialization of photocatalysis-based water treatment technologies stems from the main limitations of TiO<sub>2</sub> and photocatalysts alike: i) limited absorption in the visible part of the solar spectrum (3–5% of total energy); ii) low photoconversion efficiency of the process due to high recombination of electron-hole pairs, and iii) the strong scavenging of the produced ROS (HO<sup>•</sup>-radical) by the water matrix components (salts, organic matter).<sup>36, 53, 147</sup>

Significant effort has been devoted to decreasing the wide bandgap of TiO<sub>2</sub> (3–3.2 eV) by doping<sup>148–150</sup> or developing new narrow-gap semiconductors (WO<sub>3</sub>, SrTiO<sub>3</sub>, Bi-compounds),<sup>151–153</sup> which are active under the visible light. Additionally, the decoration of semiconductors' surfaces with quantum dots and dyes promotes the visible-light response.<sup>154, 155</sup> Overall, the percentage of publications related to visible-light photocatalysis has reached 2018 60% of all works in the field of photocatalysis.<sup>156</sup> Such inflated expectations, however, leave open the question of whether or not the improved visible-light absorption is worth the price of elevated recombination or reduced redox potential.<sup>53</sup> The high rate of recombination can be reduced by doping, introducing heterojunctions with other metals or carbonaceous materials (graphene),<sup>151</sup> though at the expense of intrinsic instability of the resulting material.<sup>53</sup> An alternative approach to achieve photodegradation and avoid the limitations of conventional TiO<sub>2</sub> photocatalyst is offered by organic photosensitizers (PS).<sup>157–160</sup>

## 2.3 Photosensitizer Selection

In the subsequent sections, the fundamental concepts of the photosensitization process, selection of promising PSs, and the challenges of using those for water treatment will be presented.



### 2.3.1 Definition and Examples of Photosensitizers

The definitions of photosensitizer and photocatalyst are similar. Upon excitation, PS molecules enable the chemical change in a substrate molecule, while photocatalyst accelerates the photoreaction. Additionally, for PSs operating via electron transfer pathway, the terms “photosensitizer” and “photocatalyst” can be used interchangeably. Up to the beginning of the 1970s, PSs were largely used for fine chemistry purposes (photooxidation or photooxygenation of different substrates). Currently, as well as synthetic goals, the applications of PSs have widened to include cancer treatment,<sup>161</sup> energy harvesting,<sup>162</sup> luminescent materials,<sup>163</sup> and photoredox catalysis.<sup>164</sup> Compared to the given above areas of research, photocatalytic water treatment using PS is a less studied application field, that remains in the shadow of the more appealing semiconductor-based photocatalysis.<sup>165</sup>

Several classes of PSs, which hold promise for water remediation purposes, are outlined in Table 2.6. Organic PS have several undeniable advantages over their inorganic counterparts: i) broad-band excitation falling in the range of the visible spectrum (300–800 nm);<sup>166</sup> ii) several distinct pathways for photooxidation and iii) high quantum efficiency of the activated reaction.<sup>167</sup> For photosensitizers to be suitable for water treatment, the subsequent requirements should be met: i) high absorption coefficient in the widest range of excitation wavelengths ( $\lambda_{exc}$ ); ii) high quantum yield of  $^1O_2$  production ( $\Phi_{\Delta}$ ) or other ROS; iii) stability over long exposure times (in the range of months); and iv) simple affordable synthesis, ideally on the basis of abundant materials. This dissertation addresses all four of these requirements, with a focus on the generation of singlet oxygen by membrane-bound PSs.

Table 2.6: The promising PS classes and their selected representatives.

	$\lambda_{exc}$ , nm	$\Phi_{\Delta}$ , (-) <sup>138, 168</sup>	Solvent	Stability	Costs (€/g) <sup>a</sup>
Classic dyes					
Methylene blue	630–660	0.5–0.6	H <sub>2</sub> O	low	low (3.4)
Rose Bengal	490–570	0.76–0.9	CH <sub>3</sub> OH	low	modest (78)
Polyaromatics					
Triphenylpyrylium tetrafluoroborate	300–450	– <sup>b</sup>	–	low	low (10.2)
Organometallic complexes					
Tris(2,2'-bipyridyl) ruthenium(II)	180–450	0.73	CH <sub>3</sub> OH	low	high (152)
Carbon nanostructures					
[C60]fullerene	340–550	0.7–1.0	C <sub>6</sub> H <sub>6</sub>	good	High (151)
Tetrapyrroles					
Iodinated BODIPYs	450–600	0.83	CH <sub>3</sub> CN	good	low (–)
Tetraphenylporphyrin	300–700	0.78	C <sub>6</sub> H <sub>6</sub>	good	modest (88)
Zinc Phthalocyanine	500–750	0.53	CH <sub>3</sub> CN	good	low (17.1)

<sup>a</sup> prices for chemicals (the purity in the range of 97–98%) were current as of 16.06.2022, as listed on the Sigma Aldrich (Germany) website;

<sup>b</sup> photoredox catalyst

### 2.3.2 Singlet Oxygen for Water Remediation

Molecular oxygen in its first excited state (referred to singlet state,  $a_1\Delta_g$ ) is highlighted in the list of existing ROS (see Table 2.5).  $^1O_2$  is a non-radical species with a substantially longer lifetime ( $\mu\text{s}$  range) compared to that of  $\text{HO}^\bullet$ -radical (ns range) produced by  $\text{TiO}_2$ . The dienophile nature of  $^1O_2$  enables the selective and fast oxidation of molecules with electron-rich moieties (unsaturated bonds, amine-, and sulfide groups).<sup>169</sup> The reactions of selected substrates with  $^1O_2$  are illustrated in Figure 2.2.

Considering the selective character, this variant of ROS is deactivated (quenched) to a lesser extent than  $\text{HO}^\bullet$ -radical by the inorganic ions occurring in water matrix.<sup>170, 171</sup> These characteristics render the process of  $^1O_2$ -mediated oxidation attractive for MP removal, specifically estrogenic SH (estrone, 17 $\beta$ -estradiol, estriol). The phenolic group in these SH molecules is necessary for the activation of estrogen receptors and, consequently, is responsible for an endocrine-disrupting effect.<sup>172</sup> Thus, the aromatic ring can also be the primary stage of the  $^1O_2$  attack on SH molecules. In contrast to the limited generation of  $^1O_2$  by bare  $\text{TiO}_2$ ,<sup>173</sup> the majority of PSs have a natural ability to produce  $^1O_2$  with a high yield under visible-light excitation.<sup>174</sup>

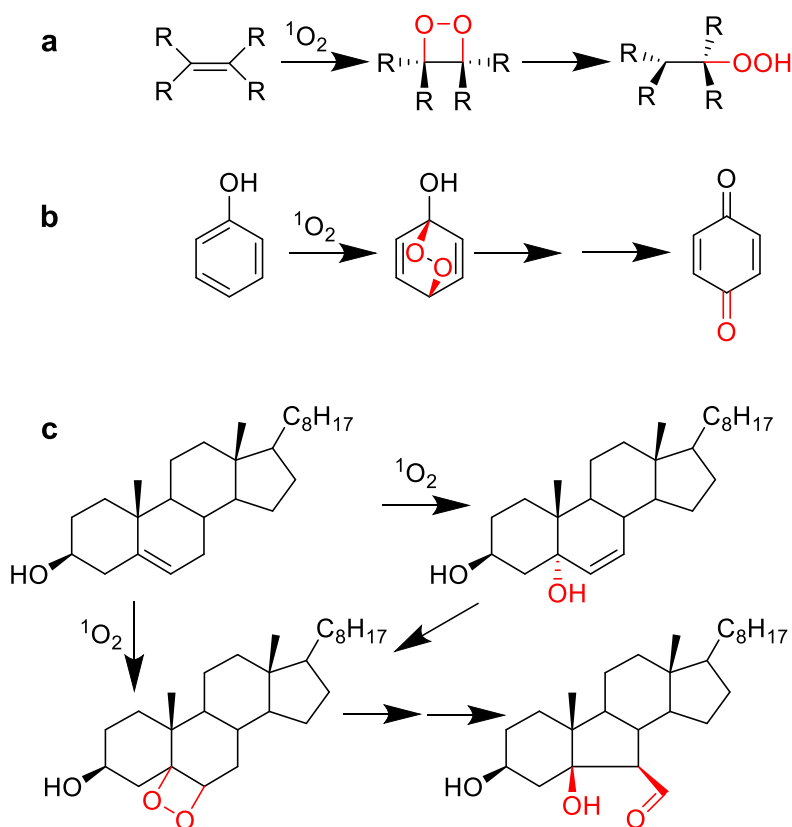


Figure 2.2: Reactions of **a**, olefin, **b**, phenol, and **c**, cholesterol molecules with singlet oxygen.<sup>175</sup>

### 2.3.3 Tetrapyrrole-Based PSs for Photocatalytic Water Treatment

In nature, there exists a plethora of substances, which are highly efficient systems for solar light harvesting. One such inspiring example is the tetrapyrroles, specifically, porphyrins (from the Greek “*porfura*” – purple). The notable derivatives of porphyrins are the plant pigments in photosynthesis (chlorophyll group)

and the precursors to haemoglobin binding oxygen in the blood of vertebrates (heme molecules). Porphyrins share the macrocyclic tetrapyrrole core (porphine), which is essentially a conjugated four-fold symmetric ring of four pyrroles. Reduction of one (chlorin) or two (bacteriochlorin or isobacteriochlorin) peripheral double bonds results in the establishment of a new compound, whose photophysical and photocatalytic properties are drastically different.

Examples of the chemical structures and electronic absorption spectra of the selected homolog of porphyrins and their derivatives are shown in Figure 2.3.

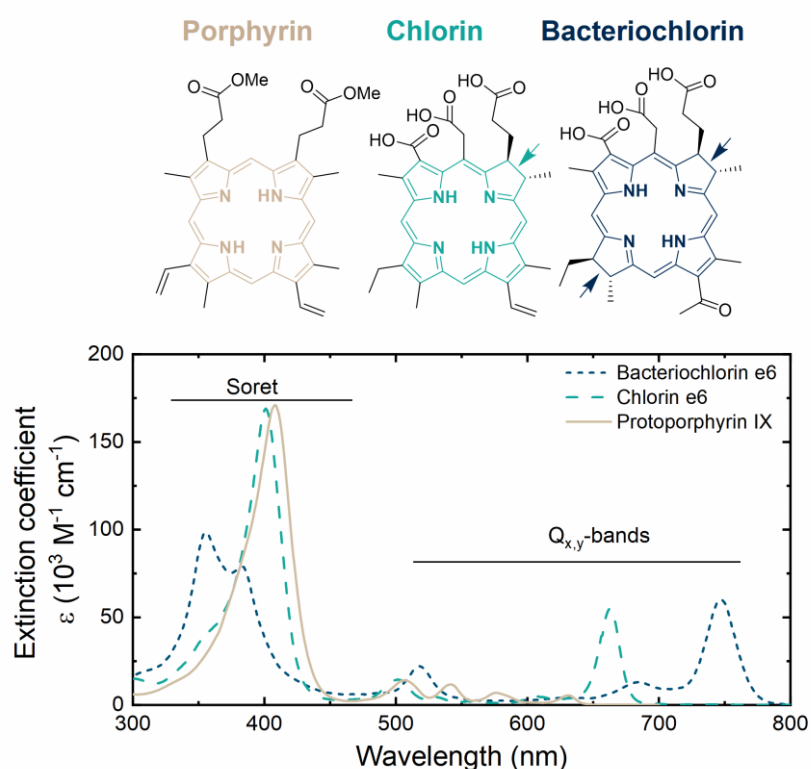


Figure 2.3: Chemical structures of selected porphyrin (Protoporphyrin IX used in photodynamic therapy), chlorin, and bacteriochlorin (occurring in nature) and their extinction coefficients as a function of wavelength. The arrows indicate the saturated bonds of the pyrrole rings for chlorin and bacteriochlorin. The spectra and extinction coefficients were obtained from PhotochemCAD 3 software<sup>176</sup> and reference.<sup>177</sup>

Usually, tetrapyrroles without a central metal ion (*free-base porphyrins*) exhibit four-banded absorption relating to the high- and low-energy states, which are called Soret-band (350–450 nm) and the Q-bands (500–800 nm). In accordance with the four-orbital model of Gouterman, the energy gap arising from the transition between the two highest occupied orbitals (HOMO) and the two lowest unoccupied orbitals (LUMO) of tetrapyrroles explains the shape of absorption spectra.<sup>178</sup> Due to the decreased symmetry of the molecules, chlorins tend to absorb more light in the red region ( $\lambda_{\text{exc}} > 650 \text{ nm}$ ) and less in the blue region. For bacteriochlorins, the Soret-band is even more blue-shifted and squashed, while the strong Q-band is in the near-infrared region. Strong absorption of light in the red region may be less useful than in the blue region (the highest transparency of light in water) or in the green region (the peak of sunlight emission). Notably, porphyrins effectively generate  $^1\text{O}_2$ , while triplet states of chlorins and bacteriochlorins may be involved in charge transfer reactions leading to radical formation. In this dissertation, porphyrins were

selected as the main class of studied PSs, because they meet the requirements for use in water treatment to a greater extent than other PSs: excellent ability to generate  $^1\text{O}_2$  under visible light excitation, great chemical versatility due to rich chemistry (see Figure 2.4), and good photostability.

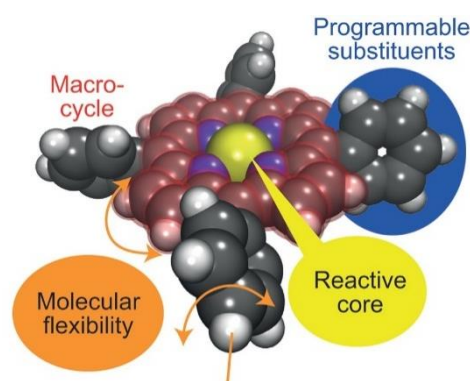


Figure 2.4: The rich chemistry of porphyrins enables the incorporation of metal centers via tetradentate coordination (yellow), molecular flexibility (orange), and tailoring the *meso*-substituents (blue) to a specific process and molecule properties. Arrows indicate the possibility of dihedral angle rotation and macrocycle distortions. Figure adapted with permission from ref.<sup>179</sup>(Nature Publishing Group).

### 2.3.4 The Mechanism of ROS Generation by Photosensitizers

The process of ROS generation either via energy or electron transfer is depicted in Figure 2.5. For the successful excitation of a PS molecule, the absorption of photon quanta ( $h\nu$ ) is necessary. If the energy of incident light ( $E_{inc,\lambda}$ ) exceeds the singlet state energy ( $E_{inc,\lambda} > E_S$  energy), the following processes occur: ① PS molecule transitions from a ground state ( $S_0$ , zero spin) to a short-lived and higher-energy singlet state (denoted  $S_1 \dots S_n$ ,  $n > 1$ ); ② the highest singlet state ( $S_n$ ) rapidly relaxes to the lowest excited state ( $S_1$ ) *via* vibration relaxation and internal conversion (IC,  $10^{-14} \dots 10^{-10}$  s); ③ from the  $S_1$  state the excited PS molecule ( $^1\text{PS}^*$ ) can return to the ground state by emitting light (fluorescence) or ④ lead to the population of triplet state ( $T_1$ ) via a non-radiative process of reversing the electron spin called intersystem crossing (ISC,  $10^{-10} \dots 10^{-8}$  s); ⑤ relaxation of excited PS molecule in  $T_1$  state ( $^3\text{PS}^*$ ) to the  $S_0$  state via emission decay (phosphorescence), ⑥ charge transfer to molecular oxygen ( $^3\text{O}_2$ ) or pollutant molecule (Q) nearby, or ⑦ energy transfer to the molecular oxygen ( $^3\text{O}_2$ ). The Type II reactions (the energy transfer to  $^3\text{O}_2$ ) lead to ⑧ the generation of metastable  $^1\text{O}_2$ , which is deactivated *via* radiative and non-radiative channels within  $\tau_\Delta$  lifetime. Despite a weak signal and short lifetime of  $^1\text{O}_2$  in water, IR phosphorescence measurement ( $\sim 1270$  nm) remains the most often used approach for both detection and quantification of produced  $^1\text{O}_2$ .<sup>173</sup>

For a PS molecule to have high  $\Phi_\Delta$ , the certain criteria need to be satisfied: i) fast ISC (quantum yield of triplet state close to unity); ii) long  $\tau_T$ ; iii) sufficient energy of triplet state ( $E_T > 94$  kJ mol $^{-1}$ ). The nature of peripheral substituents to the macrocycle and the centrally coordinated metal ion has strong implications on the given electronic properties. Introduction of a metal ion to the vacant site of free-base tetrapyrroles (*metalation*) affects: i) the shape and energy levels of frontier orbitals; and ii) the rate of ISC.<sup>180</sup> This allows metallotetrapyrroles to be highly efficient PSs as proven by PDT studies.<sup>181, 182</sup> For example, metals with high atomic weight (Pd or Pt) maximize ISC, and thus the transition to the long-lived triplet state (*heavy-atom effect*),<sup>183</sup> while increasing the probability of radiative relaxation for the excited triplet states.

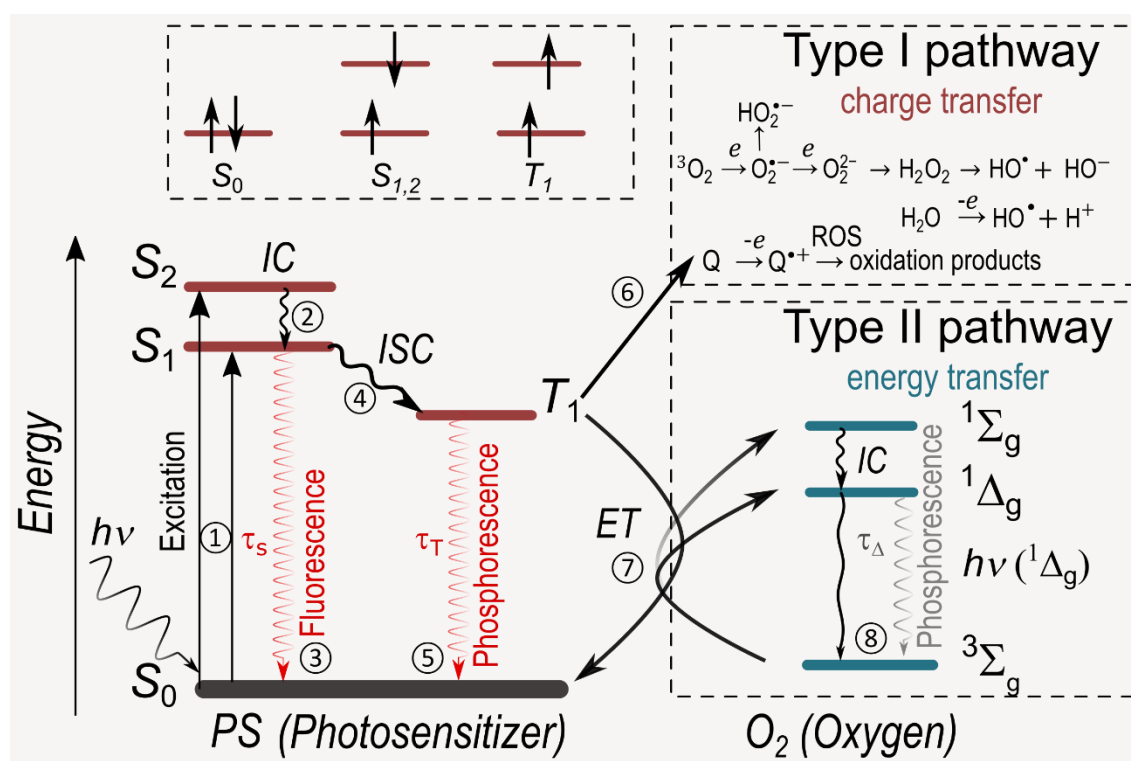


Figure 2.5: Energy diagram illustrating ① the generation (excitation) and ②–⑤ relaxation of excited states of PS molecule (not to scale) characterized by the corresponding singlet ( $\tau_s$ ) and triplet ( $\tau_T$ ) state lifetimes; two main pathways for triplet state ( $T_1$ )-induced ROS generation *via* ⑥ energy transfer ( $^1O_2$ ) or ⑦ charge transfer ( $HO^\cdot$ ,  $O_2^{\cdot-}$ ), and ⑧ (non-)radiative relaxation of singlet oxygen characterized by the  $^1O_2$  lifetime ( $\tau_\Delta$ ).  $Q$  – pollutant molecule,  $IC$  – internal conversion,  $ISC$  – intersystem crossing,  $ET$  – energy transfer. Figure adapted with permission from Lyubimenko et al. (2022)<sup>184</sup>; Copyright 2022 Elsevier.

It leaves the oxygen molecule hundreds  $\mu s$ -time to interact with the excited triplet state. The nature of the central metal ion has a strong influence on the rate of intramolecular deactivation of the excited state (*quenching*) for the studied porphyrins.

Those PSs coordinating metals with full – such as  $Zn^{+2}$  ( $3d^{10}$ ),  $Pd^{+2}$  ( $4d^{10}$ ) – or energetically unavailable ( $Mg$ ,  $3s^2$ )  $d$  subshell also tend to produce  $^1O_2$  with the highest yield.<sup>185</sup> Unlike Pd-porphyrins ( $\tau_T$  of hundreds of  $\mu s$ ),<sup>186, 187</sup> zinc counterparts exhibit limited ISC in solution, but very long lifetime (up to tens of ms)<sup>188</sup> that is favorable for photosensitized generation of  $^1O_2$ . Porphyrin complexes with transition paramagnetic metals - which do not have fully populated  $d$ -orbitals (such as manganese, cobalt, copper) – exhibit short-lived excited states and hence are poorly suitable for  $^1O_2$  generation.<sup>181</sup> Though cobalt, iron, and manganese porphyrins are able to act as photoredox catalysts,<sup>189</sup> the temperature-dependent properties of PS excited states limit their application in fields requiring high yield of ROS generation. The quenching constant of free-base porphyrin by molecular oxygen differs by an order of magnitude from Sn and Zn porphyrins.<sup>190</sup> Of particular note, is that metalation of tetrapyrroles is not a prerequisite for a highly efficient PS, because a lot of free-base porphyrins ensure a long triplet state lifetime and high yield for  $^1O_2$  generation.<sup>174, 191</sup>

Modification of peripheral substituents in the porphyrin macrocycle can add new physical functions (for instance, amphiphilic) or alter the optical properties (absorption, emission) of the macrocycle by means of changing the molecule conformation (planar or non-planar) and electronic transitions.<sup>182</sup> For example, halogen atoms can gradually induce a heavy-atom effect that raises triplet quantum yield.<sup>192</sup> A potent note

of the porphyrin molecular design is that introduction of the metal ion or peripheral groups to a macrocycle can change the redox potential of a molecule. Apart from the effect on affinity to electron transfer (Type I pathway), the rise of oxidation potential renders the PS rather more resistant to photobleaching.<sup>193</sup> Photostability, as well as ease and costs of synthesis, remains the main constraint to the widespread adoption of PS in water treatment processes. Therefore, these key points of PS selection are addressed in the Section 2.3.5.

### 2.3.5 Limited Photostability and Possible Solutions

As shown in Table 2.6, all organic PSs are not ultimately stable under continuous exposure to light, resulting in a loss of absorption, emission properties (photobleaching), decay of photocatalytic activity (deactivation), and finally photodegradation.<sup>194</sup> The PS instability can be attributed to “chemical” (ROS attack on PS molecule) and “physical” (thermodynamic instability upon frequent excitation/relaxation cycles) origins.

The factors controlling the rate of photobleaching are i) intensity and wavelength of the incident light;<sup>195</sup> ii) PS concentration in solution or on the surface;<sup>196</sup> iii) material of the host (if PS immobilized);<sup>197</sup> and iv) concentration of oxygen in the experimental environment.<sup>195</sup> Given the different reactivity of PSs towards photobleaching, an additional important criterion is the chemical structure of a PS. Due to the lack of control over the aforementioned parameters and more importantly the standard methods for verifying the photobleaching quantum yield ( $\Phi_{pb}$ ), it remains challenging to determine the photostability of a PS based on intra-laboratory studies. From the studies carried out in solution and at low excitations, it is seen that conventional chromophores (methylene blue, Rose Bengal)<sup>198</sup> and noble-metal coordination complexes (Tris(2,2'-bipyridyl)-ruthenium(II) dichloride) predominantly photobleach faster ( $\Phi_{pb} \sim 10^{-5}$ – $10^{-4}$ ) than porphyrins and phthalocyanines ( $\sim 10^{-6}$ – $10^{-4}$ ).<sup>199, 200</sup> The macrocyclic tetrapyrroles can withstand up to several days of illumination depending on the nature of substituents and the metal ion. Of particular interest are the BODIPY dyes, which offer both high  $\Phi_{\Delta}$  and high photostability ( $\Phi_{pb} \sim 10^{-7}$ – $10^{-6}$ ).<sup>201, 202</sup>

Table 2.7 summarizes the main strategies to improve photostability of PSs that focus on inhibition of i) excited triplet state formation; ii) generation of ROS and other radical species; iii) reaction of a PS molecule with produced ROS.<sup>201</sup> Among the named above strategies, only immobilization (suppression of bimolecular degradation reactions) and chemical modification of PS molecules do not influence the efficiency of photocatalytic water treatment. Indeed, the design and synthesis of PS molecules with electron-withdrawing (EWG)<sup>200</sup> or protective (rigid) groups may facilitate retardation of the oxidation process by steric or electronic factors<sup>203</sup> without interfering with the photocatalytic activity. For instance, halogen atoms allow the deactivation of the aromatic ring *via* electron-withdrawing inductive effect (–I effect) that additionally rises the molecule oxidation potential and hinders the  $^1O_2$  attack to the most labile place of PS (aromatic core, double bonds).<sup>204</sup> The positive effect of phenyl ring fluorination on photostability was observed for fluorinated tetrapyrroles used in optical sensing,<sup>205</sup> photocatalysis,<sup>206</sup> and biomedical applications.<sup>207</sup> Lee et al. reported that photoluminescent signal of 5,10,15,20-Tetrakis(pentafluorophenyl)porphyrin remains unchanged for 50 h when excited at  $\lambda_{exc} = 508$  nm.<sup>208</sup> An additional example is fluorinated bacteriochlorin that was stable for 15 months in solution exposed to  $50 \text{ mW cm}^{-2}$  laser irradiation.<sup>209</sup>

Table 2.7: Strategies and selected examples for improving the stability of organic chromophores

Inhibited steps	Strategies	Examples	Ref
$^1\text{PS}^* \xrightarrow{\text{ISC}} ^3\text{PS}^*$	Decrease population of $^3\text{PS}^*$	Plasmonic environment Addition or covalent attachment of $^3\text{PS}^*$ quenchers	210 211
$^3\text{PS}^* + ^3\text{O}_2 \xrightarrow{\text{ET}} ^3\text{O}_2 + ^0\text{PS}$	Reduce triplet state lifetime	Covalent attachment of $\tau_T$ -shortening moiety	212
$^3\text{PS}^* + ^3\text{O}_2 \xrightarrow{\text{ET}} \text{O}_2^{\cdot-} + ^0\text{PS}^{\cdot+}$	Oxygen depletion Hinder oxygen diffusion	Addition of antioxidants PS immobilization	197 213
$^0\text{PS}^{\cdot+} + \text{OH}^- \xrightarrow{\text{ET}} \text{HO}^\cdot + ^0\text{PS}$	Scavenge produced ROS	Enzymatic $\text{O}_2$ scavenging	214
$^0\text{PS} + \text{ROS} \rightarrow \text{PS}_{\text{oxidized}}$	Render a PS molecule resistant towards oxidation by ROS	Attachment of EWG <sup>a</sup> , bulky (protective) or rigid groups	215 216

<sup>a</sup>EWG – electron-withdrawing groups

Metalation of free-base tetrapyrroles can additionally improve photostability due to the effect of central metal ions on the electronic properties of PS molecules. Pd- and free-base porphyrin complexes are stated to be less photostable than their Zn-complex analogs.<sup>182</sup> This conclusion may be due to the better electron affinity of Pd-porphyrins and hence radical pathway for ROS generation than that of zinc complexes. To that end, there exists no correlation between the nature of the central metal ion and photostability and photocatalytic activity in terms of micropollutant oxidation.

This thesis work will focus on the group of 5,10,15,20-Tetrakis(pentafluorophenyl)porphyrins, which were selected on the basis of the following merits: i) high quantum yield of  $^1\text{O}_2$  generation under visible-light excitation; ii) high photostability; iii) hydrophobic character of a PS molecule preventing its leaching to water; and iv) commercial availability.

## 2.4 Challenges of Heterogeneous Photocatalysis

Immobilization of porphyrins involves several undisputed merits: i) the facilitation of a catalyst recovery step and separation from degradation by-products; ii) prevention of porphyrin agglomeration that is detrimental to  $^1\text{O}_2$  generation; iii) potentially improved photostability. Ceramic foams, polymer films, membranes, nanoparticles, nanofibers, non-woven fabrics, zeolites – are all adequate supports for the fabrication of effective porphyrin-based photocatalysts.<sup>168</sup> When selecting one of them, however, it is necessary to contemplate the disadvantages inherent in immobilization and, if possible, to minimize them.

### 2.4.1 Mass Transfer Limitation

The process of heterogeneous photocatalytic reaction, illustrated in Figure 2.6, can follow a slow interfacial oxygen mass transfer, resulting in suppression of ROS generation. Likewise, the attack of  $^1\text{O}_2$  on organic molecules within its short lifetime,  $t_\Delta = (3.3 \pm 0.5) \mu\text{s}$ <sup>138</sup>, requires the close contact of reactants. In the case of the small active (porphyrin-coated) surface area, the overall rate of pollutant oxidation may be limited

by the external diffusion of solutes through the boundary layer (steps ①, ⑧) to (from) the water-photosensitizer interface.

A popular practice to overcome external diffusion resistance is: i) reduction of the thickness of the boundary layer, for example, by stirring or increasing the flow velocity in reactors with an immobilized photocatalyst, or ii) to design the reactor with small channel dimensions in the *radial* (transverse) direction.<sup>217</sup> These methods are however futile against the hindered internal diffusion of reactants inside and outside the host matrix (steps ②, ⑦) that can be observed after PS encapsulation or impregnation of the microporous material. The application of highly porous materials allows for the distribution of PS over the large surface of a host and is hence favorable.

If the kinetics of one of the diffusion steps (①, ②, ⑦, or ⑧) is slow, the rate of mass transfer determines the overall volume-based reaction rate (mass-transfer controlled regime). Otherwise, the overall rate is limited by one of the reaction steps: ③ adsorption, ④ chemical reaction or ⑤ energy transfer reaction, or ⑥ desorption. The reaction rates are strongly dependent on the concentration in the boundary layer and for this reason not as fast as those with homogenous (one-phase) catalysts. This can be an issue for the oxidation of micropollutants found in the environment at nanogram- to microgram-per-liter concentrations.

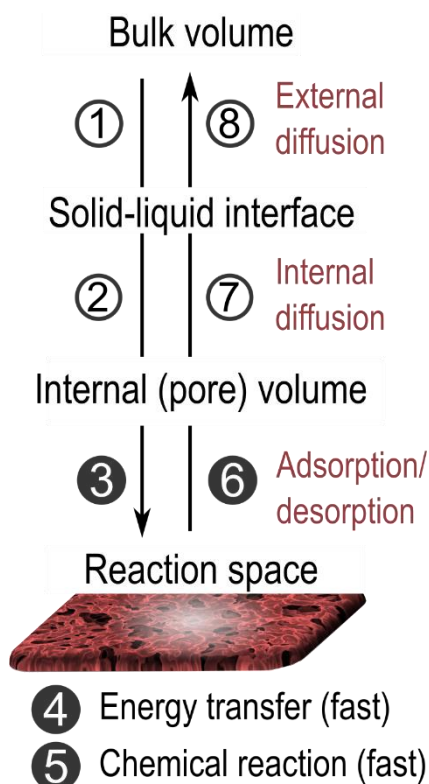


Figure 2.6: Principal steps of heterogeneous reaction between singlet oxygen and micropollutants, mass transfer and surface reactions.

## 2.4.2 Recovery of Suspended Particles from the Aqueous Phase

The external mass transfer is promoted in well-dispersed micro- or nanoparticle photocatalysts. The large illuminated interfacial area and the short distance between the reactants and the photocatalyst – both render diffusional mass transfer fast and barely rate-limiting.<sup>218</sup> This is demonstrated by the dominance of works



testing semiconductor photocatalysts in low-volume slurry reactors in batch mode, where mass transfer resistance is negligible.<sup>146, 219</sup> With little fanfare PS-functionalized nanoparticles have been assessed for water treatment applications,<sup>220, 221</sup> even though the major progress of attaching PS molecules to nanoparticles has been made in the field of photodynamic therapy.<sup>222</sup>

The major bottleneck of dealing with suspended photocatalyst is related to post-treatment, whereby the recovery of the nanoscale particles becomes a technological hurdle, in particular to large volumes of treated water. The circulation and separation of suspended photocatalyst are cost-intensive processes.<sup>146</sup> Moreover, the water quality is jeopardized via secondary pollution provided that the separation step fails. Considering the noble goal of producing safe drinking water with low operating costs, this thesis is intended to develop a photocatalytic system with PS immobilized onto a substrate.

### 2.4.3 Light Attenuation and Low Quantum Efficiency

When scaling up, photochemical reactions suffer from poor light management.<sup>223</sup> This is particularly true for heterogeneous reactions, where the absorption, scattering, and reflection effects – united by the term *attenuation* – reduce the intensity of light passing through the reaction medium as per Equation 2.1.

$$I = I_0 \cdot e^{-\mu x} \quad (2.1)$$

where  $I$  and  $I_0$  are transmitted and incident light intensities;  $\mu$  ( $\text{m}^{-1}$ ) is the attenuation coefficient consisting of absorption coefficient ( $\alpha$ ,  $\text{m}^{-1}$ ) and scattering coefficient.

In this context, the geometry and material of a photoreactor determine not only the volume of light falling on the photocatalyst layer, but also the degree of *uniformity* of light distribution. Additionally, the latter characteristic plays a crucial role in: i) the optimum PS loading, which minimizes the energy requirement; ii) the *intrinsic* (in the absence of mass transfer limitation) rate of the interfacial reaction (step ④ in Figure 2.6); and iii) the selectivity of a chemical reaction. Consequently, the photoreactor walls and the support for the photocatalyst need to be made from the highly transparent (or at least translucent) to the incident light material.<sup>224</sup>

Figure 2.7 illustrates the propagation of light in the photocatalytic reactor with immobilized PS. The excitation of PSs is realized largely in the visible-light wavelength region (see also Table 2.6), whereby light absorption of most materials for devising the photoreactor is marginal.<sup>224</sup> For example, wavelength cutoff at 50% transmittance for Pyrex glass is at 275 nm.<sup>225</sup> Light is thus attenuated due to i) discontinuity of refractive index profile (Fresnel reflection losses), and ii) scattering (related to the particle, crystal, or pore size of material). Table 2.8 summarizes the refractive indices of materials used for the fabrication of photocatalytic reactors, such as quartz, borosilicate glass, common fluoropolymers. Notably, fluoropolymers, such as polytetrafluoroethylene (PTFE), poly(vinylidene fluoride) (PVDF): i) demonstrate good UV- and high visible-light transmittance; and ii) are widely used for the manufacture of photoreactors of various shapes by extrusion.<sup>224</sup>

When light transverses from quartz ( $n_D = 1.55$ ) to water ( $n_D = 1.33$ ) and then to fluoropolymer-based substrate for PS ( $n_D = 1.3$ – $1.4$ ), the minor reflection losses may well be observed. Strong light attenuation occurs when PS molecules are loaded inside an optically thick ( $\mu\text{m}$  scale), porous material like membranes. Hence, immobilization of thin PS film on the surface of substrate helps reduce the optical path of incident light. Assuming Rayleigh scattering, materials with small pores, crystal size ( $<400$  nm) and a refractive index comparable to that of water exhibit negligible *refraction* (bending of a light ray) for visible light.

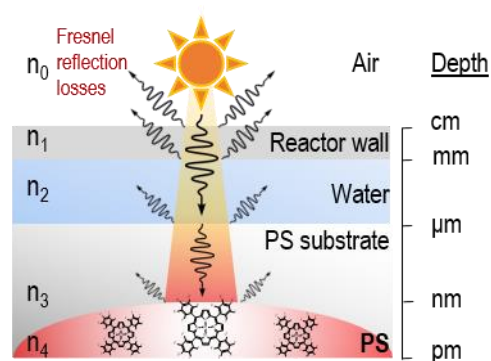


Figure 2.7: The schematic illustration of light propagation in a photocatalytic reactor consisting of media with different depth and refractive indices ( $n_{0-3}$ ).

Table 2.8: Refractive indices of materials used for the manufacture of photocatalytic reactor against the reference media (water)<sup>226</sup>

Refractive index (ref to Figure 2.7)	Medium	Refractive index, $n_D$ , (at 589 nm, 20 °C), –
$n_1$	Quartz	1.55
	Borosilicate glass	1.46–1.47
$n_2$	Water	1.33
$n_3$	Fluorinated ethylene propylene(FEP)	1.34
	Polytetrafluoroethylene (PTFE)	1.35
	Poly(vinylidene fluoride) (PVDF)	1.42

The low uniformity and attenuation of light aggravate the overall energy efficiency, which is dependent on the type of photocatalyst (or PS) and experimental conditions. The benchmarks for the efficiency of a photochemical and photocatalytic process are *quantum yield* (reaction events per absorbed photon,  $\Phi$ ) and *photonic efficiency* (reaction events per incident photon,  $\xi$ ) – calculated via Equation 2.2 and Equation 2.3:

$$\Phi = \frac{dN_A/dt}{\varphi_{abs,V}}, \quad (2.2)$$

$$\xi = \frac{dN_A/dt}{\varphi_{inc,V}} \quad (2.3)$$

where  $dN_A/dt$  is the overall reaction rate of, for example, decomposition ( $\text{mol L}^{-1}\text{s}^{-1}$ );  $\varphi_{abs,V}$  and  $\varphi_{inc,V}$  are the numbers (*flux*) of absorbed and incident photons referred to the photoreactor volume ( $\text{mol}_{\text{photon}} \text{L}^{-1}\text{s}^{-1}$ ).

Whereas  $\Phi$  is an intrinsic metric of a photocatalyst efficiency, the conversion of applied energy (incident photons) to photodecomposition reaction is frequently assessed via more accessible  $\xi$ -metric. Naturally, the thick coating or impregnated (within a porous substrate) PS cannot be uniformly illuminated throughout the photoreactor leading to internal diffusion limitations. To resolve both the light and PS distribution problems, the substrate providing the large active surface area will be tested in Chapter 7. As assistance to the interested reader, the Figure 2.9 summarizes the radiometric and photonic terms (their definitions and units) used throughout the thesis.

Table 2.9: Wavelength-integrated and wavelength-related radiometry and photonic definitions used in the dissertation

Wavelength-integrated definitions				Wavelength-related definitions			
Radiometric quantities	Sym-bol	Formula	SI Unit	Spectral radiometric quantities	Sym-bol	Formula	SI Unit
Absorbance	$A$	$A = -\lg(1-\alpha_i)$	–	Spectral absorbance	$A_\lambda$	$A_\lambda = dA/d\lambda$	–
Absorptance	$\bar{\alpha}$	$\alpha = I_a/I_o$	–	Spectral absorptance	$\alpha_\lambda$	$I_\lambda = d\alpha/d\lambda$	–
Transmittance	$\bar{T}$	$T = I_T/I_o$	–	Spectral transmittance	$T_\lambda$	$I_\lambda = dT/d\lambda$	–
Specular reflectance	$R_\Omega$	$R_\Omega = I_R/I_o$	–	Spectral reflectance	$R_{\Omega,\lambda}$	$R_\Omega = dR/d\lambda$	–
Irradiance (radiant flux)	$I_{inc}$	–	$\text{W m}^{-2}$	Spectral irradiance	$I_{inc,\lambda}$	$I_\lambda = dI/d\lambda$	$\text{W m}^{-2} \text{ nm}^{-1}$
Irradiation	$H$	–	$\text{J m}^{-2}$	Spectral irradiation	$H_\lambda$	$H_\lambda = dH/d\lambda$	$\text{J m}^{-2} \text{ nm}^{-1}$
Photon flux or photon intensity	$\varphi_{inc}$	–	$\text{s}^{-1}$ or $\text{E s}^{-1}$	Spectral photon flux	$\varphi_{inc,\lambda}$	$\varphi_\lambda = d\varphi/d\lambda$	$\text{s}^{-1} \text{ nm}^{-1}$ or $\text{E s}^{-1} \text{ nm}^{-1}$
Einstein (one mole of photons)		$1\text{E} = N_A = 6 \cdot 10^{23} \text{ ph.}$		–	–	–	–

#### 2.4.4 Dissolved Oxygen Deficiency

At the typically low oxygen levels in water (8–9 mg L<sup>-1</sup> at 20–25 °C), an intensive illumination may result in rapid oxygen depletion. The occurring anoxic regime may reduce the overall reaction rate due to hindrance of i) molecular diffusion (steps ①, ② in Figure 2.6); ii) quenching of a PS excited state.<sup>227</sup> Moreover, the quenching of a triplet/singlet excited state leads to the generation of <sup>1</sup>O<sub>2</sub> or O<sub>2</sub><sup>•-</sup> is predominantly diffusion-controlled and explained by a collisional Stern-Volmer process (Equation 2.4):<sup>228</sup>

$$\frac{I_0}{I} = 1 + k_q \tau_0 c_{f,O_2}, \quad (2.4)$$

where  $I_0$ ,  $I$  are the intensities of photoluminescence (PL) signal in absence and presence of oxygen;  $k_q$  is the bimolecular quenching constant;  $\tau_0$  is the PL signal lifetime,  $c_{f,O_2}$  is the dissolved oxygen concentration.

Hence, decreasing the concentration of dissolved oxygen – via pressure, temperature, or chemical scavenging – can reduce the quantum efficiency of ROS (<sup>1</sup>O<sub>2</sub>, O<sub>2</sub><sup>•-</sup>) generation. Notably, Monteiro et al. reported that an oxygen-free environment prolongs the PS excited-state lifetime and also reveals the contribution of electron-transfer mechanism to phenol decomposition by metalloporphyrins.<sup>190</sup> The organization of effluent recycling, oxygen or air blowing, and in situ oxygen production under the bias potential<sup>229</sup> – are all possible solutions to the problem of oxygen deficiency.

## 2.5 Photocatalytic Membranes

A promising solution to the aforementioned problems is the application of photocatalytic membranes (PCM). The following section (2.5) explains the configuration, fabrication, and challenges of PCMs in water treatment, and gives an overview of the parameters examined.

### 2.5.1 Different Configurations of Photocatalytic Membrane Reactors

The simultaneous process combining the photocatalysis phenomenon with membrane separation is realized in photocatalytic membrane reactors (PMRs). Figure 2.8 illustrates two main configurations of PMRs about the form of photocatalyst utilization: i) photocatalyst suspended in solution in a photoreactor and recovered in a separate membrane module (panel **a**); and ii) immobilized in (on) a membrane (panels **b-e**) hereinafter referred to as photocatalytic membrane or PCM.<sup>230-233</sup>

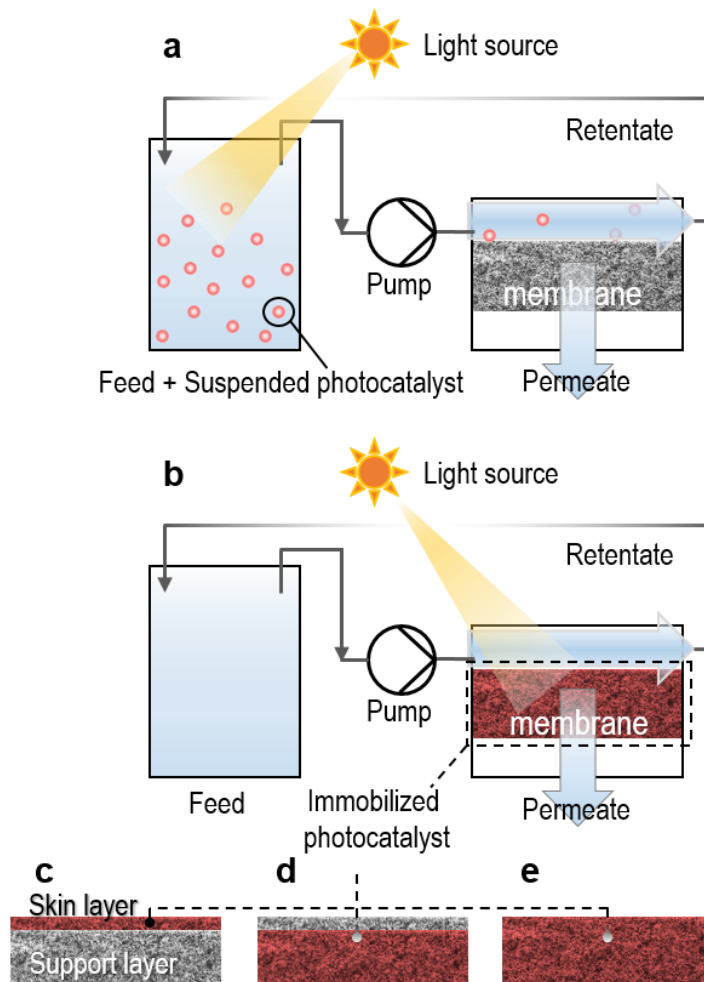


Figure 2.8: Schematics illustrating the distinct configurations of photocatalytic membrane reactors with **a**, suspended and **b**, immobilized photocatalyst. In the latter configuration, the membrane supporting photocatalyst can be **c,d** asymmetric (photoactive skin or support layer) or **e**, symmetric (fully coated).

The batch reactors with suspended photocatalyst (slurry) are generally preferred for the exceptional mass transfer due to the small inter-particle distance and hence a short diffusion path. The important drawbacks of this configuration – are also described in Section 2.4 – include i) increased light scattering (and decrease of activity) at high concentrations;<sup>234, 235</sup> ii) aggregation of the nanoparticles at a high concentration that undermines the process (quantum) efficiency;<sup>236</sup> and iii) the requirement for photocatalyst recovery from a slurry. These problems can be circumvented by using PCMs, which have a thin separation<sup>237, 238</sup> (Figure 2.8c) or thick support (Figure 2.8d) photoactive layers. There are also symmetrical (blended) PCMs or made of pure photocatalyst (free-standing PCMs)<sup>239</sup> as depicted in Figure 2.8e.

## 2.5.2 Fundamentals of Solute Mass Transfer through a Membrane

Membranes represent a physical barrier for a motion of pollutants, which can be transported through the pore channels or membrane matrix under temperature, pressure, chemical, or electric potential gradient. In this thesis, the driving force for fluid flow is the *transmembrane pressure* ( $\Delta P$ , pressure difference before and after the membrane). In this context, the mass transfer of solutes is governed by *diffusive* (concentration gradient) and *advective* (velocity gradient) flux. *Convective* mass transfer (combination of advective and diffusive phenomena) is dominant in PCMs operated at ambient temperatures and in absence of solute rejection. The correlation between advective and diffusive phenomena – estimated via Péclet number ( $Pe$ ) – depends on average flow velocity (see Equation 2.5). A higher Péclet number ( $Pe \gg 1$ ) means a higher contribution of advection phenomena to the overall mass transfer rate. An unambiguous metric of flow velocity is *superficial* velocity,  $u_s$ , which does not account for porosity of a membrane. It is obtained from flow rate using Equation 2.6 and hereinafter referred to as *water flux* ( $J_w$ ).

$$Pe = \frac{Lu_s}{D_i} \quad (2.5)$$

$$u_s \equiv J_w = \frac{Q_p}{A_{act}} \quad (2.6)$$

where  $l$  is the characteristic length (m), equal to membrane thickness for PCMs ( $L = h_m$ );  $u_s$  are the average and superficial flow velocities ( $\text{m s}^{-1}$ );  $D_i$  is the molecular diffusion coefficient ( $\text{m}^2 \text{s}^{-1}$ );  $Q_p$  is the permeate flow rate ( $\text{L h}^{-1}$ );  $A_m$  is the cross-sectional (active) membrane area ( $\text{m}^2$ ).

In chemical reactors with immobilized catalyst, high flow rates (velocity) ensure high mass transfer rates of reactants to the boundary layer that bears great implications on kinetics of photocatalytic reactions.<sup>217</sup> Similarly, due to reduced resistance to mass transfer, higher efficiency of catalytic membrane reactors is observed when the flow rate through the pores of the membrane increases.<sup>240</sup>

Furthermore, the crucial role of flow-through (dead-end) operation in process intensification compared to the surface recirculation (cross-flow) was reported in several independent studies.<sup>241-243</sup> The former operation mode greatly facilitates the contact between reactants (pollutants, ROS, and their precursors) and photocatalyst-coated surface inside the nanochannels of PCM. In this sense, a PCM with an internal photocatalyst coating can be considered as a special case of the multi-microchannel reactor (see Table 2.10). Both photoreactor architectures offer: i) the large specific surface area ( $\text{m}^2 \text{m}^{-3}$ ) for photocatalyst distribution; ii) short diffusion length; and iii) the near-uniform residence time and illumination. Despite the smaller pore channels, PCM can operate at higher flow rates that results in further enhancement of photocatalytic activity. The efficiency of chemical reactions using PCMs is remarkably improved,<sup>244</sup> and the rate constant values approach those of *intrinsic* (mass-transfer independent) kinetics usually observed in microreactors ( $k_{\text{obs}}$  of tens of  $\text{s}^{-1}$ ).<sup>245</sup>

Table 2.10: Comparison of microreactor and photocatalytic membrane for photocatalytic applications

	Microreactor technology <sup>225, 246, 247</sup>	Photocatalytic Membranes
Surface-to-volume ratio, m <sup>2</sup> m <sup>-3</sup>	10 <sup>4</sup> –10 <sup>5</sup>	10 <sup>6</sup> –10 <sup>7</sup>
Diffusion length, μm	10–1000	0.01–1
Flow rate, mL min <sup>-1</sup> (channel inner diameter)	0.001–1 (μm range) 1–10 (mm range)	0.1–10
Reusability potential	Days	Days
Residence time uniformity (flow distribution)	Excellent (<10%)	good/excellent

Enhancement of reaction kinetics stems from several factors. Firstly, confined space inside the nanochannels likely promotes the contact (the rate of successful collisions) between produced ROS and pollutant molecules<sup>248</sup> that, according to collision theory, influences the rate constant of chemical reactions. This conclusion is valid provided that the chemical reactions are not in the diffusion-controlled regime (described by Fick's laws of diffusion). Figure 2.9 illustrates the solute transport inside the channels of a PCM. In this instance, the steps associated with internal diffusion are not significant (hence not shown), because of i) the non-porous thin film of PS; ii) the convection-dominated regime in UF, MF membranes. Since the pore volume of a membrane ( $V_{por}$ ) determines the reaction space, the contact time between pollutant and immobilized porphyrin molecules ( $\bar{t}_{con}$ ) can be approximated to hydraulic residence time ( $\bar{t}_r$ ) – space time in a plug-flow reactor<sup>249</sup> – in absence of retention by a membrane. Notably, the  $\bar{t}_r$  depends on the parameters of membrane morphology (pore size, porosity, thickness)<sup>250</sup> and is determined via Equation 2.7.

$$\bar{t}_{con} \approx \bar{t}_r = \frac{V_{por}}{Q_p} = \frac{h_m \psi_m}{J_w} \quad (2.7)$$

where  $V_{por} = A_{act} h_m \varphi_m$ ,  $\psi_m (-)$  is the membrane porosity.

Secondly, mixing time ( $t_{mix}$ ) or diffusion time of the reactants in the *radial* (transverse to the flow) direction is short and ranges in microseconds as follows from Equation 2.8. Efficient mixing is achieved in PCMs, because solute residence time (defined by Equation 2.7) is several orders longer (ms-s range) than  $t_{mix}$  or <sup>1</sup>O<sub>2</sub> lifetime ( $\tau_{\Delta} = 3\text{--}4 \mu\text{s}$ , see Table 2.5).

$$t_{mix} = \frac{\bar{d}_{por}^2}{4D_i} \quad (2.8)$$

where  $\bar{d}_{por}$  (μm) is the mean pore diameter.

In most studies, the high pollutant removal was achieved only via multiple cycles through PMR, while the careful design of photocatalytic membranes allows the high degradation of pollutants in a single pass due to the constant replenishment of reactants.<sup>242</sup> On an industrial scale, the organization of the recirculation cycle increases the treatment costs due to the dilution of influent and hence the slower oxidation kinetics. The return of treated water to the feed tank complicates the mass balance of degraded pollutants per pass that is required for kinetics analysis. Hence, the study relying on a single-pass operation of PCM with the fixed porphyrin (organic PS) was undertaken in this thesis.

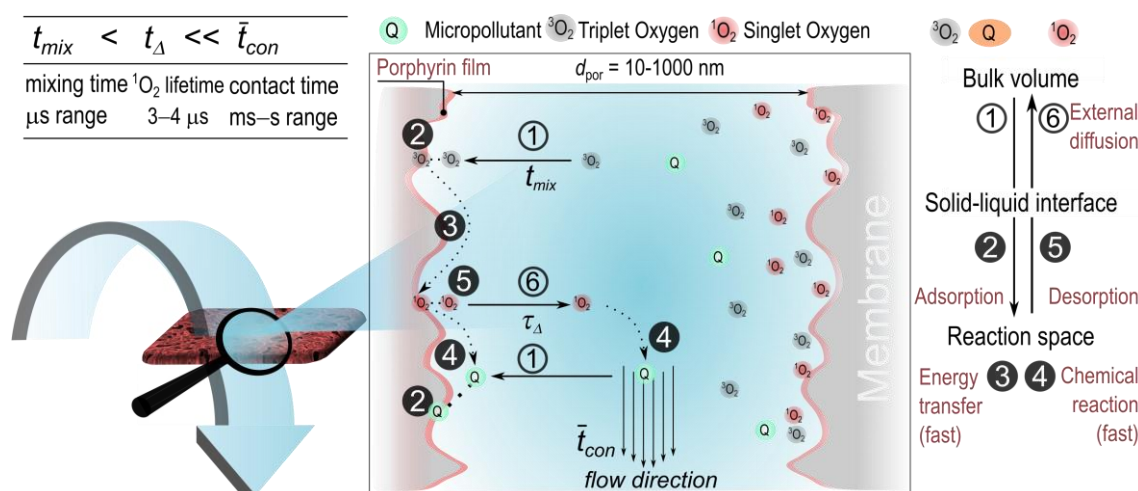


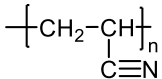
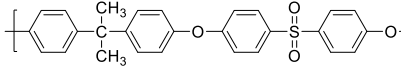
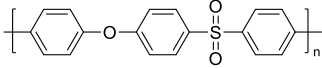
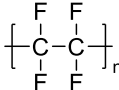
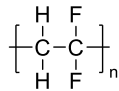
Figure 2.9: Schematics of solute transport through a PCM illustrating the negligible mass transport resistance. The contact time of solutes within the porous network ( $\bar{t}_{con}$ ) surpasses the time required for diffusion to the membrane ( $t_{mix}$ ) and a lifetime of  $^1\text{O}_2$  ( $t_{\Delta}$ ) by several orders of magnitude. The illustration is adapted from Lyubimenko et al.(2022),<sup>251</sup> with permission from Elsevier.

### 2.5.3 Selection of Membrane Material

The PMRs with immobilized photocatalyst must be made of the membrane materials, which remain stable under extended exposure to i) ultraviolet light, ii) non-specific ROS attack, and iii) applied pressure gradient. Inorganic materials, including glass fiber or ceramics, are chemically inert and mechanically robust. Though, these express several disadvantages, such as high costs, brittleness, corrosion in extreme acidic ( $\text{pH} < 2$ ), and alkaline media ( $\text{pH} > 11$ ). Additionally, ceramic membranes are poorly represented in the NF, UF range which limits their application for MP removal. Given the economic aspect, polymer-based membranes appear attractive for application in PMR, although they must meet the requirements towards the long-term photo- and chemical stability. Both attributes were investigated extensively but separately for polymer materials.

Photostability of PCM is expressed as the resistance of polymeric material to withstand continuous light irradiation without signs of ablation, discoloration, embrittlement, or cracking – all united by the term “photoaging”. The parameters governing this process include i) optical properties; ii) chemical composition of pristine membranes; and iii) incident light characteristics (wavelength, intensity, and duration). The nature of the polymer making up the membrane impacts greatly on the rate of photoaging, because the chemical bonds (depending on their type) can be cleaved by absorbed light in the process referred to as *photolysis*. The thermodynamic favorability of a photolysis reaction can be estimated from the bond dissociation energies, which were summarized in Table 2.11 for the polymers commonly used for the fabrication of UF and MF membranes. In the context of bond energy values, fluoropolymers are the most chemically durable materials. After thoroughly examining the stability of ten polymer-based membranes, Chin et al. arrived at a similar conclusion: the strength of chemical bonds of a monomer influences the polymer stability.<sup>252</sup> In that study, the PVDF and PTFE membranes exhibited i) the least total organic carbon (TOC) release upon 30 days of continuous UVA-light ( $350\text{--}400 \text{ nm}$ ,  $2 \text{ mW cm}^{-2}$ ) irradiation; and ii) the negligible change of membrane resistance (estimated as the ratio of measured to initial water flux) after 10 days of UV-induced  $\text{H}_2\text{O}_2$  photolysis leading to  $\text{HO}^\bullet$ -radical oxidative stress.

Table 2.11: Polymer structure of common membrane materials and their functional groups

Polymer/Molecular structure	Chemical bonding	Bond dissociation energy, <sup>253-255</sup> kJ/mol	Light wavelength for bond scission, nm
<b>Polyacrylonitrile</b> 	C-C [H <sub>3</sub> C-CH(CH <sub>3</sub> )CN]	332.6 ± 8.4	360 ± 9
	C-C [ <i>iso</i> -C <sub>3</sub> H <sub>7</sub> -CN]	503.8 ± 8.4	238 ± 4
	N≡C [(CH <sub>2</sub> ) <sub>2</sub> HC≡N]	750 ± 2.9	160 ± 1
	S-C <sub>ph</sub> [H <sub>3</sub> CSO <sub>2</sub> -C <sub>6</sub> H <sub>5</sub> ]	344.3 ± 8.4	348 ± 8
<b>Polysulfone</b> 	C <sub>ph</sub> -C [C <sub>6</sub> H <sub>5</sub> -CH <sub>2</sub> C <sub>6</sub> H <sub>5</sub> ]	383.7 ± 8.4	312 ± 12
	C-C [H <sub>3</sub> C-C(CH <sub>3</sub> )(C <sub>6</sub> H <sub>5</sub> ) <sub>2</sub> ]	290.8 ± 8.4	412 ± 12
<b>Polyether-sulfone (PES)</b> 	C <sub>ph</sub> -O-C <sub>ph</sub> [C <sub>6</sub> H <sub>5</sub> -OC <sub>6</sub> H <sub>5</sub> ]	326.8 ± 4.2	366 ± 3
	C <sub>ph</sub> -H ( <i>orto</i> )	321-334	358-372
	C <sub>ph</sub> -H ( <i>meta</i> )	398.7 ± 13.4	300 ± 9
<b>Polytetrafluoroethylene (PTFE)</b> 	F-C [HCF <sub>2</sub> -CF <sub>2</sub> H]	518.2 ± 18	231 ± 8
	C-C [HCF <sub>2</sub> -CF <sub>2</sub> H]	400.3 ± 15.5	299 ± 11
<b>Polyvinylidene fluoride (PVDF)</b> 	F-C [HCF <sub>2</sub> -CH <sub>2</sub> F]	482.0 ± 14.4	248 ± 8
	C-C [HF <sub>2</sub> C-CH <sub>2</sub> F]	410.1 ± 15.6	292 ± 11
	H-C [HCF <sub>2</sub> -CH <sub>2</sub> F]	430.4 ± 15.6	278 ± 10

Markedly, a hydrophilic PVDF membrane released the 30-times higher TOC than its non-modified, hydrophobic counterpart. Overall, the superior photostability of PVDF and PTFE membranes has been repeatedly demonstrated via surface-sensitive techniques, such as infrared and x-ray photoelectron spectroscopy.<sup>256-258</sup> Few reports of structural damage of TiO<sub>2</sub>-coated PVDF membranes<sup>259, 260</sup> must be checked in a systematic study conducted in a closed, controlled environment.

The effect of the wavelength and duration of light exposure on PCM stability is ambiguous that is observed by the scattered changes and quantitative parameters of PCM degradation. Moreover, it must be noted that the chemical stability under ROS-induced oxidative stress is influenced by the type and concentration of produced ROS; those are related to the nature of immobilized photocatalyst. Porphyrins – being the topic of study in this dissertation – produce predominantly the selective, electrophilic <sup>1</sup>O<sub>2</sub> species, which is kinetically reactive only with electron-rich substrates<sup>197, 261</sup> (see examples in Section 2.3.2). In the absence of polymer chain defects or blended additives, fluoropolymers do not hold atoms with free electrons (that could potentially be shared during a reaction) and hence appear to be chemically inert to <sup>1</sup>O<sub>2</sub> attack.



Both PVDF and PTFE membranes are commercially available in the MF range (0.1 – 1.0  $\mu\text{m}$ ) and have been successfully employed in PMRs.<sup>262</sup> Due to their inherent hydrophobicity, and hence high operating costs for pumping, both fluoropolymer-based membranes in their pristine form are practically extinct in the NF or UF range. Due to the higher surface tension, PVDF material ensures slightly higher water permeability and is hence favorable over PTFE material. In this thesis, partially fluorinated and non-hydrophilized PVDF material was selected for fabrication of PCMs on the basis of the combination of photo- and chemical stability, greater wettability, wide adoption of this material in membrane filtration.

## 2.5.4 Fabrication Strategies of Photocatalytic Membranes

Organic PS molecules can be immobilized on membrane support via numerous strategies, as shown in Figure 2.10. Impregnation generally realized through adsorption via weak intermolecular forces, such as hydrophobic (van der Waals forces, hydrogen bonds) or dipole-dipole interactions (Figure 2.10a). This strategy ensures the facile straightforward method to PS immobilization onto polymer materials and does not require modification in the case of the hydrophobic nature of porphyrin and the membrane. Of great benefit is that, owing to the penetration of solvent inside the porous network, both the external and internal surface of support materials can be coated. Physically adsorbed porphyrin molecules, however, desorb in organic solvents, thereby triggering loss of immobilized PS. Additionally, the leaching of porphyrin in the form of aggregates cannot be excluded under strong water flow that may result in secondary pollution (the issue similar to the recovery of suspended particles described in Section 2.4.2).

Impregnated PS molecules stay close to the water and the dissolved reactants, whereas encapsulation enables the barrier in the form of a polymer matrix of a membrane that precludes the potential loss of porphyrin. Encapsulation methodology (Figure 2.10b) includes the blending of the solutions of both PS and polymer and the subsequent casting of a membrane or electrospun nanofiber mesh. However, the isolation of PS molecules leads to hindrance of the internal mass transfer due to the limited access of oxygen to macrocycle and poor contact of produced ROS with pollutant molecules (see also Section 2.4.1).

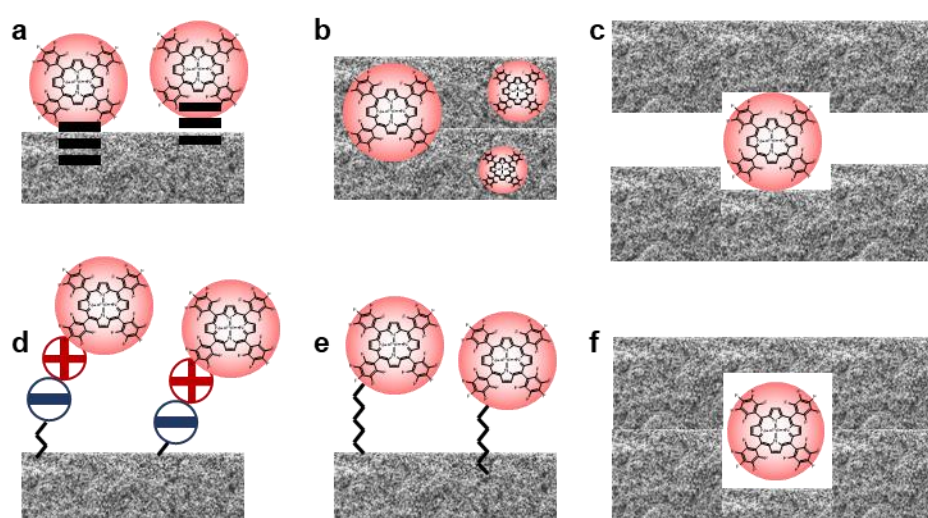


Figure 2.10: Strategies for immobilization of PS molecules (red): **a** Coating or impregnation via adsorption; **b** Encapsulation via blending; **c** Physical entrapment inside the mesoporous matrix; **d** Ion-pair formation; **e** Covalent binding; **f** In situ molecular construction/post-synthesis.

Figure 2.10c illustrates the strategy of physical entrapment of PS allows for the synthesis of photoactive molecules inside the meso- or micropores of inorganic porous material (zeolite).<sup>221</sup> The small precursor molecules (pyrrole, benzaldehyde) diffuse to the confined space, channels of support material, thereafter the macrocycle molecules are constructed like a ship in a bottle. The porphyrin molecules are physically trapped inside the pores and are hence unable to escape (leach) to the environment. Aside from the complexity of the given method, the use of zeolite or thermostable NF membranes (pore size < 1 nm) is required that enable high-temperature reactions of porphyrin assembly.

Electrostatic interaction between oppositely charged groups can form strong ion-pair binding to the membrane (Figure 2.10d). The steadfast method of avoiding leaching issues is the covalent tethering of molecules to the surface (Figure 2.10e). Both methods, however, require surface modification via electron beam-, ozone-, plasma-, ultraviolet light-induced grafting of anchoring groups or polymerization initiators. In situ construction of membrane templates around the photoactive molecules is likely the most challenging approach among the existing methodologies (Figure 2.10f). The encapsulated macrocycle molecules are well-distributed in the formed cavities due to the high surface area that promotes photocatalytic activity. The leaching and stability problem of tested PS upon reuse however persist. Self-assembly and layer-by-layer techniques have appeared for organizing advanced porphyrin architectures and frameworks such as surface-coordinated metal-organic frameworks<sup>263</sup> and covalent organic frameworks.<sup>264</sup> Limited information exists on their stability in water and the methodologies for casting on membrane substrates. Despite the high level of complexity in synthesis, these novel organic frameworks are promising catalytic materials exhibiting high specific surface area and new properties compared to the bulk material.

In this thesis, the strategy of physical adsorption is chosen for porphyrin immobilization on hydrophobic membranes because of the i) strong affinity between hydrophobic porphyrin and membrane; ii) lack of modification steps; and iii) the coating of the internal surface of membranes. An overview of appropriate work on membrane-supported PS for water remediation is given in the next section.

## 2.5.5 Photosensitizer-Coated Membranes for Water Remediation

The PCMs based on inorganic semiconductors (TiO<sub>2</sub>, ZnO) and carbonaceous materials (carbon nitride, graphene oxide) have been proven effective for the removal of water-borne contaminants.<sup>244, 265, 266</sup> They occupy the dominating position among the different types of fabricated PCM. These lie however outside of the scope of this thesis and thus the complete literature on this subject is not offered. The interested reader is referred to three excellent reviews of Leong et al. (TiO<sub>2</sub>-based membranes),<sup>267</sup> Zhang et al. (carbon nitride-based membranes),<sup>268</sup> Shi et al. (outlook to visible-light-driven PCM).<sup>54</sup> Given the main challenges of non-immobilized PS (discussed in Section 2.3.5), the implementation of organic photocatalysts in PWT application remains challenging as evidenced by the scarcity of available research.<sup>167, 174</sup>

A small number of recent publications have investigated the potential of membrane-supported porphyrins for pollutant removal,<sup>269-271</sup> although these are versatile materials used in heavy-metal adsorption,<sup>272</sup> disinfection,<sup>273, 274</sup> fine chemistry<sup>275</sup> applications. Fang et al. attached tetraphenylsulfonato-porphyrin on quaternized polysulfone membrane and achieved 93% removal of Rhodamine B (10 mg L<sup>-1</sup>) under xenon lamp excitation in cross-flow operation by continuously recycling the permeate. On the basis of the transmembrane pressure, the operating flux was determined to be  $J_w = 27 \text{ L m}^{-2} \text{ h}^{-1}$ . Wang et al. immobilized *meso*-tetrakis(1-methylpyridinium-4-yl) porphyrin via electrostatic interaction on blended polysulfone/polyethersulfone membrane. Under 300W xenon lamp illumination, the solution of Rhodamine B (10 mg L<sup>-1</sup>) was degraded up to 98.3% in flow-through operation mode. In this study, neither light intensity nor water flux was reported.

Becker-Jahn et al. anchored the dye Eosin Y and *meso*-tetrakis(1-methylpyridinium-4-yl) porphyrin via electron-beam grafting to polyethersulfone (PES) membranes. The fabricated PCMs were effective for the degradation of two types of pharmaceuticals (concentration of both at 25 mg L<sup>-1</sup>), such as Propranolol (61 and 70% for eosin- and porphyrin-coated membranes) and Ranitidine (52 and 82%, respectively), via <sup>1</sup>O<sub>2</sub>-mediated oxidation under weak visible-light LED excitation (0.4 mW cm<sup>-2</sup>). In this study, however, the membranes were operated in static conditions (no flow) in the batch reactor resulting in limited removal even after 24 h experiments. Notably, the named publications have appeared only after the first publication constituting this dissertation.<sup>276</sup> The existing gap between the attractiveness of porphyrin-coated membranes and real applications potentially can be bridged if specific energy consumption and operating costs are low.

## 2.5.6 Cost Analysis of Water Treatment Using Photocatalytic Membranes

In addition to efficiency metric of photochemical processes, such as  $\Phi$  (Equation 2.2) and  $\xi$  (Equation 2.3), an important figure-of-merit gauging the economic feasibility of solar- and electric-driven AOPs for water decontamination is specific energy consumption (SEC) per order of destroyed pollutant ( $E_{EO}$ , kWh m<sup>-3</sup> order<sup>-1</sup>). Initially introduced by Bolton et al. in the IUPAC report,<sup>277</sup> the  $E_{EO}$  describes the electric energy necessary to decrease the pollutant concentration by one order of magnitude (see Equation 2.9). The use of  $E_{EO}$  is justified for dilute solutions, for which the first-order kinetics model is valid.

$$E_{EO} = \frac{P_{el}}{Q_p \log(c_f/c_p)} \quad (\text{flow system}) \quad (2.9)$$

where  $P_{el}$  is consumed electric power (W),  $Q_p$  is the permeate flow rate (m<sup>3</sup> h<sup>-1</sup>).

The SEC for a PCM with a fixed photocatalyst is related to i) the membrane resistance (hence pumping power), and ii) the power of a light source. In the context of energy costs, the use of “free” solar irradiation is attractive, because pumping through UF or MF membranes requires low energy (0.02 to 0.4 kWh m<sup>-3</sup> for water reuse application<sup>26</sup>). Table 2.12 summarizes the data on the SEC of selected technologies for MP removal that was obtained from pilot studies or full-scale treatment facilities. The  $E_{EO}$  for solar-driven PCMs is comparable with energy consumed by adsorption on activated carbon, nanofiltration, ozonation and is significantly lower than that of other AOPs (UV/H<sub>2</sub>O<sub>2</sub>, UV-based photocatalysis). Additionally, the  $E_{EO}$  values for PCM-assisted photocatalytic oxidation are comparable to the SEC of the Swiss average WWTP (0.33 kWh m<sup>-3</sup>)<sup>278</sup> or the conventional UV-induced peroxide treatment (0.2–2.0 kWh m<sup>-3</sup> order<sup>-1</sup>).<sup>279</sup> Furthermore, energy consumption and the total energy costs can be further reduced as the size of the treatment plants increases (*scale effect*). For example, SEC of the typical WWTP is reduced by half when the volume of treated water increases from 100–1000 to 50000 m<sup>3</sup>.<sup>278</sup>

The costs of immobilized porphyrin are part of the variable operating costs, because photobleaching decreases PS system lifetime, and thus regular recoating of PCM is needed. In turn, this results in the expenses for reloading or reactivating the photoactive layer (also expressed in Table 2.13). Unlike ozonation, which requires a constant supply of oxygen, the photocatalytic oxidation is a chemical-free process. This results in the much lower variable operating costs of solar-powered PCMs (0.3–0.6 € m<sup>-3</sup>), despite the photobleaching and the high price of employed porphyrin PS. Compared to PAC/GAC adsorption and nanofiltration (<0.2 € m<sup>-3</sup>), photocatalytic oxidation is still expensive. Note that the capital costs, including the costs of membrane modules, solar light collector and the costs of land, were not considered. These expense items will be carried into the final price of treated water as well.<sup>280</sup>

Table 2.12 The energy consumption, energy of selected technologies for MP removal. The calculated costs were based on the electricity price for the industry in European Union, 2021 (0.145 € kWh<sup>-1</sup> excluding VAT).<sup>281</sup>

Treatment technology	SEC, kWh m <sup>-3</sup>	E <sub>EO</sub> , kWh m <sup>-3</sup> order <sup>-1</sup>	Energy costs, € m <sup>-3</sup>	Ref
PAC/GAC with sand filter	0.01–0.08	0.02–0.2	0.001–0.012	33, 282
PAC/GAC with UF membrane	0.14–0.35	0.45–16	0.02–0.05	283, 284
Ozone Treatment	0.04–0.28	0.0015–0.9	0.006–0.041	282, 285
Nanofiltration	0.6–1.2	0.3–3 <sup>a</sup>	0.09–0.17	26, 286
UV/H <sub>2</sub> O <sub>2</sub>	not defined	0.2–2.0	0.03–0.29	279
UV-based photocatalysis	not defined	100–500	15–75	279
Solar-driven PCMs	not defined	0.02–0.4 <sup>b</sup>	0.003–0.058	26, 287
Full-scale WWTP	0.33	3 <sup>c</sup>	0.05	278

<sup>a</sup> calculated using the SH removal ranged from 60 to 99% from Ref.<sup>28</sup>;

<sup>b</sup> calculated as pumping energy consumption when using MF or UF membranes;

<sup>c</sup> the feasibility range from Ref.<sup>279</sup>

Table 2.13: Operating costs estimation of the selected water treatment technologies for MP removal

Treatment technology	Consumables	Price	Gas/Chemical costs, € m <sup>-3</sup>	Variable costs, <sup>a</sup> € m <sup>-3</sup>	Ref
PAC or GAC with sand filter	GAC (0.01–0.06 kg m <sup>-3</sup> )	2–2.4€ kg <sup>-1</sup>	0.02–0.14	0.05–0.19 <sup>b</sup>	18, 288
GAC/UF (membrane cleaning)	32% HCl (1.2–2.4 mL m <sup>-3</sup> ) 50% NaOH (1.4–2.8 mL m <sup>-3</sup> ) 160 g L <sup>-1</sup> NaOCl (2.3–4.6 mL m <sup>-3</sup> ) Citric acid <sup>c</sup> (0.6–1.2 mL m <sup>-3</sup> )	0.33 € L <sup>-1</sup> , 0.34 € L <sup>-1</sup> , 0.29 € L <sup>-1</sup> , 2.13 € kg <sup>-1</sup>	0.02–0.15	0.07–0.23 <sup>b</sup>	283, 284
Ozone Treatment	Oxygen (15–60 m <sup>3</sup> h <sup>-1</sup> )	0.25€ m <sup>-3</sup>	3.8–15.0	3.8–15.0	18, 282, 288
Nanofiltration	Antiscalant (2–8 mL m <sup>-3</sup> ) Citric acid (0.8–1.3 g m <sup>-3</sup> ) <sup>c</sup>	2.5€ L <sup>-1</sup> 2.13 € kg <sup>-1</sup>	0.007–0.023 (chemicals)	0.09–0.20	284, 286
Solar-driven PCMs	Porphyrin (0.8–3.2 mg m <sup>-3</sup> ) <sup>d</sup>	0.11–0.85 € mg <sup>-1</sup> , <sup>e</sup>	0.4–0.7	0.5–0.9	184

<sup>a</sup> included energy costs, while the fixed operating costs for personnel, maintenance, depreciation, amortization, and interest rates were not considered;

<sup>b</sup> included the costs for the sludge disposal after PAC/GAC treatment (0.5 € kg<sup>-1</sup> or 0.03€ m<sup>-3</sup>);<sup>285</sup>

<sup>c</sup> calculated using the acid consumption (1.2 m<sup>3</sup> d<sup>-1</sup>) for quarterly cleaning of NF270 membrane ( $J_w = 17 \text{ L m}^2 \text{ h}^{-1}$ );<sup>283</sup>

<sup>d</sup> calculated for:  $Q_f = 0.12 \text{ L h}^{-1}$  ( $J_w = 600 \text{ L m}^2 \text{ h}^{-1}$ ,  $A_m = 2 \cdot 10^{-4} \text{ m}^2$ ),  $\bar{q}_{PS} = 2.2 \text{ mmol m}^{-2}$  (PS purity of 95%), recoating intervals of 56–222 days (based on photobleaching of 50% porphyrin molecules, see results in Chapter 6);

<sup>e</sup> the wholesale prices of free-base (per 10 g) and zinc (per 1 g) 5,10,15,20-Tetrakis(pentafluorophenyl)porphyrin were current as of 29.07.2022, as listed on the Frontier Scientific (USA) website.

## 2.5.7 Mechanisms of Contaminant Removal by Photocatalytic Membranes

The mechanisms of removing pollutants by PCMs can be grouped into i) rejection, ii) adsorption, iii) degradation. Given their simultaneous occurrence, resolving the mechanisms can be challenging, in particular for low-concentrated MPs.

### Rejection

As shown in Figure 2.11, the removal of trace contaminants with a molecular weight below 400 Da (for example, steroid hormones  $d_{solute} = 0.3 \text{ nm}$ ) by UF (mean pore size  $\bar{d}_{por} = 2\text{--}100 \text{ nm}$ ) and MF membranes ( $\bar{d}_{por} = 100\text{--}1000 \text{ nm}$ ) is not possible due to the prevailing sieving effect. Hence, the mechanism of MP rejection for PCMs fabricated from loose PVDF membranes and operated in the dead-end regime has been

excluded from this dissertation. The selection of non-rejecting PCMs is fortunate for the early-development stage because it allows for single-pass operation without a rise of solute concentration in the membrane boundary layer (*concentration polarization*) and thus accurate evaluation of photocatalytic activity. The removal of SH using MF or UF membranes occurs predominantly via adsorption because the nominal pore size of membranes ( $d_{\text{por}} > 10 \text{ nm}$ ) is much larger than the size of SH molecules ( $r_{17\beta\text{-estradiol}} = 0.4 \text{ nm}$  or  $M_{r,\text{SH}} \approx 0.3 \text{ kDa}$ ).<sup>289, 290</sup> In absence of a chemical reaction, the concentration gradient for UF and MF membranes (no retention of MP) is negligible.

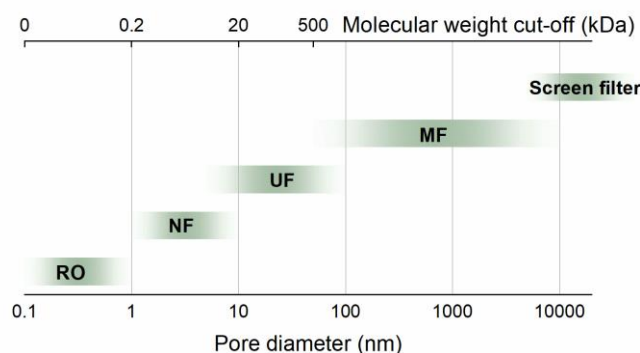


Figure 2.11: Pore size range vs. molecular weight cut-off of various membrane processes.<sup>291</sup>

### Adsorption

Due to the trace concentrations, adsorption of MP (specifically hydrophobic steroid hormones) by polymeric UF and MF membranes can still result in high retention (up to 100%).<sup>292, 293</sup> Upon reaching the saturation of adsorption sites, these loose filters however are no longer effective at removing the low-molecular-weight contaminants. The adsorption is sensitive to solution pH, which affects the surface charge of the membrane and the solute charge. For example, in alkaline media ( $\text{pH} > \text{pK}_a$  for estrogenic SHs, see Table 2.3 in Chapter 2) the charge repulsion may preclude adsorption of MPs (see more information in Section 5.2.6). A similar prohibitive effect is observed in the presence of natural organic matter due to the competition for adsorption sites.<sup>289</sup>

The adsorption of organic contaminants on porphyrin-coated PVDF membranes is not sufficiently explained in literature. Resulting from contribution to observed removal, adsorption mechanism has great implications on photocatalytic activity of PCMs. Therefore, the adsorption of steroid hormones will be explored in Chapter 5. To resolve the adsorption and degradation mechanisms in time, the photocatalytic process needs to be initiated after reaching the adsorption-desorption equilibrium, which is assumed to be little or not dependent on incident light.

### Degradation

When both rejection and adsorption mechanisms as well as the diffusive outlet flux are excluded, the concentration profile for solutes transferred through a flat-sheet membrane with chemical reaction involved (and steady-state reached) can be illustrated as per Figure 2.12.<sup>294</sup> The mass transfer of reactants is governed only by the convective solute flux (see more information in Section 2.5.2) accompanied by an  $n$ -order reaction. For first-order reactions, feed concentration exponentially reduces across the PCM thickness as given by Equation 2.10:

$$\frac{c_p}{c_f} = \exp\left(-\frac{k_{obs}\psi_m}{J_w}h_m\right) \quad (2.10)$$

where  $k_{obs}$  is observed rate constant ( $s^{-1}$ ).

The thickness of the concentration boundary layer depends on the hydrodynamic boundary layer (varied by water flux) and solute characteristics (varied with diffusion coefficient).<sup>295</sup> At high velocity (high feed flow rate), the convection dominates over diffusion, hence the concentration in the boundary layer ( $c_{BL}$ ) is approximately equal to the feed concentration in the bulk volume ( $c_{BL} \approx c_f$ ). When fluid velocity is low, the rates of diffusion and advection become comparable, and less pollutant molecules remains at the surface ( $c_{BL} < c_f$ ), that decreasing the degradation efficiency. In the absence of chemical reaction and retention, the concentration in the permeate is equal to the feed-side concentration, and the concentration profile is a flat line. The concentration boundary layer inside the membrane pore channels was neglected, because of the much shorter mixing time compared to the residence time ( $t_{mix} \ll \bar{t}_{res}$ ) as depicted also in Figure 2.9.

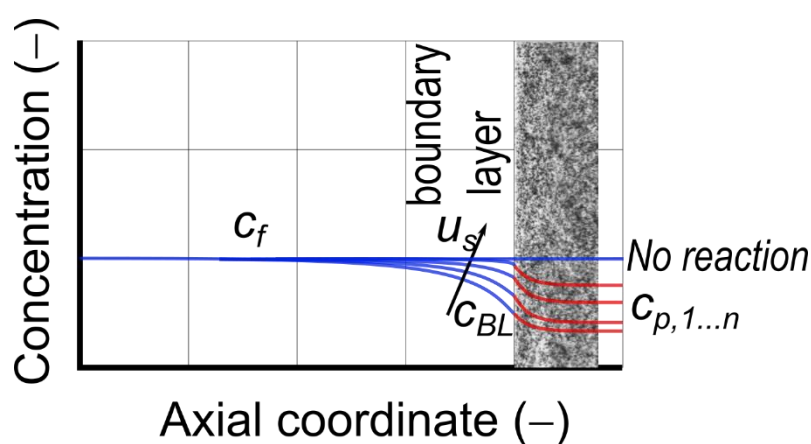


Figure 2.12: The schematic concentration profiles of a solute along the non-retaining membrane with (red) and without (blue) a chemical reaction. The shape of the concentration boundary layer depends on the kinetics (varied by light intensity) and hydrodynamics inside the membrane (varied by superficial velocity in the feed line,  $u_s$ ).

In this thesis, the prevailing mechanism of pollutant removal using the porphyrin-coated PVDF microfiltration membranes is photocatalytic degradation. In this sense, all degradation mechanisms not associated with the action of immobilized PS (photolytic or chemical degradation) were excluded or proved insignificant in control studies. Depending on the ROS reactivity and exposure time, organic pollutants can be completely or partially oxidized to  $CO_2$ , water, and other mineral acids/gases.

Complete mineralization can incur significant operating costs and is often economically impractical (a general trend for all AOPs).<sup>41</sup> Oxidation by-products are often more resistant to further decomposition.<sup>296</sup> In this context, converting MPs into inert, more biodegradable by-products seems a more feasible decision, despite the residual biological activity potentially remaining after the treatment.<sup>297</sup> The elements affecting the oxidation efficiency of a photocatalytic process using PCM are important and explained thoroughly in the next section.

## 2.6 Studies of Reaction Kinetics of PS-assisted Oxidation

Removal of organic contaminant using porphyrin-coated PCM is an emerging water treatment technology. The limited comprehension of the effects of process parameters hinders the development and application of the proposed technology with PCM. Given the several excellent reviews of kinetics and process variables for  $\text{TiO}_2$ <sup>44, 298</sup> and specifically devoted to semiconductor-coated membranes,<sup>54, 267, 268</sup> this section sets out to underline approaches to the study of limiting factors, general trends and the interplay of process parameters for PS and PS-decorated materials. These notions will serve as the theoretical basis for the experimental studies presented in Chapters 4–7.

### 2.6.1 Studies of Operating Parameters

As illustrated in Figure 2.13, the required outcome – pollutant degradation – in a process using a PCM depends on a variety of input parameters, which can be grouped as: i) operating conditions (intensity and wavelength of incident light, water flux); ii) PCM characteristics (nature, amount and distribution of photocatalyst, membrane morphology), and iii) water composition (pollutant, dissolved oxygen concentration, pH, presence of background ions).<sup>44</sup>

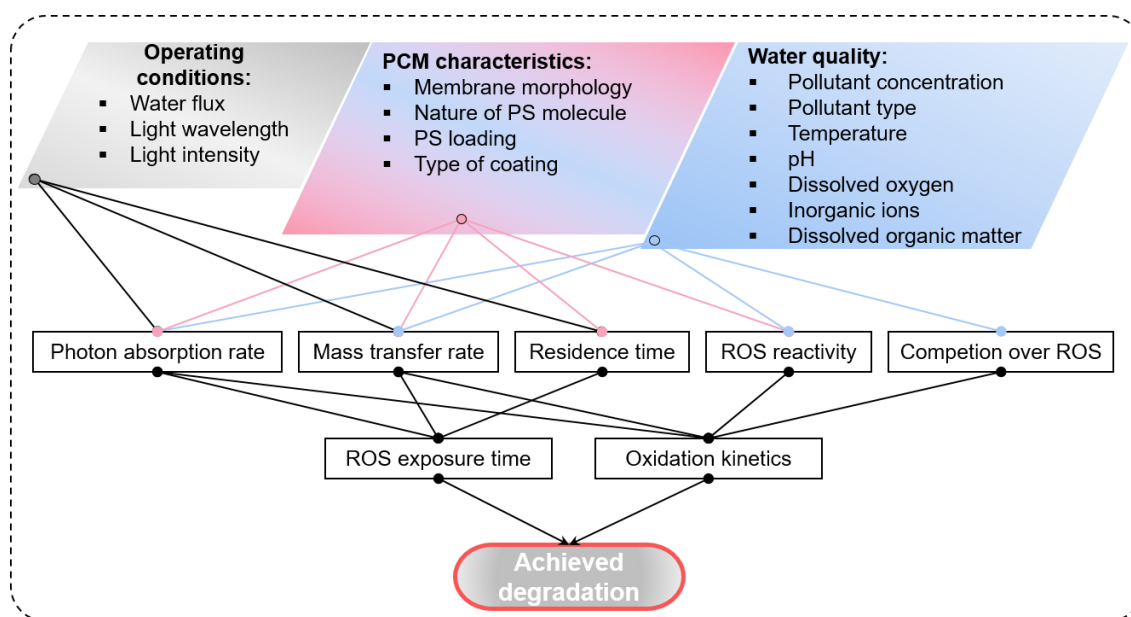


Figure 2.13: The flow chart depicting the relationship of process variables affecting oxidation kinetics and ROS-induced exposure time regarding achieved oxidation

#### Photocatalyst Loading

The relation of reaction rate to the PS loading resembles that in conventional (thermal) catalysis.<sup>299, 300</sup> As illustrated in Figure 2.14a, the reaction rate increases proportionally with the number of active sites (PS molecules in excited state) and then deviates from linearity at high loading. The appearance of a plateau or a decrease in the reaction rate indicates saturation of light absorption by the immobilized PS molecules, specifically, the *absorbed photon flux* ( $\varphi_{\text{abs}}$ ) reaches its maximum.<sup>299</sup> This transition in reaction kinetics corresponds to the value of the optimal photocatalyst loading ( $q_{\text{PS}}^{\text{opt}}$ ), which depends on the reactor geometry



and operating conditions ( $J_w$ ,  $\varphi_{\text{abs}}$ ). Noteworthy, increasing illumination (and hence  $\varphi_{\text{abs}}$ ) results in the higher  $q_{\text{PS}}^{\text{opt}}$ . The optimal loading of a new PS must be determined in all photocatalytic studies that helps avoid excessive mass of organic photocatalyst.

### Wavelength and Light Intensity

According to the First Law of Photochemistry, photochemical transformations occur only when photon quanta are absorbed by a system. Hence, the intrinsic rate of photocatalytic reaction ( $k_i$ ) is determined solely by the volumetric rate of photon absorption, which is a function of i) wavelength and photon flux of incident light; ii) optical thickness (extinction length) of the PCM, including scattering, absorption ( $\alpha$ ,  $\text{cm}^{-1}$ ) coefficients; iii) photoreactor geometry; and iv) quantum yield of oxidation reaction.<sup>301</sup> The incident light wavelength sufficient for photonic activation varies between the types of employed PS (see Table 2.6). Among them, porphyrins exhibit two broad absorption bands and low singlet state energy ( $E_S=180\text{--}200\text{ kJ mol}^{-1}$ )<sup>174</sup> that enables excitation in nearly the entire visible-light region (300–700 nm).<sup>168</sup> While light absorption by porphyrins (proportional to  $\alpha$ ) varies throughout the broad wavelength range, there is no clear evidence that excitation of PS molecules at different wavelengths alters the quantum efficiency. Thus, the type of a light source (specifically, the shape of its emission spectrum) does not play a significant role in the photocatalytic activity provided that the  $\varphi_{\text{abs}}$  is kept constant.

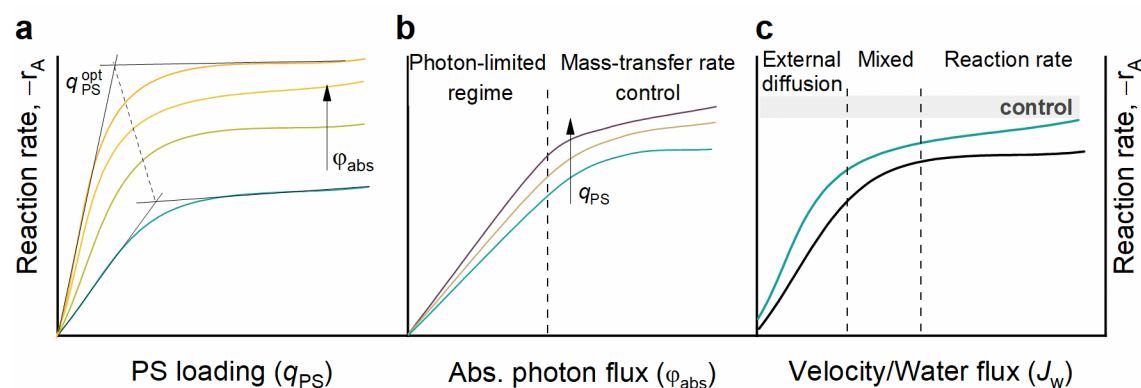


Figure 2.14: The illustration of experimental determination of the rate-limiting steps based on the changes of an initial (or overall) reaction rate ( $-r_A$ ) while studying the operating parameters: **a**, PS loading ( $q_{\text{PS}}$ ); **b** absorbed photon flux ( $\varphi_{\text{abs}}$ ); and **c** water flux ( $J_w$ ).

This conclusion follows from the Second Law of Photochemistry valid for single-photon absorption processes. Under low irradiance, both  $\Phi$  and  $\xi$  remain constant as observed in a linear rise of  $r_A$  with  $\varphi_{\text{abs}}$  (see Figure 2.14b and Equation 2.11). This photon-limited regime reveals the intrinsic reaction rate, when concentration in bulk solution is equal to that at the PS-coated surface ( $c_S$ ). An increase in the PS loading results in the higher limiting light intensity corresponding to the maximum  $\varphi_{\text{abs}}$ . At high irradiance, the surface concentration of reactant approaches zero ( $c_{\text{BL}} \rightarrow 0$ ) that renders the overall reaction rate dependent on mass transfer rather than on chemical reaction. Further increase in  $I_{\text{inc}}$  only diminishes photon efficiency (both  $\Phi$  and  $\xi$ ) as expressed in Equation 2.12. The application of powerful artificial light sources or solar concentrators is hence not economically feasible.

$$\text{Low } I_{\text{inc}} \quad -r_A \propto I_{\text{inc}}, \Phi \text{ or } \xi = \text{const} \quad (2.11)$$

$$\text{High } I_{\text{inc}} \quad -r_A \propto I_{\text{inc}}^0, \Phi \sim \xi \propto \frac{1}{I_{\text{inc}}} \quad (2.12)$$

### Velocity or Water Flux

In continuous-flow operated photoreactors, velocity (or water flux in PMRs) is another critical parameter influencing the mass transfer of reactants to the active PS sites. The studies of the aforementioned parameters allow for the experimental determination of the rate-limiting steps of photocatalytic reactions.<sup>218, 302</sup> Given the complexity of the degradation process and mutual interdependence of the reaction parameters, the kinetics study needs to be approached in a holistic manner<sup>303</sup> via consistent examination of individual variables.

The overall reaction rate (proportional to  $k_{obs}$ ) is linked to the rates of chemical reaction and mass transfer phenomena for heterogeneous reactions via Langmuir–Hinshelwood kinetics (Equation 2.13):<sup>312</sup>

$$\frac{1}{-r_A} = \frac{1}{k_i} + \frac{1}{k_i K_{ads} c_{BL}} \quad (2.13)$$

where  $K_{ads}$  is the adsorption-desorption equilibrium constant ( $K_{ads} = k_1/k_{-1}$ ),  $k_1$  and  $k_{-1}$  are reactant adsorption and desorption constants, respectively;  $c_{BL}$  is the boundary layer concentration.

For fast reactions,  $r_A \propto k_m a'_V c_{BL}$ , where  $a'_V$  is the active surface-to-volume ratio,  $k_m$  ( $\text{m s}^{-1}$ ) is the reactant-to-surface mass transfer coefficient.<sup>246,308</sup> Under a high irradiance level, the control of the rate of mass transfer is observed as a plateau of  $r_A$  (or deviation from linearity) as illustrated in Figure 2.14b.

Mass transfer of reactants to a surface (boundary layer) in a PCM is realized mainly via forced convection. (see also Section 2.5.2). Increasing velocity (or  $J_w$  for PCM) promotes the reaction rate depicted in Figure 2.14c. Yet, at high-velocity values, the fully or partially limited step of chemical reaction manifests itself in the independence of  $r_A$  on  $J_w$ .

In a PCM – a type of continuous-flow photoreactors with fixed photocatalyst – the permeate fluid velocity (or  $J_w$ ) simultaneously influences two parameters: i) mass transfer coefficient ( $k_m \propto J_w^b$ ,  $b < 1$ );<sup>304</sup> and ii)  $\bar{t}_r$  including contact time ( $\bar{t}_{con}$ ).<sup>305</sup> Indeed, an increase in velocity inevitably shortens  $\bar{t}_r$  directly linked to achieved removal.<sup>242, 306</sup> For the PCM operated in a single pass, the  $\bar{t}_r$  and  $\bar{t}_{con}$  can be used interchangeably provided that the whole PM is illuminated. This dual effect of  $J_w$  on the photocatalytic process in PCM is also observed as deviation from linearity in a plot of  $\ln(c_p/c_f)$  against reaction time for first-order reactions.<sup>307</sup>

As a result of the decrease in the radial diffusion time, (photo)reactors with reactant–catalyst distances on the micrometer scale (for instance, microreactors or PCM, see also) exhibit the faster external mass transfer compared to those with diffusion distances in the mm-cm range.<sup>218, 246</sup> The boost of photocatalytic activity in photomicroreactors is evidenced by a profound increase in interfacial area ( $A'_s/V_R < 3 \cdot 10^5 \text{ m}^2 \text{ m}^{-3}$ ) by several orders of magnitude.<sup>247, 308</sup> The enhancement of photocatalytic reaction kinetics in nanoporous PCM is likely to be even stronger, because  $a'_V$  for MF-UF membranes can reach  $10^7 \text{ m}^2 \text{ m}^{-3}$ .<sup>248</sup> Overall, the rate of mass transfer in PCM can be promoted by i) rise of  $J_w$ , ii) reduction of membrane pore size, iii) increase in  $a'_V$ , though the last two parameters are strongly interrelated. The goal of the given strategies is to improve the contact between reactants and immobilized porphyrin molecules distributed over the membrane surface. The role of contact in photocatalytic degradation of MP using porphyrin-coated membranes is however not well understood. To that end, this thesis intends to provide the results on the role of contact in Chapter 7.

### Temperature

The effect of temperature in photocatalysis differs from conventional catalysis, whereby the reaction rate correlates with temperature via activation energy as given by Arrhenius' law. In the presence of a catalyst, activation energy diminishes that allows to accelerate the reaction rate (Figure 2.15a). Activation control – associated with high activation energy in thermal catalysis – can be overcome by increasing the

temperature. In photocatalysis, the activation (hopping over the energy barrier) occurs upon excitation of photocatalyst (depicted as PS in Figure 2.15b). Hence, activation energy values are usually negligible for photocatalytic reactions, whereas intrinsic kinetics (described by  $k_i$ ) is dependent only on the absorbed photon flux. However, the temperature might indirectly influence the photocatalytic process.

Adsorption-limited reactions are sensitive to the change of adsorption constant, which obeys the Van t'Hoff equation. Consequently, the decrease in temperature may favor the binding of pollutants to the photocatalyst surface and accelerate the overall rate of reaction. Considering the temperature-dependent solubility of oxygen (as of other gases), the ability of PS to produce  $^1\text{O}_2$  – evaluated via  $\Phi_\Delta$  and linked to the concentration of dissolved oxygen<sup>309</sup> – can decrease at higher temperature. Overall, the temperature range of 20–80°C is recommended for conducting the photocatalytic degradation of water-borne pollutants that corresponds to a marginal activation energy of a few kJ/mol.<sup>310</sup> Due to the low activation energy and the detrimental effect of higher temperatures, this parameter was controlled but not varied in the studies of PCM performance carried out in this thesis.

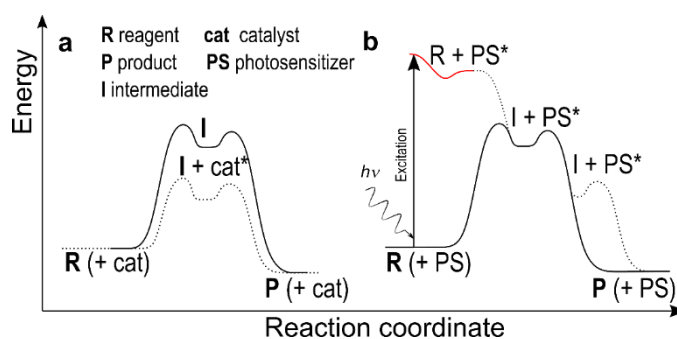


Figure 2.15: Energy paths examples: **a** traditional thermal catalysis ( $\text{R} \rightarrow \text{P}$ ) in presence of catalyst (**cat**) via intermediate (**I**), and **b** photocatalytic reaction using PS in the excited state ( $\text{PS}^*$ ) via one or few intermediate states. Figure adapted from Ref.<sup>311</sup> with permission from the Royal Society of Chemistry.

## 2.6.2 Water Quality Parameters

In a full-scale or pilot plant including potentially the PMR stage, variation of water quality can significantly dampen the degradation performance. On the basis of water analysis and knowledge of implications of solutes and key water parameters, the WTP operators can promptly respond to upcoming process changes. Therefore, providing the required knowledge is essential for the future implementation of the photocatalytic process.

### *Concentration of Pollutant and Dissolved Oxygen*

Fluctuations in the feed contaminant concentration lead to different reaction times necessary to achieve the same decomposition degree (*removal*), provided that the rate law form is unaffected. Generally, the rate of homogeneous reaction increases with the reactant concentration according to the power-law form. However, in heterogeneous reactions – such as those mediated by  $^1\text{O}_2$  generated by immobilized PS molecules – the kinetics depends on spatial location of reacting species.<sup>312</sup>

Photocatalytic reactions in PMR are often described either with the first-order reaction or Langmuir-Hinshelwood models.<sup>313</sup> Both models exhibit a linear increase in  $r_A$  with  $c_f$  at low-to-medium concentrations as illustrated in Figure 2.16a. However, at high concentrations, the photocatalyst-coated surface becomes

saturated with pollutant molecules. This effect is observed for semiconductor photocatalysts (such as  $\text{TiO}_2$ ) as a deviation of  $r_A$  from linearity signifying that the surface reaction becomes the limiting stage.<sup>44, 314</sup> At extremely high concentrations, the reaction rate can drop sharply thus indicating from the Langmuir-Hinshelwood mechanism to the Eley-Rideal mechanism<sup>315</sup> (see also Figure 2.16a).

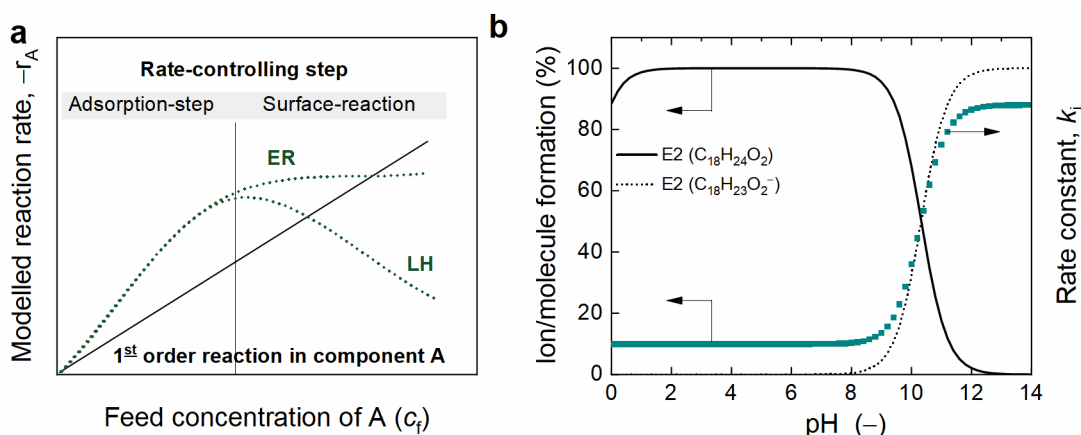


Figure 2.16: Schematic illustration of dependence of the reaction rate on the pollutant concentration and pH in the feed solution. **a** Increasing concentration can exhibit adsorption- or surface-reaction limited kinetic regimes.<sup>302</sup> **b** Change in ionized and molecular form of 17 $\beta$ -estradiol concentration as a function of pH (*speciation*) correlates with the bimolecular rate constant for  $^1\text{O}_2$ -mediated oxidation ( $k_i$  expression is derived by Scully and Hoigné).<sup>316</sup>

In photonic processes involving energy transfer (Type II PS), the molecules of pollutant or dissolved species act as quenchers of the PS excited state.<sup>183</sup> The kinetics of such a collisional deactivation process is explained via the Stern-Volmer equation (see also Equation 2.4), whereby PS excited state lifetime decreases with quencher concentration. As a result of deficiency of dissolved oxygen in aqueous phase (mentioned in Section 2.4.4), oxygen saturation of the feed solution enhances  $^3\text{PS}^*$  quenching. This typically plays a positive role in the generation of  $^1\text{O}_2$  and  $\text{O}_2^{\bullet-}$ . Remarkably, the implications of increasing pollutant concentrations on the generation of  $^1\text{O}_2$  by PS (expressed as  $\Phi_\Delta$ ) and overall  $r_A$  depend on the quenching rate constant of excited state by a compound **A** ( $k_q^A$ ).<sup>309</sup>

In kinetic studies of triphenylthiopyrylium photocatalyst, Martinez-Haya *et al.* reported the deactivation of  $^1\text{PS}^*$  and  $^3\text{PS}^*$  by MP molecules being negligible at low concentrations ( $<10^{-5}$  M) compared to solvent-induced (*intrinsic*) decay.<sup>317</sup> This finding indicates that i)  $\Phi_\Delta$  is not affected by  $c_A$ ; and ii)  $-r_A$  rises with  $c_A$  at environmentally relevant level ( $10^{-10}$ – $10^{-5}$  M) as given by Equation 2.14. A similar conclusion can also be drawn for high  $c_A$ , when compound **A** is not an effective quencher of  $^1\text{PS}^*$  and  $^3\text{PS}^*$  (see Equation 2.15). Conversely, high  $c_f^A$  values ( $>10^{-5}$  M) are assumed to be detrimental to the efficiency of  $^1\text{O}_2$  generation, provided that the quenching rate of excited states by **A** molecules kinetically competes with that by triplet oxygen molecules (see Equation 2.16). This is evidenced by a significant decrease in  $\tau_S$  and  $\tau_T$  (in agreement with Stern-Volmer relation) that results in a reduced probability of quenching of  $^1\text{PS}^*$  or  $^3\text{PS}^*$  states by triplet oxygen ( $P_{\text{O}_2^3}$ ). The same logic holds true for any dissolved (organic or inorganic) species.

$$\text{Low } c_f^A \quad k_q^{\text{O}_2}[\text{O}_2] \gg k_q^A[\text{A}] \quad \left| \quad -r_A \propto c_f, \Phi_\Delta = \text{const} \quad (2.14)$$

$$\text{High } c_f^A, k_q^{O_2} \gg k_q^A \quad k_q^{O_2}[O_2] \gg k_q^A[A] \quad \left| \quad -r_A \propto c_f, \Phi_\Delta = \text{const} \quad (2.15)$$

$$\text{High } c_f^A, k_q^{O_2} \leq k_q^A \quad k_q^{O_2}[O_2] \leq k_q^A[A] \quad \left| \quad -r_A \propto c_f^{n < 1}, \Phi_\Delta \propto 1/c_f^A \quad (2.16)$$

In the wake of scarce studies on PS-assisted degradation of 17 $\beta$ -estradiol,<sup>306, 318</sup> the first steps in understanding the photocatalytic process using PCM to remove 17 $\beta$ -estradiol and other SH at environmentally appropriate levels up to the solubility limit in water are critical.

#### *pH of Reaction Medium*

The change of negative logarithm of proton concentration (pH) in reaction medium determines: i) charge (including isoelectric point) of photocatalyst-coated surface; ii) degree of pollutant molecule ionization.<sup>298</sup> Both factors affect the (physical) adsorption of pollutants by promoting or disrupting electrostatic interaction with the photocatalyst-coated surface.<sup>298</sup> As pointed out above, the reaction rate can vary greatly depending on whether the adsorption reaction or the surface chemical reaction is the limiting step.

For compounds with phenolic moieties (including estrone and 17 $\beta$ -estradiol), the reaction rate of <sup>1</sup>O<sub>2</sub>-mediated oxidation linearly correlates with deprotonation degree of the –OH group (as illustrated in Figure 2.16b. Miller<sup>319</sup> and García<sup>320</sup> provided evidence of improved photocatalytic degradation of phenolic substances in alkaline media using dissolved PS. Likewise, an increased bimolecular rate constant (*k<sub>i</sub>*) for the oxidation reaction of 17 $\beta$ -estradiol (in basic-methanol solution),<sup>318</sup> benzyl-<sup>321</sup> and butylparaben, 4-t-Octylphenol,<sup>322</sup> has been observed for PS investigated in alkaline solutions. The similar beneficial effect of carrying out degradation tests at pH > pK<sub>a</sub> was observed for nanoparticle-,<sup>323</sup> nanofiber-immobilized PS,<sup>324</sup> and porphyrin-coated membranes.<sup>270</sup> The understanding of the implications of pH change on photocatalytic degradation of steroid hormones using PS-coated membranes is limited due to the scarcity of relevant studies. Overall, given the complexity of pH effect, its optimum value must be determined for each combination of PCM and pollutant.

#### *Water Matrix*

The observed degradation efficiency of MPs is the result of the cumulative effect of water matrix components, which are abundant in surface and industrial waters. Water matrix constituents can be categorized by nature into i) inorganic ions (salts, metals); ii) dissolved organic matter (humic substances); and iii) insoluble particulates (turbidity). Their influence on the efficiency of photocatalytic decomposition is a complex research area, wherein (often both) synergistic and antagonistic effects are manifested simultaneously.<sup>325</sup> Antagonistic effects of water matrix originate from i) the quenching of PS excited state; ii) scavenging of ROS;<sup>326</sup> iii) light shielding effect due to water opacity (from dissolved organic matter, DOM);<sup>327</sup> or iv) scattering effects from particulates.<sup>44</sup> For example, chloride, sulfates, carbonates, metal cations, and organic matter are strong scavengers of radicals and thus may suppress or even deactivate the catalyst or ROS precursors.

Humic and other polyphenolic compounds can adsorb on the catalyst surface thereby impeding access to pollutants. More information on the effect of natural organic matter on photocatalytic degradation is given in the review.<sup>328</sup> Nevertheless, when photocatalytic treatment is conducted with real water, a synergistic effect can be observed. Surface water contains DOM, which under sunlight exposure generates different type of ROS, including HO•, <sup>1</sup>O<sub>2</sub> and DOM triplet state,<sup>329, 330</sup> thereby contributing to the achieved photocatalytic oxidation.<sup>331</sup>

When it comes to quenching the excited state of PS, the type of quencher ion is more important than ionic strength. The strong decrease of PL signal – correlated with the corresponding  $\tau_S$  or  $\tau_T$  – have been

demonstrated in presence of halide ions ( $k_q = 2 \cdot 10^8 \text{ M}^{-1} \text{ s}^{-1}$  for  $\text{Cl}^-$ ,  $k_q = 2 \cdot 10^9 \text{ M}^{-1} \text{ s}^{-1}$  for  $\text{Br}^-$ ),<sup>332</sup> paramagnetic species ( $k_q = 10^{10} \text{ M}^{-1} \text{ s}^{-1}$  for  $\text{O}_2$ ,<sup>186</sup>  $\text{NO}$ ), and heavy metal cations ( $10^9$ – $10^{10} \text{ M}^{-1} \text{ s}^{-1}$ ).<sup>333</sup> Given the highly efficient quenching of fluorinated porphyrins by  $\text{O}_2$ , the formation of  $^1\text{O}_2$  is likely to be impeded only in highly saline media ( $[\text{Cl}^-] > 100 \text{ mM}$ ,  $[\text{Br}^-] > 10 \text{ mM}$ ) or heavy-metal polluted water. Irrespective of the reliable photophysical attributes of porphyrins, ubiquitous dissolved inorganic/organic matter can efficiently scavenge the produced ROS, thus undermining their utilization.<sup>36</sup> Among ROS,  $^1\text{O}_2$  is considered, though, less affected by water matrix (see also Section 3.2.2). In this thesis, the detailed investigation of effects of inorganic/organic matter will not be conducted. Instead, maintaining the ionic strength in working solution with bicarbonate buffer will suffice to prevent pH drift, which can alter the photocatalytic activity during experiments.<sup>334</sup> Moreover, the use of a chloride-bicarbonate background solution for this objective acknowledges the role of dissolved carbon dioxide ( $\text{CO}_2$ ), which almost completely accounts for the alkalinity of surface waters.

## 2.7 Summary

The lack of fundamental understanding of the mechanism behind MP oxidation using PS-coated membranes is a major obstacle to their design and adoption as a viable technology for photocatalytic water treatment. The mass transfer of reactants and pollutant degradation kinetics rely on operating parameters (water flux, light intensity), solution chemistry (concentration and type of pollutant, pH, inorganic background ions), factors related to photosensitizer (nature of central metal ion, total loading, and porphyrin distribution), membrane characteristics (charge, hydrophobicity, pore size distribution, porosity, thickness). In a variety of studies devoted to semiconductor-based materials, the limiting factors of PS-assisted oxidation process have barely been addressed.

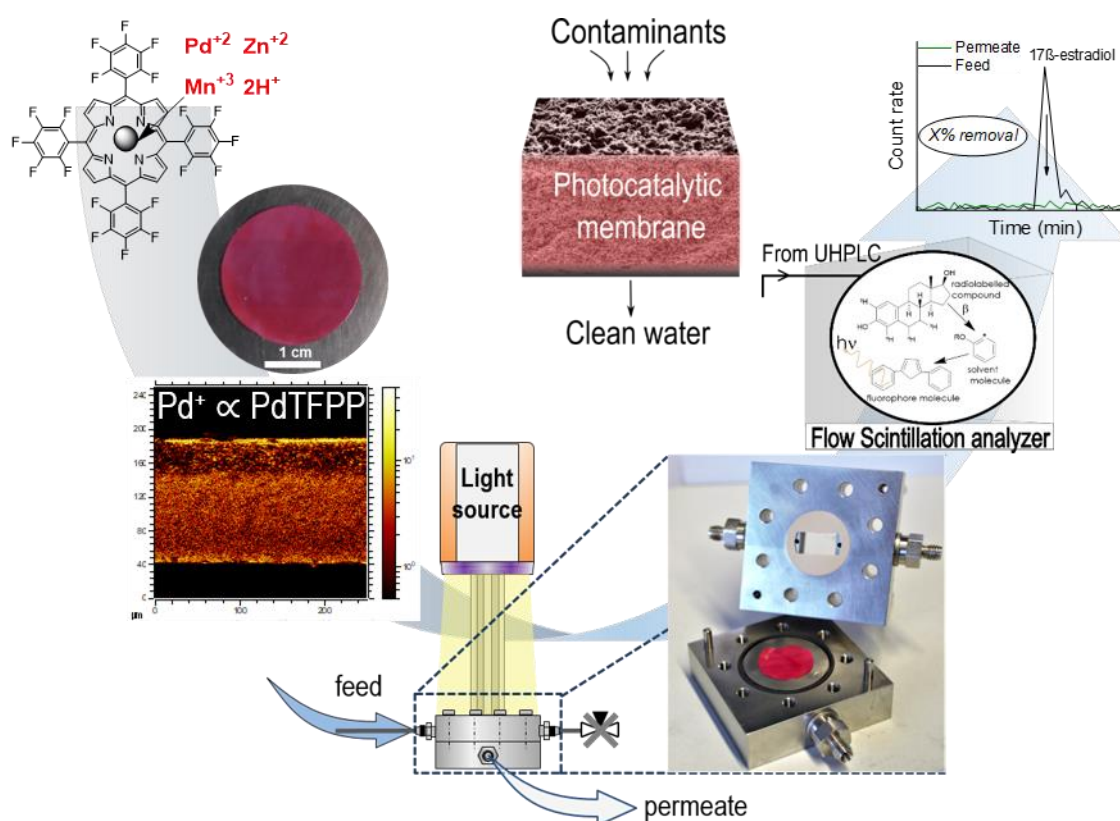
Firstly, the effectiveness of membrane-immobilized porphyrins for water-borne pollutant removal in the brief timeframe of a few seconds is unknown. Thus, this knowledge gap will be spanned using probe molecules of readily available dye while testing operating parameters in Chapter 4. Considering the well-known issue of PS photobleaching and aging of polymer materials, insights into photostability of immobilized porphyrin molecules will be obtained in Chapter 6.

Secondly, the majority of the research is conducted in laboratories with pollutant concentrations from  $\mu\text{g L}^{-1}$  to  $\text{mg L}^{-1}$  level, while the environmentally relevant level remains in the  $\text{ng L}^{-1}$  range (ppt level). Thus, the study is needed to bridge the gap between laboratories and the environment regarding the pollutants concentrations. For that, the method for separation and detection of mixture and by-products of SH at  $\text{ng L}^{-1}$  level will be developed on the basis of liquid chromatography and scintillation methods. Based on the developed methodology using a sensitive analytical instrument, the mechanism of photocatalytic oxidation of mimics of real water pollutants (radiolabeled steroid hormones) will be elucidated in Chapter 5

Thirdly, the implications of these studies will have an impact on technical feasibility of the photocatalytic treatment using PS-coated membranes. In an attempt to decrease dependence on the noble metals (from using palladium-porphyrin), Chapter 6 will investigate how the nature of central metal ion in porphyrins alters their photocatalytic activity.

Finally, the interplay of membrane characteristics and photocatalytic activity of PS-coated membranes has not been revealed in literature. For the kinetic regime in mass-transfer controlled regime, acceleration of reaction rate is realized via enhanced mass transfer inside PCM. For that matter, Chapter 7 will offer the implications of improved contact in PCM on the effectiveness and kinetics of SH oxidation.

# 3 Materials and Methods



This chapter provides an overview over the materials and methods, which were used for fabrication and characterization of porphyrin-coated membranes. In addition, analytical equipment used for analysis of model and real-water pollutants is described. The experimental system and protocols used to determine photocatalytic activity of the studied photocatalytic membranes are outlined. The chapter describes an error analysis applied to the data obtained in the studies of membrane characterization and photocatalytic experiments.

### 3.1 Chemicals and Solvents

All chemicals and solvents were of analytical grade as summarized in Table 3.1.

Table 3.1: List of chemicals and solvents used in this thesis

Compound	Formula	Grade	Source
<b>Chemicals</b>			
1,4- Diazabicyclo[2.2.2]octan	C <sub>6</sub> H <sub>12</sub> N <sub>2</sub>	≥99.0%	Sigma-Aldrich, China
Hydrogen Chloride	HCl	37%	Carl Roth, Germany
Methylene Blue	C <sub>16</sub> H <sub>18</sub> ClN <sub>3</sub> S·3H <sub>2</sub> O	99.0%	Sigma-Aldrich, China
Potassium chloride	KCl	99.9%	VWR chemicals,
Potassium hydroxide	KOH	99.9%	Germany
Sodium bicarbonate	NaHCO <sub>3</sub>	p.a.	
Sodium chloride	NaCl	p.a.	Merck, Germany
Sodium hydroxide	NaOH	99.0% (pellets)	
Sodium sulfite	Na <sub>2</sub> SO <sub>3</sub>	>98.0%	
Uric acid	C <sub>5</sub> H <sub>4</sub> N <sub>4</sub> O <sub>3</sub>	>99%	Sigma-Aldrich, USA
5,10,15,20-	C <sub>44</sub> H <sub>8</sub> F <sub>20</sub> N <sub>4</sub> Pd	palladium (>95%)	
Tetrakis(pentafluoro-	C <sub>44</sub> H <sub>8</sub> F <sub>20</sub> N <sub>4</sub> Zn	zinc (95%)	
phenyl)porphyrins	C <sub>44</sub> H <sub>10</sub> F <sub>20</sub> N <sub>4</sub>	free-base (95%)	Frontier Scientific,
	C <sub>44</sub> H <sub>8</sub> F <sub>20</sub> N <sub>4</sub> MnCl	manganese (III) chloride (95%)	USA
	C <sub>44</sub> H <sub>8</sub> F <sub>20</sub> N <sub>4</sub> Pt	platinum(II) (97%)	
<b>Solvents</b>			
Acetone	C <sub>3</sub> H <sub>6</sub> O	99.5%	
Dimethylformamide	C <sub>3</sub> H <sub>7</sub> NO	99.9%	Merck, Germany
Ethanol	C <sub>2</sub> H <sub>5</sub> OH	>99.8%	
Methanol (for PCM)	CH <sub>3</sub> OH	>99.8%	
(for chromatography)		99.7%, UHPLC gr.	Fischer Scientific
Phosphate buffer solution	Na <sub>2</sub> HPO <sub>4</sub> ,	0.044 M Na <sub>2</sub> HPO <sub>4</sub> ,	Sigma-Aldrich, USA
(pH =7.2 ±0.2) BioUltra	NaH <sub>2</sub> PO <sub>4</sub> , H <sub>2</sub> O	0.022 M NaH <sub>2</sub> PO <sub>4</sub>	
Tetrahydrofuran	C <sub>4</sub> H <sub>8</sub> O	>99.9%	Merck, Germany or Honeywell, USA
Ultrapure Water	H <sub>2</sub> O	Type 1, >18.2 MΩ cm <sup>-1</sup> (at 25 °C)	Milli-Q Direct system, Merck Millipore Germany



Porphyrin chemicals were used without further purification. The following impurities were disclosed by the manufacturer: Zn(II) meso-Tetra(pentafluorophenyl) chlorin, free base meso-Tetra(pentafluorophenyl) porphine, residual solvents (for Zn-porphyrin), meso-Tetra(pentafluorophenyl) chlorin, residual solvents (for free-base porphyrin), Pd(II) meso-Tetra(pentafluorophenyl) chlorin, free-base meso-Tetra(pentafluorophenyl) porphine, residual solvents (for Pd-porphyrin)

The radiolabeled steroid hormones used in the work were shipped in ethanol from Perkin Elmer LAS GmbH, Germany. Table 3.2 contains the data on specific activity and purity of used radiochemicals (for chemical properties and chemical structures, see Table 2.3). Additionally, a sample of diluted tritium water (volume activity of  $2.4 \cdot 10^{10}$  Bq L<sup>-1</sup>) was supplied for internal use from the Institute of Technical Physics (ITEP, KIT). For high feed concentrations ( $c_f > 100$  ng L<sup>-1</sup>), radiolabeled steroid hormones were mixed with the non-labelled versions of estrone ( $\geq 99.0\%$ ), 17 $\beta$ -estradiol ( $\geq 98.0\%$ ), testosterone ( $\geq 98.0\%$ ), progesterone ( $\geq 99.0\%$ ) – all purchased from Sigma-Aldrich, Germany. Stock solutions of radiolabeled hormones (10  $\mu$ g L<sup>-1</sup>) were prepared by diluting a native (ethanol-based) solution with water, whereas non-labelled steroid hormones (1–1,000  $\mu$ g L<sup>-1</sup>) were prepared by dissolving a powder in methanol due to the limited solubility in water (see also Table 3.2). Both types of stock solutions were kept in dark at temperature below 4 °C.

Table 3.2: Information on the batch of radiolabeled SHs used in this work

Radiochemicals	Volume activity, mCi/mL	Specific activity, Bq/mmol	Lot number	Purity, %
[2,4,6,7- <sup>3</sup> H(N)]-estrone	1	$3.69 \cdot 10^{12}$	No 2354825	>97
		$3.48 \cdot 10^{12}$	No 2165951	
		$2.96 \cdot 10^{12}$	No 2526125	
		$3.12 \cdot 10^{12}$	No 2155774	
[2,4,6,7- <sup>3</sup> H(N)]-estradiol	1	$3.48 \cdot 10^{12}$	No 2165951	>97
		$3.26 \cdot 10^{12}$		
		$3.56 \cdot 10^{12}$	No 2852571	
[1,2,6,7- <sup>3</sup> H(N)]- testosterone	1	$3.53 \cdot 10^{12}$	No 2136265	>97
		$2.94 \cdot 10^{12}$	No 1976041	
[1,2,6,7- <sup>3</sup> H(N)]- progesterone	1	$3.57 \cdot 10^{12}$	No 2151380	>97
		$3.63 \cdot 10^{12}$	No 2001957	

## 3.2 Preparation of Photocatalytic Membranes

### 3.2.1 Types and Characteristics of PVDF Used Membranes

In this study, only hydrophobic variation of commercial PVDF membranes was employed that enabled i) strong membrane interaction with porphyrin; and ii) avoiding the unknown hydrophilic additives prone to degradation as shown in Figure 3.1 (see also discussion in Section 2.5.3).

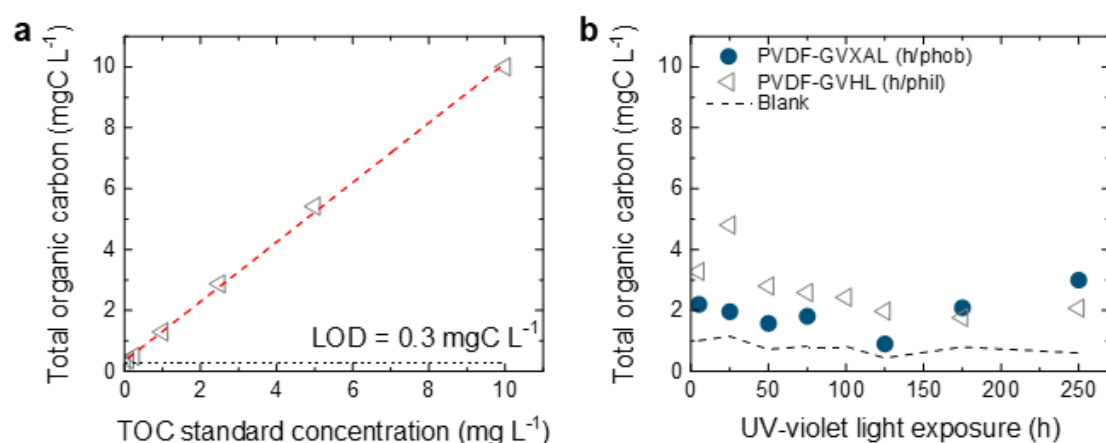


Figure 3.1: **a** The calibration curve of the TOC instrument using sodium hydrogen phthalate as standard solution (1–10 mg L<sup>-1</sup>) and **b** evolution of TOC content in water samples collected after the accelerated ageing of pristine hydrophilic (Millipore, GVXAL, 0.2 μm) and hydrophobic PVDF (Millipore, GVHL, 0.2 μm) membranes aged in the UV-violet light soaking chamber ( $I_{inc} = 222.2 \text{ mW cm}^{-2}$ )

The supplier information and selected properties of the given membranes are compiled in Table 3.3. Among these, Millipore's GVXAL (0.2 μm, supplied in the roll form) was selected as the default membrane type for the experiments presented in Chapters 4–6. Noteworthy, this particular membrane was commercially produced, but is no longer available due to its previous use in (now discontinued) composite membrane modules. The most similar commercially available membrane to the GVXAL-PVDF is Durapore GVHP (hydrophobic, 0.22 μm, Millipore)<sup>335</sup> relating to porosity, mean pore size and thickness (Merck Millipore Germany, personal communication, December, 2018). In Chapter 7, the photocatalytic performance of PVDF membranes with different pore size was compared with that using MP200 membranes.

Table 3.3: The list of commercial hydrophobic PVDF membranes used in this thesis and their characteristics. Thickness and polymer density were measured experimentally.

ID	Membrane code	Mean pore size, μm	Thickness, μm	Polymer density, g cm <sup>-3</sup>	Porosity, %
Novamem (Switzerland)					
NM20	PVDF20	0.02 <sup>336</sup>	30 ± 5	1.42	49 <sup>336</sup>
NM100	PVDF100	0.10 <sup>336</sup>	92 ± 2	1.48	55 <sup>336</sup>
Merck Millipore (Germany)					
MP100	VVHP	0.10 <sup>337</sup>	101 ± 2	1.46	70 <sup>337</sup>
<b>MP200<sup>a</sup></b>	<b>GVXAL</b>	<b>0.20<sup>335</sup></b>	<b>130 ± 1</b>	<b>1.47</b>	<b>70<sup>335</sup></b>
MP450	HVHP	0.45 <sup>338</sup>	89 ± 2	1.48	70 <sup>338</sup>
Hawach Scientific (China)					
HW650 <sup>b</sup>	MPDVPP	0.65	90 ± 5	1.31	Not defined

<sup>a</sup> in boldface type, the membrane type was used as a reference in this dissertation;

<sup>b</sup> sandwich membrane prepared by coating thin PVDF layers on the top and the bottom of polyethylene-terephthalate microfiber mesh.

### 3.2.2 Experimental Procedure

In this dissertation, porphyrin-coated membranes were fabricated using an impregnation method based on the physical adsorption of hydrophobic porphyrin molecules on a hydrophobic PVDF membrane. The organization of the adsorption process in addition to the preparation and post-cleaning procedures are illustrated in Figure 3.2 using the photographs of palladium-porphyrin (red-colored) as an example.

Firstly, the solution with the preferred concentration of selected porphyrin was prepared in tetrahydrofuran (THF). Among all the studies organic solvents (ethanol, acetone, toluene, hexane, propylene carbonate), THF offered both the highest solubility and the largest uptake of fluorinated porphyrins by a PVDF membrane. Next, the PVDF membranes were cut (if supplied in roll form) to circular samples (25 mm diameter) and ultrasonically cleaned in acetone (bath, USC 300 T, VWR) and then rinsed in methanol. On the basis that acetone dissolves PVDF membrane at high temperature, the time and temperature of ultrasonic bath were carefully controlled: 8 min at 22–27 °C (the range is due to the bath heating). In Chapter 7, acetone used for ultrasonic cleaning was replaced with methanol to eliminate any potential damage to the membrane pore structure. Instead, the PVDF membranes were rinsed in acetone for just 2 minutes prior to the ultrasonic bath. The cleaned PVDF membranes were placed in a glass petri dish and left in a fume hood to evaporate the solvent for 10 minutes.

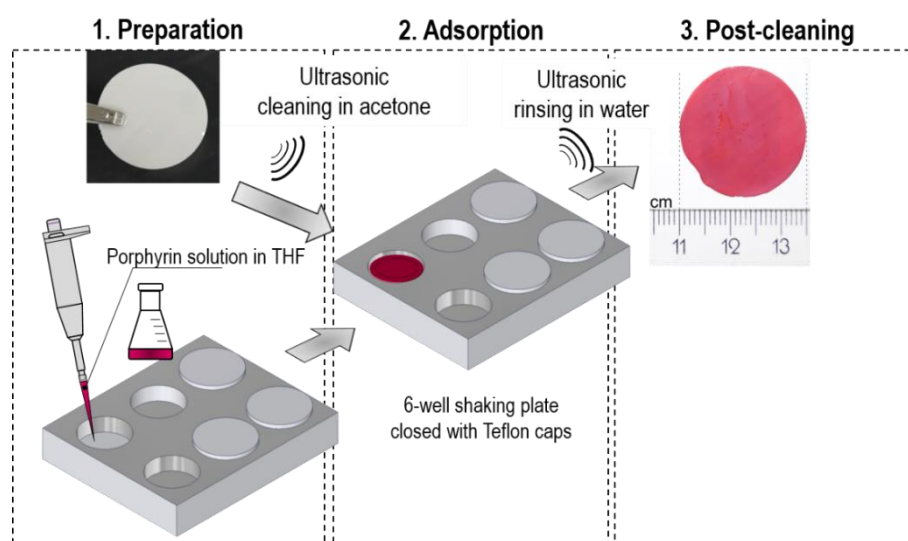


Figure 3.2: Schematic representation of PS immobilization process on PVDF membranes. Figure adapted with permission from Lyubimenko et al. (2019);<sup>276</sup> Copyright 2019, American Chemical Society.

In the second step, the dried membranes were immersed in one of six wells of a stainless-steel shaking plate filled with 1.5 mL (Chapter 4) or 2 mL (Chapters 5–7) porphyrin solution at temperature of  $(22 \pm 1)^\circ\text{C}$ . The solution volume was increased to reduce the error in the loaded porphyrin mass due to the THF volatility (loss of 0.3–0.4 mL). For the same reason, the shaker plate was devised and manufactured with tight Teflon lids using the workshop of the Institute of Microstructure Technology (IMT, KIT). Soaking of PVDF membranes in porphyrin solution was stopped after 4 h, which was the standard duration of the experiment.

At the final stage, the as-prepared membranes were quickly transferred to ultrapure water without letting them dry. The loosely bound porphyrin molecules or aggregates were removed from the membranes by sonication in water for 10 minutes. Considering the miscibility of THF and water (non-solvent for

fluorinated porphyrins), adsorbed porphyrin molecules were intact, whereas the membranes stayed wet in water (also depicted by the intense color in Figure 3.2) that was essential for effective degradation experiments. Before the experiments, all the PCM were stored in water in amber-glass vials for up to two weeks.

### 3.2.3 Evaluation of Photosensitizer Loading

The quantity of adsorbed photosensitizer per active membrane area – loading ( $\bar{q}_{PS}$ ) – was estimated via absorbance measurement in a spectrophotometer after dissolution of the entire PCM in dimethylformamide (DMF). For that, the membrane dried in rotary evaporator (at 40 °C) was weighed, immersed in a vial filled with 10 mL of DMF and heated for 2 h at 60 °C. The resulting solution was cooled and analyzed on a UV-Vis spectrophotometer (Perkin Elmer Lambda 950) at a wavelength corresponding to the strongest Q-band peak of the studied porphyrin. Hence, the  $q_{PS}$  ( $\mu\text{mol cm}^{-2}$ ) was determined from the optical density ( $OD_\lambda$ ) via Equation 3.1:

$$\bar{q}_{PS} = \frac{OD_\lambda}{\varepsilon_\lambda l_{opt} A_m} V_{solv} 10^6 \quad (3.1)$$

where  $\varepsilon_\lambda$  is the molar extinction coefficient of the studied porphyrin in DMF at a wavelength  $\lambda$  ( $\text{M}^{-1}\cdot\text{cm}^{-1}$ ),  $V_{solv}$  is the volume of DMF solvent (0.01 L),  $l_{opt}$  is the optical light path of the used cuvette (1 cm),  $A_m$  is the membrane area ( $4.9 \text{ cm}^2$  for a membrane coupon of 25 mm in diameter).

Palladium(II) tetrakis(pentafluoro-phenyl)-porphyrin (Pd-TFPP) was the main type of studied porphyrins, while an additional three noble-metal-free porphyrins – free-base ( $\text{H}_2$ -TFPP), zinc(II) (Zn-TFPP), and manganese(III) (MnCl-TFPP) – were studied in Chapter 6. Their chemical structures, photophysical and electrochemical properties will be given in Chapter 6 as well. The error in  $\bar{q}_{PS}$  was kept within 8% via careful correction of porphyrin concentration in the solution used for adsorption. For that, the absorbance of diluted (1:200v/v) porphyrin solution in THF was measured at the strongest Q-band peak, whereas the maximum error of optical density was below 2.5%. The calibration curves of the studied porphyrins in THF and DMF solutions are provided in Figure 3.3.

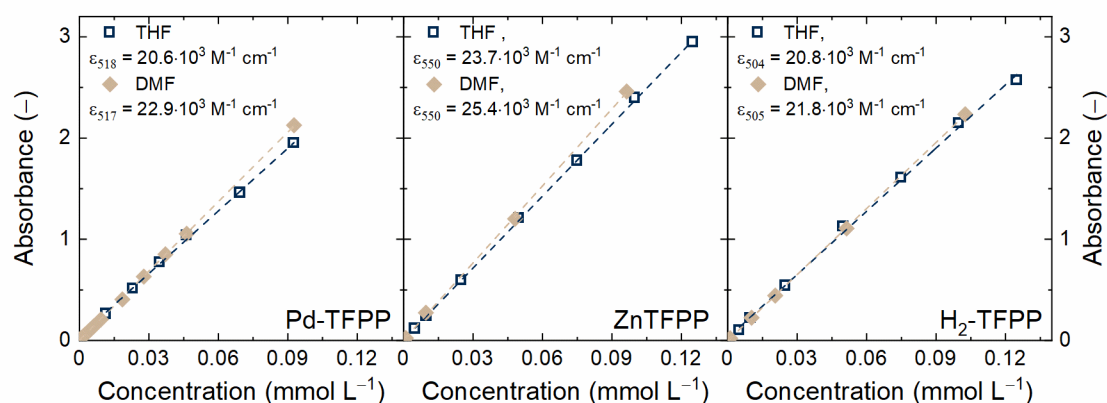


Figure 3.3: The calibration curves of Pd-, Zinc-, and free-base porphyrins employed in this work in THF (adsorption studies) and DMF (for determination of porphyrin loading).

The palladium- and zinc-porphyrins are highly soluble in THF ( $< 45 \text{ mM}$ )<sup>184</sup> at  $(25 \pm 2) \text{ }^\circ\text{C}$  and DMF ( $< 139 \text{ mM}$ ),<sup>186</sup> while the solubility limit of  $\text{H}_2\text{-TFPP}$  was not discovered. The solutions of all employed porphyrins (except Mn-TFPP) in THF have been regularly corrected using the corresponding calibration curves (Figure 3.3). For that, a  $50 \text{ }\mu\text{L}$  aliquot of the solution was diluted in  $9.95 \text{ mL}$  THF (200 times). The optical density of the resulting solution was determined using the bench-top spectrophotometer. Based on the absorbance value, the concentration of PS in solution was determined using the Lambert-Beer Law. The PS loading on as-prepared PCM was determined by measuring the optical density of the solution obtained from the dissolution of porphyrin-coated membrane in  $10 \text{ mL}$  DMF.

## 3.3 Experimental Systems for Photocatalytic Membranes

### 3.3.1 Description of the Photocatalytic Membrane Filtration Set-up

In this thesis, the degradation of pollutants was realized in the continuous-flow photocatalytic membrane reactors in the custom-built experimental set-up, which is the modified version of the micro cross-flow system described by Imbrogno and Schäfer.<sup>339</sup> The experimental set-up for PCM has been validated in numerous peer-reviewed publications.<sup>243, 307, 340</sup> Figure 3.4a depicts a photograph of the photocatalytic set-up consisted of five core elements: ① a temperature-regulated flask with feed solution; ② a high-precision dosing pump; ③ a cell with the mounted membrane and window for incident light; ④ a light source (solar simulator in panel Figure 3.4a); and ⑤ a diverter valve for sample collection/distribution.

The detailed description of the main components making up the photocatalytic system is illustrated in Figure 3.4b. High-pressure (up to  $100 \text{ bar}$ ) double-piston pump with a titanium  $500\text{-mL}$  head (Blue Shadow 80P, Knauer, Germany) was used for high-precision delivery of solution ( $< 2\%$  deviation of flow rate). The pump delivered a flow rate from  $0.1$  to  $499.9 \text{ mL min}^{-1}$ . The feed solution was maintained in a temperature-regulated double-jacketed beaker at  $(23 \pm 1) \text{ }^\circ\text{C}$  (max. volume  $1,000 \text{ mL}$ ) using a cooling bath thermostat (⑥, Pilot One CC-K6s, Huber). An electronic balance ⑦ ( $0.01\text{--}620 \text{ g}$  AX622/E, Adventurer Pro, Ohaus, Germany) continuously measured the permeate mass for flow rate control.

#### *Valves*

A diverter valve ⑤ was used to direct the permeate stream to the sample vials ( $1.5 \text{ mL}$ , Rotilabo, Carl Roth) fixed in a homemade (3D-printed) 16-well rack ⑧. A purge valve ⑨ of the pump was used to remove the air bubbles in the inlet lines. The pump outlet line was connected to the membrane cell ③ with stainless-steel tubing. To isolate the content of the system from the dosing pump, the shut-off valve ⑩ was installed. To protect the system from overpressure, the pressure relief valve ⑪ was installed. The filtration system was operated in a dead-end regime, whereby the retentate-side needle valve ⑫ was closed. Tubing, shut-off, needle, and relief valves were bought from MHK GmbH (Ham-Let Group, Germany). The flow rate was set by the pump, whereas transmembrane pressure was not regulated, and served as a metric of membrane resistance. Due to the dead-end filtration, the residence time inside the PCM was maintained throughout the experiment that helped achieve a stable level of pollutant degradation.

#### *Sensors and Data Acquisition*

The following parameters were monitored in the feed solution: i) pH using a glass electrode (SenTix81, WTW) connected to a meter (pH/Cond 3320, WTW); ii) dissolved oxygen concentration and temperature utilizing an optical (FDO-925, WTW) sensor connected to a multiparameter meter (MultiLine 3510 IDS, WTW); iii) electrical conductivity ( $\kappa$ ) using a BlackLine CR-GT/-EC/-GS sensor ( $0.1\text{--}2000 \text{ }\mu\text{S cm}^{-1}$ , JUMO, Germany) connected to a DAQ card transmitter (Ecotrans Lf03, JUMO, Germany) and iv) pressure

using A-10 (0–40 bar), S-10 (0–1 bar) or S-10 (0–2.5 bar) transducers (WIKA, Germany). Conductivity, temperature, and pressure data were collected and transferred to a computer using a DAQ card (13, USB-600, National Instruments).

The permeate line was equipped with in-line sensors for: i) electrical conductivity using a contactless sensor (8–2000  $\mu\text{S cm}^{-1}$ , ET131, eDAQ) connected to a DAQ card and to a multi-channel C4D Detector (eDAQ, Germany); ii) temperature using a thermocouple (Type T) connected to a separate data acquisition card (USB TC01, National Instruments); and iii) pressure from a built-in sensor (0–0.4 bar, S-20, WIKA). Data visualization and storage were conducted using the interface of a program written in LabVIEW 2014 software (National Instruments). An LED controller (14) was also connected to a LabVIEW interface that allowed to turn on the light source and vary the intensity of incident light in real-time. In Chapter 4, the permeate outlet of the PCM cell was connected to an in-line spectrophotometer (15) instead of the switching valve that enabled the real-time monitoring of MB and UA model pollutants (see Figure 3.4c).

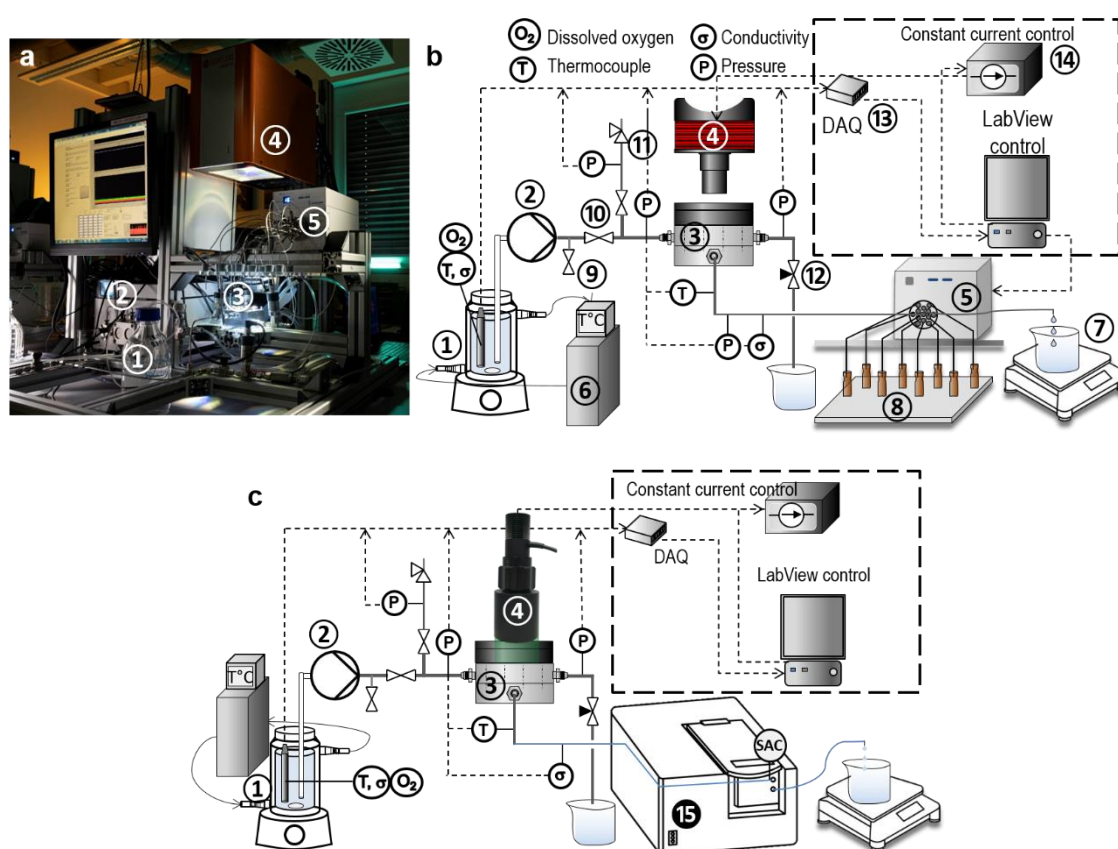


Figure 3.4: **a** Photograph and **b,c** schematic drawings of experimental system used in photodegradation studies. The system is equipped with in-line pressure, temperature, conductivity, and dissolved oxygen sensors. ① a temperature-controlled flask with feed solution; ② an HPLC dosing pump; ③ a stainless steel membrane cell with a quartz window, ④ a light source (solar simulator in **a**, white LED in **b**, gLED in **c**); ⑤ a diverter (switching) valve; ⑥ a cooling bath thermostat; ⑦ a balance with a flask for permeate collection; ⑧ a 16-well vial holder for permeate sample collection; ⑨ a purge, ⑩ a pump shut-off, ⑪ a pressure relief, and ⑫ a retentate-side needle valves; ⑬ a data acquisition card; ⑭ an LED controller. Exclusively used in Chapter 4: ⑮ an in-line connected UV-Vis spectrophotometer. Photograph (in **a**) was adapted with permission from Markus Breig (KIT, 2021); Copyright 2021, Karlsruhe Institute of Technology.

### Membrane Cell

The photocatalytic membrane cell used to house PCM (area  $4.9 \text{ cm}^2$ , 25 mm outer diameter) is based on the design of an existing micro-crossflow cell, which represented a scaled-down version of a macro cross-flow system and spiral-wound module in terms of hydrodynamic conditions (cross-flow velocity, Reynolds number).<sup>339</sup> Figure 3.5 depicts the PCM cell in open view, consisting of an upper and a lower parts made of 316 stainless-steel. Both parts are connected with 8 screws using a torque meter (see the holes in this upper part). The upper part has a cutout for a quartz window (area  $1.7 \text{ cm}^2$ , Zell Quarzglas, Germany) for inclusion of the incident light. The quartz glass was glued to the cutout of the PCM cell by Dipl.-Ing. Heinz Lambach at the Institute for Micro Process Engineering (IMVT, KIT) and tested by the present author.

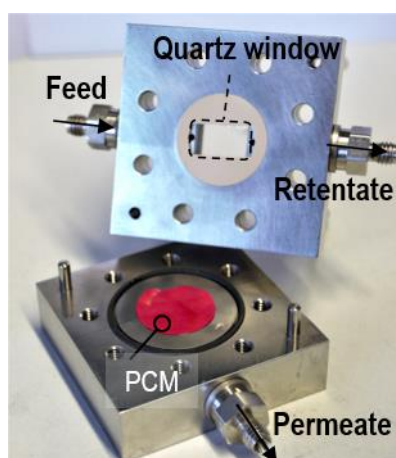


Figure 3.5: Photograph of the open photocatalytic membrane cell with an example of mounted PCM

A polyether-ether-ketone (PEEK) gasket (25 mm outer diameter) is placed below the quartz window, covering the most of top surface of membrane coupon. The active filtration area ( $2 \text{ cm}^2$ ) was constrained by a hexagonal cutout in the PEEK seal (see Figure 3.6a). While the reported filtration area was smaller than that of a membrane coupon, the dispersion of the flow in the radial direction ( $u_r$ , cross-flow) that could potentially influence the photodegradation results (Figure 3.6b) was neglected.

The findings of staining experiment with methylene blue dye served as an additional support to the negligible radial dispersion (see Figure 3.6c and Figure 3.6d) thereby validating the provided  $A_{\text{act}}$ . The intense blue color in the central area of a membrane coupon resembled the shape of the PEEK seal both on the top and bottom surface, though the minor light-blue regions outside the filtration area were observed (the area of a stainless-steel pad,  $12 \times 22 \text{ mm}$ ).



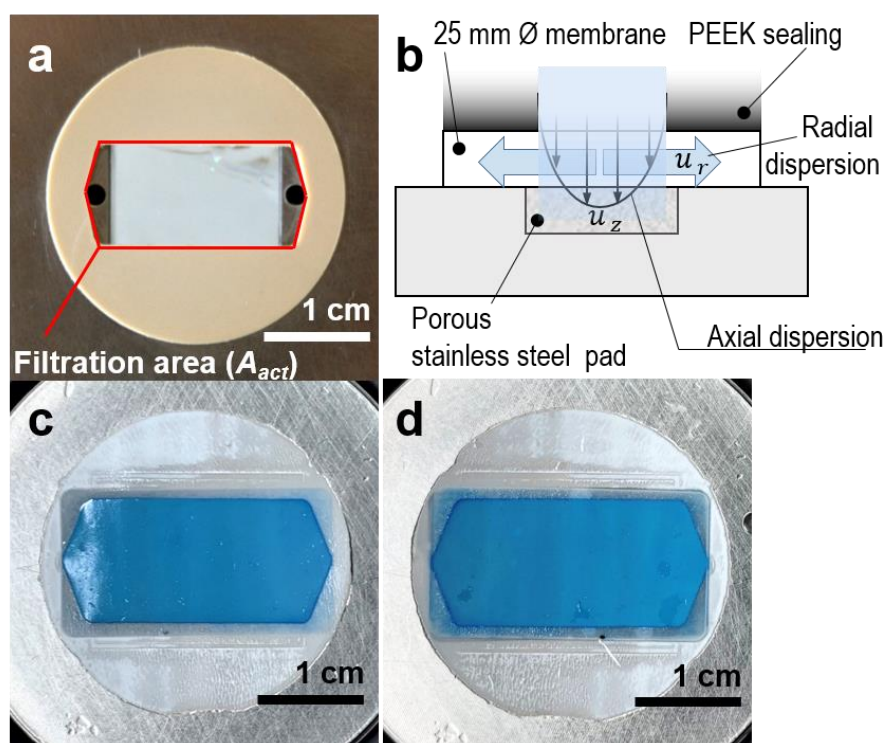


Figure 3.6: The photographs of **a**, the PEEK seal limiting the active filtration area (marked in red); **c**, top and **d**, bottom areas of the pristine PVDF membranes after filtering  $1 \text{ mg L}^{-1}$  MB solution with the background electrolyte ( $1 \text{ mM NaHCO}_3$ ,  $10 \text{ mM NaCl}$ ). **b** The schematics of the dispersion pattern of the membrane mounted to the stainless-steel cell in the experimental set-up. Figure adapted with permission from Lyubimenko et al. (2021);<sup>341</sup> Copyright 2021, Elsevier.

### 3.3.2 Light Sources

#### *Overview of the light sources used in this work*

Light-emitting diodes (LED) is a perfect choice for the light source in terms of longevity (10,000+ hours) and versatility of emission spectra (from narrow-band LEDs to broad-band multi-LED source such as solar simulator). In this study, three different LED-based lamps were used for excitation of PCM mounted to the photocatalytic system. The type of light source used in a particular chapter of the thesis, in addition to its maximal output power are summarized in Table 3.4.

Table 3.4: Overview of light sources used in the dissertation and their technical characteristics.

Light source	Model	Supplier	Maximal output power, W	Peak emission wavelength, nm	Used in the thesis
Green LED (gLED)	M530L3	Thorlabs	0.35	532	Chapter 4
White LED (wLED)	SOLIS-3C	Thorlabs	3.5	453	Chapter 5
Solar Simulator (SolSim)	SINUS-70	Wavelabs	270 (at 1 sun)	470	Chapters 6 and 7



In Chapter 4, a green LED was chosen as a light source to diminish *photolysis* (light-induced self-oxidation) of MB selected as model pollutant and absorbing light in red region (see the breadth of the emission band in Figure 3.7a). Figure 3.8a depicts the calibration curves of gLED before and after the quartz window of the membrane cell. Based on the difference in slope values, an 48% decrease in light intensity is observed after the quartz window that was due to: i) the light exposure (quartz glass window) area being smaller than that of thermal sensor and ii) non-ideal beam collimation.

The next steps to prospective use of sunlight were made with broad-band white light using wLED (Chapter 5) for degradation of steroid hormones (Figure 3.7b). The calibration curve of wLED current against the incident light intensity is shown in Figure 3.8b. Similar to the gLED, the measured  $I_{inc}$  reduced by 22% after the quartz window that agrees with the results of work using an identical photocatalytic cell and an UV-LED ( $\lambda_{exc} = 365$  nm) as a light source (reduction by 35% of  $I_{inc}$  after the quartz glass window).<sup>307</sup>

A significant advance over the two light sources was SolSim (used in Chapters 6 and 7), which provided a close spectral match (<5% difference per 100 nm of bandwidth) to the standard terrestrial solar (AM1.5g) spectrum<sup>342</sup> in the 350–1150 nm range over an area of 5 cm × 5 cm. The spectral difference per 100 nm of bandwidth was below 5% (see also Figure 3.7b). The SolSim was equipped with a pre-calibrated in-built spectrometer, which enabled continuous measurement of light intensity and emission spectrum. The height of the SolSim above the membrane cell was adjusted to 15 cm that ensured the light from the various LED channels was collimated, that is parallel rays.

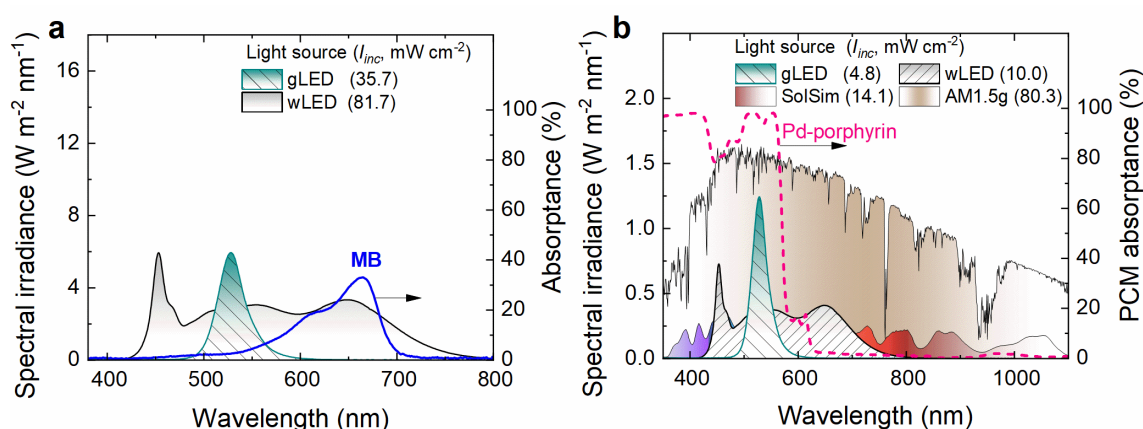


Figure 3.7: **a** The spectral irradiance of gLED and wLED light sources against the absorption spectrum of MB dye ( $1 \text{ mg L}^{-1}$ ); and **b** the spectral irradiance of gLED, wLED, SolSim light sources (used in experiments of SH degradation, Chapters 5-7), and the air-mass 1.5 global (AM1.5g) standard solar spectrum<sup>342</sup> plotted against absorption spectrum of the Pd-TFPP/PVDF membrane for  $q_{PS} = (0.23 \pm 0.02) \mu\text{mol cm}^{-2}$ . The  $I_{inc}$  of the gLED, wLED, SolSim on panel **b** were adjusted to correspond to  $\phi_{abs}^{ref} = 1.19 \cdot 10^{20} \text{ s}^{-1} \text{ m}^{-2}$

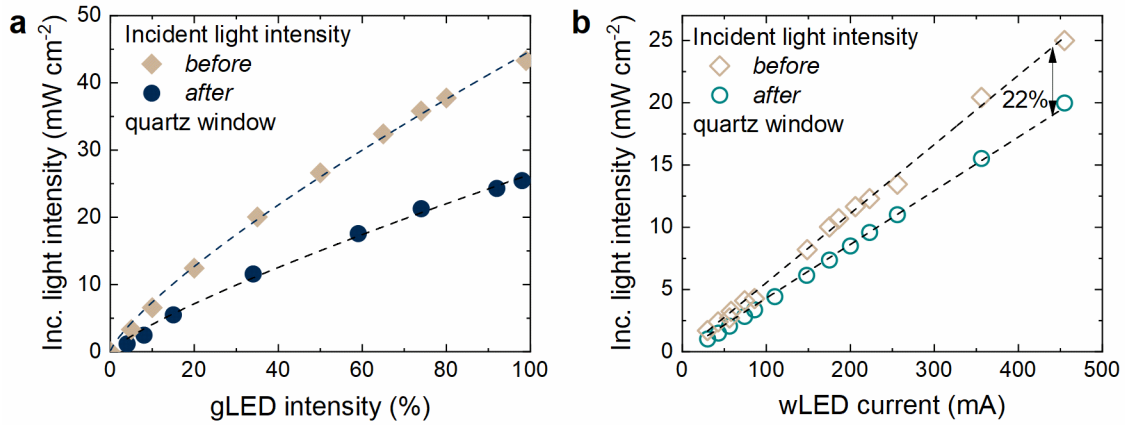


Figure 3.8: Calibration curves of incident light intensity ( $I_{inc}$ ) before and after the quartz window of the stainless-steel cell housing the membrane as a function of **a** intensity of green gLED,  $\lambda_{em} = (532 \pm 18)$  nm, and **b** the wLED current.

*Comparison of the Employed Light Sources*

The spectral irradiance of the wLED light source used for comparison with solar light was obtained by following this step-by-step guide:

1. Spectral distribution of incident photon flux ( $\varphi'_{inc,\lambda}$ ,  $s^{-1} nm^{-1}$ ) was measured with a spectrometer (Avantes, AvaSpec-ULS2048  $\times$  64TEC) by guiding lamp emission into the integrating sphere. The spectrometer was calibrated using a calibration lamp (Ocean Optics, HL-3plus-INT-CAL-EXT). The normalized value of  $\varphi'_{inc,\lambda}$  (-) (see Figure 3.9a)

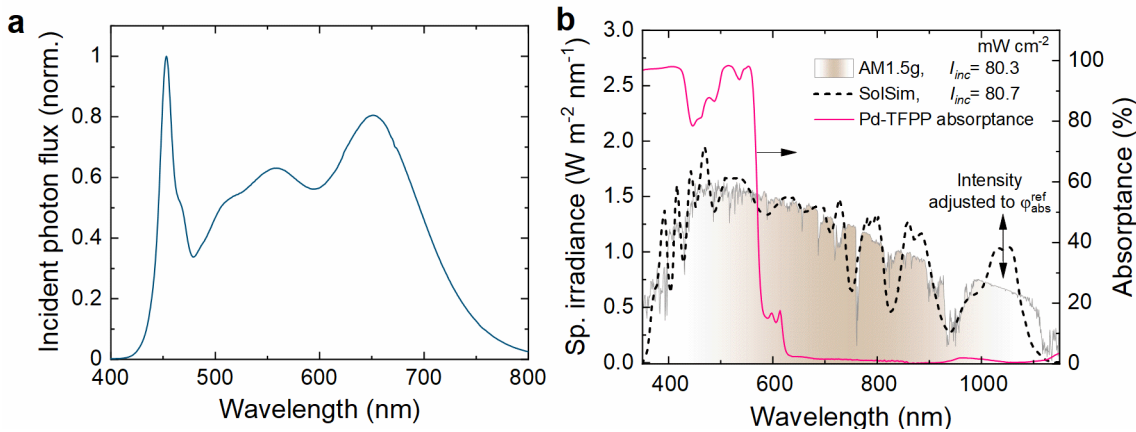


Figure 3.9: **a** Spectral distribution of the incident photon flux of the white-light LED (wLED), normalized to the range 0–1; **b** The spectral light intensity (spectral irradiance) of SolSim and air-mass 1.5 global (AM1.5g) standard solar spectrum.

2. Then,  $\varphi'_{inc,\lambda}$  was converted to spectral irradiance ( $I'_{inc,\lambda}$ ,  $W nm^{-1}$ ) using Equation 3.2:

$$I'_{inc,\lambda} = \frac{hu_L}{\lambda} \varphi'_{inc,\lambda} \quad (3.2)$$

3. The  $I'_{inc,\lambda}$  ( $\text{W nm}^{-1}$ ) spectrum was normalized ( $I''_{inc,\lambda}$ ,  $-$ ) and then integrated ( $I''_{inc}$ ,  $-$ ) as per Equation 3.3;

$$I''_{inc} = \int_{\lambda_1}^{\lambda_2} I''_{inc,\lambda} d\lambda \quad (3.3)$$

4. The light intensity measured by a thermal sensor ( $I_{inc}$ ,  $\text{mW cm}^{-2}$ ) and the calculated  $I''_{inc}$  ( $-$ ) are proportionally related. Their ratio is a matching factor  $\nu$  ( $\text{W m}^{-2} \text{nm}^{-1}$ ) used to obtain  $I_{inc,\lambda}$  ( $\text{W m}^{-2} \text{nm}^{-1}$ ), which was presented in Equation 3.4

$$I_{inc,\lambda} = \nu I''_{inc,\lambda} \quad (3.4)$$

Finally, the  $I_{inc,\lambda}$  was converted *via* Equation 3.2 to the relevant  $\varphi_{inc,\lambda}$  ( $\text{s}^{-1} \text{m}^{-2} \text{nm}^{-1}$ ).

The value of  $\varphi_{abs}$  was obtained by integration of the spectral distribution of absorbed photons ( $\varphi_{abs,\lambda}$ ,  $\text{s}^{-1} \text{m}^{-2} \text{nm}^{-1}$ ) in the wavelength region  $\lambda_1, \lambda_2$  as per Equation 3.5:

$$\varphi_{abs} = \int_{\lambda_1}^{\lambda_2} \varphi_{inc,\lambda} \alpha_\lambda d\lambda \quad (3.5)$$

where  $\varphi_{abs,\lambda}$  spectrum is calculated from  $\varphi_{inc,\lambda}$  and  $\alpha_\lambda$  ( $-$ ) is the absorptance spectrum of a PS-coated PVDF membrane in the wavelength region of 350–1150 nm. For the multiplication procedure, the spectra were interpolated.

The value of absorbed photon flux using wLED light source ( $I_{inc}^{ref} = 10 \text{ mW cm}^{-2}$ , see Chapter 5) and a Pd-TFPP/PVDF membrane ( $\bar{q}_{PS} = 0.21 \mu\text{mol cm}^{-2}$ ) is denoted as reference ( $\varphi_{abs}^{ref}$ ). When using the different light sources, such as gLED or SolSim ( $\varphi_{abs}^{LS}$ ) or noble-metal free PS-coated membranes ( $\varphi_{abs}^{PS}$ ), the light intensity was adjusted to match  $\varphi_{abs}$  as described by Equation 3.6 and Equation 3.7:

$$I_{inc}^{LS} = \beta_{LS} I_{inc}^{ref} \quad (3.6)$$

$$I_{inc}^{PS} = \beta_{PS} I_{inc}^{ref} \quad (3.7)$$

where  $I_{inc}^{LS}$  and  $I_{inc}^{PS}$  are the light intensities adjusted to a new type of light source or a new photosensitizer; the matching coefficients for a light source ( $\beta_{LS}$ ) or a novel photosensitizer ( $\beta_{PS}$ ) were derived as the ratio of absorbed photon flux and the reference value ( $\varphi_{abs}^{ref}$ ) as given by Equation 3.8 and Equation 3.9:

$$\beta_{LS} = \frac{\varphi_{abs}^{LS}}{\varphi_{abs}^{ref}} \quad (3.8)$$

$$\beta_{PS} = \frac{\varphi_{abs}^{PS}}{\varphi_{abs}^{ref}} \quad (3.9)$$

### 3.3.3 Light Soaking Chamber for Accelerated Aging of Membranes

Figure 3.10a pictures a light-soaking chamber (Compact UV-LED Chamber BSL-01 ECO+, Opsytec Dr. Gröbel GmbH), which provided the simulated UV-violet light illumination for accelerated testing of pristine and PCM. The chamber was illuminated by two light-emitting diode arrays: UV-LED ( $\lambda_{em} = (365 \pm 13) \text{ nm}$ ,  $0\text{--}1090 \text{ W m}^{-2}$ ) and violet-LED ( $\lambda_{em} = (405 \pm 13) \text{ nm}$ ,  $0\text{--}1350 \text{ W m}^{-2}$ ). The emission spectra of UV-LED and violet-LED are shown Figure 3.10b. Aluminum membrane holders (Xceldent Official,  $4.0 \times 2.5 \text{ cm}$ ) were always placed in the in the  $12 \times 12 \text{ cm}$  region inside the chamber, where the light intensity profile (from the supplier) is the most uniform ( $>85\%$  relative light intensity). The duration and intensity of light exposure was controlled using a LedControl unit. In this work, both LED channels of the chamber were set at 100% intensity, and the light dose ( $\text{kWh m}^{-2}$ ) was varied in a time-controlled manner. Due to reflection at the air: glass interface the borosilicate glass sheets (Schott BF33,  $10 \times 10 \times 0.33 \text{ cm}$ ) covering the membrane holders resulted in the loss of transmission: 8% (405 nm region) and 10% (365 nm region). Figure 3.10b depicts the transmission spectrum of the glass sheets recorded in front of the integrating sphere of a UV-Vis spectrophotometer.

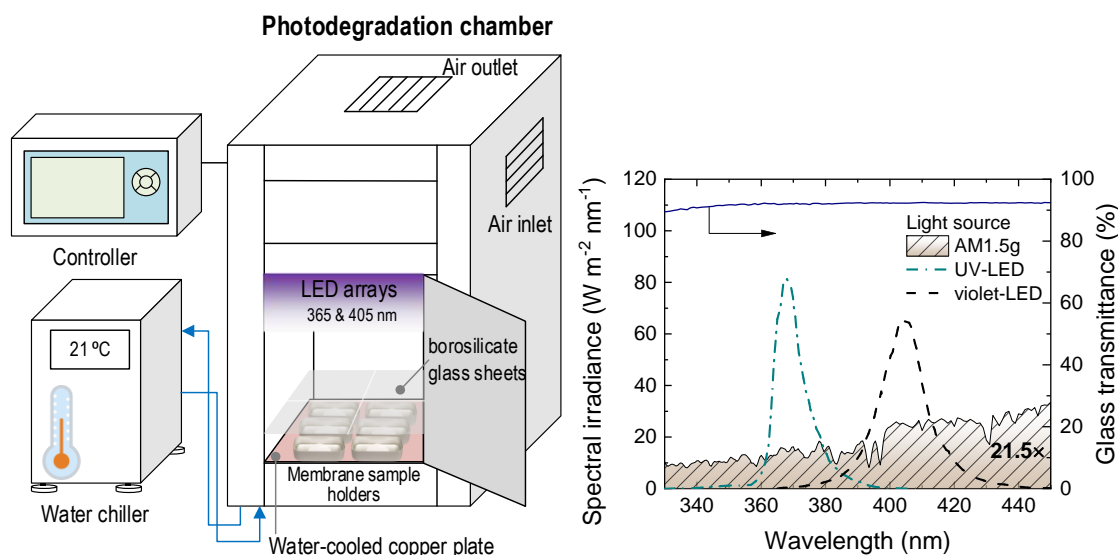


Figure 3.10: **a** Schematic configuration of the light soaking chamber equipped with UV-violet-LEDs and water-cooled copper plate connected to the water chiller. **b** Spectral irradiance of UV-violet LED light chamber compared to standard terrestrial solar spectrum with a mass of 1.5 global (AM1.5 g) (21.5 $\times$  magnification shown in graph) plotted against the transmission spectra of borosilicate BF33 glass cover in air. Panel **a** adapted with permission from Raota et al. (paper submitted).

The total irradiance from two LED arrays ( $I_{inc, ch}$ ) was calculated thus:

- The normalized emission spectra of LED arrays (expressed as spectral irradiance,  $\text{W m}^{-2} \text{ nm}^{-1}$ ) were reconstructed from the specification sheet using the digitizer tool in the Origin software (OriginPro 2020b, OriginLab);
- The obtained spectra were multiplied by the correction factor (90.25 and 71.20 for UV-LED and violet LED, respectively) such the integration of the resulted spectra corresponded the reported light intensity;
- The maximum light intensity values of the LED-channels were used as reported in the specification list:  $109 \text{ mW cm}^{-2}$  for UV-LED and  $135 \text{ mW cm}^{-2}$  for violet-LED;

- iv. The irradiance spectra were converted to photon flux spectra by dividing them by the photon energy for each wavelength ( $E = hu_L/\lambda$ );
- v. The resulting spectra were corrected for transmission loss by multiplying by 0.9 for the UV-LED array and 0.92 for the violet-LED array;
- vi. The corrected photon flux spectra were interpolated and summarized;
- vii. The final spectrum was converted back to irradiance spectrum, which upon integration resulted in the sought value ( $I_{\text{inc, ch}} = 222.2 \text{ mW cm}^{-2}$ ).

Under strong illumination, the interior of the chamber quickly heated up causing water evaporation. To decrease water loss, a water-cooled copper plate was designed and installed at the bottom part of the chamber. The work was carried out by Shabnam Lotfi (IAMT, KIT) and the supplier company (Opsytec Dr. Gröbel GmbH). The temperature of the connected water chiller (Minichiller 300, Peter Huber Kältemaschinenbau AG) was set at  $(21 \pm 1)^\circ\text{C}$ , so the evaporation of water from the holders was decreased to 4–5 mL in 125 hours of continuous illumination (initial volume of water 10 mL).

## 3.4 Analytical Methods

### 3.4.1 Total Organic Carbon Analysis

The release of organic matter during the accelerated aging of polymer membranes was measured using a total organic carbon (TOC) analyser (Sievers M9 portable, GE Analytical Instruments, USA). The calibration curve of the TOC instrument using sodium hydrogen phthalate was shown above in Figure 3.1a. Prior to analysis, all collected samples (10 mL) excluding control measurements were diluted 10 times so that the measured concentration was below  $10 \text{ mgC L}^{-1}$ . The flow rate of oxidizer (ammonium persulphate) and acidification agent (6M phosphoric acid) were set at  $1 \mu\text{L min}^{-1}$ . As tetrakis(pentafluoro-phenyl)-porphyrins are insoluble and do aggregate in pure water, a TOC calibration curve for the given PS class in water could not be recorded. The risks of potential contamination from the air were mitigated due to the location of the TOC analyser in the laboratory, where handling of organic solvents was not permitted.

### 3.4.2 UV-Vis Analysis of Permeate Outlet

The optical density of permeate containing model pollutant was determined in-line at  $\lambda = 664 \text{ nm}$  (for MB) and at  $\lambda = 292 \text{ nm}$ ,  $\text{pH} = 7.4$  for uric acid (UA), with a dual-beam UV-Vis spectrophotometer (Lambda 365, PerkinElmer, South Korea). Uric acid was used as a specific molecule preferably reacting with  $^1\text{O}_2$  (the rate constant  $k_i = 1.5 \cdot 10^8 \text{ M}^{-1} \text{ s}^{-1}$ ).<sup>343</sup> The measurement was conducted every 30 s in a flow-through cuvette (light path of 10 mm, Hellma Analytics) with a reference cuvette filled with Milli-Q water. The measured optical density was converted to concentration using an extinction coefficient:  $\epsilon_{292} = (1.17 \pm 0.07) \cdot 10^4 \text{ M}^{-1} \text{ cm}^{-1}$  for UA<sup>343</sup> and  $\epsilon_{664} = (7.45 \pm 0.07) \cdot 10^4$  for MB (see Figure 3.11). Due to the high extinction coefficient of MB, it was possible to quantify its concentration down to  $4 \mu\text{g L}^{-1}$ .

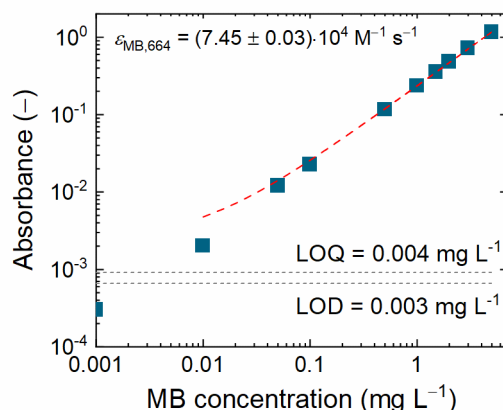


Figure 3.11: The calibration curve of MB in ultrapure water ( $\text{pH } 5.6 \pm 0.1$ ) using an in-line connected spectrophotometer. The linear regression was fitted in linear coordinates. The dashed line marks the absorbance value corresponding to the limit of quantification (LOQ) of the instruments

### 3.4.3 Identification of Degradation By-products with Mass Spectrometry

For the identification of intermediates of the Pd-TFPP photobleaching, methylene blue and  $17\beta$ -estradiol degradation (see the discussion in Chapters 5 and 6), the samples were analyzed using direction injection ( $10 \mu\text{L}$  sample loop) to a single quadrupole mass spectrometer (CMS, spectrometer Expression<sup>L</sup>, Advion) using electrospray ionisation (ESI) or atmospheric pressure chemical ionization (APCI). No internal standards were used, and the external calibration of the ion mass-to-charge ratio was performed using an ESI tuning mix (Part Number G2431A, Agilent). The CMS settings for recording mass spectra of degradation products of Pd-TFPP, methylene blue, and  $17\beta$ -estradiol using the ESI or APCI source are outlined in Table 4.1. Although many ions were identified, only those exceeding the threshold of 1% intensity of the parent compound were demonstrated in the final mass spectra. To avoid peaks associated with matrix and noise, background MS spectra recorded after injection of at least three blank samples (ethanol for PS or deionized water for MB,  $17\beta$ -estradiol) were subtracted.

The aqueous samples containing MB and  $17\beta$ -estradiol by-products were collected from the permeate side during the photocatalytic treatment at  $V_p = 350 \text{ mL}$  and  $V_p = 700 \text{ mL}$ , respectively. For that, the feed solutions with methylene blue ( $1 \text{ mg L}^{-1}$ ) or non-labeled  $17\beta$ -estradiol ( $3 \text{ mg L}^{-1}$ ) were prepared and then subjected to photocatalytic oxidation using Pd-TFPP/PVDF membranes,  $q_{PS} = (0.21 \pm 0.02) \mu\text{mol cm}^{-2}$ . The samples containing photoproducts of Pd-TFPP were obtained by dissolution of the photobleached Pd-TFPP/PVDF membrane in dimethylformamide. The samples collected from a feed solution containing MB or  $17\beta$ -estradiol or taken from DMF solution of a freshly prepared Pd-TFPP-PVDF membrane ( $\bar{q}_{PS} = 0.21 \mu\text{mol cm}^{-2}$ ) were used as a control measurement.

Table 4.1: The MS source conditions for analysis of porphyrin and pollutant intermediates

Parent compound	Capillary		Source voltage		Source gas temperature	Source voltage	Polarity
	Temp.	Voltage	Offset	Span			
MB	180	160	20	0	250 (ESI)	3000	positive
Pd-TFPP	250	170	20	20	250 (ESI)	2500	negative
$17\beta$ -estradiol	250	180	25	20	350 (APCI)	–	negative

### 3.4.4 Ultra-High Pressure Liquid Chromatography Coupled with Flow Scintillation Analyzer

As part of my doctorate work, I have developed the method for routine analysis of radiolabeled SHs at nanogram-per-liter concentrations based on ultra-high performance liquid chromatography coupled with flow scintillation analyzer (UHPLC-FSA). This analytical method has been published in a peer-reviewed journal (Lyubimenko et al., 2020),<sup>123</sup> which is summarized in the following section. Additionally, I have developed different separation methods, allowing for faster gradient times for single-component analysis and the delayed start-up time of the FSA pump resulting in a safe and flexible workflow. The UHPLC-FSA proved useful to other researchers with separation and detection of SH micropollutants. Up until now, the methodology has been used in four<sup>184, 251, 340, 341</sup> peer-reviewed papers, and two other works are currently in preparation.

#### *Principle of Scintillation Analysis*

Liquid scintillation counting is used for quantification of low-energy radioisotope activity by measuring the photons emitted resulting from the transfer of energy from the radionuclide decay to chromophores in a scintillation liquid.<sup>120</sup> Tritium-labelled compounds are frequently used due to their high specific activity, ease of handling and simple synthesis.<sup>124</sup> The principle of flow scintillation analysis is much like that of the LSC instrument as illustrated in Figure 3.12. Rather than using the scintillation vials filled with mixture of sample and scintillation liquid, the scintillator is continuously fed into the FSA detector's flow cell, where two photomultiplier tubes (PMT) are used for photon counting by the coincidence counting circuit.<sup>120</sup> The activity of the resulting mixture is monitored as a count rate (counts per minute).

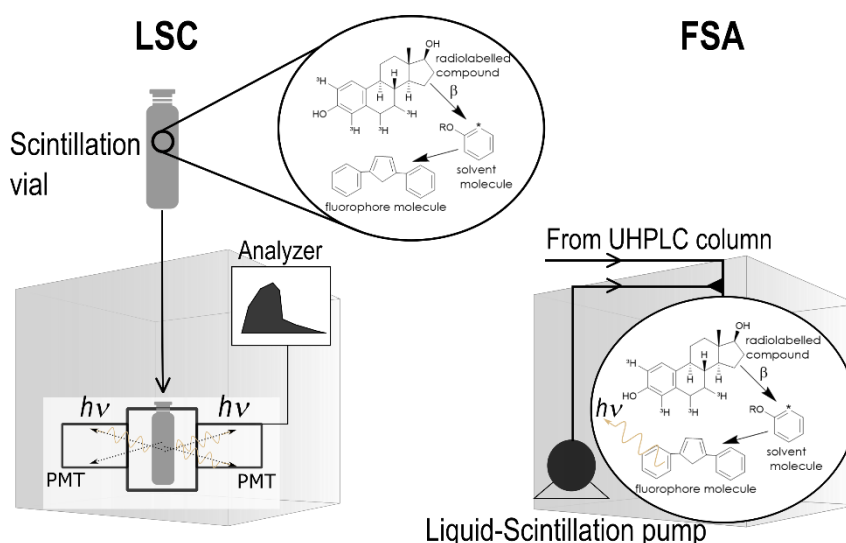


Figure 3.12: Schematic illustration of working principle of liquid scintillation counting (LSC) and flow scintillation analysis (FSA) instruments. PMT stands for photomultiplier tubes.

#### *Instrument Coupling and Analytical Procedure*

The UHPLC system (PerkinElmer, USA) comprised of i) the binary UHPLC pump (Flexar FX-20), ii) an autosampler equipped with a Peltier-cooled tray (Flexar FX UHPLC), iii) UHPLC column (C18 phase, 1.7  $\mu\text{m}$  particle diameter, 100  $\text{\AA}$ , 150  $\times$  2.1 mm, Kinetex, Phenomenex, USA), iv) a column oven (Flexar LC). The main challenge of coupling a UHPLC instrument and FSA detector (Radiomatic 625TR,

PerkinElmer) is their limited compatibility in terms of dead volume (the volume between the injection and detection points excluding the column void volume). Generally, the low-volume peaks leaving the UHPLC column (1–20  $\mu\text{L}$ ) experience strong dispersion upon entering the large flow cell (150–1000  $\mu\text{L}$ ) of FSA detectors.<sup>130</sup> In this work, the dead volume (and hence peak broadening) was reduced by connecting the outlet of a UHPLC column directly to a mixing tee (via by-passing the control valves) located inside the FSA-detector, as depicted in Figure 3.13a. The standard flow rate of liquid-scintillation pump delivering the scintillation liquid (Ultima Flo M, PerkinElmer LAS GmbH, Netherlands) was fixed at 4  $\text{mL min}^{-1}$ .

Prior to injection, the samples were kept on an autosampler tray at temperature of 4°C. A gradient elution from 40% to 80% methanol was realized at a flow rate of 0.25  $\text{mL min}^{-1}$  using methanol-water mixture as mobile phase. Considering the low concentrations of analytes, large sample volumes (100–200  $\mu\text{L}$ ) could be injected without overloading a column. The long column with C18 core-shell stationary phase was chosen for the high separation efficiency required to resolve the close eluting SH peaks. A guard column (C18, SecurityGuard Ultra, Phenomenex, USA) was installed to safeguard the UHPLC column from particulate matter. The radiochromatograms were collected (at a counting time of 6 s) and analyzed using the ProFSA v.3.4.3 software (PerkinElmer).

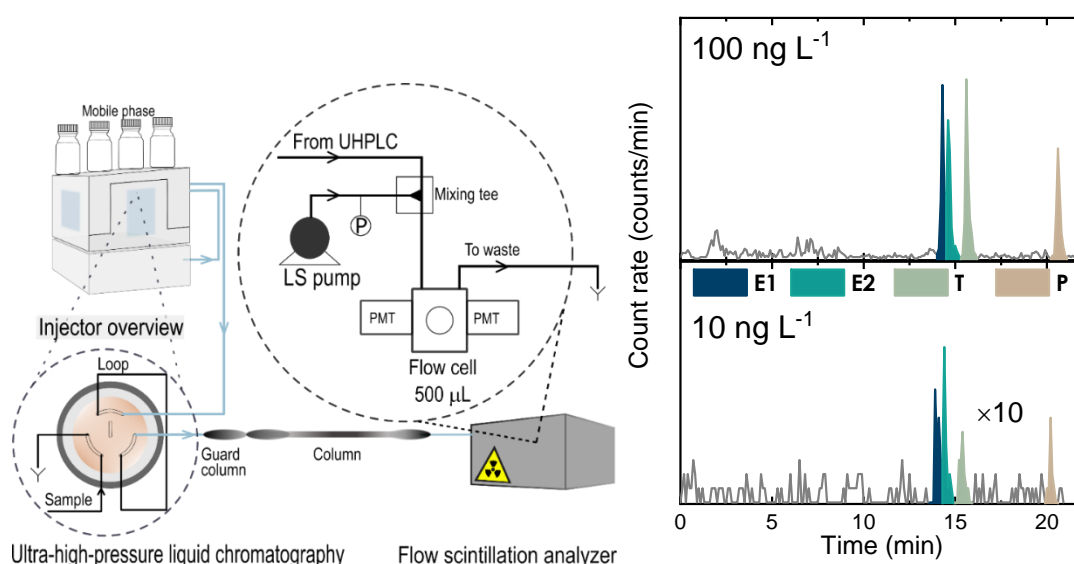


Figure 3.13: **a** Schematic drawing of an ultra-high-pressure liquid chromatography-flow scintillation analysis (UHPLC-FSA). The internal structure of the autosampler injector and the FSA detector are highlighted; **b** UHPLC-FSA radiochromatograms of mixtures of steroid hormones at two different concentrations (10 and 100  $\text{ng L}^{-1}$  for each analyte, injection volume 100  $\mu\text{L}$ ). Figure adapted with permission from Lyubimenko et al. (2020);<sup>123</sup> Copyright 2020, Nature Publishing Group.

#### Optimization of the UHPLC-FSA Analytical Method

The flow rate of the FSA internal pump feeding the scintillation liquid was chosen after preliminary optimization. The solution of 17 $\beta$ -estradiol was injected and isocratically eluted using 50%-50% acetonitrile-water mobile phase (no retention pursued). Figure 3.14 exhibits that an increase in the area of 17 $\beta$ -estradiol peak and narrowing of the peak width (estimated at FWHM) as the flow rate of an LC pump increases up to 4  $\text{mL min}^{-1}$ . Therefore, a counting efficiency is improved at high FSA pump flow rates.



This finding was attributed to a decrease in the dispersion of the peaks within the flow cell due to a decrease in residence time.<sup>130</sup>

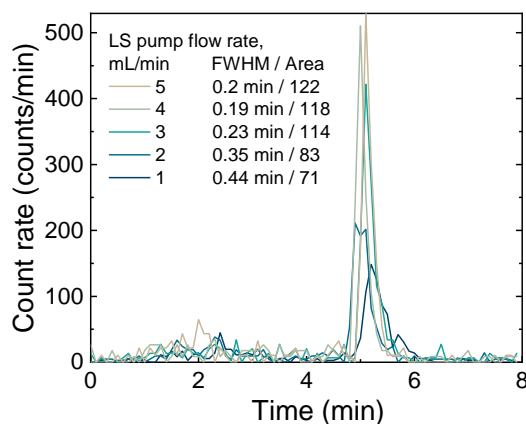


Figure 3.14: Influence of the FSA-pump flow rate on the shape of 17 $\beta$ -estradiol peak (100 ng L<sup>-1</sup>) using UHPLC-FSA instrument. UHPLC pump flow rate  $Q_f = 0.4$  mL min<sup>-1</sup>;  $V_{inj} = 50$   $\mu$ L; column temperature 30°C, isocratic elution (acetonitrile:water 50%:50%). Figure adapted with permission from Lyubimenko et al. (2020);<sup>123</sup> Copyright 2020, Nature Publishing Group.

The goal of the method was to separate SH and their degradation by-products with sufficient peak resolution ( $R_S > 1.5$ ) while ensuring the lowest limit of detection ( $c_{LOD}$ ) in ng L<sup>-1</sup> range. The peak resolution ( $R_S$ -value) was used as a metric of chromatographic separation and was calculated using Equation 3.10:<sup>344</sup>

$$R_S = 1.18 \frac{t_{ret,2} - t_{ret,1}}{w_1 + w_2} \quad (3.10)$$

where  $t_{ret,1,2}$  (min) are the retention times, and  $w_{1,2}$  (min) are the widths of the peak at half-height of analytes.

The optimisation of separation parameters enabled baseline separation chemically similar to 17 $\beta$ -estradiol and testosterone, as well as partial separation of estrone–17 $\beta$ -estradiol pair as depicted in Figure 3.13b. For that, UHPLC flow rate (0.2–0.4 mL min<sup>-1</sup>), gradient elution time (5–30 min), column temperature (30–60°C), and injection volume (10–100  $\mu$ L) were varied as demonstrated in Figure 3.15. The duration and the flow rate of gradient elution have the greatest effect on chromatographic resolution allowing to reach the baseline separation and  $R_S > 2$  recommended by U.S. Food and Drug Administration (FDA) guideline.<sup>345</sup> Notably, the increase in analyte mass did not significantly affect the peak width, thereby leaving space for improvement in the detection limit of UHPLC-FSA instrument by increasing the injection volume.

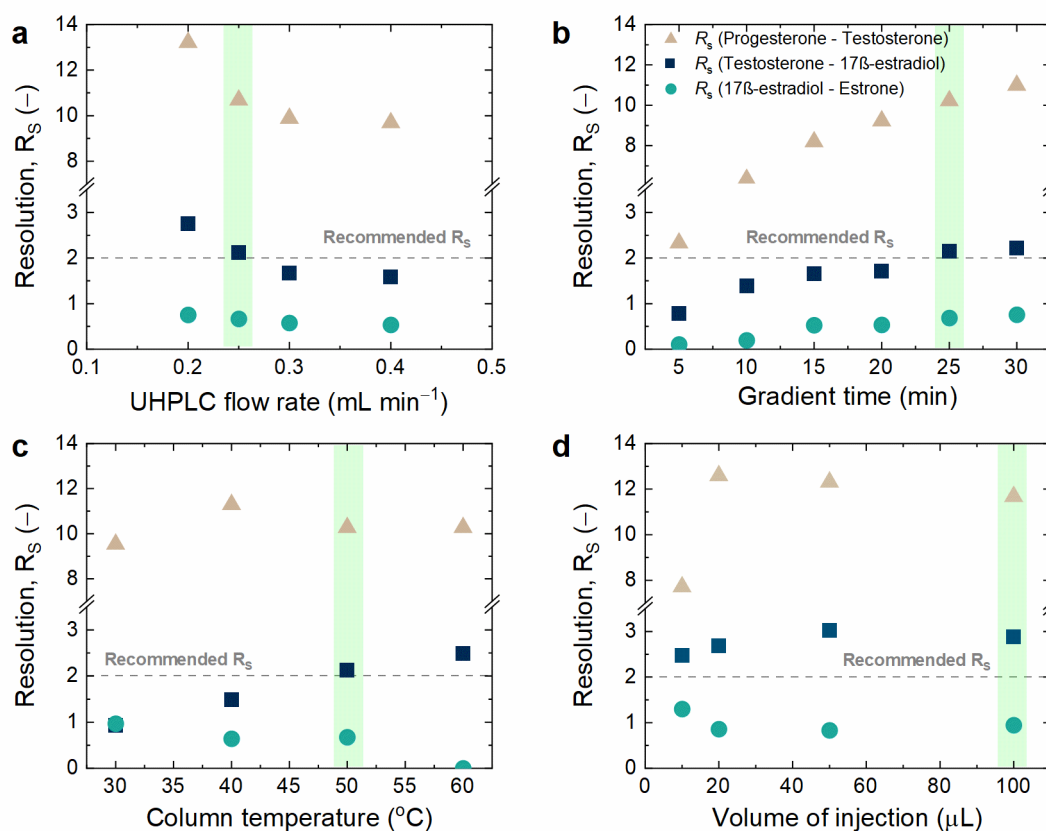


Figure 3.15: Influence of the UHPLC instrument parameters on separation of estrone, 17 $\beta$ -estradiol, testosterone, and progesterone: **a** UHPLC pump flow rate, **b** Gradient elution time, **c** column temperature, **d** injection volume. Green bars highlight the conditions fixed as standard for routine analysis of SHs.

### Calibration Curves

Figure 3.16 summarizes the calibration curves for estrone, 17 $\beta$ -estradiol, testosterone, and progesterone using the scintillation methods. The concentrations at the limit-of-detection ( $c_{LOD}$ ) and limit-of-quantification ( $c_{LOQ}$ ) were determined from Equation 3.11 and Equation 3.12:

$$c_{LOD} = \frac{\bar{y}_b + 3\sigma_b}{S} \quad (3.11)$$

$$c_{LOQ} = \frac{\bar{y}_b + 10\sigma_b}{S} \quad (3.12)$$

where  $\bar{y}_b$  (counts/min) is the mean value, and  $\sigma_b$  (counts/min) is the standard deviation of the blank injection (no analyte);  $S$  is the slope of calibration curve for a given SH;  $y_{LOD/LOQ}$  is the instrument response at the LOD/LOQ level, respectively (marked with dashed lines in Figure 3.16).

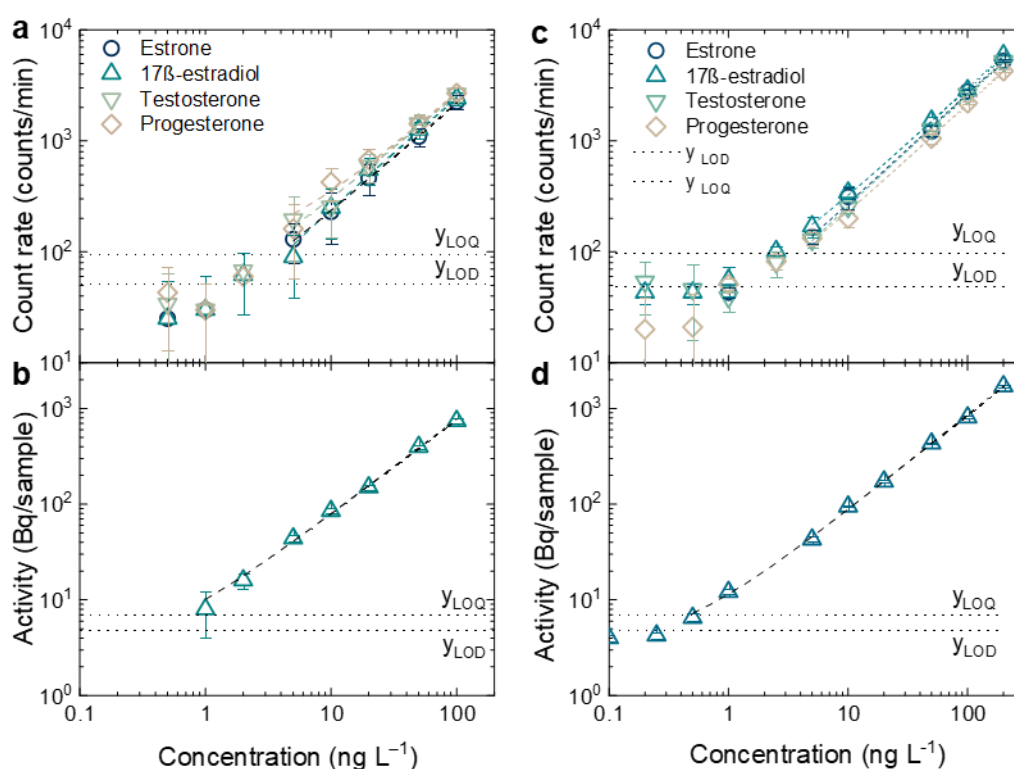


Figure 3.16: The calibration curves for estrone, 17 $\beta$ -estradiol, testosterone, progesterone used in **a,b** Chapters 5,6 and **c,d** Chapter 7: **a,c** UHPLC-FSA ( $V_{inj}$  = 100 and 200  $\mu$ L, respectively) and **b,d** LSC (sample volume of 1 mL) instruments (for 17 $\beta$ -estradiol only). Fitting is performed in linear coordinates. The dashed lines ( $y_{LOD}$ ,  $y_{LOQ}$ ) mark the peak area corresponding to the LOD and LOQ levels of the instruments.

### 3.4.5 Liquid Scintillation Counting

The concentration of the most biologically active 17 $\beta$ -estradiol in the feed samples was also analyzed using the LSC instrument (Tri-Carb 4910TR, Perkin Elmer), the counting efficiency of which was estimated at 25%. Radioactivity (in Becquerel per sample) was determined after mixing 1 mL of collected aqueous hormone samples with 1 mL of Ultima Gold LTT scintillation liquid (PerkinElmer, Netherlands) in 20 mL glass scintillation vials. A linear calibration curve (1–200  $\text{ng L}^{-1}$ ) was used to convert the measured activity into concentration in  $\text{ng L}^{-1}$  (Figure 3.16b,d). The detection limit for estradiol was in the range of 1–2  $\text{ng L}^{-1}$  depending on the activity of the freshly prepared stock solution.

## 3.5 Characterization Methods

### 3.5.1 Optical Characterization of Photosensitizers

#### *UV-visible Absorption Spectroscopy*

As follows from the first, the Grotthuss-Draper law of photochemistry, light must be absorbed to initiate a photochemical reaction. To quantify the fraction of light absorbed, the negative logarithm of the ratio of

the transmitted light to the incident light ( $-\log \frac{I_T}{I_0}$ ) is determined. In homogenous media, absorption is proportional to the light-absorbing according to Beer-Lambert law (see Equation 3.13)

$$A = -\log \frac{I_T}{I_0} = \varepsilon_{\lambda} l_{opt} C \quad (3.13)$$

where  $C$  is a molar concentration ( $\text{mol L}^{-1}$ ),  $l_{opt}$  is an optical pathlength (cm).

Absorbance measurements were conducted using a dual-beam UV-Vis spectrophotometer (Lambda 950, PerkinElmer, USA) equipped with a PMT (200–860 nm) and an InGaAs (860–2500 nm) detectors, a deuterium lamp (for the wavelengths of 200–350 nm) and a tungsten-halogen lamp (350–2500 nm). The solution with PS was measured in a 10 mm quartz cuvette against the reference cuvette filled with a suitable (THF or DMF) solvent. The reference beam allowed to compensate for fluctuations in light intensity.

Due to the large mismatch in refractive indices between air and the membrane material (see Table 2.8), the Fresnel reflection losses can be significant. Additionally, membranes as porous materials strongly scatter incident light. Therefore, absorbance measurements of PS-loaded membranes must be carried out in water inside the integrating sphere. This method allows the PCM to remain wet, to the point that light can penetrate through the membrane and reach the impregnated photocatalyst (see Figure 3.17). This configuration also resembles the experiment conditions of photocatalytic experiments. The measurement of pristine and porphyrin-coated membranes was conducted in a water-filled fluorescence cuvette made of Spectrosil quartz ( $L40 \times W40$ , light path 10 mm, Starna Scientific, UK). The cuvette was situated in the middle of an integrating sphere (coated with Spectralon) located in the UV-Vis spectrophotometer. Figure 3.13c depicts a cuvette holder, which was specifically designed for this objective and then manufactured using a 3D-printer technology by Tobias E. Berger (IMT, KIT). During the measurement, the specular exclusion port stayed open to exclude any specular reflection from the quartz cuvette. This approach enabled an increase in the upper measurement limit due to reduction of light reabsorption effects (for instance, absorption of emission from membrane-immobilized porphyrin).

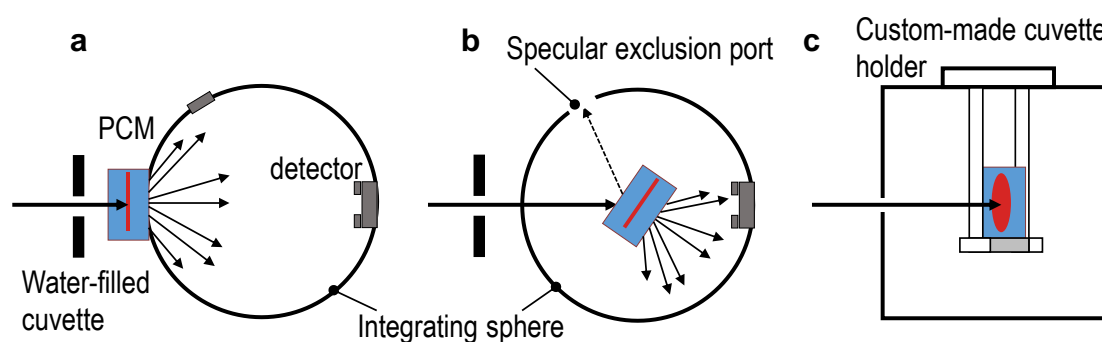


Figure 3.17: Schematic overview of measuring **a** diffuse transmittance; and **b** absorbance (absorptance) of PCM using an integrating sphere. The graph **c** pictures a side view of the graph **b** the integrating sphere contains a water-immersed PCM in a cuvette held on a custom-made holder.

### Photoluminescence Studies

The absorption is related to photocatalytic performance via quantum yield of produced ROS (see Equation 2.2). Section 2.3.4 also described that  $\Phi_{\Delta}$  is obtained by measuring the specific  $^1\text{O}_2$  phosphorescence signal at 1271 nm in respect to the reference material (relative quantum yield).<sup>173</sup> The air-

saturated PS solution in ethanol was excited with 405 nm laser and the recorded PL intensity signals were converted to  $\Phi_{\Delta}$  via Equation 3.14:

$$\Phi_{\Delta} = \frac{I_{ref}A_{\Delta_s}}{I_S A_{\Delta,ref}} \Phi_{\Delta,ref} \quad (3.14)$$

where  $I_{ref}$  and  $I_S$  (–) are the relative intensities of absorbed light for the reference PS and the sample,  $A_{\Delta_s}$  and  $A_{\Delta,ref}$  (a.u.) are the integrated area of emission spectra of the reference and investigated PS,  $\Phi_{\Delta,ref}$  (–) is the quantum yield of  $^1\text{O}_2$  of a reference PS.

In this work, a reference PS from the same group of fluorinated porphyrins – platinum *meso*-tetra(pentafluorophenyl)porphine (Pt-TFPP) – was chosen due to its photostability and the known quantum yield value ( $\Phi_{\Delta,ref} = 0.96$  in ethanol).<sup>346</sup> Using the  $\Phi_{\Delta,ref}$  uncertainty (10%) and measuring the PS-samples in triplicate, the relative error for  $\Phi_{\Delta}$  values was estimated to be 15%.

Photocatalytic ( $\Phi_{\Delta}$ ) and photophysical characteristics (intensity and lifetime of triplet state, ISC) in porphyrin PSs are interlinked (more details in Section 2.3.4). Absorbed light can be also released via radiative channel (photoluminescence, PL) as illustrated in Figure 2.5. The intensity and lifetime of PL signal can be used to characterize the excited (triplet and singlet) states of porphyrin molecules. PL studies were undertaken using steady-state and time-resolved (in  $\mu\text{s}$  range) methods in a custom-built optical set-up. Photoexcitation of porphyrin solutions in organic solvents or porphyrin-coated membranes immersed in a Milli-Q water-filled quartz cuvette was realized with a 405 nm continuous-wave diode laser (DL-7146–101S, Roithner) mounted in a laser diode mount (LDM21, Thorlabs), which was connected to a laser diode controller (ITC4001, Thorlabs). The excitation power density (the intensity of the laser, in  $\text{mW cm}^{-2}$ ) was determined as the power of the laser divided by the beam size, which was measured with a beam profiler (BP209-VIS, Thorlabs). The laser power was measured in-line using a pre-calibrated benchtop power meter (PM320E, Thorlabs). The excitation power density was attenuated with a continuously variable neutral-density filter (NDC–100C-2, Thorlabs). The PL signal was collected using a lens and focused on the slit of a double monochromator (DTMS300, Bentham). Wavelength-resolved emission data was recorded using a photomultiplier tube (PMT, R928P, Hamamatsu) mounted in a cooled housing (CoolOne, Horiba). The PMT electrical signal was collected by a multi-channel scaling card (Timeharp 260, PicoQuant). The instrument response function (IRF) was measured to enable separation of the long-lived from the short-lived PL components. The degassing of solution was achieved by argon gas purging, whereas time-resolved measurements in vacuum were conducted at pressures  $<10^{-4}$  mTorr.

The average lifetime of excited triplet state ( $\langle\tau_T\rangle$ ) of porphyrins in solutions or on membranes was determined by fitting the decay of the PL signal with single and double-exponential functions, respectively. The  $\langle\tau_T\rangle$  from the double-exponential fitting curves was calculated via Equation 3.15:

$$\langle\tau_T\rangle = \frac{\sum x_i \tau_i}{\sum \tau_i} \quad (3.15)$$

where  $\tau_i$  is the decay time of the  $i$ -th component and  $x_i$  is the amplitude of the  $i$ -th component

Time-resolved PL measurements of short-lived emission (indicating the singlet state) were conducted in a streak-camera setup (single sweep mode, Hamamatsu Universal Streak Camera C10910) connected to a spectrometer (Acton SpectraPro SP2300). A 405 nm mode-locked ytterbium laser (Light Conversion, Pharos) with a pulse width of 260 fs and a full-width half-maximum of 0.2 ns for IRF was used for excitation of the PS solution in anhydrous THF. In streak camera studies of all PS solutions, the laser fluence was  $2 \mu\text{J cm}^{-2}$ , except for  $\text{H}_2$ -TFPP ( $0.3 \mu\text{J cm}^{-2}$ ). Fitting the mono-exponential function to the decay of fluorescence signal derived the PL lifetime value.

In Chapter 6, the thermodynamic probability of photoinduced electron transfer ( $\Delta G_{PET}$ ) from a porphyrin molecule to molecular oxygen was estimated using Rehm-Weller equation (Equation 3.16):

$$\Delta G_{PET} = -F(E^0(O_{2(aq)}/O_2^{\bullet-}) - E_{ox}^{T*}) \quad (3.16)$$

where  $F$  is the Faraday constant ( $23.061 \text{ kcal V}^{-1} \text{ mol}^{-1}$ ),  $E_{ox}^{T*}$  is the excited state oxidation potential (eV),  $E^0(O_{2(aq)}/O_2^{\bullet-})$  is the redox potential of dissolved oxygen/superoxide couple (eV).

### 3.5.2 Surface Characterization of Pristine and Photocatalytic Membranes

#### *Fourier-Transform Infrared Spectroscopy*

The surface chemical composition of pristine and PS-coated membrane was characterized using a Fourier transform infrared (FT-IR) spectrophotometer (Vertex 70, Bruker, Germany) equipped with an attenuated total reflectance (ATR) module (resolution  $4 \text{ cm}^{-1}$ , 32 scans). Prior to measurement, the membrane samples were thoroughly dried in a rotary evaporator (Büchi Rotovapor R-210, Sigma Aldrich) for 1 h at 30 mbar vacuum and  $40 \text{ }^\circ\text{C}$ .

#### *Zeta Potential Measurements*

The surface charge of membrane surface was measured in an adjustable gap cell ( $20 \text{ mm} \times 10 \text{ mm}$ ) using an electrokinetic analyzer (SurPASS, Anton Paar GmbH, Austria). The membranes were mounted in wet state and studied in 1 mM KCl solution in streaming potential mode. The dependence of zeta ( $\zeta$ )-potential on solution pH was studied via dosing 50 mM HCl or 50 mM NaOH. In Chapter 5, a  $\zeta$ -potential analysis was conducted in the background solution (1 mM  $\text{NaHCO}_3$ , 10 mM NaCl) to reveal the trend relevant to photocatalytic studies. As a result of the increased ionic strength, the pH was adjusted with 100 mM HCl and 100 mM NaOH.

#### *Scanning Electron Microscopy*

Before imaging, all membrane samples were dried thoroughly and then sputter-coated with a 10 nm layer of silver. To study cross-sectional images, a piece of membrane was frozen in liquid nitrogen and cleaved by bending both ends of a specimen. The morphology of pristine and porphyrin-coated (both fresh and aged) membranes was characterized using a Zeiss Supra 60VP (Germany) at 2kV electron energy.

#### *Time-of-Flight Secondary Ion Mass Spectrometry*

The distribution of Pd-porphyrin inside the PCM was visualized and quantified by conducting time-of-flight secondary ion mass spectrometry (ToF-SIMS) analysis on a ToF-SIMS 5 machine (ION-TOF, 25 keV  $\text{Bi}^{+3}$  ion beam, vacuum  $5 \cdot 10^{-9}$  mbar). To reveal the cross-section of the PCM, the sample was frozen and broken in a manner similar to that of the procedure for cross-sectional SEM images. First, the signals of  $\text{Pd}^+$  isotopes ( $^{104}\text{Pd}^+$ ,  $^{105}\text{Pd}^+$ ,  $^{108}\text{Pd}^+$ ,  $^{110}\text{Pd}^+$ ) were identified upon zooming the camera at the mounted PCM. Next, the mapping images (500 scans,  $256 \times 256$  pixel on a field of view of  $250 \times 250 \text{ } \mu\text{m}^2$ ) of the named Pd isotopes and Pd-TFPP molecules were acquired using a delayed extraction mode and charge compensation by low-energy (21 eV) electron flooding. This method minimized the topographic effects compared to other approaches, thus confirming the shape of the  $\text{Pd}^+$  ion distribution in the PCM. Finally, the Pd isotope signals were summed along the x axis of the membrane (perpendicular to the depth) thus resulting in the depth profile distribution of  $\text{Pd}^+$  ions ( $q_{Pd^+,z}$ ). The variation of Pd-TFPP across the PCM thickness ( $\bar{q}_{PS,z}$ ) was estimated via Equation 3.17 using: i) the averaged and normalized distribution ( $n = 3$ ) of  $q_{Pd^+,z}$ ; and ii) the  $\bar{q}_{PS}$  of a given PCM (as per Equation 3.1). The conversion coefficient ( $\eta$ ) was determined by dividing  $\bar{q}_{PS}$  by the integral of  $q_{Pd^+,z}$  over the membrane thickness, as per Equation 3.18:

$$\bar{q}_{PS,z} = \eta \cdot q_{Pd^+,z} \quad (3.17)$$

$$\eta = \frac{\bar{q}_{PS}}{\int_0^{h_m} q_{Pd^+,z} dz} \quad (3.18)$$

### 3.5.3 Characterization of Membrane Structure

#### *Argon Adsorption-Desorption Isotherms for Surface Area Evaluation*

Specific surface area ( $a_s$ ,  $\text{m}^2 \text{g}^{-1}$ ) of the pristine PVDF membranes were determined from argon adsorption-desorption isotherms measured at 87 K (Autosorb1-MP, Quantachrome). The accuracy of the instrument was validated using the standard samples with  $a_s = (156 \pm 7) \text{m}^2 \text{g}^{-1}$  (CRM BAM PM 106, Quantachrome). The relative error in the estimated surface area was less than 8%. The weight of the membranes ( $m_m = 0.2\text{--}0.6 \text{g}$ ) was chosen such that surface area was above the lower detection limit ( $1 \text{m}^2$  in the cell). The samples were pre-cleaned in methanol, air-dried, and cut into thin strips. These membrane stripes were exposed to outgassing for 24 h at  $95^\circ\text{C}$  under vacuum (0.01 Torr). Multipoint ( $n = 5\text{--}7$ ) Brunauer-Emmett-Teller (BET) and density functional theory (DFT) analysis was used for isotherm interpretation. The calculated  $a_s$  was converted to the membrane surface-to-volume ratio ( $a_v$ ,  $\text{m}^2 \text{m}^{-3}$ ) as given by Equation 3.19.

$$a'_v \approx a_v = \frac{a_{s,BET} m_m}{V_{por}} \quad (3.19)$$

where  $V_{por}$  was determined by porosity measurements using the method of helium pycnometry. As the theoretical number of monolayers (see the results in Chapter 4) surpassed one, the contact area in PM was evaluated via active surface-to-volume ratio ( $a'_v$ ), which is close to the  $a_v$  of pristine PVDF membranes.

In Chapter 7, the contact area in PCMs was evaluated as active surface-to-volume ratio ( $a'_v$ ), which is close to the membrane surface-to-volume ratio ( $a_v$ ) of pristine PVDF membranes (see also Equation 3.16). This assumption is based on the calculated surface coverage by porphyrin molecules ( $\theta_{PS} > 1$ ) (see findings in Section 4.2.1).

#### *Porosity Measurement with Helium Pycnometry*

To calculate the membrane porosity ( $\psi_m$ , %), the helium pycnometry method was applied, which is based on gas displacement and the Boyle's Law.<sup>347</sup> The porosity was defined as the ratio of experimentally known volume of bulk polymer material ( $V_{pol}$ , mL) to the membrane volume ( $V_m = n_m A_m h_m$ ) as per Equation 3.20.<sup>348</sup>  $V_{pol}$  (0.1–0.3 mL) of the membrane samples was experimentally determined according to Equation 3.21 at  $(20.00 \pm 0.01)^\circ\text{C}$  as an average of five measurements (a highest relative standard deviation of 0.75%) using a pycnometer (Pycnomatic ATC, Porotech).

$$\psi_m = \left(1 - \frac{V_{pol}}{n_m A_m h_m}\right) \cdot 100\% \quad (3.20)$$

$$V_{pol} = \left(V_1 - \frac{V_1 P_{eq,2} (P_{eq,1} - P_{ref,2})}{P_{eq,2} (P_{eq,1} - P_{ref,1})}\right) \quad (3.21)$$

where  $n_m$  is the number of membrane samples ( $n_m = 10\text{--}12$  corresponding to the total sample mass of 0.2–0.6 mg),  $A_m$  is the geometrical area of a membrane ( $\text{m}^2$ ),  $h_m$  is the membrane thickness (m);  $V_1$  is the calibrated volume of a sample chamber (27.39843 mL);  $P_{eq,1}$ ,  $P_{eq,2}$  (bar) are the equilibrium pressures of a reference chamber with open and closed valve; and  $P_{ref,1}$ ,  $P_{ref,2}$  (bar) the pressure in a reference chamber with and without the membrane sample.

The helium pycnometry was favorable over Hg-intrusion method due to i) the high precision; and ii) the strong decrease in applied pressure (1–3 bar).<sup>349, 350</sup> Further to this, the application of the polymer density values given in the literature can result in errors due to the unknown composition of commercial membranes.

#### *Pore Size Distribution Using Mercury Intrusion Porosimetry*

To calculate the porosity and the pore size distribution, the mercury intrusion approach was applied. Air-dried PVDF membranes were cut, weighed (0.2–0.5 g) and placed in a measurement chamber with a volume of  $(0.356 \pm 0.004)$  mL.

The pressure applied by mercury (density  $13.534 \text{ g cm}^{-3}$  at  $25^\circ\text{C}$ ) increased stepwise until reaching 350 MPa (CEI Pascal 1.05, Thermo Electron). This pressure gradient allowed mercury to penetrate into pores ranging in size from  $150 \mu\text{m}$  to 4 nm. The measurements were conducted at a temperature of  $(23 \pm 2)^\circ\text{C}$ .

The polymer bulk density used for calculation of apparent porosity was calculated using the helium pycnometry method. For comparison with the mean pore size provided by the membrane manufacturer, the median pore diameter ( $\tilde{d}_{pore}$ ) was calculated as the pore diameter at the median cumulative pore volume ( $\text{mm}^3 \text{ g}^{-1}$ ). The pore size histogram was constructed by the software (Thermo Scientific), according to the Washburn equation given by Equation 3.22. It must be noted that the mercury contact angle varies between the range  $130^\circ$  and  $140^\circ$  for polymer substrates with different polarity and roughness<sup>349, 351, 352</sup>. Hence, the values of  $\tilde{d}_{pore}$  reported in Chapter 7 can be overestimated by 16%.

$$r = -\frac{2\gamma_{Hg} \cos\theta_c}{P_{Hg}} \quad (3.22)$$

where  $r$  is the pore radius (nm),  $\gamma_{Hg}$  is the surface tension of mercury ( $\gamma_{Hg}$  is  $0.48 \text{ N m}^{-1}$ ),  $\theta_c$  is the contact angle of mercury ( $\theta_c = 140^\circ$ ), and  $P_{Hg}$  is the applied pressure of mercury.

## 3.6 Experimental Protocols

### 3.6.1 Operating and Water Quality Parameters

#### *Standard Operating Parameters*

To ensure a holistic approach to study of the photocatalytic degradation of model- and water-borne pollutants, all process parameters (except for the studied one) were fixed. The standard values of the operating parameters and water quality parameters are summarized in Table 3.5. The duration of the experiment was defined when the concentration of studied pollutants in the permeate achieved the steady-state level. For a clear comparison of the results of water flux studies, the operation time ( $t_{op}$ ) was converted to permeate volume ( $V_p$ ) via Equation 3.23:

$$V_p = J_w \cdot A_m \cdot t_{op} \quad (3.23)$$

Light intensity and water flux were varied such that the achieved removal ranged from 40 to 60%. In the studies of a probe molecule (methylene blue and uric acid) degradation, the process was realized at low water flux ( $30 \text{ L m}^{-2} \text{ h}^{-1}$ ), which resulted in long contact time ( $10.9 \text{ s}$ ) required for high removal of the organic dyes ( $R > 80\%$ ). For SH micropollutants, high removal was possible at larger water flux,  $J_w = 600 \text{ L m}^{-2} \text{ h}^{-1}$ , so the permeate volume was increased to  $V_p = 700 \text{ mL}$ . Note that the examined water flux values ( $J_w = 60\text{--}1500 \text{ L m}^{-2} \text{ h}^{-1}$ ) were comparable with those of typical UF and MF membranes.<sup>353</sup>



Table 3.5 The standard experimental and water quality parameters controlled in photocatalytic experiments

Parameter	Unit	Value (for MB)	Value (for SH)
Permeate volume	mL	350 ± 1	700 ± 1
Water flux	L m <sup>-2</sup> h <sup>-1</sup>	30 ± 5	600 ± 12
Contact time	s	10.9 ± 1.0	0.55 ± 0.1
Porphyrin loading	μmol cm <sup>-2</sup> <sub>memb</sub>	0.2 ± 0.02	0.22 ± 0.02
Incident light intensity	mW cm <sup>-2</sup>	21.0 ± 0.1 (gLED)	10.0 ± 0.1 (wLED) SolSim <sup>a</sup> 14.1 ± 0.2 (Pd-TFPP) 12.3 ± 0.2 (Zn-TFPP) 11.3 ± 0.3 (H <sub>2</sub> -TFPP) 6.3 ± 0.2 (Mn(Cl)-TFPP)
Pollutant concentration	ng L <sup>-1</sup> mg L <sup>-1</sup>	1.0 ± 0.1	100 ± 10
Feed temperature	°C	22.0 ± 1.0	23.0 ± 0.2
Feed pH	–	6.5 ± 0.5	8.3 ± 0.2 (8.6 ± 0.4) <sup>b</sup>
Buffer	–	no	yes
Dissolved oxygen concentration	mg L <sup>-1</sup>	8.5 ± 0.2	8.5 ± 0.2

<sup>a</sup> calculated from wLED radiant flux (see Figure 3.9a) as described in Section 3.3.2;

<sup>b</sup> due to the aging of stock solution of sodium bicarbonate (more details in Chapter 5)

The standard value of light intensity was selected for gLED, wLED light source on the basis of the preliminary photocatalytic tests. The irradiation level using SolSim,  $I_{inc} = (14.1 \pm 0.2) \text{ mW cm}^{-2}$ , and other porphyrins (findings shown in Chapter 6) was calculated using the absorbed photon flux of a Pd-TFPP/PVDF membrane (as a reference). The light intensity of the SolSim light source or when using a new porphyrin-coated membrane was adjusted so that the resulting number of absorbed photons corresponded to the  $\varphi_{abs}$  using the Pd-TFPP/PVDF membrane. More details can be found in Section 3.3.2.

The standard concentration for SH (100 ng L<sup>-1</sup>) was selected on the basis of the environmentally relevant levels outlined in Table 2.2. The high 17β-estradiol concentrations were reached by mixing radiolabeled with non-labeled SH prepared in methanol and spiked to the feed solution before the experiment. Although no effect of methanol on the photocatalytic degradation of 17β-estradiol was established, its concentration in the feed solution (80 mg L<sup>-1</sup>) was maintained.

#### *Effect of Methanol Traces and Dissolved Oxygen*

The effect of methanol and dissolved oxygen was shown in the control experiments (see Figure 3.18), where the feed solution containing 17β-estradiol was prepared ○ in absence of methanol, ◆ under nitrogen purging and compared to ◆ the typical photodegradation experiment (with all water quality components). Given the almost identical trend of  $c_p/c_f$  with and without methanol in the feed solution, its effect on photocatalytic activity was found negligible. A decrease in oxygen concentration stemming from nitrogen purging of the feed solution resulted in a steeper rise of 17β-estradiol in permeate over experiment time. The physical or chemical background underlying the concentration profiles after start of irradiation remains

not completely understood. Plausible mechanisms for a steady increase in permeate concentration over several hours of operation are suggested in Chapter 5.2, where this phenomenon was first encountered.

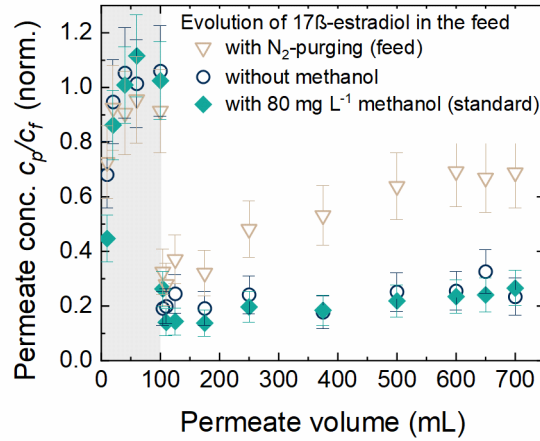


Figure 3.18: Evolution of normalized 17β-estradiol concentration in the permeate for control experiments. The feed solution of 17β-estradiol was: ○ prepared without adding methanol (80 mg L<sup>-1</sup>), ▽ purged with nitrogen (residual  $c_f(\text{O}_2) = 6 \mu\text{g L}^{-1}$ ) and ◆ prepared as usual with all solution components present (dissolved oxygen, methanol, background solution).  $J_w = 600 \text{ L m}^{-2} \text{ h}^{-1}$ ,  $l_{inc} = 10 \text{ mW cm}^{-2}$ ,  $c_f(17\beta\text{-estradiol}) = (100 \pm 5) \text{ ng L}^{-1}$  in background solution (1 mM NaHCO<sub>3</sub>, 10 mM NaCl, pH 8.6 ± 0.4).

Contact Time in NM20 Membrane Stacks

In Chapter 7, the role of contact time was investigated using NM20 membrane stacks. The number of PCM mounted to the cell ( $n_{\text{NM20}}$ ) increased, while the water flux was maintained (see Figure 3.19). On the contrary, the contact time in a thick MP200 membrane was adjusted via water flux. To reduce the concentration of 17β-estradiol in the permeate to the drinking water guideline value using PCM, the low water flux (and hence the long  $\bar{t}_{con}$ ) and the elevated irradiance (equivalent to that of one sun) were maintained. However, membrane stack configuration is subject to low permeability as evidenced from Figure 3.19b, which depicts the evolution of feed pressure with  $J_w$  for NM20 membrane stacks and MP200 membranes.

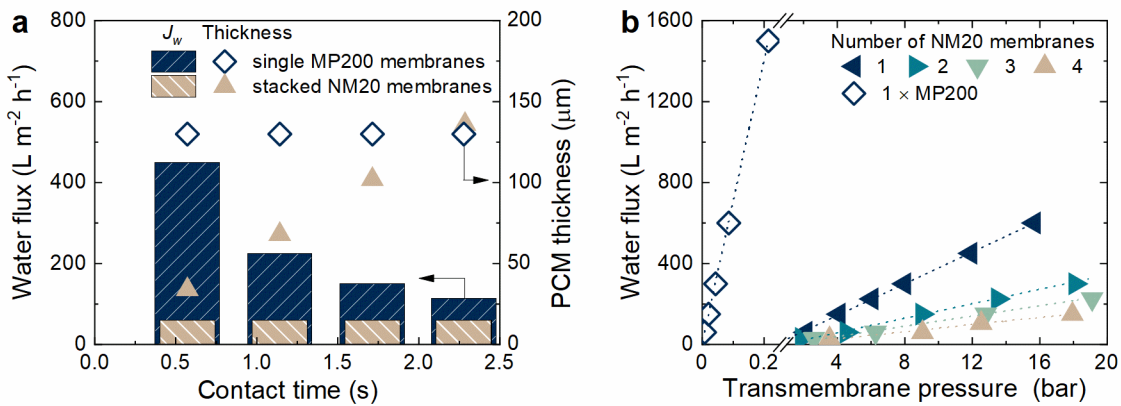


Figure 3.19: **a** Variation of contact time with water flux (MP200) and the thickness of NM20 membrane stack; **b** Evolution of transmembrane pressure with the water flux using the stacked NM20 membranes and the single MP200 membrane.

### 3.6.2 Photocatalytic Degradation of Organic Pollutants

An experimental protocol was devised to ensure reliable data collection during the photodegradation studies. The experimental protocol included: i) pre-compactation (pure water flux measurements); ii) dark phase (no light) required to achieve the adsorption-desorption equilibrium; and iii) the photodegradation phase (light on). Table 3.6 outlines the experimental protocol for MB and UA probe molecules. Moist pristine and porphyrin-loaded PVDF membrane coupons were carefully mounted to the filtration cell, closed and subjected to dead-end filtration according to the experimental protocol. Permeability studies were used to determine whether membranes had dried out or been damaged during porphyrin adsorption or transfer to the laboratory. If the feed pressure measured at pre-defined water flux was outside the standard operating range (see Table 3.6, Step 5), the membrane was discarded. After permeability studies were completed, the feed MB solution was connected to the inlet of the dosing pump. In this protocol, the permeate outlet of the membrane cell is connected to an inlet of the flow-through cuvette of the in-line UV-Vis spectrophotometer. Consequently, the change in absorbance of the MB or UA solution was measured in real time. Maintaining the volume of permeate during the dark phase (70 mL) allowed to capture the full breakthrough curve ( $c_p > 0.95 \cdot c_f$ ). The permeate volume corresponding to an end of experiment (70 mL) was fixed to achieve a steady-state concentration of the model pollutant. Hence, the duration of the dark and photodegradation phases varied depending on the flow rate through the PCM.

Table 3.6: Experimental protocol in the studies of photocatalytic degradation of MB and UA

No	Step	Conditions (duration, volume, flow rate)	Justification
0	Storage of membranes	Membranes were kept in dark and moist in water before all experiments.	a) Dried (even partially) membranes demonstrate irreproducible results; b) Mitigate photobleaching
1	Mounting a new membrane coupon	a) Place the membrane onto the center of the porous filtration pad with a top surface as positioned in the shaking plate; b) Tighten 8 screws of the cell using a torque wrench (2 N·m)	Prevent the liquid bypassing the membrane (the strong decrease in MB removal); Ensure experimental consistency by the same membrane orientation
2	Pump purging/flushing	Run 500 mL min <sup>-1</sup> for 15 sec of Milli-Q with purge valve of the pump ⑨ open and valve on the pump outlet ⑩ closed	Prevent clogging of valves; Remove any air bubbles
3	System flushing with Milli-Q water	Run 100 mL min <sup>-1</sup> for 2 min of Milli-Q with valve ⑨ closed and ⑩ valve on the retentate side ⑫ open (cross-flow)	Remove any air bubbles in the system
4	Preconditioning of a membrane	Run 10 mL min <sup>-1</sup> for 10 min of Milli-Q with valve ⑫ closed (dead-end)	a) Membrane Pre-compactation; b) Discard the sample if the $P_f$ deviates more than 20% from $(0.75 \pm 0.15)$ bar

Table 3.6: continue

No	Step	Conditions (duration, volume, flow rate)	Justification
5	Water flux studies	a) Run the various flow rates (5, 2, 1, 0.5 & 0.1 mL min <sup>-1</sup> ) for 5 min; b) Collect the feed pressure data and compare with the standard values	a) Measure the $\Delta P$ required for evaluation of $L_p$ ; b) Observe deviations from the standard values (bar): $0.38 \pm 0.08$ , $0.16 \pm 0.03$ , $0.09 \pm 0.02$ , $0.05 \pm 0.01$ , $0.02 \pm 0.005$
6	Preparing the UV-Vis spectrophotometer for an experiment	a) Set the time of experiment and wavelength followed; b) Set an auto-zero of UV-Vis spectrophotometer at the desired flow rate	Incorrect time or wavelength setting may lead to the loss of data
7	Pump flushing with MB solution	a) Change the inlet of the pump from Milli-Q to MB solution; b) Run 100 mL min <sup>-1</sup> for 30 sec with valve ⑨ open and valve ⑩ closed	a) Ensure a sharp change from Milli-Q water to MB solution; b) Flush out air bubbles after changing the feed tank
8	Set the pump to the desired flow rate	Set the pump at 0.1–1.0 mL min <sup>-1</sup> flow rate with valves ⑨ closed and ⑩ open	
9	Adsorption step in the dark	Collect 70 mL permeate (by default 700 min at $Q_f = 0.1$ mL min <sup>-1</sup> ) with LED off	a) Record the breakthrough curve for MB adsorption; b) Reach the steady-state adsorption value for MB before the LED lights up
10	Photocatalytic decomposition (light phase)	a) Switch on the LED without changing the previous flow rate; b) Achieve the $V_p = 50$ mL (500 min for 0.1 mL min <sup>-1</sup> )	a) Reach the MB steady-state value before the end of degradation test. b) Determine $c_{p,ss}/c_f$ value required for MB removal value
11	System flushing	Repeat step 2 & 3 with Milli-Q	Clean the system from MB
12	Water flux studies	Repeat step 5 with Milli-Q	Evaluate the changes in $L_p$

Table 3.7 outlines the revised photodegradation protocol for experiments with radiolabeled SH micropollutants. The main difference is that a permeate stream was periodically directed through a diverter valve into vials ready for analysis with the UHPLC-FSA instrument. Thus, the off-line analysis of SH was performed. The duration of the dark phase was extended to collect a total of 100 mL of permeate to account for the slower SH adsorption. Automatic switching on the wLED light initiated the photodegradation phase.

Increasing the permeate volume up to 600 mL allowed to approach a steady-state concentration of SH in the permeate. Each experiment ended with flushing the switching valve lines and purging them with nitrogen to avoid sampling errors in the next experiment.

Table 3.7: Experimental protocol for filtration and photocatalytic experiments using radiolabeled steroid hormones

No	Step/Justification	Conditions (duration, volume, flow rate)
1	Mount the membrane coupon	Close the cell using a torque wrench (Gedore, Torcofix-K) set at 2 Nm
2	Pump purging and flushing of the feed lines to prevent membrane clogging	Run Milli-Q water at 500 mL min <sup>-1</sup> for 10 seconds with purge valve ⑨ open and pump shut-off valve ⑩ closed
3	Flushing out of the air bubbles	Run Milli-Q water at 100 mL min <sup>-1</sup> for 2 minutes in cross-flow filtration: purge valve ⑨ closed, pump shut-off valve ⑩ and retentate needle valve ⑫ open
4	Precondition the membrane and monitor the feed pressure	Run Milli-Q water at 10 mL min <sup>-1</sup> for 10 minutes in dead-end filtration: retentate needle valve ⑫ closed
5	Permeability test, check for possible membrane damage or leaks in the system	Set different flow rate (5, 2, 1, 0.5 and 0.2 mL min <sup>-1</sup> ) for 5 min and record the $\Delta P$ data
6	Connecting the SH feed solution to the inlet tubing of the pump	Transfer the pump inlet tubing from the pure water bottle to the feed solution
7	Pump flushing with the SH feed solution to reduce its dispersion	Run the feed solution at 100 mL min <sup>-1</sup> for 0.5 min. (purge valve ⑨ open, pump shut-off valve ⑩ closed)
8	Start of a photocatalytic experiment	Close the purge valve ⑨ and open the pump shut-off valve ⑩. The retentate valve ⑫ remains closed during an experiment (dead-end operation)
9	Adsorption step in the dark	Collect permeate samples in HPLC vials using a diverter valve at $V_p = 10, 20, 40, 60$ and 100 mL with the light source off
10	Photodegradation phase	Switch on the light source ④ and collect permeate samples in HPLC vials at $V_p = 104, 110, 125, 175, 250, 375, 500, 600, 650$ and 700 mL
11	Purging and flushing of the pump, inlet/outlet lines	Repeat steps 2 & 3 with Milli-Q water
12	Conduct permeability test	Repeat steps 4 & 5 with Milli-Q water
13	System cleaning	Flush the lines of a switching valve with Milli-Q water and purge them with nitrogen

### 3.6.3 Figure-of-Merits of Photocatalytic Membranes Performance

#### Filtration performance

The filtration performance of a membrane was evaluated via *permeability* ( $L_P$ ,  $\text{L m}^{-2} \text{h}^{-1} \text{bar}^{-1}$ ) calculated from the *water flux* ( $J_w$ ,  $\text{L m}^{-2} \text{h}^{-1}$ ), which is the equivalent term of superficial (not considering porosity) linear flow velocity ( $u_s$ ,  $\text{m s}^{-1}$ ) in the membrane-based water treatment. The  $L_P$  was determined using Equation 3.24:

$$L_P = \frac{J_w}{\Delta P} \quad (3.24)$$

#### Photocatalytic Oxidation

The general expression for removal of a pollutant using PCMs ( $R$ , %) is defined as per Equation 3.25:

$$R = 100 \left( 1 - \frac{c_{p,ss}}{c_f} \right) \quad (3.25)$$

where  $c_{p,ss}$  and  $c_f$  are the steady-state concentrations ( $\text{g L}^{-1}$ ) in the collected permeate and feed vessel, respectively.

With respect to characterizing the photocatalytic process, the removal metric represents a percentage of degraded compound, that reveals little of how quickly the chemical reaction happens. To understand the kinetics of a process, one must determine the rate equation, which can be then used to obtain removal for any concentration of pollutant. The classical of the rate equation as a *power law* is described in Equation 3.26. With an excess of component B (ROS concentration), the rate equation is simplified to Equation 3.27:

$$-r_A = k_i C_A^n C_B^m \quad (3.26)$$

$$-r_A = k_{obs} C_A^n \quad (3.27)$$

where  $k_i$  ( $\text{mol}^{-1} \text{L s}^{-1}$ ) is the bimolecular rate constant;  $n$ ,  $m$  and  $C_A$ ,  $C_B$  are reaction orders and molarity of  $A$ ,  $B$ ,  $k_{obs}$  ( $\text{s}^{-1}$ ) is the observed rate constant, which includes the  $k_i$  term and the effects of mass transfer.

For continuous-flow reactors (which are PCM), the rate of photocatalytic reaction can be experimentally estimated from the rate of disappearance of  $A$  referred to  $V_{por}$  ( $\bar{r}_A$ ,  $\text{mol L}^{-1} \text{s}^{-1}$ , Equation 3.28) or referred to  $A_{act}$  ( $\bar{r}_A''$ ,  $\text{mol m}^{-2} \text{s}^{-1}$ , Equation 3.29):

$$-\bar{r}_A = -\frac{1}{V_{por}} \frac{dN_A}{dt} \approx J_w \frac{(C_f - C_p)}{h_m \psi_m} \quad (3.28)$$

$$-\bar{r}_A'' = -\frac{1}{A_{act}} \frac{dN_A}{dt} \approx J_w \frac{(C_f - C_p)}{\psi_m} \quad (3.29)$$

where  $dN_A$  is the amount of component  $A$  (mol) consumed in  $dt$  (s) time;  $C_f$  and  $C_p$  are the feed and permeate molarity of reactant  $A$ , respectively ( $\text{mol L}^{-1}$ ).

As mentioned in the protocol in Table 3.7, the quantity of collected permeate samples SH was limited by the number of switching valve ports (15 positions). So as to determine the  $c_{p,ss}$  more accurately, the experimental data points determined from the calibration curve SH were fitted in the range of  $V_p = 125$ –

700 mL with a non-linear function ( $y = ax^b$ , see Figure 3.20a). Hence, the equilibrium permeate concentration ( $c_{p,ss}$ ) was determined using the last point of the fitting curve at  $V_p = 700$  mL.

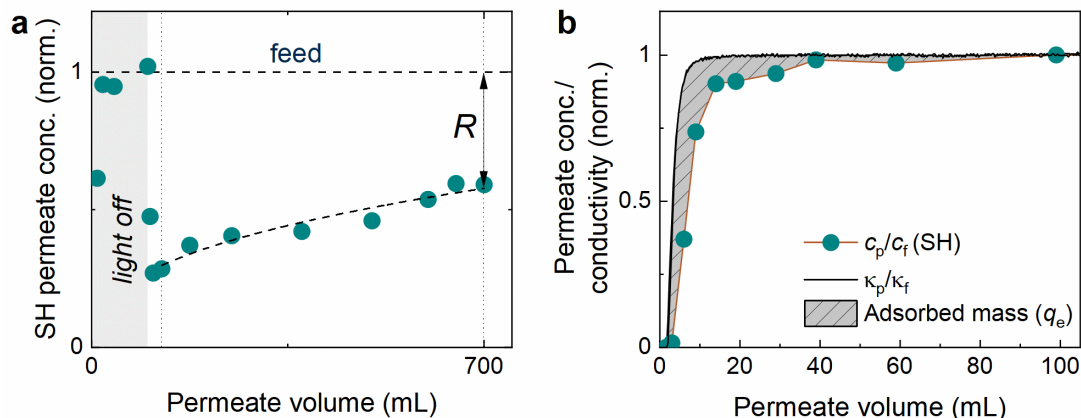


Figure 3.20: The determination of **a** removal (via a non-linear fitting in the range of  $V_p = 125\text{--}700$  mL) and **b** SH adsorption uptake by a PCM ( $V_p = 0\text{--}100$  mL) using the plots of evolution of normalized SH concentration in the permeate ( $c_p/c_f$ ). The evolution of  $c_p/c_f$  indicates the experimental system dispersion. Figure adapted with permission from Lyubimenko et al. (2021);<sup>341</sup> Copyright 2021, Elsevier.

### Pollutant Adsorption

Contribution of removal mechanisms, which are not related to degradation, was estimated by conducting control experiments. The strong removal of SH was also ascribed to adsorption as observed in experiments using the pristine PVDF membrane (MP200). The equilibrium adsorption capacity of PCM ( $q_e$ , ng cm<sup>-2</sup>) was used as a metric of SH adsorption (see findings in Chapter 5). The adsorbed mass ( $m_{SH,ads}$ , ng) was determined from the breakthrough curve recorded during the dark phase of photodegradation experiments (also highlighted as gray area in Figure 3.20b). For that, the area above the breakthrough curve was integrated using Equation 3.30. The dead volume of the experimental system was subtracted; hence Equation 3.30 was modified (Equation 3.31). Note that the adsorbed mass refers to the total surface area of a pristine membrane using the specific BET surface area ( $a_s$ ) as given by Equation 3.32.

$$m_{SH,ads} = c_f \int_0^{V_p} \left(1 - \frac{c_p}{c_f}\right) dV \quad (3.30)$$

$$m_{SH,ads} = c_f \int_0^{V_p} \left(\frac{\kappa_p}{\kappa_f} - \frac{c_p}{c_f}\right) dV \quad (3.31)$$

$$q_e = \frac{m_{SH,ads}}{m_{PCM} a_s} \quad (3.32)$$

where  $\frac{\kappa_p}{\kappa_f}$  is the ratio of the feed and permeate conductivity (-), which serves as an estimate of the system dispersion,  $m_{PCM}$  is the mass of PCM of the same size as the filtration (active) area ( $A_{act} = 2$  cm<sup>2</sup>).

Since the adsorption of SH by the PCM used is low, a high experimental error was observed when using UHPLC-FSA for the analysis. Therefore, the LSC analytical method is used, and the experiments were performed in triplicate to reduce the high  $q_e$  error.

### 3.6.4 Error Analysis

#### *Pollutant concentration*

An error propagation method was employed to evaluate the variability in reported concentrations of radiolabeled SH before and after photodegradation studies. A similar approach has been used by other researchers<sup>307, 339</sup> to calculate the relative error, which was then converted to absolute error (error bars) displayed in experimental plots. The error in the concentration of SH in the initial solution can be also exacerbated by slight decomposition of radiochemicals (up to 3% within first two months).

Table 3.8 summarizes the parameters contributing to the error of pollutant concentration that can be broken down to three groups: i) preparation of feed solution; ii) systematic errors (from the photocatalytic set-up,  $\Delta S_{ph,rel}$ ), and iii) sample analysis. The error in determining the equilibrium concentration in the collected permeate ( $\Delta c_{p,ss}/c_p$ ) was calculated using Equation 3.33 and included the uncertainty stemming from the experimental system ( $\Delta S_{ph,rel}$ ), and the analytical instrument (injection volume and peak area).

$$\frac{\Delta c_p}{c_p} = \frac{\Delta A_{FSA}}{A_{FSA}} + \frac{\Delta V_{inj}}{V_{inj}} + \Delta S_{ph,rel} \quad (3.33)$$

The systematic errors stemmed from the photocatalytic set-up and variation of the process parameters. Since the partial derivatives for all process variables are not known in this work, they have been replaced by uncertainties and are assumed to contribute with equal weights to the total error of measured concentration. The errors of analytical measurement were connected to the analytical equipment (FSA detector  $\frac{\Delta A_{FSA}}{A_{FSA}}$ , UHPLC autosampler  $\frac{\Delta V_{inj}}{V_{inj}}$ , and LSC instrument  $\frac{\Delta N_{LSC}}{N_{LSC}}$ ). The errors stemming from the laboratory environment or the cleaning of the experimental setup were found insignificant and were hence ignored. The error of pollutant concentration in the feed solution stemmed from: i) the error in preparation of feed solution ( $\pm 0.26$  mL or  $\pm 0.05\%$  for MB,  $\pm 1$  mL or  $\pm 0.13\%$  for SHs) using the pipettes and volumetric flasks; ii) the LSC analysis (see Equation 3.34).

$$\frac{\Delta c_f}{c_f} = \frac{\Delta V_f}{V_f} + \frac{\Delta N_{LSC}}{N_{LSC}} \quad (3.34)$$

The error in the concentration of SH in the initial solution can be also exacerbated by slight decomposition of radiochemicals (up to 3% within first two months).<sup>106-109</sup>

The total error introduced by the photocatalytic membrane set-up was estimated using Equation 3.35:

$$\Delta S_{ph,rel} = \sqrt{\left(\frac{\Delta Q_f}{Q_f}\right)^2 + \left(\frac{\Delta T}{T}\right)^2 + \left(\frac{\Delta I_{inc}}{I_{inc}}\right)^2 + \left(\frac{\Delta q_{PS}}{q_{PS}}\right)^2} \quad (3.35)$$

As indicated in Table 3.8, the most crucial parameter for the  $\Delta S_{ph,rel}$  is the loading of porphyrin photocatalyst in a PM. The error in porphyrin loading ( $\Delta q_{PS}/q_{PS} = 6.4\%$ ) was determined based on a batch of six porphyrin-coated membranes prepared from a single 13.9 mM Pd-TFPP solution in THF.



Table 3.8: The parameters contributing to the total error of permeate concentration imposed by the preparation, photocatalytic and analytical systems

Symbol	Parameter	Instrument/ Device	Relative error, %	Absolute error (standard value)
$\frac{\Delta V_f}{V_f}$	Volume of feed solution	pipettes, volumetric flasks	0.05	±0.26 mL (500, MB)
			0.13	±1 mL (800, SH)
$\frac{\Delta T}{T}$	Feed temperature	Bath circulation thermostat (Huber Pilot One)	0.1	±0.2 K (296.2 K)
$\frac{\Delta Q_f}{Q_f}$	Feed flow rate	HPLC pump (BlueShadow 80P)	2.0	±0.04 mL min <sup>-1</sup> (0.3) ±0.2 mL min <sup>-1</sup> (15)
$\frac{\Delta q_{PS}}{q_{PS}}$	Photosensitizer loading	6-well adsorption plate	6.4	1.6 µmol g <sub>memb</sub> <sup>-1</sup> (25) 0.013 µmol cm <sup>-2</sup> (0.2)
$\frac{\Delta I_{inc}}{I_{inc}}$	Light intensity	WLED (Thorlabs SOLIS-3C)	1.0	±0.1 mW cm <sup>-2</sup> (10.0)
$\frac{\Delta V_{inj}}{V_{inj}}$	Injection volume	Flexar Auto-sampler (FX UHPLC)	1.5	±1.5 µL (100) ±3.0 µL (200)
$\frac{\Delta A_{FSA}}{A_{FSA}}$	Peak area of eluting SHs	Radiomatic 625TR	12–64	±20 cpm (100) ±160 cpm (2860)
$\frac{\Delta N_{LSC}}{N_{LSC}}$	Activity of SH sample	Tri-Carb 4910TR	3–6	±1 Bq (12) ±25 Bq (810)

#### Analytical Errors in Scintillation Methods

When decreasing the concentration, the error of analytical instrument ( $\frac{\Delta A_{FSA}}{A_{FSA}}$  or  $\frac{\Delta N_{LSC}}{N_{LSC}}$ ) rises strongly and approaches to the maximum close to the instrument detection limit. The variation of the relative errors of the analytical instruments (LSC and FSA) with 17β-estradiol concentration are presented in Figure 3.21. The error of analytical instruments was determined using the standard deviation from the mean value of prepared SH standards. The error of the UHPLC device (pump, autosampler, photodiode array detector) did not exceed 2% after injecting 12 standard solutions (PerkinElmer).

The LSC offers high reproducibility (based on 10 samples containing standards), resulting in an error of 1–5%. The analytical error of the FSA detector ( $\Delta A_{FSA}$ ) depends on the net number of counts, which is a function of radiochemical concentration, counting efficiency, and counting time.  $\Delta A_{FSA}$  can be calculated with the 95.5% confidence limit using the Equations 3.36–3.40:<sup>354</sup>

$$\frac{\Delta A_{FSA}}{A_{FSA}} = \frac{2\sigma_{NC}}{N_{NC}} \quad (3.36)$$

$$\sigma_{NC} = \sqrt{\sigma_{TC}^2 + \sigma_{BG}^2} \quad (3.37)$$

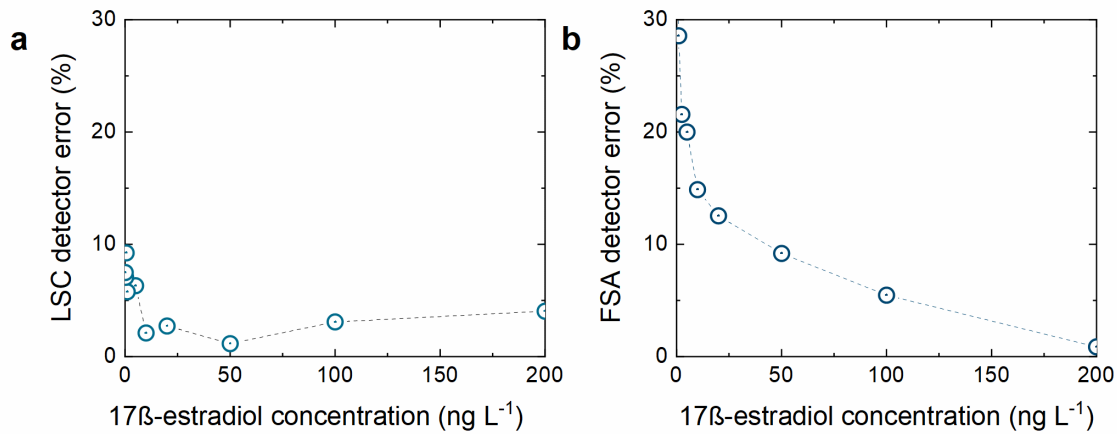


Figure 3.21: Evolution of the **a** LSC and **b** FSA detector errors as a function of 17 $\beta$ -estradiol concentration. The error value per each concentration is based on at least four repetitions.

$$\sigma_{TC} = \sqrt{N_{TC}} \quad (3.38)$$

$$N_{NC} = N_{TC} - N_{BG} \quad (3.39)$$

$$N_{TC/BG} = n_{TC/BG} \cdot \frac{Q_{FSA}}{V_{FSA}} \quad (3.40)$$

where  $\sigma_{NC}$  is the standard deviation of net counts ( $2\sigma$  corresponds to 95.5% confidence limit),<sup>355</sup>  $N_{NC}$  is the number of net counts from the FSA detector, which is equal to the number of total counts ( $N_{TC}$ ) after subtraction of the number of background counts ( $N_{BG}$ );  $N_{TC}, N_{BG}$  are derived via multiplication of the cumulative count rate ( $n_{TC}, n_{TC}$ ) in the elution region by the residence time in the FSA-detector flow cell (volume  $V_{FSA}$ , mL);  $Q_{FSA}$  (mL min<sup>-1</sup>) is the flow rate of LS pump through the flow cell.

#### Figures-of-Merit of Photocatalytic Process

Via the error propagation method applied to Equation 3.25 ( $R$ ), Equation 3.28 ( $r_A$ ), Equation 2.7 ( $\bar{t}_{con}$ ), the relative errors for the removal, rate of disappearance and contact time were calculated as given by Equations 3.43–3.46.

$$\Delta R_{SH,abs} = 100\% \cdot \frac{c_p}{c_f} \cdot \sqrt{\left(\frac{\Delta c_f}{c_f}\right)^2 + \left(\frac{\Delta c_p}{c_p}\right)^2} \quad (3.43)$$

$$\Delta \bar{r}_{SH,abs} = \bar{r}_{SH} \cdot \sqrt{\left(\frac{\Delta(c_f - c_p)}{c_f - c_p}\right)^2 + \left(\frac{\Delta \bar{t}_{con}}{\bar{t}_{con}}\right)^2} \quad (3.44)$$

$$\Delta(c_f - c_p) = \sqrt{\Delta c_f^2 + \Delta c_p^2} \quad (3.45)$$

$$\frac{\Delta \bar{t}_{con}}{\bar{t}_{con}} = \sqrt{\left(\frac{\Delta h_m}{h_m}\right)^2 + \left(\frac{\Delta \psi_m}{\psi_m}\right)^2 + \left(\frac{\Delta Q_f}{Q_f}\right)^2} \quad (3.46)$$

where  $(c_f - c_p)$  is the difference between feed and permeate concentrations;  $\Delta(c_f - c_p)$  is the uncertainty in the difference between feed and permeate concentrations. Note that the concentration covariance was assumed insensitive to changes in contact time.

#### Membrane Characteristics

The main source of errors contributing to the uncertainties of reported membrane porosity, and surface-to-volume ratio is inhomogeneity of employed membranes. Using Equation 3.20 ( $a_V$ ) and Equation 3.21 ( $\psi_m$ ), the error propagation analysis was performed, resulting in Equation 3.47 and Equation 3.48:

$$\frac{\Delta a_V}{a_V} = \sqrt{\left(\frac{\Delta \psi_m}{\psi_m}\right)^2 + \left(\frac{\Delta m_m}{m_m}\right)^2 + \left(\frac{\Delta a_{s,BET}}{a_{s,BET}}\right)^2} \quad (3.47)$$

$$\frac{\Delta \psi_m}{\psi_m} = \sqrt{\left(\frac{\Delta V_{bulk}}{V_{bulk}}\right)^2 + \left(\frac{\Delta h_m}{h_m}\right)^2 + \left(\frac{\Delta A}{A}\right)^2} \quad (3.48)$$

where  $\frac{\Delta m_m}{m_m}$  is the relative error of membrane weight obtained after weighing five individual membranes (0.6–3.2%);  $\frac{\Delta a_{s,BET}}{a_{s,BET}}$  is the relative error of specific surface area determined using BET multi-point analysis (8%);  $\frac{\Delta V_{bulk}}{V_{bulk}}$  is the relative error of the bulk polymer volume obtained from helium pycnometry (0.75%);  $\frac{\Delta h_m}{h_m}$  is the relative error of PVDF membrane thickness (0.8–5.2%);  $\frac{\Delta A}{A}$  is the relative error of the coupon area of PVDF membrane (4%);

Table 3.9 outlines the values of PVDF membranes necessary for calculation of  $a'_V$ : i) BET ( $a_{s,BET}$ ) and DFT ( $a_{s,DFT}$ ) specific surface area; ii) total surface area ( $A_S$ ); iii) the pore volume ( $V_{por}$ ), iv) the membrane porosity ( $\psi_m$ ); v) membrane thickness ( $h_m$ ); and vi) membrane coupon area ( $A_m$ ). The table is accompanied with the relative and absolute errors. The relative errors of  $a_{s,BET}$  and  $a_{s,DFT}$  are based on one standard deviation for the determined slope/intercept of the fitting curve.

Table 3.9: Characteristics of the studied PVDF membranes and the corresponding relative and absolute errors

	NM20		NM100		MP100		MP200		MP450		HW650	
	Mean value	Abs. error	Mean value	Abs. error	Mean value	Abs. error	Mean value	Abs. error	Mean value	Abs. error	Mean value	Abs. error
$A_m, 10^{-4} \text{ m}^2$	4.9	0.2	4.9	0.2	4.9	0.2	4.9	0.2	4.9	0.2	4.9	0.2
$m_m, 10^{-3} \text{ g}$	9	0.3	25	0.2	32	0.2	42	0.3	34	0.9	2.6	2.6
$h_m, 10^{-6} \text{ m}$	30	2	92	2	101	2	130	1	89	2	2.2	5
$\psi_m, \%$	45.7	2.6	62.8	3.3	56.1	2.5	54.5	1.4	48.2	2	4.1	2.7
$a_{s,BET}, \text{m}^2 \text{ g}^{-1}$	30.8	3.1	14	1.4	8.4	0.8	5.9	0.6	2.8	0.3	10.1	0.4
$a_{s,DFT}, \text{m}^2 \text{ g}^{-1}$	24.1	2.4	11.7	1.2	7.1	0.7	4.5	0.5	2.2	0.2	3.4	0.3
$A_{s,BET}, \text{m}^2$	0.29	0.02	0.35	0.03	0.27	0.02	0.25	0.02	0.09	0.03	0.11	0.01
$V_{por}, 10^{-8} \text{ m}^3$	0.67	0.07	2.84	0.14	2.78	0.18	3.48	0.17	2.11	0.13	2.13	0.19
$a_v, 10^{-7} \text{ m}^2 \text{ m}^{-3}$	4.3	0.5	1.2	0.2	1.0	0.1	0.7	0.1	0.5	0.2	0.34	0.1
			11.1	16.7	1.0	0.1	0.12	0.1	0.15	0.2	0.34	0.1
			4.1	0.8	4.1	0.2	4.1	0.2	4.1	0.2	4.1	0.2
			3.3	0.8	0.6	0.6	0.7	0.7	0.7	0.9	2.6	2.6
			6.7	2.2	2.0	2.0	0.8	0.8	2.2	2.2	2.2	5.3
			5.7	5.2	4.5	4.5	2.5	2.5	4.1	4.1	4.1	5.8
			10.1	10.1	10.1	10.1	10.1	10.1	10.1	10.1	10.1	10.1
			2.4	1.2	0.7	0.7	0.5	0.5	0.2	0.2	0.3	0.3
			6.9	8.6	7.4	7.4	8.0	8.0	33	33	33	8.1
			9.7	4.9	2.78	0.18	6.5	0.17	4.9	0.13	6.2	0.19
			11.1	16.7	1.0	0.1	0.12	0.1	0.15	0.2	0.34	0.1
			4.1	0.8	4.1	0.2	4.1	0.2	4.1	0.2	4.1	0.2

### 3.6.5 Accelerated Aging of Pristine and Photocatalytic Membranes

When studying the long-term photostability of PCM materials, there is no need to carry out studies for a number of months, or even years. In laboratory conditions, the accelerated ageing method allows it to reach the light dose corresponding to the longevity of conventional membranes in water treatment applications (almost 5 years for a NF membrane).<sup>356</sup> In response to the lack of existing standards for stability of photocatalytic materials the experimental protocol of the photostability evaluation under accelerated aging performed within 10 days was developed and summarized in Table 3.10.

Table 3.10: The suggested protocol for evaluation of PCM photostability under accelerated aging conditions

No	Step/justification	Description (conditions, details)
1	Preparation of membrane trays	Fill each of eleven (cleaned) aluminum trays with 10 mL of Milli-Q water
2	Immersion of fresh membranes in water-filled trays	Place the moist, fresh membranes (7 PCM and 2 pristine) in the prepared trays
3	Preparation of the control samples	Keep one tray without a membrane and one tray with membrane outside the chamber as control samples
3	Setting the irradiation time	Set the irradiation time on 250 h and turn on the light source using the LedControl unit
4	Accelerated aging phase	Stop the light, remove one tray at intervals of 5, 25, 50, 75, 100, 125, or 250 h and transfer the membrane to a water-filled vial
5	Visual observation technique	Take one set of photos with all aged PCM
6	TOC analysis	Collect water for TOC analysis from the tray to a TOC-procedure-cleaned vial, bring to 10 mL (9.986 g at 23 °C) using a balance; conduct the TOC analysis of all samples + blank samples
7	Absorbance measurements	Carry out the absorbance studies of moist (inside the integrating sphere) or dissolved PCM (in a cuvette)
8	FTIR-ATR and top-view SEM analysis	Cut two small pieces of aged and dried membranes; perform the FTIR-ATR and top surface SEM analysis
9	MB degradation tests coupled with permeability studies	Mount a wet aged membrane (min. 22 × 12 mm) to the membrane cell and follow the protocol describing the MB degradation tests (see Table 3.6)
10	Optional: SEM cross-sectional images	Take the cross-sectional SEM images of fresh, aged PCM and pristine membranes
11	Optional: Zeta potential studies	Perform zeta potential studies of fresh, aged PCM and pristine membranes

Accelerated aging of porphyrin-coated membranes allowed to perform the life-cycle assessment of PCM for water treatment application under solar illumination (the results shown in Section 6.5). For that, the cumulative dose of absorbed radiation in the UV-violet LED chamber ( $H_{abs}$ , kWh m<sup>-2</sup>) was calculated via Equation 3.49:

$$H_{abs} = t_{op} h u_L \int_{\lambda_1}^{\lambda_2} \frac{\varphi_{inc,\lambda}^{ch}}{\lambda} \alpha_\lambda d\lambda, \quad (3.49)$$

where  $t_{op}$  is the operation (illumination) time (h),  $h$  is Planck's constant (J·s),  $u_L$  is the light speed (m s<sup>-1</sup>),  $\lambda_1, \lambda_2$  define the wavelength region (320–450 nm) for integration of the spectral incident photon flux inside the UV-violet-LED chamber ( $\varphi_{inc,\lambda}^{ch}$ , s<sup>-1</sup> m<sup>-2</sup> nm<sup>-1</sup>).  $\varphi_{inc,\lambda}^{ch}$  was calculated from the spectral irradiance of both LED channels of the UV-vis-LED chamber ( $I_{inc,\lambda}^{ch}$ ), and corrected by the transmission loss of the glass cover sheet (see Figure 3.10b),  $\alpha_\lambda$  is the absorptance spectrum of a photocatalytic membrane (–).

The kinetics of porphyrin photobleaching was related to a potential outdoor exposure test by calculating the equivalent number of days ( $t_{1/2,eq}$ ) corresponding to half-life time of photobleached PS ( $t_{1/2}$ , where  $c_{t,PS} = 0.5 \cdot c_{0,PS}$ ) in the UV-violet-LED chamber via Equation 3.50 and Equation 3.51:

$$t_{1/2,eq} = \frac{H_{abs,1/2}}{H_{abs,av}^{sol}}, \quad (3.50)$$

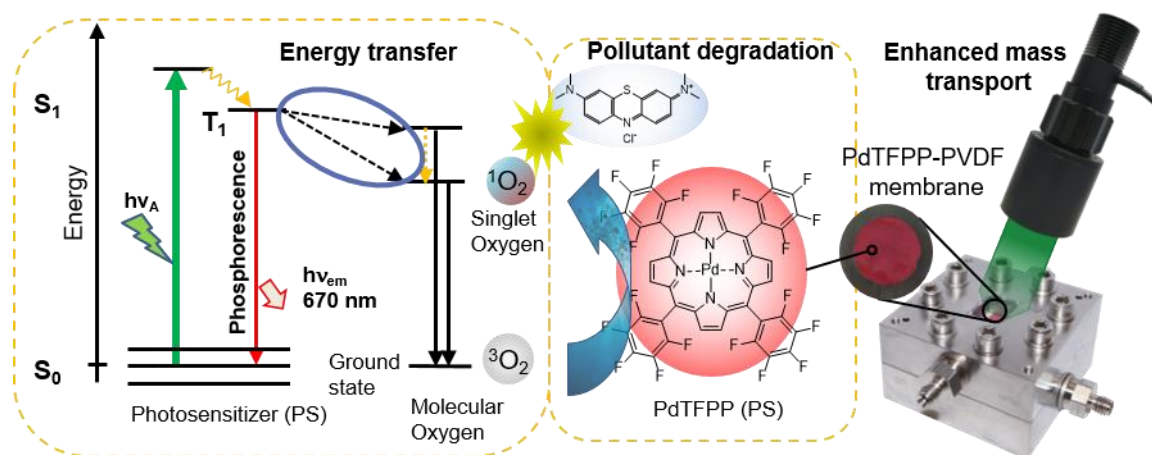
$$D_{abs,av}^{sol} = I_{eff}^{sol} \frac{H_{abs,an}^{sol}}{I_{inc}^{sol} 365} \quad (3.51)$$

where  $H_{abs,av}^{sol}$  (kWh m<sup>-2</sup> day<sup>-1</sup>) is the daily average dose of absorbed solar light radiation on a horizontal surface;  $H_{abs,1/2}^{ch}$  was defined as per Equation 3.51 using  $t_{op} = t_{1/2}$  (see Table 3.11);  $H_{abs,an}^{sol}$  is the annual global solar irradiation on a horizontal surface in the Karlsruhe North region (49.094°, 8.429, from 2016), ( $D_{abs,an}^{sol} = 1118$  kWh m<sup>-2</sup> year<sup>-1</sup>),<sup>357</sup>  $I_{inc}^{sol}$  is the solar irradiance on a horizontal plane (assumed  $I_{inc}^{sol} = 1000$  W m<sup>-2</sup>),  $I_{eff}^{sol}$  (W m<sup>-2</sup>) is the effective irradiance of AM1.5g global solar spectrum corresponding to the absorbed photon flux ( $\varphi_{abs}^{sol}$ ) of Pd-TFPP-, Zn-TFPP-, and H<sub>2</sub>-TFPP/PVDF membranes (see Table 3.11) in the wavelength region of 350–1150 nm.

Table 3.11: Summary of parameters for estimation of PCM photostability by the equivalent number of days during the outdoor testing

	AM1.5g global solar spectrum		UV-violet-LED chamber			$t_{1/2,eq}$ , days
	$I_{eff}^{sol}$ , W m <sup>-2</sup>	$D_{abs,av}^{sol}$ , kWh m <sup>-2</sup>	$I_{eff}^{ch}$ , W m <sup>-2</sup>	$t_{1/2,PS}$ , h	$t_{1/2}(D_{abs,1/2}^{ch})$ , kWh m <sup>-2</sup>	
Pd-TFPP	273.7	0.84	2161	31.5	68.1	81
Zn-TFPP	308.5	0.94	2115	99.0	209.4	222
H <sub>2</sub> -TFPP	332.8	1.02	2056	27.7	57.0	56

# 4 Pd-Porphyrin-Loaded Membranes for MB Removal



The contents of this chapter have been published in the separate work. Figures and Tables have been adapted with permission from Lyubimenko, R. et al. (2019);<sup>276</sup> Copyright 2019 American Chemical Society. The citations in the following text are omitted.

**Lyubimenko, R.;** Busko, D.; Schäfer, A. I.; Richards, B. S.; Turshatov, A. (2019). Efficient photocatalytic removal of methylene blue using a metalloporphyrin–poly(vinylidene fluoride) hybrid membrane in a flow-through reactor. *ACS Appl. Mater. Interfaces*, 11 (35), 31763–31776.

## *Acknowledgments and Contributions*

The experimental plan and methodology of this chapter were designed by the author, Andrey Turshatov, and Bryce S. Richards. The fabrication of Pd-TFPP/PVDF membranes, the absorbance studies, the photocatalytic degradation experiments and the mass spectrometry analysis were carried out by the author. Photoluminescence studies (both steady-state and time-resolved) were conducted by Dmitry Busko (IMT, KIT) in presence of the author. ToF-SIMS analysis of the Pd-TFPP/PVDF membrane was performed by Alexander Welle (IFG, KIT), who also helped with interpretation of the results. Data analysis was conducted by the author with assistance from Andrey Turshatov, Bryce S. Richards, and Andrea I. Schäfer.

## 4.1 Introduction

Among the existing metalloporphyrins, palladium (pentafluorophenyl)porphyrin (or Pd-TFPP) promises excitation under visible light, improved photostability and highly efficient production of singlet oxygen – a type of selective ROS with a lifetime in the microsecond range. This chapter outlines the optical, photophysical, photostability and photocatalytic properties of Pd-TFPP/PVDF membranes. The photocatalytic activity of PCM was probed using the MB dye – a water-soluble model contaminant. Understanding the nature of photocatalytic experiments with Pd-TFPP/PVDF membranes using probe molecules (MB or UA) establishes a basis for further experiments with real water-borne contaminants, such as SH micropollutants. A short summary concludes the section.

### Objectives

The key scientific objectives of this chapter are:

- i. Fabrication of a PCM exhibiting strong photocatalytic activity when excited by light from the visible part of the solar spectrum;
- ii. Examination of the interaction mechanisms of excited Pd-TFPP adsorbed to a PVDF membrane with dissolved oxygen and dissolved organic pollutants (MB and UA);
- iii. Demonstration and determination of the degradation performance in a single-pass continuous-flow membrane reactor via variation of operating parameters, Pd-TFPP and MB concentrations.

A short summary with key results concludes the chapter.

## 4.2 Characterization of Pd-TFPP/PVDF Membranes

### 4.2.1 Adsorption Studies

The successful adsorption of porphyrin on PVDF membrane can be judged by the color change from white (pristine PVDF) to red (after Pd-TFPP adsorption) as illustrated in Figure 3.2. Membranes impregnated with Pd-TFPP solution in THF exhibit an intense red color, which persists after the membrane is transferred to water. This is likely caused by the strong hydrophobic interaction between the membrane and Pd-porphyrin molecules.

Figure 4.1a provides experimental evidence of a high affinity between the adsorbate (Pd-TFPP molecules) and adsorbent (membrane). The study of Pd-TFPP adsorption kinetics on a PVDF membrane reveal that adsorption occurs almost instantaneously, reaching equilibrium in less than a minute. The adsorption isotherm (see Figure 4.1b) recorded by changing the concentration of Pd-TFPP in THF solution at  $(23 \pm 1)^\circ\text{C}$  exhibits a linear rise of the porphyrin uptake with equilibrium concentration up to the solubility limit of Pd-TFPP in THF solvent (42–44 mM). Both the Freundlich ( $K_F c_{\text{eq}}^n$ ) model and the linear adsorption model ( $K_H c_{\text{eq}}$ ) can account for the linear isotherm, which works well for hydrophobic organic molecules.



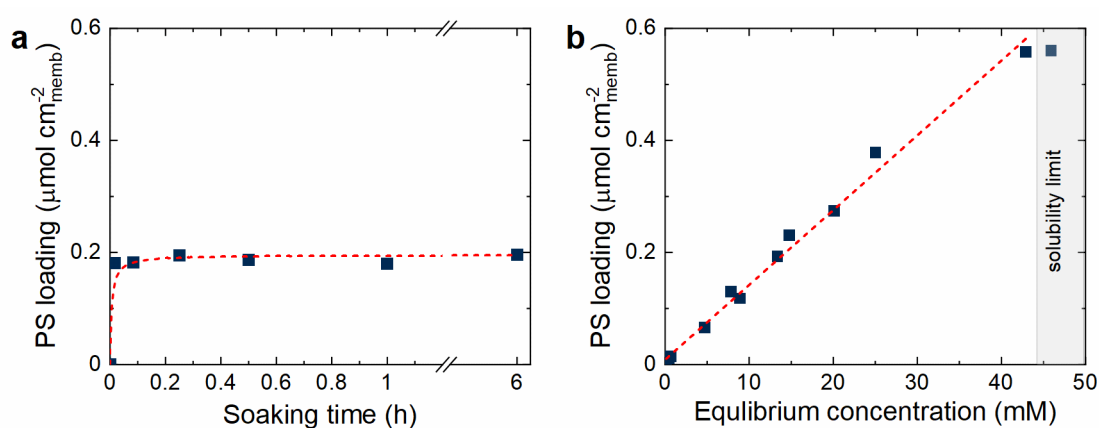


Figure 4.1: **a** Adsorption kinetics,  $c_{PS} = (13.8 \pm 0.2)$  mM, and **b**, adsorption isotherm (at 23 °C, time 4 h) for Pd-TFPP on a PVDF membrane. The curves in plots **a** and **b** serve as a guide to the eye.

To investigate whether Pd-TFPP forms a multilayer upon adsorption, the surface coverage of the membrane specimen  $\theta_{PS}$  (–) was calculated using Equation 4.1 and Equation 4.2:

$$\theta_{PS} = \frac{N_{PS}}{N_{ML}} \quad (4.1)$$

$$N_{ML} = \frac{a_S m_m}{A_{mol} N_A} \quad (4.2)$$

where  $N_{PS}$  is the amount of adsorbed Pd-TFPP molecules covering a membrane ( $A_m = 4.91$  cm<sup>2</sup>,  $q_{PS} = 0.22$  μmol cm<sup>-2</sup>);  $N_{ML}$  is the theoretical monolayer capacity (mol);  $a_S$  is the specific surface area of a pristine membrane (defined by Brunauer-Emmett-Teller theory,  $a_S = 5.9$  m<sup>2</sup> g<sup>-1</sup>);  $A_{mol}$  is the approximate area of a Pd-TFPP molecule (including the van der Waals radii);  $N_A$  is the Avogadro number ( $6.022 \cdot 10^{23}$  mol<sup>-1</sup>).

Figure 4.2 illustrates the simulated total charge density surface, which approximates van der Waals atom radii and represent three-dimensional space occupied by the molecule in flat and upright orientations.

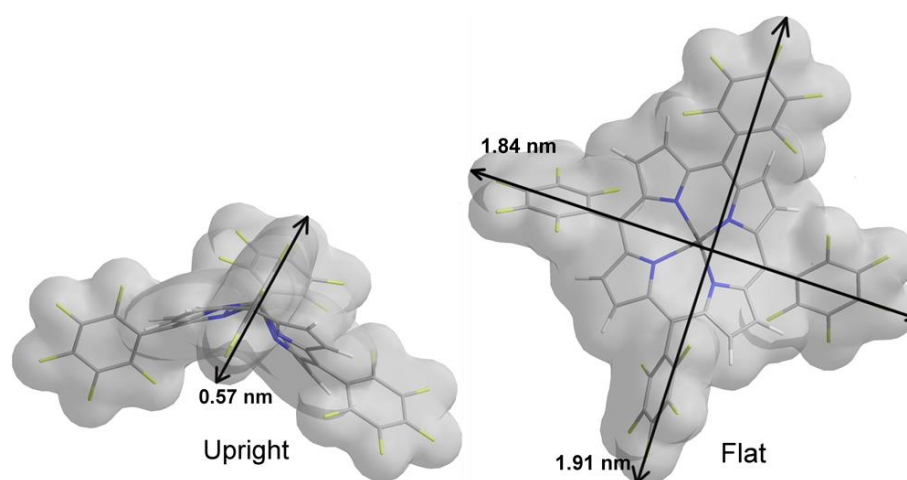


Figure 4.2: The total charge density surface of PdTFPP molecule obtained from Chem 3D (CambridgeSoft). Flat (left) and upright (right) orientations were shown. The ImageJ software was used to calculate the area of simulated surfaces taking the hydrogen atom as a reference.

On the basis of the simulated surface area,  $A_{mol}$  for the upright ( $1.75 \cdot 10^{-18} \text{ m}^2$ ) and flat ( $2.85 \cdot 10^{-18} \text{ m}^2$ ) Pd-TFPP molecule orientations were calculated using the *Image J* software. Since  $a_s$ ,  $m_m$ ,  $N_{PS}$  ( $1.08 \text{ } \mu\text{mol}$  Pd-TFPP per membrane of 25 mm diameter) are experimentally known,  $\theta_{PS}$  ( $0.62 \text{ m}^2 \text{ membrane}^{-1}$ ) and  $A_s$  ( $0.25 \text{ m}^2 \text{ membrane}^{-1}$ ) were calculated. The theoretical number of monolayers is hence  $n_{ML} > 1$  that may indicate the formation of a multilayer. This hypothesis however holds only if porphyrin molecules are homogeneously distributed over the membrane surface.

Exposure of contaminants to ROS throughout the membrane is vital for an efficient and complete degradation process. Therefore, it is desirable that the porphyrin molecules are homogeneously distributed. A particular analysis called time-of-flight secondary ion mass spectrometry (ToF-SIMS) provides this information. Because of the palladium in Pd-TFPP, the Pd-TFPP distribution can be visualized by measuring the  $\text{Pd}^+$  distribution and mapping that to that to intact Pd-TFPP molecules along the PCM cross section. The low-resolution images (Figure 4.3a, top row) reveal an identical distribution of the Pd isotopes and the intact Pd-porphyrin molecules. This finding suggests that palladium ions are coordinated in the porphyrin macrocycle. The high-resolution images (Figure 4.3a, bottom row) provide a detailed picture of Pd-porphyrin distribution. The largest signal of  $\text{Pd}^+$  ions (lighter color means stronger signal) comes from the upper surface, followed by a region with lower porphyrin concentration with a broad maximum, and finally a considerable rise on the back side of the membrane. As depicted in Figure 4.3b, the depletion of Pd-porphyrin in the bulk membrane can be as low as 80%. Nevertheless, about 70% of the total Pd-TFPP uptake is in middle 79% of the PVDF membrane. Hence, the PCM may enable the ROS generation throughout the whole membrane depth.

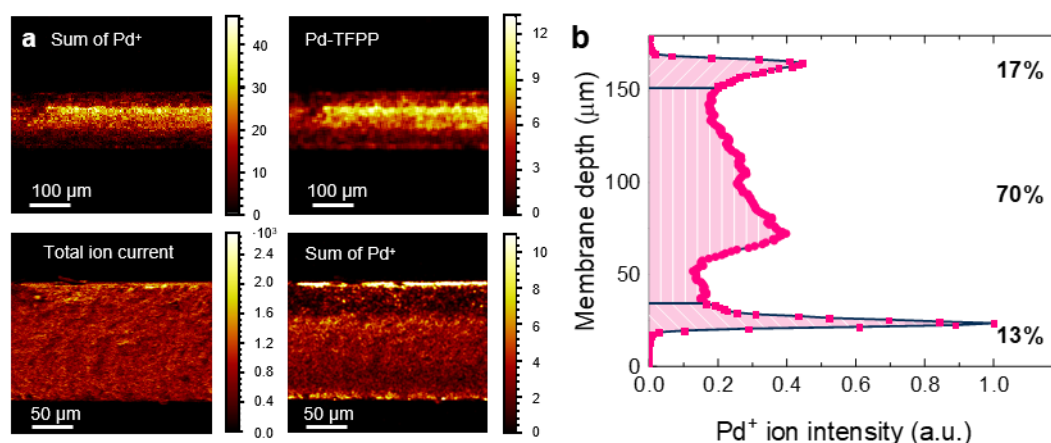


Figure 4.3: **a** The low-resolution (top) and high-resolution (bottom) chemical mapping of  $\text{Pd}^+$  isotope ions, intact Pd-TFPP molecules and total mass count of a PCM cross-section. **b** Distribution of Pd along the thickness of a Pd-TFPP/PVDF membrane obtained from ToF-SIMS measurements. Top, central and bottom regions of the PCM are highlighted with the different hatching patterns.

## 4.2.2 Optical Characterization of Porphyrin-Coated Membranes

Optical spectroscopy studies provide qualitative evidence for PS immobilization on a membrane. Figure 4.4a depicts the FTIR spectra of the Pd-TFPP powder, dried pristine PVDF membrane, and a Pd-TFPP/PVDF membrane. In the spectrum of the Pd-TFPP/PVDF membrane, the peaks ascribed to porphyrin disappear between  $1495$  and  $1519 \text{ cm}^{-1}$  (pyrrole and phenyl ring C–C vibrations, respectively,  $\nu_{C-C}$ ), between  $991$  and  $1018 \text{ cm}^{-1}$  (C–H in-plane deformation,  $\delta_{C-H}$ ), at  $947 \text{ cm}^{-1}$  (Pd–N stretching,  $\delta_{Pd-N}$ ), and at  $703 \text{ cm}^{-1}$  (C–H out-of-plane deformation,  $\gamma_{C-H}$ ). These absorption bands, highlighted in the Figure 4.4a by gray stripes, are present in the FTIR spectrum of porphyrin powder.

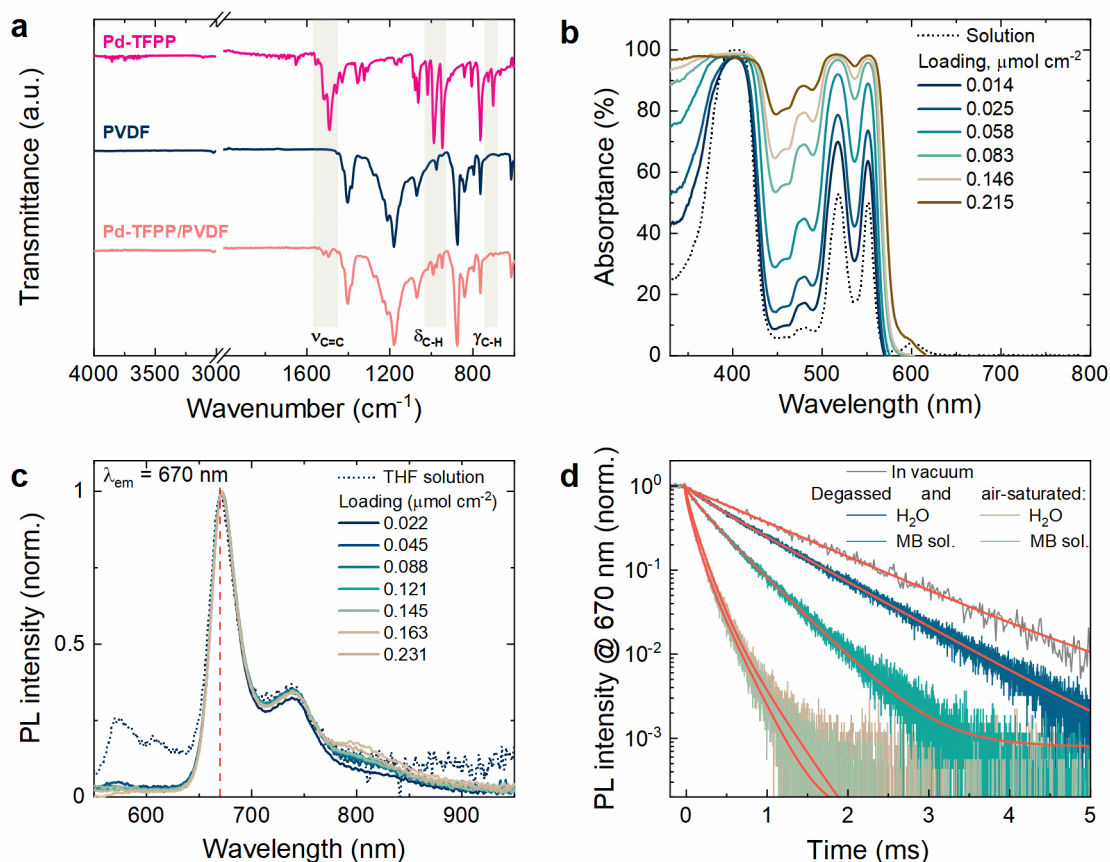


Figure 4.4: **a** FTIR-ATR spectra of Pd-TFPP, pristine PVDF and Pd-TFPP/PVDF membranes. **b** UV-Vis absorption and **c** steady-state PL spectra of the PCM measured in water at different loadings (solid lines) and the spectra of 15.5  $\mu\text{M}$  Pd-TFPP solution in THF (dotted line). **d** Time-resolved PL decay of Pd-TFPP/PVDF membranes measured in water or 1 mg  $\text{L}^{-1}$  MB solution (degassed or air-saturated) under 405 nm excitation, at Pd-TFPP loading of 0.23  $\mu\text{mol cm}^{-2}$ . A single (in vacuum) or biexponential fit (in solution) was applied.

The immobilization of Pd-TFPP to a membrane does not alter its chemical structure, although a slight shift in peak positions ( $1491\text{ cm}^{-1} \rightarrow 1495\text{ cm}^{-1}$ ,  $990\text{ cm}^{-1} \rightarrow 987\text{ cm}^{-1}$ , and  $949\text{ cm}^{-1} \rightarrow 947\text{ cm}^{-1}$ ) is observed. Likewise, the chemical structure of PVDF membrane remains unchanged as seen from the characteristic peaks (highlighted as dashed lines) before and after exposure to PS-containing THF solution.

Strong light absorption is critical for effective ROS generation. Figure 4.4b displays the UV-Vis absorption spectra of Pd-TFPP in solution and in the impregnated form in a PVDF membrane (expressed as fraction of absorbed light). The recorded spectra exhibit two strong absorption bands with characteristic peaks at 403 nm (Soret) and 518 and 551 nm (Q-bands),<sup>206</sup> the same wavelengths as in the solution spectrum. Already at  $\bar{q}_{PS} = 0.014\text{ }\mu\text{mol cm}^{-2}$  loading, all light is absorbed in the Soret band (absorbance  $\sim 100\%$ ) and roughly 50% in the Q-band wavelength region. Increasing the loading leads to an overall increase in absorbance, eventually approaching 100% light absorption in the Q-band as well.

Since adsorption of macromolecules such as porphyrins often leads to their aggregation and reduced efficacy of  $^1\text{O}_2$  generation, it is vital to investigate the shifts in the energy levels of the electrical transitions. The spectral changes indicate the presence of aggregated forms of PS.<sup>358</sup> As can be seen from

Figure 4.4c the PL emission spectra retain their shape and the peak positions (peak at 670 nm) for the entire range of Pd-TFPP loadings. Hence, this finding suggests that the adsorption of Pd-TFPP does not result in aggregate formation on the surface of PVDF membrane. This conclusion can be explained by the strong repulsion between the pentafluorophenyl rings of porphyrin molecules.<sup>207</sup>

The PL decay time in the presence of triplet molecular oxygen ( $^3\text{O}_2$ ) contains valuable information on the efficiency of the energy transfer (ET), which is an essential step in  $^1\text{O}_2$  generation by a photosensitizer (more information in Section 2.3.4). The ET processes can also occur between excited triplet  $^3\text{PS}^*$  state and pollutant molecules. These reactions are described as Type II mechanism in processes (i-iii):



The excited triplet  $^3\text{PS}^*$  and singlet  $^1\text{PS}$  states can interact with organic solutes (quenchers, Q) by means of charge (CT) transfer, convert to a porphyrin radical anion/cation and produce various ROS (superoxide anion, hydrogen peroxide, organic radicals). These processes (ii-iv) are combined in Type I oxidation pathways:<sup>174</sup>



Type I and Type II processes can be distinguished by recording the phosphorescence decay curves. Figure 4.4d depicts the phosphorescence signal of PCM measured at 671 nm in vacuum ( $< 10^{-4}$  Pa) that allows to exclude  $^3\text{PS}^*$  quenching by molecular oxygen. The long-lived PL signal (average lifetime  $\langle \tau_{\text{T},0} \rangle = 1.05$  ms) follows the relaxation of the triplet excited state via phosphorescence. In deoxygenated water (see Figure 4.4d), the residual oxygen and solvent molecules increase  $^3\text{PS}^*$  quenching thus reducing  $\langle \tau_{\text{T}}^0 \rangle$  to 0.74 ms. The PL lifetime of PCM decreases even further ( $\langle \tau_{\text{T},\text{MB}} \rangle = 0.38$  ms) in solution of methylene blue (MB) dye – a frequent model pollutant for testing photocatalytic materials.<sup>359</sup> The pronounced reduction in PL lifetime reflects the interaction between MB and immobilized Pd-TFPP molecules, which can lead to oxygen-free degradation pathway via Type I (charge transfer) reactions (iv,v).

The MB-molecule induced quenching can be assigned to various processes (ii-iv): photoexcited electron transfer, triplet–singlet energy transfer, or triplet–triplet energy transfer. Distinguishing these processes lies beyond the scope of the work, and hence they are all assumed to be potentially involved in the quenching of porphyrin excited states by MB molecules. In air-saturated water and MB solution the PL signal decays faster over a few hundred microseconds (0.13 ms and 0.10 ms, respectively). Such a drastic change indicates quenching induced by molecular oxygen. The contribution of quenching induced by either molecular oxygen ( $k_{q,\text{O}_2}$ , Type II) or MB ( $k_{q,\text{MB}}$ , Type I) can be compared by calculating the ratio of the rate constants of  $^3\text{PS}^*$  quenching using Equation 4.3. The resulted value  $k_{q,\text{O}_2}/k_{q,\text{MB}} = 4.97$  indicates that oxygen-induced quenching is the dominant channel of  $^3\text{PS}^*$  deactivation, whereas the role of direct quenching by MB in this process is less significant.

$$\frac{k_{q,O_2}}{k_{q,MB}} = \frac{\left(\frac{1}{\langle\tau_T\rangle} - \frac{1}{\langle\tau_T^0\rangle}\right)}{\left(\frac{1}{\langle\tau_{T,MB}^0\rangle} - \frac{1}{\langle\tau_T^0\rangle}\right)} \quad (4.3)$$

where  $\langle\tau_T^0\rangle$ ,  $\langle\tau_T\rangle$ , and  $\langle\tau_{T,MB}^0\rangle$  are the phosphorescence lifetimes measured in deoxygenated, aerated water, and deoxygenated MB solution, respectively.

### 4.3 Evaluation of Photocatalytic Performance

It has been demonstrated above that molecular oxygen plays a crucial role in quenching the excited state of Pd-porphyrin. Yet, not every collision between an excited-state PS molecule and oxygen leads to singlet oxygen generation. Thus, before proceeding to the study of PCM activity via the degradation of model pollutants, it is necessary to confirm the  $^1O_2$  generation.

#### 4.3.1 Probing Singlet Oxygen Generation with Uric Acid

Experiments with specific chemical trap molecules are a common practice to confirm photosensitized  $^1O_2$  generation. Among the available water-soluble chemical traps, uric acid (UA) exhibits both excellent selectivity and reactivity with  $^1O_2$ .<sup>360</sup> However, it cannot be ruled out that photoinduced electron transfer from  $^3PS^*$  to UA (process (ii) described above) or physical quenching of  $^3PS^*$  may affect the UA degradation.<sup>343</sup> Hence, a preliminary test revealing the effect of UA on the PL decay may help to avoid overestimating the  $^1O_2$  output. Figure 4.5a displays that phosphorescence signal (670 nm) of a Pd-TFPP/PVDF membranes excited at 405 nm. The PL signals are identical in deoxygenated water with and without UA. These results suggest that no direct interaction between UA and excited Pd-TFPP occurs. In presence of oxygen, the PL signal decays more steeply (similarly to Figure 4.5b), indicating the effective quenching by molecular oxygen. The difference in PL decay curves in aerated PBS and PBS-UA solutions may indicate a small obstruction of oxygen diffusion by the immobilized PS molecules.

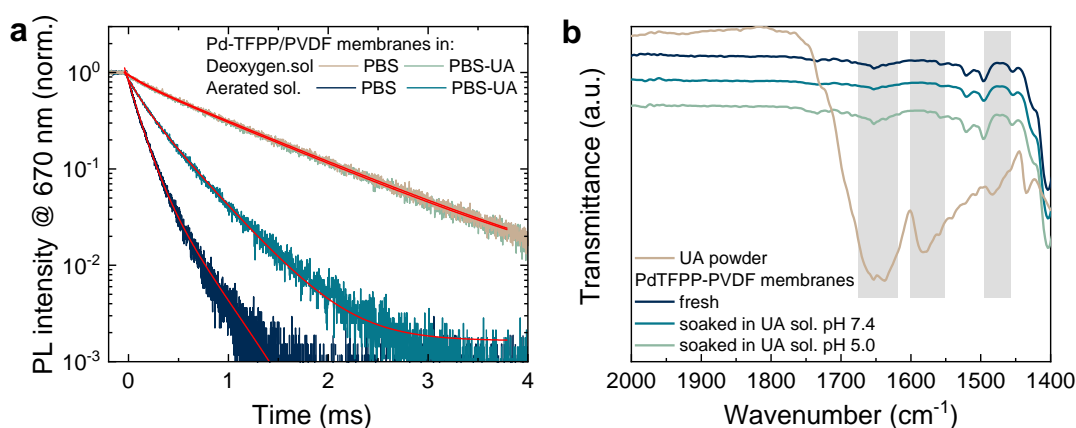


Figure 4.5: **a** PL kinetics of Pd-TFPP/PVDF membranes in deoxygenated and aerated phosphate-buffered saline (PBS, pH 7.4) solutions with and without UA (100  $\mu$ M) and **b**, the FT-IR spectra of Pd-TFPP/PVDF membranes after 16h soaking in UA solutions (50  $\mu$ M). No effect of UA on the PL lifetime and surface composition of used membranes.

The negligible effect of UA on PL decay is consistent with the lack of adsorption of UA on the PVDF membrane. Non-specific (hydrophobic) and electrostatic (due to attraction of UA molecules to PCM surface) interactions are excluded, because the UA molecule is hydrophilic and negatively charged ( $pK_a = 5.4$ ). Figure 4.5b supports this claim by showing the FTIR spectra of Pd-TFPP/PVDF membranes soaked for 16 h in solutions with both neutral (pH 5.0) and negatively charged UA (pH 7.4). The membranes exposed to UA solutions do not exhibit the broad IR absorption bands assigned to UA ( $1650, 1582, 1483 \text{ cm}^{-1}$ ). It is also expected that the absence of UA adsorption extends to the pore volume level of the membrane. If the mechanism of surface oxidation is excluded, only the relatively long diffusion path of  $^1\text{O}_2$  ( $l_{3D} \sim 270 \text{ nm}$  before the relaxation to  $^3\text{O}_2$ )<sup>361</sup> can allow efficient diffusion into the bulk pore volume (mean pore size of the membrane is 200 nm) and subsequent reaction with mobile pollutants.

UA bleaching experiments can support the above-mentioned hypothesis that oxidation can occur in solution. For that purpose, the photocatalytic filtration set-up (see Figure 3.4c) operated in a dead-end filtration regime was employed following the experimental protocol (see Table 3.6). The reaction between UA and  $^1\text{O}_2$  molecules leads to UA bleaching (loss of absorbance), which is monitored by an in-line connected spectrophotometer. Typically, the results of such an experiment are visualized as the evolution of solute concentration in the permeate over the experiment's run time, as depicted in Figure 4.6. The initial phase of the experiment is characterized by an increase of permeate concentration until saturation (called "breakthrough curve"). When steady-state conditions are reached (for UA in less than one hour), the light source is switched on, and the concentration of the pollutant decays to a steady-state value ( $c_{p,ss}$ ). Given the specificity of the UA trap molecule and the lack of interaction with the PCM surface, the observed bleaching of UA in the membrane pore volume suggests  $^1\text{O}_2$ -induced character.

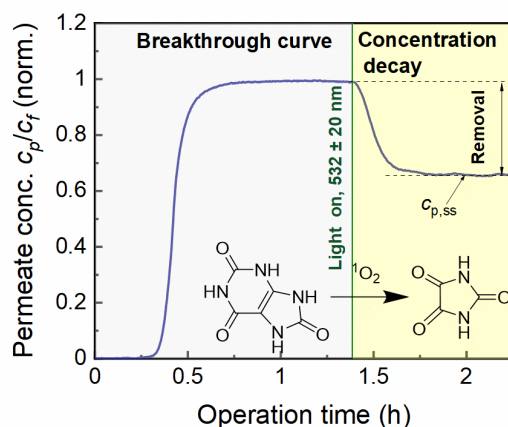


Figure 4.6: Concentration profile in a photocatalytic experiment using Pd-TFPP/PVDF membranes based on the oxidation of uric acid (UA,  $10 \mu\text{M}$ ) as the  $^1\text{O}_2$  trapping agent ( $J_w = 30 \text{ L m}^{-2} \text{ h}^{-1}$ ,  $\bar{q}_{PS} = 0.21 \mu\text{mol cm}^{-2}$ ,  $I_{inc} = 21 \text{ mW}\cdot\text{cm}^{-2}$ ).

### 4.3.2 Methylene Blue as a Model Pollutant in Photocatalytic Experiments

The role of electrostatic interaction between PS-coated membrane surfaces and pollutants can be significant with respect to the photochemical reaction rate. Measuring the  $\zeta$ -potential of a membrane surface can yield information about its surface charge and thus about the likelihood of interaction with solutes. Figure 4.7a displays that the pristine and hydrophobic PVDF membrane have a negative charge over almost the entire pH range (isoelectric point at pH 3.8). Coating the membrane with hydrophobic Pd-TFPP does not alter the surface charge range ( $pH_{IEP} 3.4$ ). Notably, the MB dye – recommended for gauging the activity of photocatalytic membranes<sup>359</sup> – has a  $pK_a$  of 3.2–3.3 and hence is positively charged at pH 4–10.

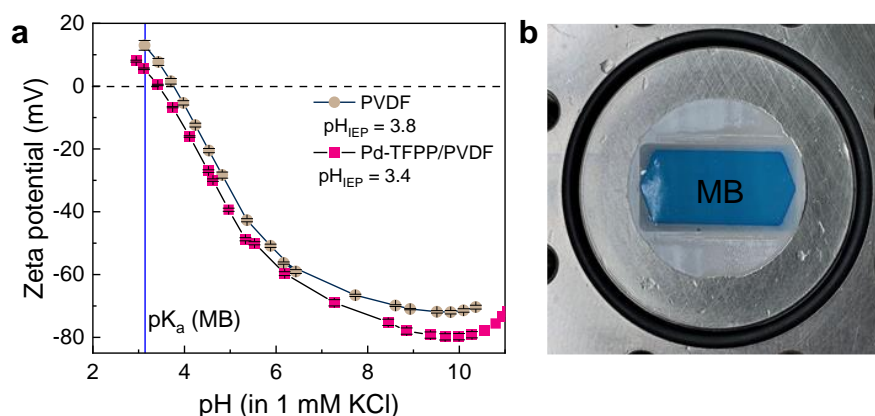


Figure 4.7: Zeta potential of pristine and Pd-TFPP-coated PVDF membranes as a function of solution pH (in 1 mM KCl) with the provided isoelectric point ( $pH_{IEP}$ ) and **b**, a photograph of a PVDF membrane after 5 h filtration of MB solution ( $1 \text{ mg L}^{-1}$ , pH 6.0) at water flux  $60 \text{ L m}^{-2} \text{ h}^{-1}$ .

The electrostatic interaction between the positively charged MB and the negatively charged membrane leads to significant adsorption, which is evidenced by the appearance of blue color on the tested membrane (Figure 4.7b). Remarkably, MB can turn a PVDF membrane into an active PCM when adsorbed. Figure 4.8 exhibits that, depending on the light source, the photolysis (light-induced self-degradation using a pristine membrane) can be either a side process or the dominating channel of MB removal. As shown in Figure 4.8a, the direct excitation of MB adsorbed on the PVDF membrane by broad-band wLED light results in strong MB photolysis (55%) that contributes to MB degradation via immobilized Pd-TFPP (84%). These findings confirm that the use of solar irradiation is sufficient to drive the photocatalytic process. However, the evaluation of the activity of novel photocatalytic materials (for example, PCM) using MB as a model pollutant demands a light source with a narrow-band emission.

Compared to the results with wLED, MB photolysis (15%) under excitation of PCM with gLED is far from being the dominant process (see Figure 4.8b), which still cannot be neglected because of the existing overlap between the gLED emission and MB absorption spectra (540–700 nm, see also Figure 3.7a). The different distribution of Pd-TFPP on opposite membrane surfaces (see also the ToF-SIMS studies in Figure 4.3b) shows no significant effect on MB removal: difference in removal ( $\Delta R$ ) is  $< 2\%$ . This conclusion follows from the experiments conducted under different PCM orientations in the membrane cell. Hence, the gLED was used as the light source in further experiments to mitigate MB photolysis and ensure excitation of Pd-TFPP via the Q-bands (500–600 nm).

In addition to the issue of MB photolysis, the current literature suggests that some photocatalytic materials may induce a reversible conversion of MB to its reduced colorless form (leucomethylene blue).<sup>362, 363</sup> This photoreversible product can be detected on the UV-Vis absorption spectra at  $\lambda = 256 \text{ nm}$ .<sup>364</sup> However, the permeate samples collected during the experiment under wLED excitation (see Figure 4.9a) do not reveal any new absorption peaks, whereas absorbance at 664 and 292 nm (assigned to MB peaks) is strongly and permanently decreased. Hence, there are no signs of photoreduction of MB to LB.



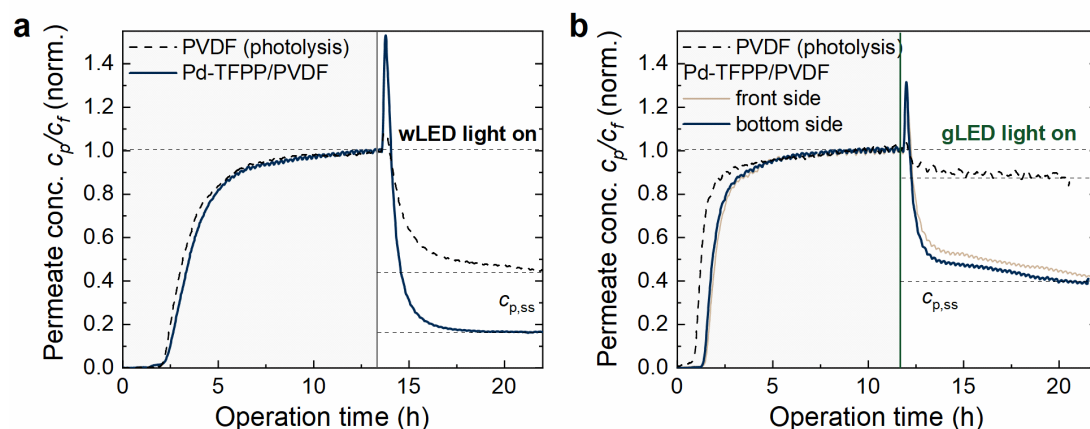


Figure 4.8: Single-pass flow-through oxidation of MB dye using Pd-TFPP/PVDF membranes: **a** wLED excitation ( $81.7 \text{ mW cm}^{-2}$ ) and **b** gLED excitation with different membrane orientations in the membrane cell (front or bottom side as positioned on the shaking plate).  $J_w = 30 \text{ L m}^{-2} \text{ h}^{-1}$ ,  $\bar{q}_{PS} = 0.3 \mu\text{mol cm}^{-2}$ ,  $I_{inc} = 81.7 \text{ mW cm}^{-2}$ ,  $c_{f,MB} = 1 \text{ mg L}^{-1}$ . Grey areas indicate the dark phase (light source off).

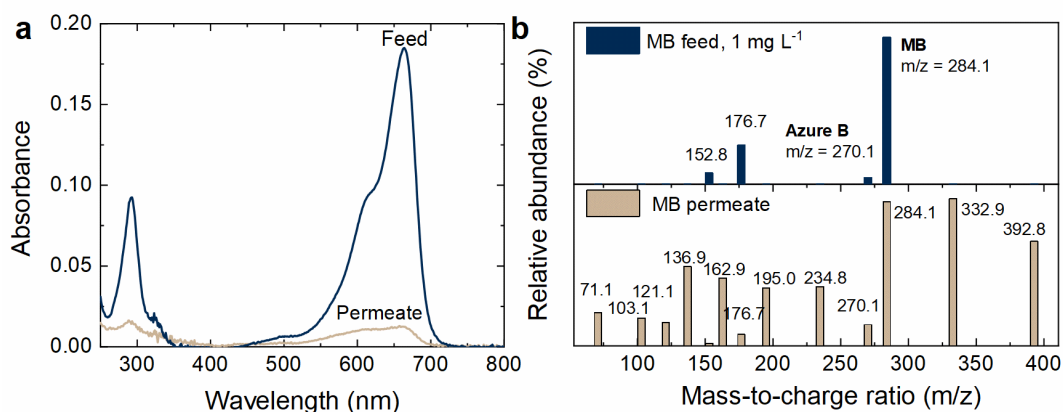


Figure 4.9: **a** UV-Vis absorbance and **b** mass spectra of MB feed ( $1 \text{ mg L}^{-1}$ ) and collected MB permeate after photocatalytic degradation experiment (removal 93%) using wLED light source.

Further evidence of the irreversible nature of the MB degradation using Pd-TFPP/PVDF membranes is provided by mass spectrometry (see Figure 4.9b). Only the parent peaks assigned to MB<sup>+</sup> ( $m/z = 284.1$ ), its impurity (Azure B<sup>+</sup>,  $m/z = 270.1$ )<sup>363</sup> and their fragments ( $m/z = 152.8$  and  $176.7$ ) are found in the feed sample mass spectra. When analyzing the permeate samples with highly degraded MB (about 93%), the MB itself with reduced signal intensity and numerous fragment ions in the range of  $m/z$  71–234 can be detected. Although it is not possible to claim the mineralization of organic solutes in the employed PCM or identify the formed by-products, the detection of several types of degradation byproducts suggests that the oxidation process induced by  $^1\text{O}_2$  is not strictly restricted to one type of byproducts. This conclusion inspires further studies of porphyrin-based PCM, as selective oxidation provided by safe, versatile and sunlight-activated photocatalysts is very much in demand in water treatment.<sup>36</sup>



### 4.3.3 Influence of Process Parameters on the MB Degradation

The photochemical reaction in the PCM-based reactor can be controlled by multiple process parameters. According to their influence, these parameters are conventionally divided into those that affect  $^1\text{O}_2$  generation (PS loading, irradiance) and reactant mass transfer (water flux, pollutant concentration). This section presents the results of photocatalytic studies of removal (effectiveness metric) and the rate of disappearance (efficiency metric), as well as an analysis of the contribution of photolysis. The uncertainty values were defined via an error analysis described in Materials and Methods (Section 3.6.4).

#### *Influence of Porphyrin Loading and Irradiance*

Figure 4.10a exhibits the results of MB degradation when varying the PS loading. At low PS loading ( $\bar{q}_{PS} < 0.1 \mu\text{mol}\cdot\text{cm}^{-2}$ ), MB removal remains at the photolysis threshold ( $14 \pm 3\%$ ) signifying the self-induced degradation of MB as the dominant process. At higher loadings, removal rises with increased loading and reaches ( $75 \pm 14\%$ ) at  $\bar{q}_{PS} = 0.21 \mu\text{mol}\cdot\text{cm}^{-2}$ . At this loading level, the PCM absorbs nearly all photons in the excitation regions of Pd-TFPP (350–450, 500–600 nm) as can be seen in Figure 4.4b. The saturation of light absorption is also consistent with the nearly identical MB degradation curves using PCM with different orientations (see Figure 4.10b).

Higher catalyst loadings ( $0.25\text{--}0.35 \mu\text{mol}\cdot\text{cm}^{-2}$ ) do not increase the MB removal, while the transmembrane pressure rises and the reproducibility of experiments suffers. The mechanism of deterioration of photocatalytic and filtration functions is unclear, so the value of  $\bar{q}_{PS}$  set at  $0.21 \mu\text{mol}\cdot\text{cm}^{-2}$  has been denoted as “standard” for the sake of PS economy without further investigations. Notably, the chosen Pd-TFPP loading has no effect on pure water permeability of a PVDF membrane: ( $7200 \pm 300$ )  $\text{L m}^{-2} \text{h}^{-1} \text{bar}^{-1}$  (pristine) and ( $7100 \pm 250$ )  $\text{L m}^{-2} \text{h}^{-1} \text{bar}^{-1}$  (PCM,  $\bar{q}_{PS} = 0.21 \mu\text{mol cm}^{-2}$ ). This value is about 22% higher than the permeability of a similar commercial membrane ( $5910 \text{ L m}^{-2} \text{h}^{-1} \text{bar}^{-1}$ ) (mean pore size  $0.22 \mu\text{m}$ , GVHP, Millipore).<sup>365</sup> Overall, the trend of removal (in direct correlation with disappearance rate) in continuous-flow experiments using Pd-TFPP/PVDF membranes is slightly different than the linear trend observed in reactors with suspended photocatalyst (see discussion in 2.5.2). It is suggested that light propagation can cause this behavior due to partial blocking of light by adsorbed MB molecules, membrane material, or both.

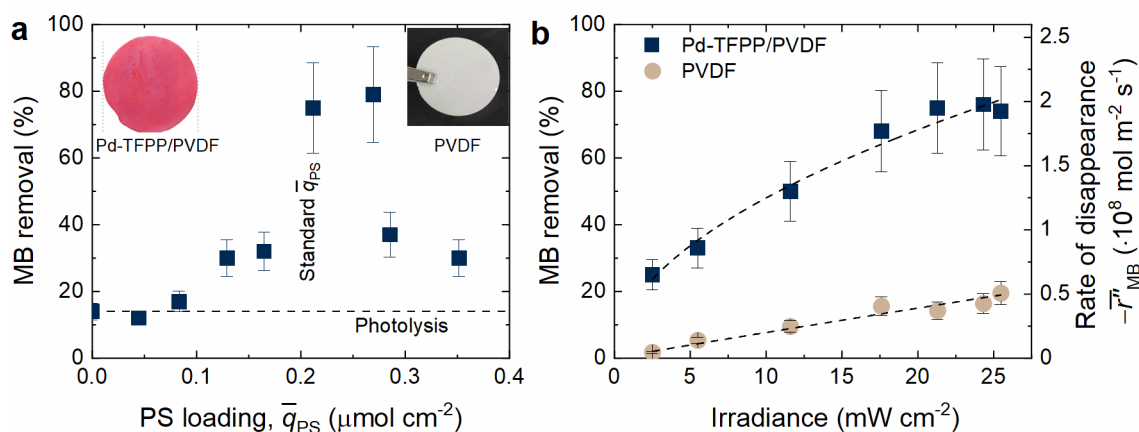


Figure 4.10: Influence of **a** the photosensitizer loading ( $\bar{q}_{PS}$ ) and **b** irradiance on the level of MB removal after the degradation process under single-pass flow-through filtration mode using Pd-TFPP/PVDF and pristine membranes (with their photographs inserted). In graph **a**, the dashed line indicates the photolysis contribution. The dashed lines (graph **b**) are for the visual guideline. Conditions:  $J_w = 30 \text{ L m}^{-2} \text{h}^{-1}$ ,  $I_{inc} = 21 \text{ mW}\cdot\text{cm}^{-1}$  (graph a),  $\bar{q}_{PS} = 0.21 \mu\text{mol cm}^{-2}$  (graph a),  $C_{f,MB} = 1 \text{ mg L}^{-1}$ .

When the mass of photocatalyst is fixed, the degradation process can be controlled by incident irradiance,  $I_{inc}$  (light intensity). The MB removal is proportional to rate of disappearance, so their data sets overlap in Figure 4.10b. MB removal rises linearly with the light intensity from 25% at  $1 \text{ mW}\cdot\text{cm}^{-2}$  up to 75% at  $21 \text{ mW}\cdot\text{cm}^{-2}$  and levels off at  $I_{inc} > 21 \text{ mW}\cdot\text{cm}^{-2}$ ,  $R = (75 \pm 13)\%$ . Similarly, MB photolysis using pristine PVDF membranes increases from 1 to 20% in this range. Its contribution to the overall removal – estimated as the ratio of MB removal using pristine and PCM – remains roughly the same (19–26%) at  $I_{inc} > 11 \text{ mW}\cdot\text{cm}^{-2}$ . This observation underlines the crucial role of the immobilized Pd-TFPP in the photodegradation process at low-to-medium light intensities ( $< 21 \text{ mW}\cdot\text{cm}^{-2}$ ).

As follows from 2<sup>nd</sup> law photochemistry, up to one  $^1\text{O}_2$  molecule per absorbed photon is created. Hence, the linear rise of MB removal with irradiance suggests that the number of absorbed photons also scale linearly until light saturation is reached. This is also observed in previous experiments with different PS loading (Figure 4.10a), where the number of PS molecules affected the number of absorbed photons. Overall, the results depicted in Figure 4.10 show that the reaction rate of photocatalytic decomposition ( $r_{MB}$ ) is proportional to the number of absorbed photons ( $r_{MB} \propto \varphi_{abs}$ ) and related to  $I_{inc}$  as per Equation 4.4:

$$r_{MB} \propto I_{inc}^{\beta} \quad (4.4)$$

At low light intensities, the reaction rate is proportional to the irradiance ( $\beta = 1$ ). When the number of photocatalytic centers (PdTFPP molecules) limits the production of ROS, the trend deviates from linearity ( $\beta < 1$ ). At high  $I_{inc}$ , the  $\bar{r}_{MB}''$  reaches a plateau and becomes independent of the irradiance. This regime is described as mass-transfer limited, where the diffusion of dissolved oxygen, ROS or pollutant molecules become the rate-limiting steps. One of the common practice to accelerate the mass transfer limited process is to increase the velocity in the photoreactor or the molar flux of the depleted reactant.

#### *Influence of Water flux and MB Concentration*

Increasing the water flux from  $30$  to  $300 \text{ L m}^{-2} \text{ h}^{-1}$  (flow rate per filtration area) through the PCM improves the rate of disappearance ( $\bar{r}_{MB}''$ ) by a factor of 2 (Figure 4.11a). In parallel, Figure 4.11b depicts that the MB removal achieved by the end of the photocatalytic process drops by a factor of five (from 75 to 15%). The MB photolysis follows the same trend of decreasing MB removal (from 15% to 2%). The photolysis rate appears to be not affected by water flux ( $\bar{r}_{MB}'' = 0.4\text{--}0.5 \cdot 10^8 \text{ mol m}^{-2} \text{ s}^{-1}$ ), while being 4 to 8 times slower than oxidation process driven by PCM ( $1.9\text{--}3.9 \cdot 10^{-6} \text{ mol}\cdot\text{m}^{-2}\cdot\text{s}^{-1}$ ). The water flux employed in this chapter are up to 100 times lower for PVDF MF membranes but correspond to those applied in nanofiltration process, whereas the transmembrane pressure monitored in the photocatalytic experiments at various feed flow rate through PCM is significantly lower (0–0.4 bar, see Figure A.2).

In PCMs operated in the flow-through regime, the oxidation reactions occur predominantly in the pore volume. Since the contact time (equivalent of  $\bar{t}_{con}$ ) is inversely proportional to the water flux (see also Equation 2.7), the 5-fold decrease in MB removal is associated with a reduction in residence time (from 8.6 to 0.9 s). The effective MB degradation at such extremely low residence time strongly suggests that the external mass transfer in PCM is fast, although one of the diffusion steps can be still rate-limiting. The effects of diffusion and advection in mass transfer can be compared using Péclet number ( $Pe = 0.5\text{--}13.5$  at  $J_w = 30\text{--}300 \text{ L m}^{-2} \text{ h}^{-1}$ , Equation 2.5) or the ratio of the mixing time (calculated from Equation 2.8) to the contact time ( $\bar{t}_{con}$ ).

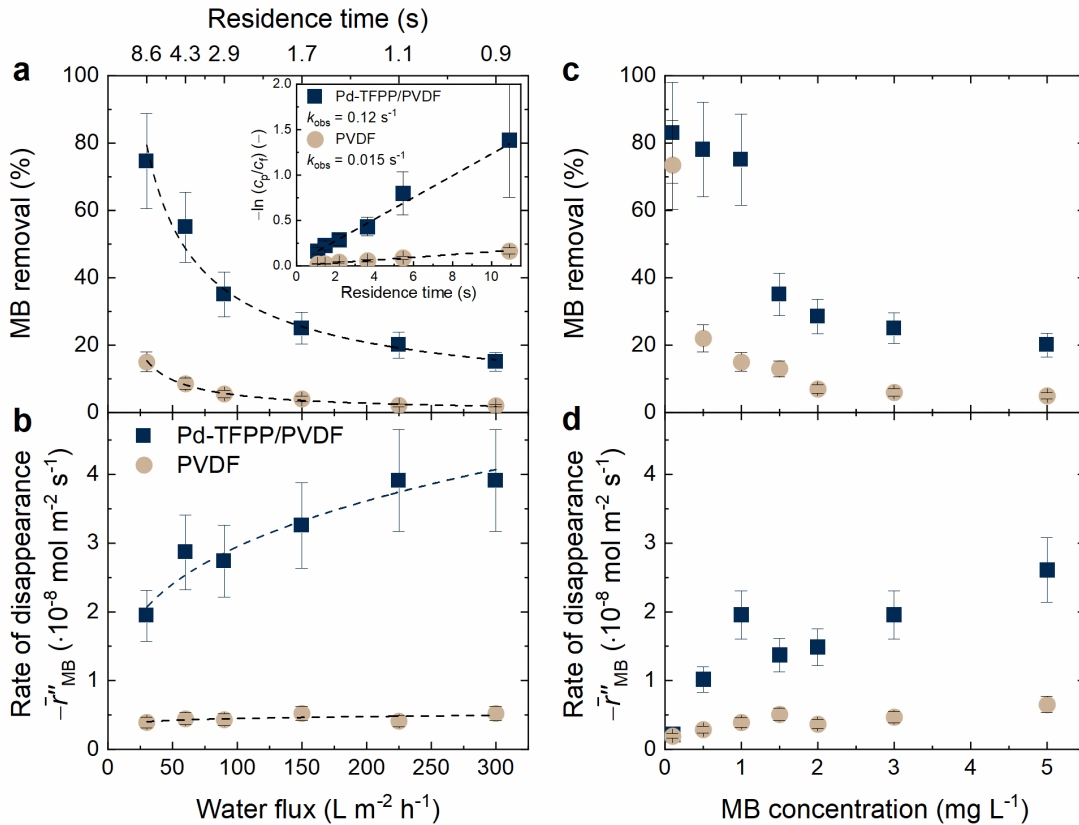


Figure 4.11: Influence of **a,b** the water flux and **c,d** MB concentration on the effectiveness (removal) and efficiency (expressed as a rate of disappearance) of the MB degradation process under single-pass flow-through filtration mode using Pd-TFPP/PVDF and pristine membranes (default parameters:  $J_w = 30 \text{ L m}^{-2} \text{ h}^{-1}$ ,  $\bar{q}_{PS} = 0.21 \mu\text{mol cm}^{-2}$ ,  $I_{inc} = 21 \text{ mW} \cdot \text{cm}^{-2}$ ,  $c_{f,MB} = 1 \text{ mg L}^{-1}$ ). The dashed lines serve as a visual guideline for water flux trend (graphs **a,c**). Inset: the kinetics assessment by linear regression analysis of the logarithmic relative concentration as a function of residence time.

For  $\bar{d}_{por} = 0.2 \mu\text{m}$  (see Table 3.3),  $D_i = 2.1 \cdot 10^{-9} \text{ m}^2 \text{ s}^{-1}$  (oxygen in water)<sup>366</sup> and  $D_i = 0.77 \cdot 10^{-9} \text{ m}^2 \text{ s}^{-1}$  (MB in water),<sup>367</sup> the mixing time of oxygen ( $t_{mix} = 4.8 \cdot 10^{-6} \text{ s}$ ) and MB molecules ( $t_{mix} = 1.3 \cdot 10^{-5} \text{ s}$ ) is 5–6 orders of magnitude shorter than the contact time in the pore volume of MF membrane ( $\bar{t}_{con} = 0.9\text{--}8.6 \text{ s}$ ). Therefore, the mass transfer process is predominately driven by convection and depends on the water flux, as also evidenced by its beneficial effect on  $\bar{r}''_{MB}$  (see also schematic in Figure 2.9). To compensate for the lower removal at high water flux (and short  $\bar{t}_{con}$ ), the concentration of  $^1\text{O}_2$  should be increased. Besides  $^1\text{O}_2$  concentration, PS loading, irradiance or active surface area are other parameters that can be used to increase the effectiveness of the degradation process.

Assuming a constant steady-state  $^1\text{O}_2$  concentration, the MB degradation process can be described by the pseudo-first-order kinetics with respect to the MB pollutant. As shown in the inset of Figure 4.11a, the rate constants for the photolysis and Pd-TFPP-assisted degradation process of MB are estimated to be  $k_{obs} = 0.015 \text{ s}^{-1}$  and  $k_{obs} = 0.12 \text{ s}^{-1}$ , respectively. This result confirms that  $^1\text{O}_2$  generation by immobilized Pd-TFPP is at least one order of magnitude more efficient for the MB degradation than a photolysis process. Note also that these values are 2–3 orders of magnitude higher than in the reported works using both batch and  $\text{TiO}_2$ -coated membrane photoreactors.<sup>267</sup> This finding suggests that the MB degradation process in flow-through regime using PCM is highly efficient and is likely to originate from enhanced mass transfer.

In a real water treatment process, the initial pollutant concentration can fluctuate. This leads to different degradation efficiency at similar operating conditions and residence time. The results of changing the initial MB concentration are displayed in Figure 4.11c,d. MB removal varies between 83% at  $c_{f,MB} = 0.1 \text{ mg}\cdot\text{L}^{-1}$  to 20% at  $5 \text{ mg}\cdot\text{L}^{-1}$  (50 times higher concentration), while the  $\bar{r}_{MB}''$  rises from  $0.2\cdot 10^{-8}$  to  $2.6\cdot 10^{-8} \text{ mol m}^{-2} \text{ s}^{-1}$  in this range of concentrations.

Removal and the rate of disappearance of the photolysis process are relatively lower than those obtained using PCM, whereas their trends are similar. The MB removal using pristine and Pd-TFPP-coated PVDF membranes is comparable (74% against 83%) at very low MB concentrations ( $0.1 \text{ mg L}^{-1}$ ). However, drawing solid conclusion about the degradation efficiency is difficult at low concentration ( $<0.5 \text{ mg}\cdot\text{L}^{-1}$ ) close to the detection limit of the analytic instrument (in-line UV-Vis spectrophotometer). Remarkably,  $\bar{r}_{MB}''$  is as high as the water flux or MB concentration in solution suggesting that both parameters affect the reactant molar flux (in  $\text{mol}_{MB} \text{ L}^{-1} \text{ s}^{-1}$ ) and hence the mass transfer. Note that the highest removal is achieved at low MB concentration ( $<1 \text{ mg}\cdot\text{L}^{-1}$ ), which makes the process promising for potential treatment of micropollutants. This topic will be discussed in the Chapter 5.

## 4.4 Stability of Pd-TFPP/PVDF Membranes

A relevant criterion of the broader development and successful application of PCMs is their stability under different environmental conditions (light, humidity, physical and oxidative-agent stress). However, organic photocatalysts – in particular photosensitizers – are prone to photobleaching under prolonged exposure to light and oxidative agents. Photographs of porphyrin-coated membranes demonstrate that shear flow ( $J_w = 150 \text{ L m}^{-2}\text{h}^{-1}$ ) of Milli-Q water does not change the color in the central region of Pd-TFPP coated membranes (see Figure 4.12a,b). This finding suggests that the hydrophobic interaction is strong enough for the hydrophobic PdTFPP molecules to firmly attach to the PVDF membrane surface. In the contrary, the central area of the membranes exposed to both light and water flow for 14 h darkens as observed right the experiments Figure 4.12c,d. Note that the color change from pink to green-ish is much more prominent in the dried PCM state.

Structural and visual changes are correlated using FT-IR spectra of dried and aged PCM (Figure 4.12e). Despite the generally similar shape of IR absorption spectra, new absorption bands with peaks at  $1730$  and  $1653 \text{ cm}^{-1}$  are observed in the aged samples and assigned to carbonyl (C=O) stretching vibration. This result suggests that one of the components of PCM (membrane or PS) undergoes an oxidative transformation, when exposed to prolonged light irradiation. This conclusion is confirmed by the UV-Vis spectra recorded after dissolution of the freshly prepared and aged PCM (Figure 4.12f). The Pd-TFPP absorbance at the main Q-band ( $\lambda = 518 \text{ nm}$ ) and hence  $\bar{q}_{PS}$  drops by 35% (from  $0.21$  to  $0.14 \mu\text{mol cm}^{-2}$ ) after 14 h light illumination with gLED ( $21 \text{ mW cm}^{-2}$ ). Notably, new absorption bands with peaks at  $582$ ,  $606$  and  $662 \text{ nm}$  appear, indicating the photochemical transformation of Pd-porphyrin to unknown porphyrinoid products. Metabolites of porphyrin degradation known to result in a red shifting of the Q-band absorption are chlorins and bacteriochlorins,<sup>368</sup> which are formed via oxidation of the double bond in the pyrrole ring.

Indeed, the mass spectra of the dissolved photobleached membrane reveal the new compounds with a mass-to-charge ratio close to the chlorin ( $m/z = 1096.1, \text{ M}^-$ ) or bacteriochlorin derivatives ( $m/z = 1110.0, \text{ M}^-$ ) of Pd-TFPP ( $m/z = 1078.0, \text{ M}^-$ ) as shown in Figure 4.13a. The suspected by-products retain their hydrophobic structure (hence remain attached to the membrane) and can efficiently generate various ROS, including  $^1\text{O}_2$ .<sup>207, 215</sup> Figure 4.13b provides evidence for the suggested claim. The decay of PL signal of i) fresh, ii) exposed to ultrapure water filtration, and iii) water flow combined with gLED illumination ( $I_{inc} = 25 \text{ mW cm}^{-2}$ , 24 h) result in a similar PL lifetime in deoxygenated water ( $0.732$ ,  $0.692$ , and  $0.730 \text{ ms}$ , respectively).

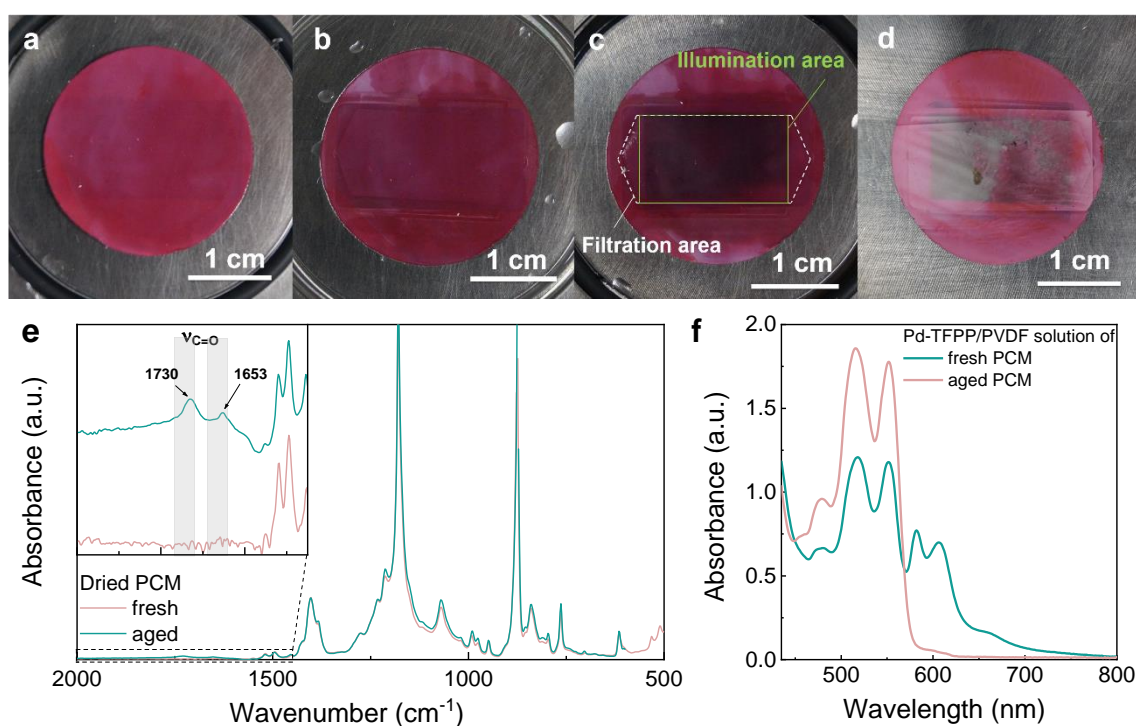


Figure 4.12: Photographs of moist (a-c) and dried (d) Pd-TFPP/PVDF membranes ( $q_{PS} = 0.21 \mu\text{mol cm}^{-2}$ ): a freshly prepared, b exposed to 6 h water filtration, and c,d exposed to 14 h gLED illumination,  $\lambda_{\text{exc}} = (532 \pm 20) \text{ nm}$ ,  $I_{\text{inc}} = 21 \text{ mW cm}^{-2}$  when mounted to the PCM cell. e FT-IR spectra and f UV-vis absorption spectra of fresh and aged PCM (after 14 h light illumination). The inset: the magnified region of the IR spectra (2000–1450 cm<sup>-1</sup>).

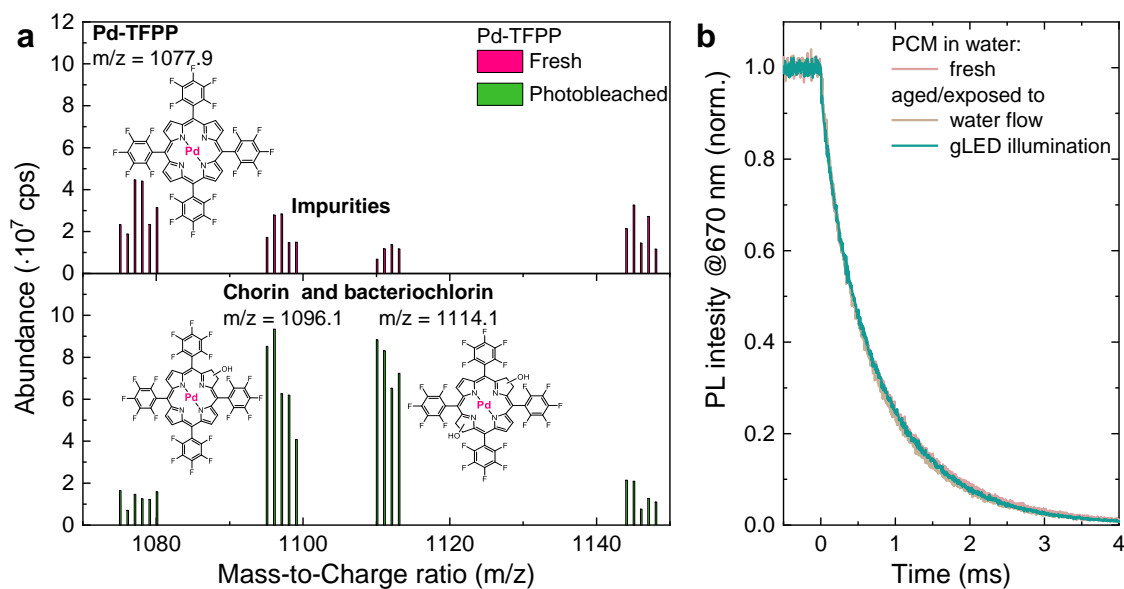


Figure 4.13: a Mass spectra of Pd-TFPP and its photoproducts. b The PL decay curves measured at 670 nm for fresh PCM and exposed to flow-through water filtration (2 h,  $J_w = 150 \text{ L m}^{-2} \text{ h}^{-1}$ ) and simultaneous 24 h filtration ( $J_w = 150 \text{ L m}^{-2} \text{ h}^{-1}$ ) and irradiation with gLED light ( $\lambda_{\text{exc}} = 25 \text{ mW cm}^{-2}$ ).

A final proof that the porphyrin-like photoproducts do not deteriorate the photocatalytic activity of the PCM in the long term is obtained by conducting an extended (90 h) photocatalytic experiment in a single-pass, continuous mode (Figure 4.14). Note that the photocatalytic membrane reactor is continuously fed with fresh MB solution at every moment of the experiment without reuse of MB solution. Upon turning on the gLED, the MB concentration in the permeate sharply decreases by 60% ( $c_p/c_f = 0.4$ ) and remains at this level until the runtime reaches 20 h. Surprisingly, the performance of MB removal improves ( $\Delta R = 17\%$ ) over the remaining 80 h (permeate volume  $V_p = 490$  mL) as observed by a decrease of the MB concentration in the permeate. The control experiment conducted in the dark exhibits only the extended MB breakthrough curve followed by the drift of the spectrophotometer baseline. Note that the PCM with an active area of only  $2 \text{ cm}^2$  enables treatment of around 520 mL without pronounced decrease in photocatalytic performance.

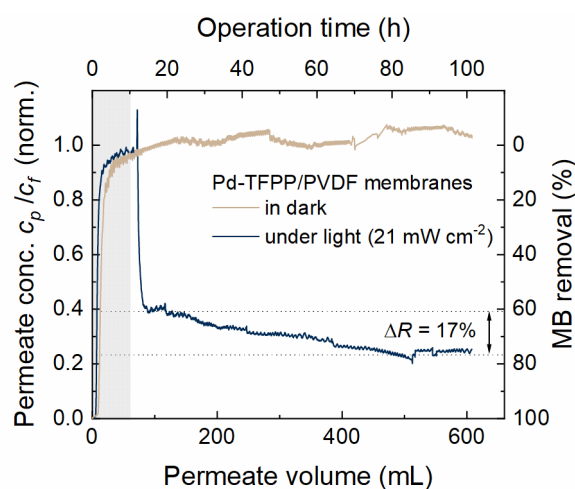
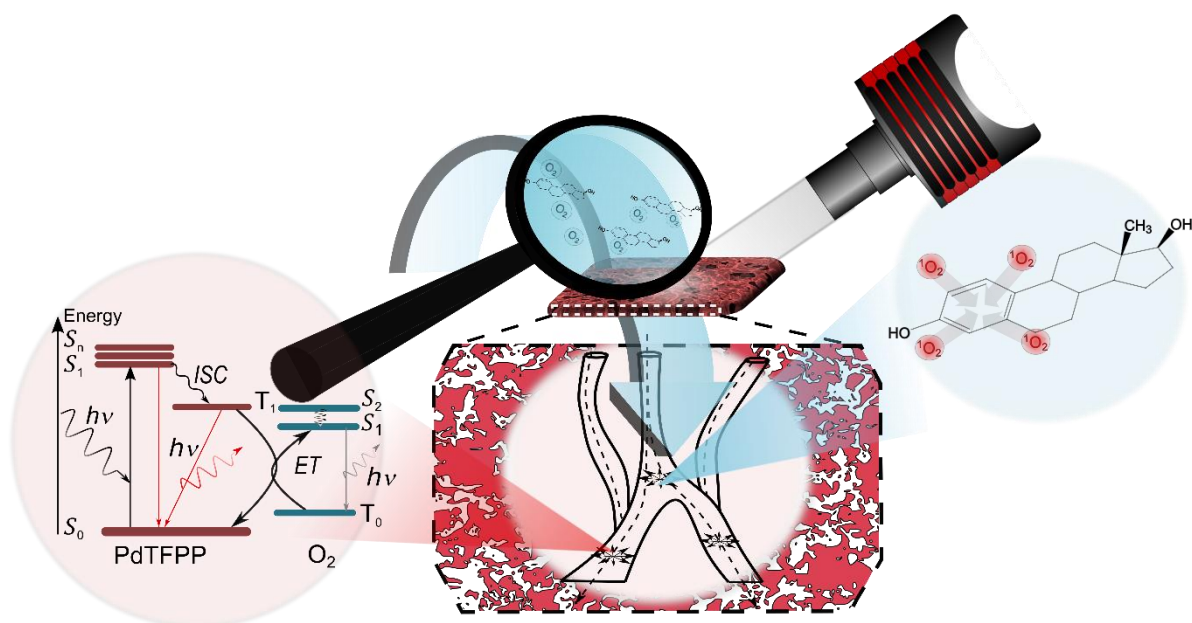


Figure 4.14: Prolonged performance stability test using Pd-TFPP/PVDF membranes in the dark and under gLED exposure ( $J_w = 30 \text{ L m}^{-2} \text{ h}^{-1}$ ,  $\bar{q}_{PS} = 0.21 \text{ } \mu\text{mol cm}^{-2}$ ,  $I_{inc} = 21 \text{ mW cm}^{-2}$ ,  $c_{f, MB} = 1 \text{ mg L}^{-1}$ ). Note that the change of  $c_p/c_f$  in the dark after  $V_p$  above 50 mL is due to the baseline drift of a spectrophotometer.

## 4.5 Summary

This chapter showed that the photocatalytic active membranes can be prepared by a facile impregnation method, which also enables coating of the internal membrane surface. After adsorption on a PVDF membrane, Pd-porphyrin retains the ability to be excited with visible light, whereas the membrane properties remain largely unchanged. Due to the long triplet lifetime ( $\langle \tau_T \rangle = 0.74 \text{ ms}$ ) and efficient quenching by molecular oxygen ( $\langle \tau_T \rangle / \langle \tau_T^0 \rangle = 0.81$ ), the porphyrin chromophores can effectively produce singlet oxygen, which is also confirmed by studies on bleaching of uric acid and methylene blue. The Pd-porphyrin-coated membranes exhibit excellent photocatalytic performance reaching up to 83% removal of MB in a single-pass continuous-flow membrane reactor in less than 9 seconds. Such a superior degradation performance is attributed to enhanced external mass transfer and can last up to several days of continuous-flow feeding of MB solution. These exciting results provide a solid foundation for the degradation of real micro-pollutants such as steroid hormones, which will be the main theme of the following chapters.

# 5 Pd-Porphyrin-Loaded Membranes for SH Removal



The contents of this chapter have been published in the separate work. Figures and Tables have been adapted with permission from Lyubimenko, R. et al. (2021),<sup>341</sup> Copyright 2021 Elsevier. The citations in the following text are omitted.

**Lyubimenko, R.;** Gutierrez Cardenas, O. I.; Turshatov, A.; Richards, B. S.; Schäfer, A. I.; *Appl. Catal. B: Environ.*, 291 (2021) 120097.

## *Acknowledgments and Contributions*

The methodology, design of experiments was prepared by the author of the dissertation and Andrea I. Schäfer. The initial experiments were conducted by Oscar I. Gutierrez within the scope of a master project, who also contributed to the writing of the original paper draft. Data validation was ensured by the present author. Data analysis was performed by the author with assistance from Andrey Turshatov, Bryce S. Richards, and Andrea I. Schäfer.

## 5.1 Introduction

The process of steroid hormone (SH) abatement at environmentally relevant levels is complicated with micropollutant analysis and inherently slow mass transfer in photoreactors with the fixed photocatalyst. The former issue can be solved by scintillation methods, which enable the steroid hormone analysis at extremely low detection limits ( $1 \text{ ng L}^{-1}$ ) without time-consuming preparation steps. The efficient generation of singlet oxygen within the nanoscale space render porphyrin-impregnated membranes extremely attractive for overcoming the second challenge. The relatively long three-dimensional diffusion length ( $l_{3D} = \sim 270 \text{ nm}$ )<sup>361</sup> of the  $^1\text{O}_2$  suggests that its reaction with steroid hormone molecules is not spatially confined to the pore walls and can also occur in the pore space of a microfiltration membrane (mean pore size of 200 nm). Hence, the question arises whether SH micropollutants can be removed as effectively as MB dye, despite the  $10^4$ -fold difference in concentration.

### Objectives

The following objectives were outlined in this chapter:

- i. Evaluate the degree of removal of steroid hormone micropollutants using Pd-porphyrin-coated MP200 membranes in a single-pass mode;
- ii. Provide the implications of changing the operating parameters (light intensity, water flux) on the removal and kinetics of the photocatalytic degradation process;
- iii. Gauge the impact of water quality and the feed solution components on the efficacy of the photocatalytic process.

A short summary with key results concludes the chapter.

### Modification of the Experimental Filtration System

The modified experimental system (see Figure 3.4a,b) ensured the compliance with the revised experimental protocol (see also Table 3.7). For excitation of Pd-TFPP/PVDF membranes, the wLED was selected instead of the previously used gLED (see Chapter 5) due to: i) high intensity in the visible part of the solar spectrum ( $I_{inc, max} = 550 \text{ mW cm}^{-2}$ ); ii) rough match to the air-mass 1.5 global (AM1.5 g) solar spectrum (AM1.5g was adopted here as the reference standard from the field of photovoltaics), and iii) improved coverage of the absorption bands of Pd-porphyrin; iv) lack of photolysis of steroid hormones under the visible light illumination and v) relatively long lifetime ( $>10000 \text{ h}$ ). The normalized incident photon flux and current-irradiance calibration curves can be found in Figure 3.8b and Figure 3.9.

The steroid hormone analysis was performed off-line by the UHPLC-FSA and LSC methods (see Figure 3.16 for calibration curves). Hence, the 16-port-switching valve ② was incorporated into the experiment set-up from the permeate outlet side of the membrane cell to aid in autonomous permeate sampling. At preset intervals, the valve diverted the permeate flow into sample vials (1.5 mL), which were held in a 3D-printed 16-well rack ③.



## 5.2 The Effect of Process Parameters on SH Degradation

### 5.2.1 Change in 17 $\beta$ -estradiol Degradation during a Prolonged Run

For calculation of degradation performance metrics, it is necessary to know when the 17 $\beta$ -estradiol concentration in the permeate reaches a steady state. After changing the type of pollutant and operating conditions, the duration of experiment that will provide steady-state conditions is unknown. This information, however, can be taken from a typical photocatalytic run extended to 7 days (Figure 5.1), provided that the Pd-porphyrin loading is kept the same as in the previous studies (see Section 4.3). An experiment starts with a dark phase that ensures the saturation of SH adsorption to a membrane. Once 100 mL of permeate is collected, the porphyrin-coated membranes are illuminated with a wLED light source. The normalized 17 $\beta$ -estradiol concentration in the permeate plummets, reaching  $c_p/c_f = (0.1 \pm 0.06)$  at  $V_p = 125$  mL, and then gradually rises until 800 mL of permeate is produced. Within the remaining 100 h of experiment ( $V_p = 1200$  mL), the 17 $\beta$ -estradiol concentration in the permeate remains in the range of  $c_p/c_f = 0.31 \pm 0.09$ , equivalent to removal,  $R = (69 \pm 9)\%$ . As steady state of the process is achieved in the range of  $V_p = 650$ –800 mL, all further experiments will be run until 700 mL of permeate is accumulated.

The mechanism behind deterioration of 17 $\beta$ -estradiol degradation performance over the experiment time is not fully understood. A similar trend of  $c_p/c_f$  was observed for TiO<sub>2</sub>-coated polyethersulfone membranes.<sup>340</sup> The two most plausible hypotheses to explain the phenomenon are: i) the change of equilibrium adsorption capacity for 17 $\beta$ -estradiol molecules at the PCM surface; ii) the change in activity of immobilized photosensitizer. Equilibrium adsorption capacity affects surface coverage, which in case of heterogenous reaction can be the rate-limiting factor. It is doubtful that porphyrin photobleaching is solely responsible for the results presented in Figure 5.1. As previously shown in Chapter 4, the degradation of methylene blue dye by Pd-TFPP/PVDF membranes was not significantly altered by prolonged illumination.

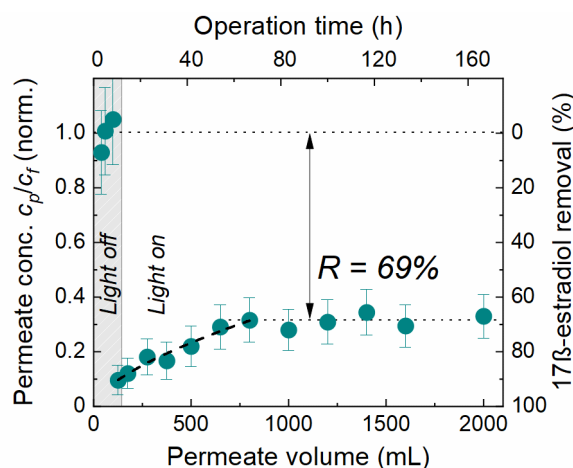


Figure 5.1: Evolution of normalized 17 $\beta$ -estradiol concentration and respective removal as a function of permeate volume (linked to operation time). The grey area indicates the dark phase (wLED off). The dotted lines serve for estimation of removal. Conditions:  $\bar{q}_{pS} = 0.21 \mu\text{mol cm}^{-2}$ ,  $c_f = 100 \text{ ng L}^{-1}$  in 1 mM NaHCO<sub>3</sub>, 10 mM NaCl background solution,  $c_f(\text{O}_2) = 8.5 \text{ mg L}^{-1}$ ,  $J_w = 60 \text{ L m}^{-2} \text{ h}^{-1}$ ,  $I_{inc} = 1.6 \text{ mW cm}^{-2}$ .

### 5.2.2 Influence of Water flux on the Degradation Performance

Figure 5.2a outlines the results of experiments conducted at various water flux using the modified protocol.

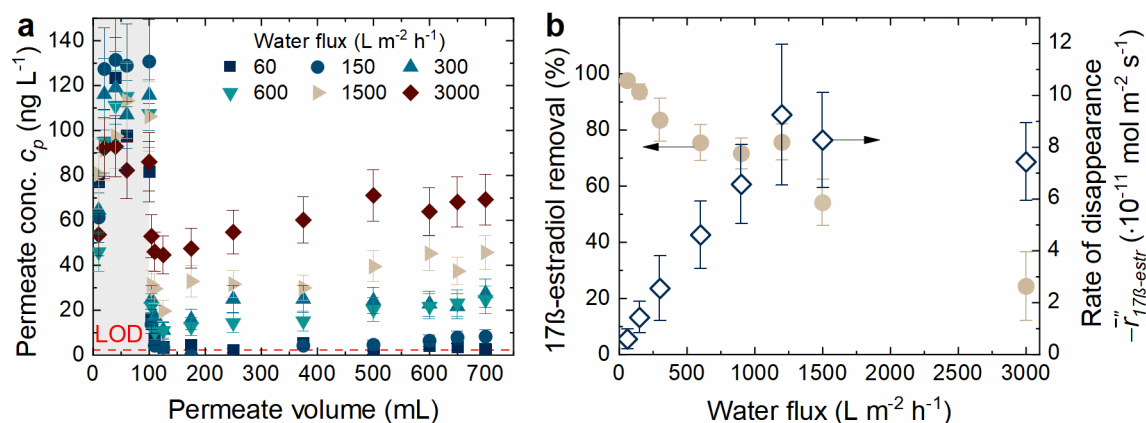


Figure 5.2: Influence of water flux on the process of 17 $\beta$ -estradiol photocatalytic degradation. **a** Evolution of 17 $\beta$ -estradiol permeate concentration with permeate volume; **b** 17 $\beta$ -estradiol removal and the corresponding rate of disappearance plotted against the water flux. Conditions:  $c_f = (100 \pm 10) \text{ ng L}^{-1}$ , background solution of 1 mM NaHCO<sub>3</sub>, 10 mM NaCl, pH = 8.6  $\pm$  0.4,  $c_f(\text{O}_2) = (8.5 \pm 0.4) \text{ mg L}^{-1}$ ,  $I_{\text{inc}} = 10.0 \text{ mW cm}^{-2}$ .

Similar to the results shown in Figure 5.1, the 17 $\beta$ -estradiol concentration in the permeate sharply decreases upon illumination of PCM and then crawls up throughout the experiment with the relatively fixed rising slope. Note that the concentration in the permeate is reduced to the detection limit of the analytical instrument (LOD = 1.7 ng L<sup>-1</sup>) at the lowest feed water flux (60 L m<sup>-2</sup> h<sup>-1</sup>).<sup>123</sup> This degree of degradation is close to the guideline value for 17 $\beta$ -estradiol proposed by European Union (1 ng L<sup>-1</sup>).<sup>15</sup>

Figure 5.2b exhibits that decrease in water flux from 3000 to 60 L m<sup>-2</sup> h<sup>-1</sup> improves the 17 $\beta$ -estradiol removal by a factor of four (from 24% to 98%) as estimated from the  $c_p/c_f$  at the end of experiment ( $V_p = 700 \text{ mL}$ ). The improved removal at lower water flux is associated with a longer residence time in the PCM. This relation ( $J_w \propto 1/\bar{t}_{\text{con}}$ ) is consistent both with the other works using PMR<sup>369, 370</sup> and the results shown in Chapter 4. The Pd-TFPP/PVDF membranes operated under  $J_w = 60\text{--}3000 \text{ L m}^{-2} \text{ h}^{-1}$  achieve the similar or higher 17 $\beta$ -estradiol removal compared to nanofiltration membranes ( $J_w = 50 \text{ L m}^{-2} \text{ h}^{-1}$ ).<sup>371</sup>

In contrast, rate of disappearance continuously increases with the water flux until finally levelling off in the range of  $\bar{r}''_{17\beta\text{-estr}} = 7 \cdot 10^{-11}\text{--}9 \cdot 10^{-11} \text{ mol m}^{-2} \text{ s}^{-1}$  (see also Figure 5.2b). The influence of hydrodynamic regime in a reactor (via stirring, velocity or temperature) on reaction rate marks the mass-transfer-limited reactions. Hence, it is assumed that the increased velocity (= water flux) through the Pd-TFPP/PVDF membranes promotes the mass transfer of 17 $\beta$ -estradiol and O<sub>2</sub> molecules to the immobilized PS. Note that the water flux in a PCM affects two parameters (residence time and volumetric mass transfer coefficient), which are in a trade-off with it. Thus, the appearance of a plateau at high water flux ( $J_w > 1200 \text{ L m}^{-2} \text{ h}^{-1}$ ) indicates that the enhanced mass-transfer no longer compensates for the reduced residence time.<sup>235</sup>

Figure 5.3 depicts the exponential growth of  $\bar{r}''_{17\beta\text{-estr}}$  with reducing residence time via water flux. Yet, reducing the residence time beyond a certain limit ( $\bar{t}_{\text{con}} < 0.21 \text{ s}$ ) does not further improve the reaction rate. This finding is also reflected in the kinetic plot, namely the change of logarithm of normalized concentration with time. The 17 $\beta$ -estradiol degradation process cannot be described by the first-order reaction kinetics (no linear relationship). The concentration decay is assumed to reach steady state within the PCM faster than the given residence time. Hence, the  $k_{\text{obs}}$  must be estimated exclusively from the studies conducted at fixed water flux as will be detailed in the next section. For that, the water flux of 600 L m<sup>-2</sup> h<sup>-1</sup> is selected based on the trade-off between 17 $\beta$ -estradiol removal and  $\bar{r}''_{17\beta\text{-estr}}$ .

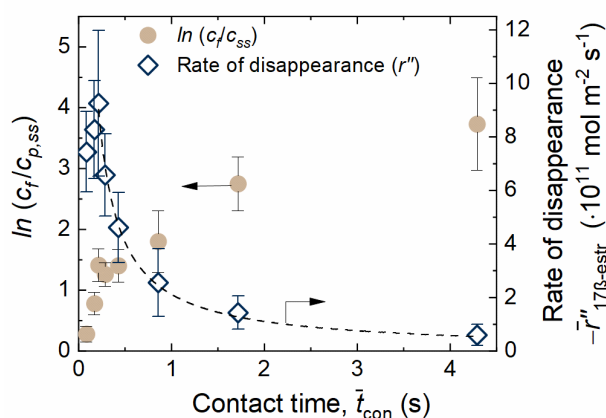


Figure 5.3: Logarithm of normalized permeate concentration and the  $\bar{r}''_{17\beta-estr}$  plotted against the mean contact time. The dashed line (reciprocal fit) represents an eye guideline for  $\bar{r}''_{17\beta-estr}$  data

### 5.2.3 Implications of Studies of 17 $\beta$ -Estradiol Concentration in the Feed

As mentioned above, the rate of photocatalytic degradation of 17 $\beta$ -estradiol using Pd-TFPP/PVDF membranes is mass-transfer controlled at  $J_w < 1200 \text{ L m}^{-2} \text{ h}^{-1}$  and in the  $\text{ng L}^{-1}$  concentration range. The diffusional transport of pollutant to the photocatalyst is affected by its initial (bulk) concentration. Figure 5.4a shows the results of the photodegradation studies using 17 $\beta$ -estradiol concentrations ranging from detection to solubility limit (reached by spiking non-labeled 17 $\beta$ -estradiol prepared in methanol).

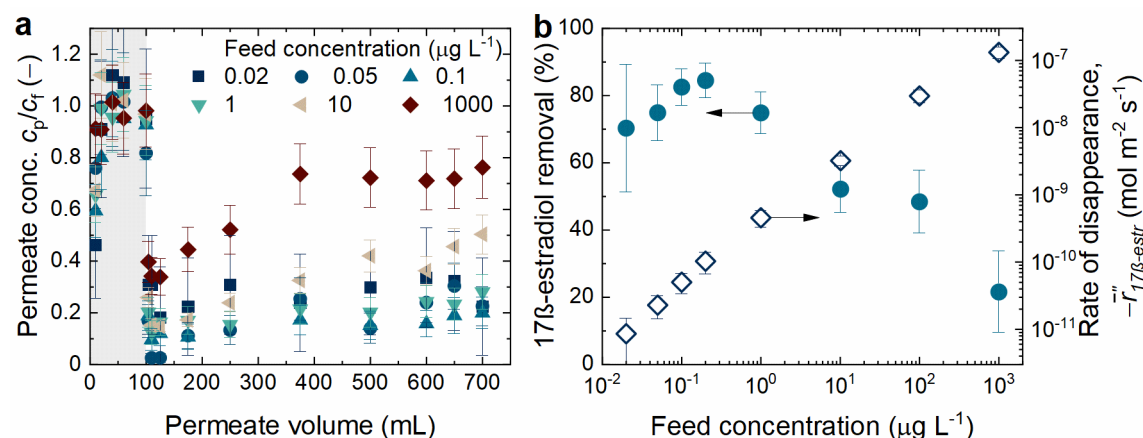


Figure 5.4: Influence of feed concentration on the process of its photocatalytic degradation. **a** Evolution of normalized 17 $\beta$ -estradiol concentration in the permeate as a function of permeate volume, **b** removal and **c** the corresponding  $r''$  versus 17 $\beta$ -estradiol feed concentration. Conditions: background solution of 1 mM  $\text{NaHCO}_3$ , 10 mM  $\text{NaCl}$ ,  $\text{pH} = 8.6 \pm 0.4$ ,  $c_f(\text{O}_2) = 8.5 \pm 0.4 \text{ mg L}^{-1}$ ,  $J_w = 600 \text{ L m}^{-2} \text{ h}^{-1}$ ,  $I_{nc} = 10.0 \text{ mW cm}^{-2}$ .

Similar to the studies of water flux, the initial drop of 17 $\beta$ -estradiol concentration in the permeate is followed by a gradual rise throughout the experiment. Note that the rising slope of  $c_p/c_f$  is more pronounced at high 17 $\beta$ -estradiol concentrations ( $> 1 \mu\text{g L}^{-1}$ ), whereas the steady-state conditions may be not reached. Figure 5.4b depicts the removal of 17 $\beta$ -estradiol estimated from its steady-state concentration in the permeate. At environmentally relevant concentrations ( $c_f < 1 \mu\text{g L}^{-1}$ ), there is a persistently high removal

of 17 $\beta$ -estradiol ( $R = 70\text{--}85\%$ ). In more concentrated solutions, the removal of 17 $\beta$ -estradiol drops, showing the lowest performance of 17 $\beta$ -estradiol degradation at  $1\text{ mg L}^{-1}$ ,  $R = (22 \pm 13)\%$ . Unlike the trend of removal, rate of disappearance –plotted also in Figure 5.4b – rises monotonically over four orders of magnitude when increasing the 17 $\beta$ -estradiol concentration in the feed solution from  $0.02$  to  $1000\text{ }\mu\text{g L}^{-1}$ . Furthermore, the enhanced effect of 17 $\beta$ -estradiol concentration and water flux are somewhat similar until a certain point ( $J_w < 1200\text{ L m}^{-2}\text{ h}^{-1}$ ). Figure 5.5a clearly exhibits the same effect of the water flux and feed concentration on the disappearance rate of 17 $\beta$ -estradiol when the both data sets are converted to solute molar flux ( $J_s$ ,  $\text{mol m}^{-2}\text{ s}^{-1}$ ). Both parameters are combined into a single parameter, the solute molar flux ( $J_s = J_w \cdot c_f$ ). The growth trends of rate of disappearance overlap until a certain value ( $J_s = 2 \cdot 10^{-10}\text{ mol m}^{-2}\text{ s}^{-1}$ ). At higher solute molar flux, the difference in  $\bar{r}''_{17\beta\text{-estr}}$  is more distinct, as the residence time becomes a limiting factor of degradation. This limitation can be however overcome by increasing irradiance as evidenced by the  $\bar{r}_{17\beta\text{-estr}}$  plateau occurring at higher water flux (as demonstrated in Chapter 7).

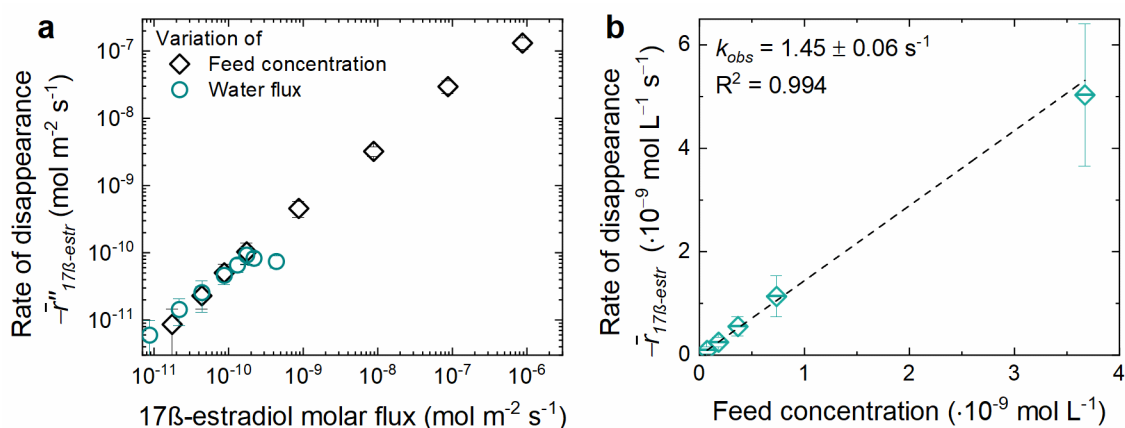


Figure 5.5: **a** The change of rate of disappearance with 17 $\beta$ -estradiol molar flux calculated using the data from the studies of water flux and initial 17 $\beta$ -estradiol concentration. Standard conditions:  $J_w = 600\text{ L m}^{-2}\text{ h}^{-1}$ ,  $I_{inc} = 10\text{ mW cm}^{-2}$ ,  $\text{pH} = 8.6 \pm 0.4$ ,  $c_f(O_2) = (8.5 \pm 0.2)\text{ mg L}^{-1}$ . **b** The change of disappearance rate based on the volume of a PCM ( $-r_{17\beta\text{-estr}}$ ) as a function of 17 $\beta$ -estradiol molar concentration in the feed. The slope of a fitting curve results in the  $k_{obs}$  value

The degradation performance of Pd-TFPP/PVDF membranes is comparable with other works using photocatalytic membranes. Ultrafiltration TiO<sub>2</sub>-PVDF membrane can realize 73% removal of 17 $\beta$ -estradiol ( $c_f = 200\text{ ng L}^{-1}$ ) at  $J_w = 450\text{ L m}^{-2}\text{ h}^{-1}$ ,<sup>372</sup> while Pd-TFPP/PVDF membranes achieve 48% removal ( $c_f = 100\text{ ng L}^{-1}$ ) using the higher water flux of  $J_w = 600\text{ L m}^{-2}\text{ h}^{-1}$ . The deterioration of removal at high 17 $\beta$ -estradiol concentrations can be ascribed to deviation from the pseudo-first order kinetics. This phenomenon occurs when the  $k_{obs}$  is not stable. Figure 5.5b depicts the  $\bar{r}_{E2}$  as a function of molar concentration. Its linear fit yields the relatively high rate constant ( $k_{obs} = 1.45\text{ s}^{-1}$ ). Note that the range of  $c_f$  from  $0.02$  to  $1\text{ }\mu\text{g L}^{-1}$  has been used, because steady-state concentrations may have not been reached by the end of experiments (see also Figure 5.4a). As  $k_{obs}$  includes the concentration of ROS –presumably only the <sup>1</sup>O<sub>2</sub> steady-state concentration  $c_{1O_2,ss}$  – it is possible to calculate rate constant in absence of mass transfer limitations ( $k_i$ ).

## 5.2.4 Calculation of the Bimolecular Rate Constant

For further analysis, it is instructive to reveal the main type of ROS produced by Pd-TFPP photosensitizer. Figure 5.6 displays the strong specific PL signal attributed to efficient generation of <sup>1</sup>O<sub>2</sub> ( $\Phi_{\Delta} = 0.94$ ). It is assumed that singlet oxygen is the main species involved in the degradation process, because of i) the

dominating role of energy transfer (see discussion in Section 4.2.2), ii) not successful detection of other types of ROS by trapping experiments, iii) involvement of  $^1\text{O}_2$  in the UA bleaching experiments. This conclusion allows to describe the rate equation as per Equation 3.26, where the  $k_i$  value can serve as a metric of reactivity of  $^1\text{O}_2$  with pollutant molecules. Then, it is possible to calculate  $k_i$  from the  $k_{obs}$  ( $k_i = k_{obs}/c_{^1\text{O}_2,ss}$ ), provided that the steady-state concentration of  $^1\text{O}_2$  does not alter with time.

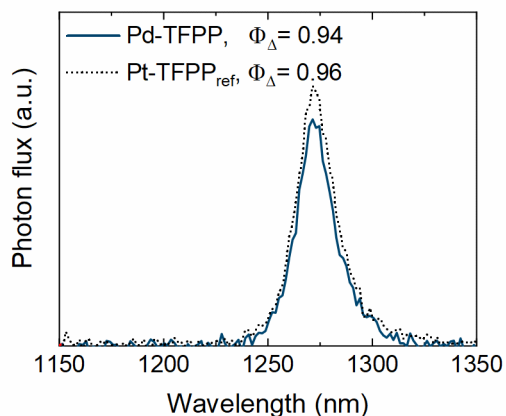


Figure 5.6: Specific phosphorescence signal of singlet oxygen relaxation process for Pd-TFPP and reference Pt-TFPP dissolved in ethanol. The optical density of Pd-TFPP and the reference photosensitizer at  $\lambda = 405$  nm matched (0.6–0.7).

This statement is true under the following assumptions: i) at low 17 $\beta$ -estradiol concentrations the major deactivation pathway of Pd-TFPP excited state is the intrinsic deactivation ( $k_{\Delta}$ ) by solvent molecules;<sup>317</sup> ii) the direct physical or chemical quenching of  $^1\text{O}_2$  by 17 $\beta$ -estradiol molecules can be neglected due to  $k_{\Delta} \gg k_{q,17\beta\text{-estr}}C_f$  at low pollutant concentrations; iii) marginal diffusional limitations of molecular oxygen to the immobilized porphyrin. The last assumption is confirmed by the efficient quenching of membrane-fixed Pd-TFPP by molecular oxygen in air-saturated aqueous solution ( $\Phi_{\Delta} \approx P_{T,O_2} = 0.82$ , see discussion in the Chapter 4).

Photogeneration rate of  $^1\text{O}_2$  under continuous illumination can be approximated by Equation 5.1. Given the above assumptions, the formula can be rewritten as Equation 5.2:

$$c_{^1\text{O}_2,ss} = \frac{\varphi_{abs}\Phi_{\Delta}}{(k_{\Delta} + k_{q,17\beta\text{-estr}}C_f)N_A} \quad (5.1)$$

$$c_{^1\text{O}_2,ss} = \frac{t_{\Delta}P_{T,O_2}}{N_A}\varphi'_{abs} \quad (5.2)$$

where  $\varphi_{abs}$ ,  $\varphi'_{abs}$  is the absorbed photon flux per area and volume ( $\text{s}^{-1} \text{m}^{-2}$ ;  $\text{s}^{-1} \text{L}^{-1}$ );  $\Phi_{\Delta}$  is the quantum yield of singlet oxygen generation ( $\Phi_{\Delta} \approx P_{T,O_2} = 1 - \frac{\tau_T}{\tau_T^0}$ );  $P_{T,O_2}$  is the probability of Pd-TFPP triplet state quenching by molecular oxygen;  $\tau_T^0$  and  $\tau_T$  are the triplet-state lifetime of PL from Pd-TFPP-PVDF membrane in deoxygenated and air-saturated water, respectively ( $\tau_T = 0.13$  ms,  $\tau_T^0 = 0.74$  ms, see Section 4.2.2).  $k_{\Delta}$  is the intrinsic decay rate constant for  $^1\text{O}_2$ ,  $k_{\Delta} = (\tau_{\Delta})^{-1}$ ;  $\tau_{\Delta}$  is the lifetime of  $^1\text{O}_2$  in aqueous buffered solution ( $\tau_{\Delta} \sim 3 \cdot \mu\text{s}$ );<sup>361</sup>  $k_{q,17\beta\text{-estr}}$  is the rate constant of  $^1\text{O}_2$  quenching by 17 $\beta$ -estradiol molecules ( $\text{L mol}^{-1} \text{s}^{-1}$ ); and  $N_A$  is the Avogadro constant ( $6.02 \cdot 10^{23} \text{ mol}^{-1}$ ).

The calculated  $c_{1O_2,ss}$  ( $1.8 \cdot 10^{-9} \text{ mol L}^{-1}$ ) is larger than the standard 17 $\beta$ -estradiol molar concentration in the feed ( $0.37 \cdot 10^{-9} \text{ mol L}^{-1}$ ). This finding justifies the choice of the pseudo-first-order kinetics for low 17 $\beta$ -estradiol concentrations, because at  $c_f > 1 \text{ } \mu\text{g L}^{-1}$  a lack of singlet oxygen starts to develop in the oxidation process that results in reduction of 17 $\beta$ -estradiol removal (see also Figure 5.4b). This decrease in oxidation performance at high 17 $\beta$ -estradiol levels can be associated with increased term of  $^1O_2$  physical quenching ( $k_{q,17\beta\text{-estr}} \cdot C_f$ , see Equation 5.1).

Using the earlier obtained  $k_{obs}$  value, the rate constant is estimated as  $k_i = 7 \cdot 10^8 \text{ M}^{-1} \text{ s}^{-1}$ . This value is several orders of magnitude higher than in the work investigating a mixture of PS and 17 $\beta$ -estradiol in methanol solution ( $10^5\text{--}10^6 \text{ M}^{-1} \text{ s}^{-1}$ ).<sup>318, 373</sup> The possible explanation of such disparity may include: i) a nanoconfinement effect of the PMR due to an increased frequency of  $^1O_2$  and 17 $\beta$ -estradiol molecular collisions;<sup>248</sup> ii) contributions of heterogeneous reactions to 17 $\beta$ -estradiol disappearance. The nanoconfinement effect can merely explain the difference to an order of magnitude. The large disparity between the calculated and literature-given  $k_i$  for freely dissolved species likely stems from surface interactions. Notably, the order of magnitude of  $k_i$  indicates that the reaction between singlet oxygen and 17 $\beta$ -estradiol within PCM is close to the diffusion-controlled limit of rapid reactions ( $k_{i,lim} = 7.4 \cdot 10^9 \text{ M}^{-1} \text{ s}^{-1}$ ). The threshold for diffusion-controlled regime in photocatalysis can be determined by examining the intensity of incident light – a critical operating parameter in photocatalytic water treatment.

## 5.2.5 Influence of Light Intensity

As pointed out above, the generation rate of singlet oxygen depends on the radiant flux of absorbed photons ( $\varphi_{abs}$ ). Provided that other parameters are fixed, the effect of singlet oxygen concentration on 17 $\beta$ -estradiol degradation performance can be observed by performing photocatalytic experiments at different levels of irradiance. Figure 5.7 exhibits the results of these experiments, where intensity of light emitted by the wLED varies in the range  $I_{inc} = 0\text{--}25 \text{ mW cm}^{-2}$ . When the wLED light source is turned on, the concentration of 17 $\beta$ -estradiol in the permeate drops sharply to the values correlating with light intensity (Figure 5.7a). Note that the gradual rise of  $c_p/c_f$  during the experiments is much less pronounced than that in studies of water flux and initial 17 $\beta$ -estradiol concentration. Unlike methylene blue, 17 $\beta$ -estradiol and other steroid hormones do not absorb light in the visible spectrum, and therefore are stable under wLED emission.

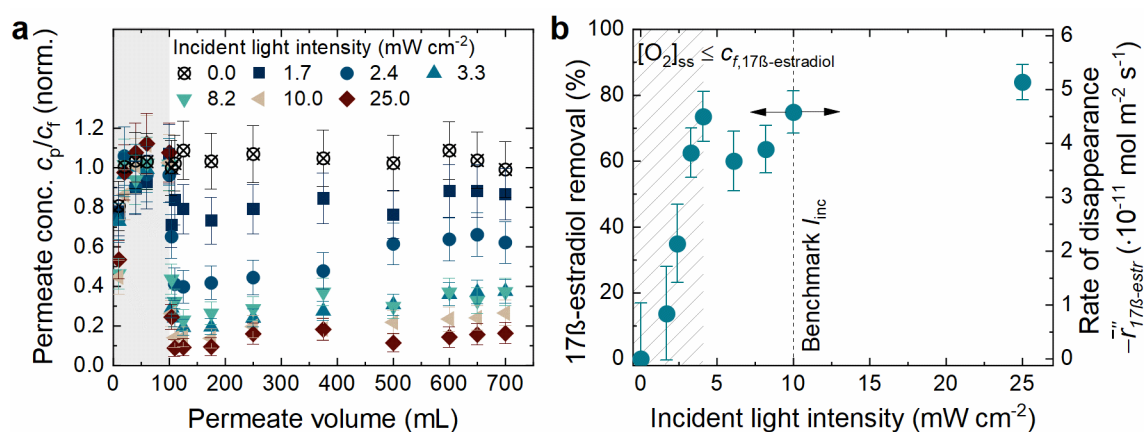


Figure 5.7: Influence of incident light intensity on the process of 17 $\beta$ -estradiol photocatalytic degradation. **a** Evolution of normalized permeate concentration of 17 $\beta$ -estradiol as a function of permeate volume, **b** 17 $\beta$ -estradiol removal and the corresponding  $r''$  shown as one set of data. Conditions: background solution of 1 mM  $\text{NaHCO}_3$ , 10 mM  $\text{NaCl}$ ,  $c_f$  (17 $\beta$ -estradiol) =  $(100 \pm 10 \text{ ng L}^{-1})$ ,  $\text{pH} = 8.6 \pm 0.4$ ,  $c_f$  ( $O_2$ ) =  $(8.5 \pm 0.4) \text{ mg L}^{-1}$ ,  $J_w = 600 \text{ L m}^{-2} \text{ h}^{-1}$ . The benchmark  $I_{inc}$  is used in all experiments of this chapter.

Increasing the light intensity from 0 to  $4.1 \text{ mW cm}^{-2}$  strongly promotes the process observed as a sharp increase in 17 $\beta$ -estradiol removal to  $R = (74 \pm 7)\%$  (see the shaded area in Figure 5.7b). Above the certain limiting value (here,  $4.1 \text{ mW cm}^{-2}$ ), illumination of PCM with stronger light hardly improves further removal ( $R = 60\text{--}84\%$ ). Similarly,  $\bar{r}''$  fluctuates around  $(4\text{--}5) \cdot 10^{-11} \text{ mol m}^{-2} \text{ s}^{-1}$  at  $I_{inc} > 4.1 \text{ mW cm}^{-2}$ . As there is no change in the 17 $\beta$ -estradiol molar flux in this study, the data sets of removal and the rate of disappearance overlap and are hence plotted against each other ( $R \propto \bar{r}''$ ).

In the region of low light intensity (marked as the shaded area), reaction kinetics is described by a linear dependence for most of the photocatalytic materials studied.<sup>218, 299, 309</sup> It has been demonstrated earlier (see Section 5.2.2), that the deviation of  $\bar{r}''_{E_2}$  from linearity indicates the change of rate-limiting step. It is assumed to be the mass-transfer of one of the reactants to the PCM surface.<sup>218</sup> However, the nature of reactant (17 $\beta$ -estradiol, molecular or singlet oxygen) experiencing the hindered diffusion is unknown in this instance. Given the stoichiometric excess of singlet oxygen ( $1.8 \cdot 10^{-9} \text{ mol L}^{-1}$  at  $I_{inc} = 10.0 \text{ mW cm}^{-2}$ ) compared to 17 $\beta$ -estradiol ( $0.07 \cdot 10^{-9} \text{ mol L}^{-1}$  at  $R = 80\%$ ), it is expected that depletion of 17 $\beta$ -estradiol at the membrane surface may render the collision of  $^1\text{O}_2$  and 17 $\beta$ -estradiol molecules less likely.

The photocatalytic degradation of 17 $\beta$ -estradiol in the continuously nitrogen-purged feed solution was suppressed, as indicated by an increase in permeate concentration from  $c_p/c_f = 0.26 \pm 0.07$  (at standard  $c_{f,O_2} = 8.5 \text{ mg L}^{-1}$ ) to  $c_p/c_f = 0.69 \pm 0.13$  at residual  $c_{f,O_2} = 6 \text{ }\mu\text{g L}^{-1}$ . More discussion on experiments in deoxygenated feed solution can be found in Chapter 6. It must be noted that pH of the feed solution increased during the nitrogen purging, because carbon dioxide was purged along with dissolved oxygen. An increase in pH can be associated with diminished removal due to the electrostatic repulsion between deprotonated 17 $\beta$ -estradiol and PCM surface (as shown next in Figure 5.8b).

Deoxygenation of feed solution invokes the depletion of available  $^1\text{O}_2$ . Concurrently, this procedure causes degassing of  $\text{CO}_2$  ubiquitously present in the feed solution prepared in chloride-bicarbonate background electrolyte. According to Le Chatelier's principle, the hydrolysis reactions (of both sodium bicarbonate and carbonic acid) are out of equilibrium that leads to the formation of alkali (NaOH) and a strong pH shift. Hence, it is necessary to investigate the effect of such important water quality parameter as feed solution pH and reveal the effect of salt matrix.

## 5.2.6 Influence of Feed Solution pH on the 17 $\beta$ -Estradiol Removal

The selected works on PS-based photocatalytic materials suggest that highly alkaline media ( $\text{pH} > 9$ ) accelerate the  $^1\text{O}_2$ -induced oxidation of estrogenic SH and other compounds with a phenol ring.<sup>318, 320</sup> Given the likely fluctuation of influent pH during the water treatment process under real condition, Figure 5.8 outlines the effect of feed solution pH ranging from 2 to 12 on the photocatalytic activity of the Pd-TFPP/PVDF membranes. Similar to the studies of other process parameters, illuminated PCM significantly reduce the 17 $\beta$ -estradiol concentration in the permeate (Figure 5.8a). Note that the continuous rise of the normalized 17 $\beta$ -estradiol concentration in buffered solutions during the experiment is much more distinct compared to the experiment conducted with Milli-Q based solution.

Figure 5.8b shows that the experiments conducted at the standard values of feed solution pH (between 8 and 9) exhibit the local maximum of achieved 17 $\beta$ -estradiol removal,  $R = (83 \pm 6)\%$ . The similar 17 $\beta$ -estradiol removal in the range 8–9 also indicates that a slightly elevated pH ( $8.6 \pm 0.4$  compared to a standard pH 8.3 of chloride bicarbonate buffer) has no effect on photocatalytic removal. The effectiveness of 17 $\beta$ -estradiol degradation deteriorates in acidic, neutral (50%–60%) and highly alkaline media ( $\text{pH} > 9$ ,  $R = 40\text{--}50\%$ ). Strikingly, the experiments conducted with 17 $\beta$ -estradiol solution prepared without a background electrolyte demonstrate even lower removal,  $R = (36 \pm 12)\%$ . The slightly acidic pH of pure MilliQ water-based solution ( $5.6 \pm 0.1$ ) may incur such a performance loss. Yet, the influence of inorganic



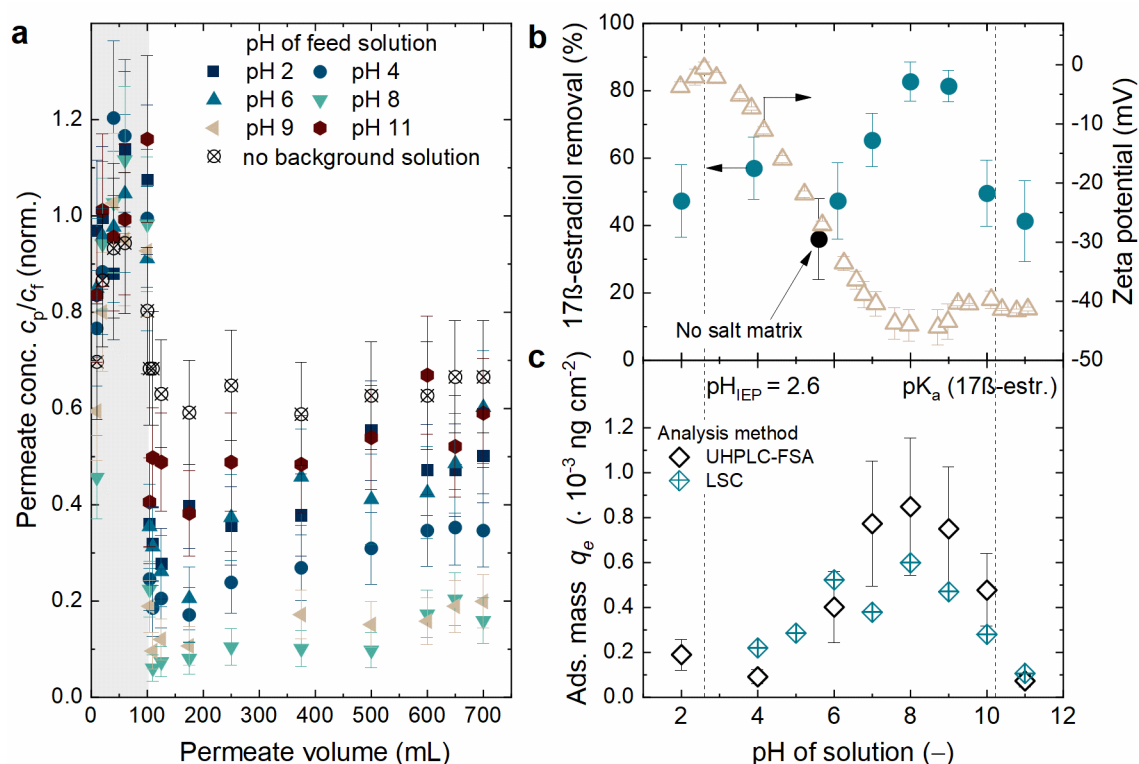


Figure 5.8: **a** Evolution of normalized 17β-estradiol concentration as a function of permeate volume at different pH values of feed solution. **b** Removal and **c** the mass adsorbed of 17β-estradiol per surface of PdTFPP-PVDF membranes determined by HPLC-FSA and LSC methods.  $c_f$  (17β-estradiol) =  $(100 \pm 10) \text{ ng L}^{-1}$  in 1 mM NaHCO<sub>3</sub>, 10 mM NaCl,  $c_f(\text{O}_2) = (8.5 \pm 0.4) \text{ mg L}^{-1}$ ,  $J_w = 600 \text{ L m}^{-2} \text{ h}^{-1}$ ,  $l_{inc} = 10 \text{ mW cm}^{-2}$ . The dashed lines mark the isoelectric point ( $pH_{IEP}$ ) of the PCM and the  $pK_a$  of the 17β-estradiol molecule.

ions on 17β-estradiol adsorption step cannot be excluded. Overall, these results look promising for treating natural waters that contain chloride and bicarbonate ions at millimolar concentrations. Figure 5.8b also exhibits that membrane surface charge is the most negative at pH 8–9 ( $\zeta_{PCM} = (-43 \pm 2) \text{ mV}$ ), at which conditions the topmost removal is achieved. The isoelectric point ( $pH_{IEP}$  2.6) in the far acidic side suggests that membrane is negatively charged over the entire pH range. This outcome is largely attributed to the PVDF membrane material (see the zeta-potential studies of pristine membranes and PCM in Figure 4.7).

In contrast to the strong “sticking” of MB to a PCM, only electrostatic repulsion can exist between the deprotonated 17β-estradiol molecules and the membrane surface at pH approaching  $pK_a$  value (10.2–10.3, see Table 2.3). This conclusion is consistent with the reduced efficiency of 17β-estradiol degradation at pH 10–11. Although the exact mechanism has not been elucidated, electrostatic interaction may inhibit both steps of adsorption and diffusion to the surface that will result in the depletion of 17β-estradiol in the vicinity of the membrane pore walls.<sup>374</sup> The striking similarity between photocatalytic removal and adsorption of 17β-estradiol on porphyrin-coated membranes is seen on Figure 5.8c. In slightly alkaline media, the 17β-estradiol uptake by a PCM is the highest ( $q_e = 0.005\text{--}0.006 \text{ ng cm}^{-2}$  of BET surface area). When using the acidic or alkaline 17β-estradiol solution, the adsorbed per surface area decreases roughly by a factor of 10. The degree of adsorbed mass is also consistent (the same order of magnitude) with the studies using PVDF polymer. Table 5.1 outlines the results of the mass of adsorbed 17β-estradiol per surface area ( $q_e$ ) and compares then with the previous work on micropollutant adsorption on PVDF (weak affinity to 17β-estradiol) and polyamide polymers (higher affinity to 17β-estradiol).



Table 5.1: The data of 17 $\beta$ -estradiol adsorbed mass in the present work compared to the other scientific work

Type of membrane/polymer	Schäfer <i>et al.</i> , 2011 <sup>289</sup>		This work
	PVDF granular polymer (Solvay)	Polyamide granular polymer (Goodfellow)	PVDF membrane (GVXAL, Millipore)
Surface area, cm <sup>2</sup>	169	169	1170 $\pm$ 150
17 $\beta$ -estradiol adsorbed mass per surface area, ng cm <sup>-2</sup>	3.7 $\cdot$ 10 <sup>-3</sup>	23 $\cdot$ 10 <sup>-3</sup>	(0.9 $\pm$ 0.3) $\cdot$ 10 <sup>-3</sup>

The surface area ( $A_s$ ) of spherical PVDF and polyamide polymer used in the reference work<sup>289</sup> was calculated *via* Equation 5.3:

$$A_s = n_{pol}A_{pol} \quad (5.3)$$

$$n_{pol} = \frac{m_m}{m_{pol}} = \frac{m_m}{\rho(\frac{1}{6}\pi d_{pol}^3)} \quad (5.4)$$

where  $n_p$  is the number of polymer particles per mass of PVDF polymer used ( $m_m = 2.5$  g from Equation 5.4),  $A_{pol}$  is the surface area of polymer particle ( $A_{pol} = \pi d_{pol}^2$ , cm<sup>2</sup>),  $m_m$  is the mass of PVDF membrane sample with area of 2 cm<sup>2</sup> ( $m_m = 0.018$  g);  $\rho$  is the density of PVDF polymer ( $\rho = 1.78$  g cm<sup>-3</sup>),  $d_{pol}$  is the diameter of polymer particles ( $d_{pol} = 0.05$  cm). The Brunauer-Emmett-Teller (BET) analysis of the argon adsorption/desorption isotherm provided the specific surface area of PVDF (MP200) membrane ( $a_s = 5.9$  m<sup>2</sup> g<sup>-1</sup><sub>PVDF</sub>, see also Table 3.9).

The correlation of the data sets for removal and adsorption suggests that 17 $\beta$ -estradiol adsorption is indeed hindered by electrostatic repulse at pH > 9 thereby explaining the local maximum of 17 $\beta$ -estradiol removal. The phenolic ring plays important role not only in degree of 17 $\beta$ -estradiol adsorption, but also the estrogenic activity of the entire molecule. Hence, it is necessary to investigate the degradation of other SHs without phenolic groups.

## 5.3 Photocatalytic Degradation of Multiple Steroids

### 5.3.1 Oxidation of Steroid Hormones in Mono-Component Solutions

Although the reactivity of singlet oxygen with 17 $\beta$ -estradiol is sensitive to pH, the type of pollutant has a much more drastic effect on the degradation kinetics. The electrophile singlet oxygen readily reacts with olefinic and aromatic units and electron-rich atoms.<sup>375</sup> Hence, it is necessary to investigate whether other steroid hormones are prone to <sup>1</sup>O<sub>2</sub>-induced degradation as effectively as 17 $\beta$ -estradiol.

Figure 5.9a indicates the results of photocatalytic experiments using the feed solution separately containing estrone, 17 $\beta$ -estradiol, testosterone or progesterone. Unlike testosterone (< 16%) and progesterone (< 18%), estrone and estradiol are effectively removed,  $R = (85 \pm 5)\%$ . The kinetics data help unveil the reason of such difference in removal. The bimolecular rate constants of estrone and estradiol oxidation by <sup>1</sup>O<sub>2</sub> are significantly higher than those found for derivatives of testosterone and progesterone.<sup>309</sup> Thus, the limited

degradation of testosterone and progesterone is attributed to their inhibited reactivity with  $^1\text{O}_2$ . The influence of SH structure on removal is discussed in detail in Chapter 6.

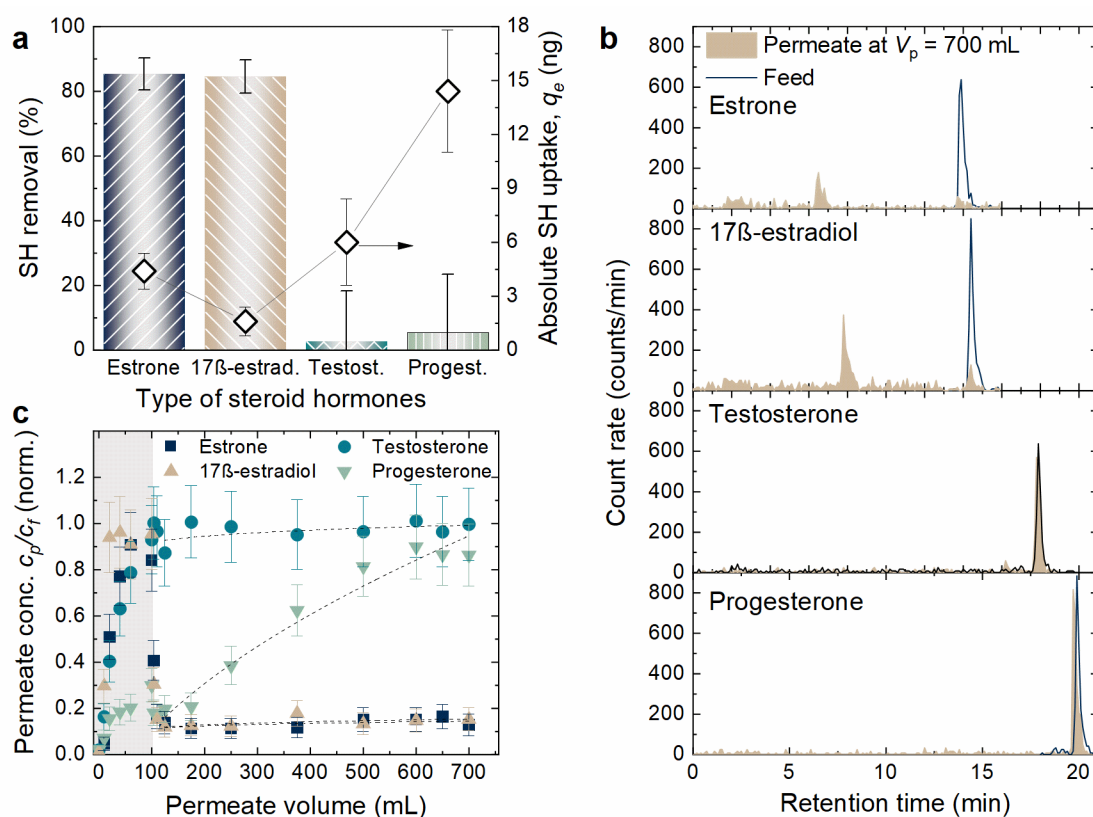


Figure 5.9: Efficacy of photocatalytic oxidation of individual SH in a single-pass continuous-flow photocatalytic membrane reactor. **a** SH removal plotted against their uptake by PCM. **b** The radiochromatograms examples of feed and permeate samples (at cum. permeate volume 700 mL) collected in the experiments using individual SH. **c** Evolution of normalized SH concentration in the permeate as a function of permeate volume. The error bars for  $q_e$  represent the data from at least duplicated experiments. Conditions:  $c_f(\text{SH}) = (200 \pm 10) \text{ ng L}^{-1}$  in background electrolyte (1 mM  $\text{NaHCO}_3$ , 10 mM  $\text{NaCl}$ ),  $c_f(\text{O}_2) = (8.5 \pm 0.2) \text{ mg L}^{-1}$ ,  $J_w = 600 \text{ L m}^{-2} \text{ h}^{-1}$ ,  $I_{inc} = 10 \text{ mW cm}^{-2}$ ,  $\text{pH} = 8.6 \pm 0.4$ .

The radiochromatograms depicted in Figure 5.9b reveal the new peaks, attributed to new oxidation products of estrone and 17 $\beta$ -estradiol. The peak shape of the feed and permeate samples containing testosterone and progesterone is nearly identical, suggesting that the manner of their removal is not related to oxidation. Given the substantial role of adsorption in 17 $\beta$ -estradiol removal, the adsorbed mass of other steroid hormones can provide the insight into the reason for the differences in photocatalytic removal (see also Figure 5.9a). Notably, the adsorption of progesterone towards the end of the dark phase ( $V_p = 100 \text{ mL}$ ) exhibits significantly higher membrane uptake of  $q_e = (14.4 \pm 3.4) \text{ ng}$  compared to other steroid hormones: estrone with  $q_e = (4.4 \pm 1.0) \text{ ng}$ , 17 $\beta$ -estradiol with  $q_e = (1.6 \pm 0.8) \text{ ng}$ , or testosterone with  $q_e = (6 \pm 2.4) \text{ ng}$ . Based on the  $q_e$  value, the affinity of the studied steroid hormones to the Pd-TFPP/PVDF membrane changes in the following order: 17 $\beta$ -estradiol < estrone  $\approx$  testosterone < progesterone, and thus is related to physical-chemical properties of the solutes<sup>289</sup> (the information on the number of OH hydrogen bond donors/acceptors, dipole moment,  $\text{pK}_a$  values for the studied steroid hormones can be found in Table 2.3). Noteworthy, the masses of adsorbed 17 $\beta$ -estradiol molecules –  $(1.6 \pm 0.8) \text{ ng}$  – and those in the bulk volume within the PCM ( $1.6 \text{ pg}$  in  $16 \text{ }\mu\text{L}$  pore volume of the PCM per  $100 \text{ ng L}^{-1}$  concentration) by a factor of

1000. This difference indicates a large surface concentration of 17 $\beta$ -estradiol that probably promotes a heterogeneous reaction rather than a homogeneous one. Therefore, the heterogeneous reaction steps likely predominate in the Pd-TFPP/PVDF systems. This finding argues in favor of surface interaction as the cause of the discrepancy between the calculated ( $k_i = 7 \cdot 10^8 \text{ M}^{-1} \text{ s}^{-1}$ ) and the literature rate constants (Chapter 5.2.4).

Figure 5.9c reveals the strong difference in the evolution of normalized SH concentration in the permeate. The concentration of the chemically similar and readily oxidized estrone and 17 $\beta$ -estradiol drops after the light source is on. In contrast, the concentrations of testosterone and progesterone in the permeate do not decline and for the latter SH even increase for the rest of experiment. Note that the steady state concentration of progesterone does not reach the steady state values even at the end of experiments, also accompanied by the poor reproducibility of experiments. Figure 5.10 exhibits the results of four repetitions with testosterone and progesterone conducted with freshly prepared PCM. The graphs indicate that the  $c_p/c_f$  during both adsorption ( $V_p$  up to 100 mL) and light phases ( $V_p = 100\text{--}700 \text{ mL}$ ) is poorly reproducible for both SH types.

Note that the higher affinity (and hence adsorption) of progesterone to a PCM surface – observed as a less steep rise in  $c_p/c_f$  – does not contribute to effective photocatalytic oxidation. In semiconductor photocatalysis, preliminary adsorption of organic compounds can to some extent promote the charge transfer and hole scavenging, and thus is a crucial step in photodegradation.<sup>298</sup> Apparently, this is not the case for the studied Pd-porphyrin photosensitizer, which predominantly produces the freely diffusing singlet oxygen ( $I_{3D} = \sim 270 \text{ nm}$ ).<sup>361</sup> Thus, the effect of the hindered reactivity of  $^1\text{O}_2$  with such contaminants as testosterone or progesterone prevails over their adsorption strength.

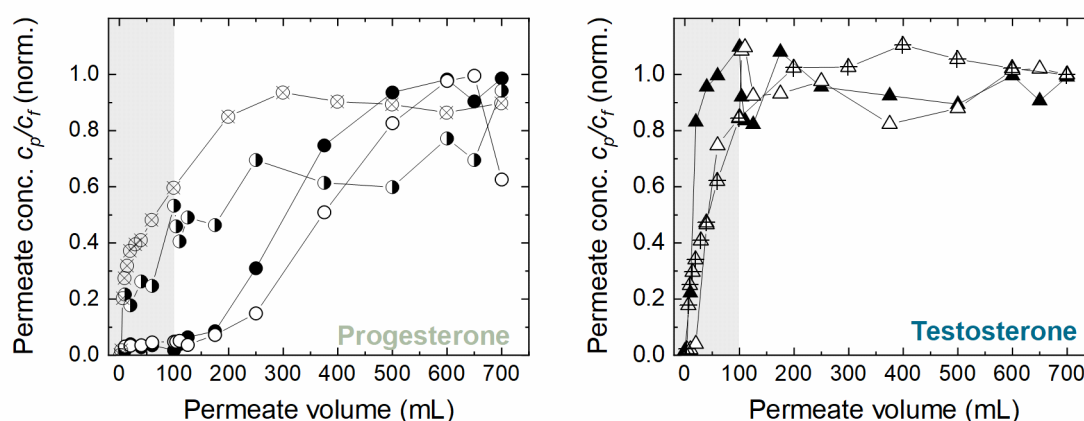


Figure 5.10: Evolution of normalized progesterone and testosterone concentration in the permeate as a function of permeate volume. Conditions:  $c_r = (200 \pm 10) \text{ ng L}^{-1}$  in background electrolyte (1 mM  $\text{NaHCO}_3$ , 10 mM  $\text{NaCl}$ ).  $J_w = 600 \text{ L m}^{-2} \text{ h}^{-1}$ ,  $I_{inc} = 10 \text{ mW cm}^{-2}$ ,  $\text{pH} = 8.6 \pm 0.4$ ,  $c_r(\text{O}_2) = (8.5 \pm 0.2) \text{ mg L}^{-1}$ . The dark phase (0–100 mL) for saturation of adsorption is marked as grey areas.

### 5.3.2 Oxidation of Steroid Hormones in Multi-Component Mixtures

An experiment with a mixture of steroid hormones can reveal whether the treatment efficiency of a particular pollutant changes in a multi-component system. Figure 5.11a indicates the high removal of estrone,  $R = (69 \pm 10)\%$ , and 17 $\beta$ -estradiol,  $R = (71 \pm 9)\%$ , and the limited removal of testosterone ( $R < 5\%$ ) and progesterone ( $R < 1\%$ ). These results are consistent with the studies using the single-component solutions: high removal of estrogenic substances and little to no removal of testosterone, progesterone. No effect of the number of components on degradation is due to: i) the unchanged total concentrations of steroid hormones ( $c_{SH} \approx 200 \text{ ng L}^{-1}$ ); ii) relatively high concentration of produced singlet

oxygen ( $c_{1O_2,ss} = 1.8 \cdot 10^{-9} \text{ mol L}^{-1}$ ). A study by Díez-Mato *et al.* describes a similar result for  $^1O_2$ -mediated oxidation of individual pharmaceuticals and their mixture – including a recalcitrant pollutant (paracetamol) – but at much higher concentration ( $9 \text{ mg L}^{-1}$ )<sup>157</sup> than in this work.

Small discrepancies between the removal in single-compound solution,  $R = (85 \pm 5)\%$ , and the mixture,  $R = 70 \pm 10\%$ , can be explained by the partial co-elution of estrone and  $17\beta$ -estradiol at retention times of 15.2 and 15.8 min, respectively (see Figure 5.11b). The resulting peak overlap complicates the area analysis. Yet, two new distinct peaks are clearly separated and assigned to metabolites of estrone and  $17\beta$ -estradiol (also observed in Figure 5.11b). Based on the radiochromatograms of permeate samples containing only estrone or  $17\beta$ -estradiol, the possible biotransformation of  $17\beta$ -estradiol to estrone<sup>376</sup> can be excluded. The peak shape of testosterone and progesterone has not undergone any considerable changes. When looking at evolution of the SH concentration in the permeate (Figure 6.10c), a similar pattern of their degradation is observed as in Figure 5.11c. Testosterone and progesterone are less prone to react with  $^1O_2$  throughout the experiments, while the concentrations of estrone and  $17\beta$ -estradiol drops after the dark phase and remain relatively stable at the level  $c_p/c_f = 0.29\text{--}0.31$ . The concentration of progesterone rises slightly faster during the experiment using SH mixture because of the lower concentration. However, the evolution of  $c_p$  (breakthrough curve) is poorly reproducible. Overall, the photocatalytic oxidation of  $17\beta$ -estradiol and estrone remains effective despite the two non-reactive chemicals present in the mixture solution.

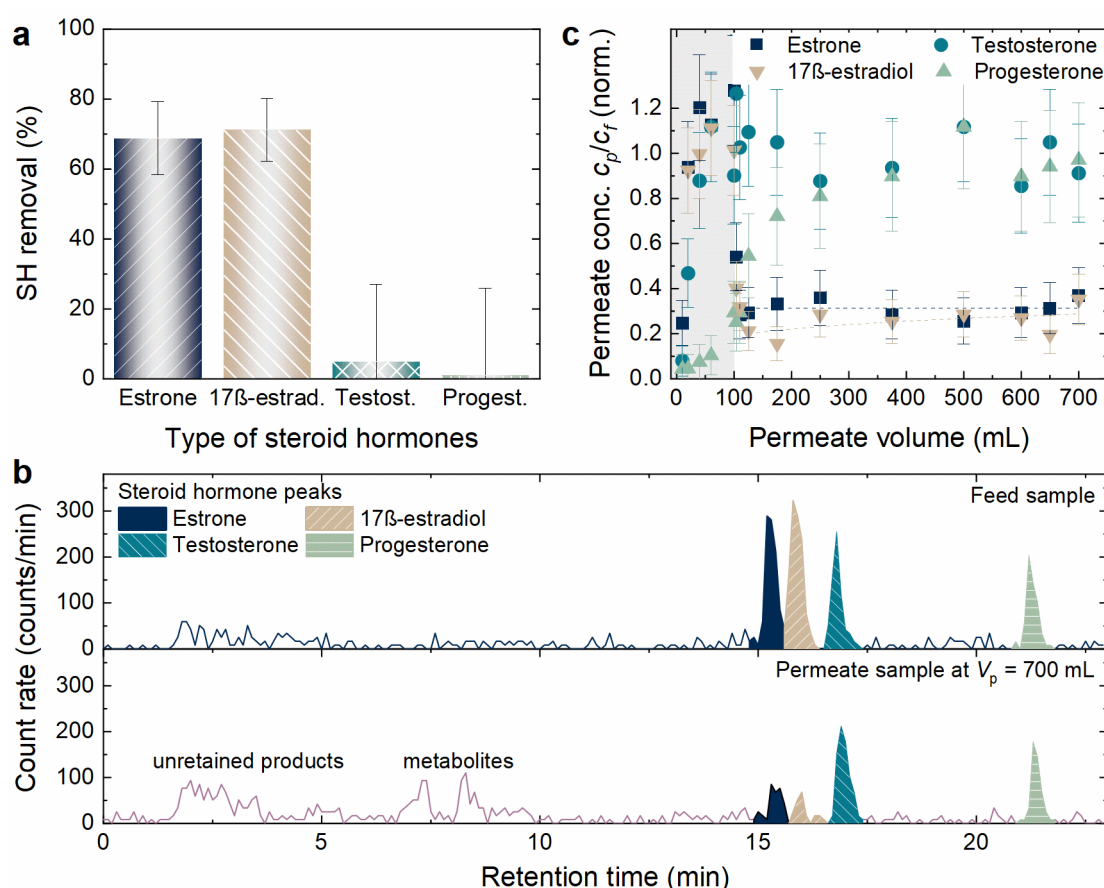


Figure 5.11: The photocatalytic oxidation of SH mixture solutions (estrone,  $17\beta$ -estradiol, testosterone, progesterone). **a** Removal of individual SHs, **b** the radiochromatograms of the feed and permeate samples (at  $V_p = 700 \text{ mL}$ ), showing changes in the peak areas of SHs. **c** Evolution of normalized SH concentration in the permeate as a function of permeate volume.  $c_f$  (each SH) =  $(50 \pm 10) \text{ ng L}^{-1}$  in  $1 \text{ mM NaHCO}_3$ ,  $10 \text{ mM NaCl}$ ,  $c_f(O_2) = (8.5 \pm 0.2) \text{ mg L}^{-1}$ ,  $J_w = 600 \text{ L m}^{-2} \text{ h}^{-1}$ ,  $I_{inc} = 10 \text{ mW cm}^{-2}$ ,  $\text{pH} = 8.6 \pm 0.4$ .

### 5.3.3 Suggested Mechanism of 17 $\beta$ -estradiol Oxidation

It has been demonstrated above (Section 5.2.2) that 17 $\beta$ -estradiol concentration in the permeate can be reduced below the detection limit. However, the high levels of degradation do not always provide the marginal estrogenic activity in the treated water due to the formation of intermediate products.<sup>297</sup> In addition, the nature of intermediate products observed in the UHPLC-FSA radiochromatograms at  $t_{ret} = 6-7$  min (see also Figure 5.9b) remains unknown. For that purpose, the mass spectra of the feed and permeate samples after photocatalytic oxidation were recorded (Figure 5.12a). The intensity of the main compound (17 $\beta$ -estradiol,  $m/z = 272.2$ ) significantly lowers after the photocatalytic treatment. The oxidation pathway of phenolic compounds (like 17 $\beta$ -estradiol) by  $^1O_2$  includes the step of electron transfer to or hydrogen abstraction from the phenolic group. As a result, unstable hydroperoxide group is formed (at the *ortho*- , or *para*-position,  $m/z = 304.2$ ).<sup>320</sup> Depending on the position of hydroperoxide group, the conversion product ( $m/z = 287.2$ ) with phenolic or quinone-like moiety can be formed. Further hydroxylation of the phenol ring can lead to other intermediates ( $m/z = 304.2$ ,  $m/z = 308.2$ ,  $m/z = 320.2$ ), and even to collapse of a phenol ring<sup>377</sup> (not identified in the provided mass spectra).

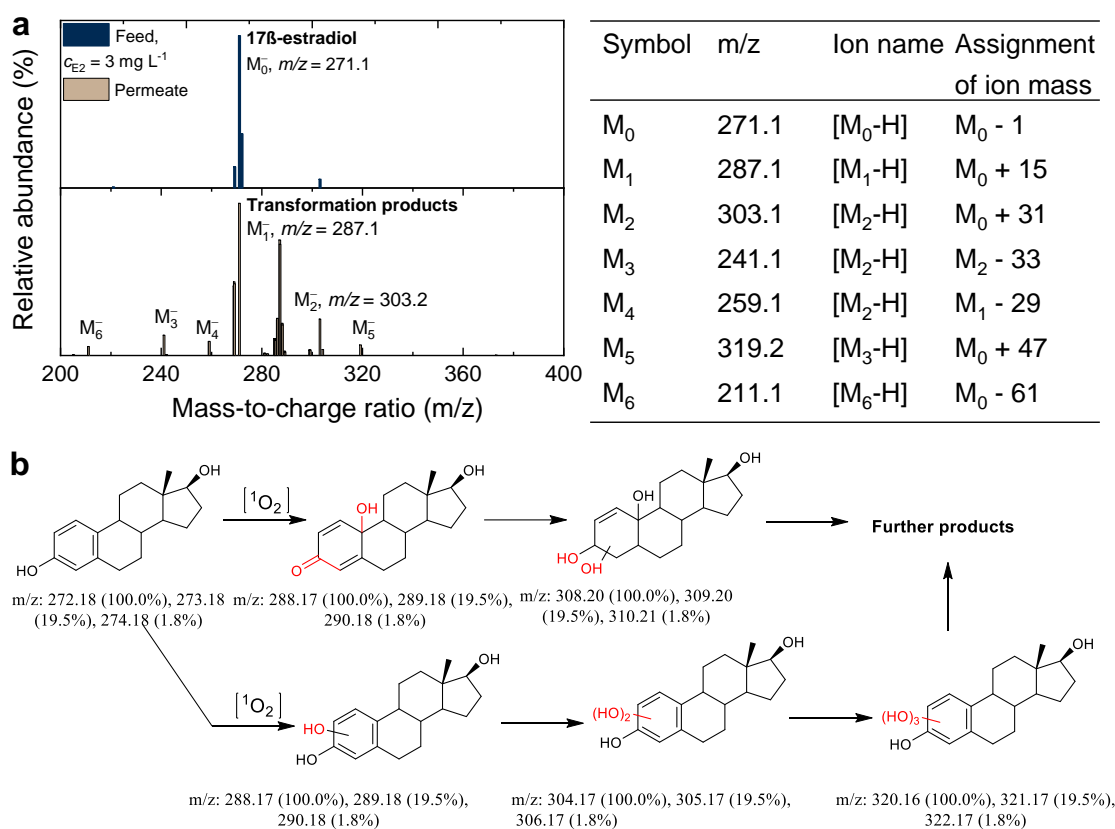


Figure 5.12: **a** Mass spectra of 17 $\beta$ -estradiol feed and permeate samples after the photocatalytic treatment using PCM, including the identified photodegradation by-products of 17 $\beta$ -estradiol; **b** the suggested mechanism of  $^1O_2$ -induced oxidation of 17 $\beta$ -estradiol. The differences in molecules are highlighted.

The major identified by-products of 17 $\beta$ -estradiol are consistent with those reported in other works.<sup>297, 318, 378</sup> On its basis, the mechanism of  $^1O_2$ -induced oxidation of 17 $\beta$ -estradiol has been suggested (Figure 5.12b). Given that the major detected metabolites retain phenolic group – a moiety crucial for the binding to the estrogen receptors – the estrogenic activity of the anticipated by-products is likely to be still potent.<sup>378</sup> To

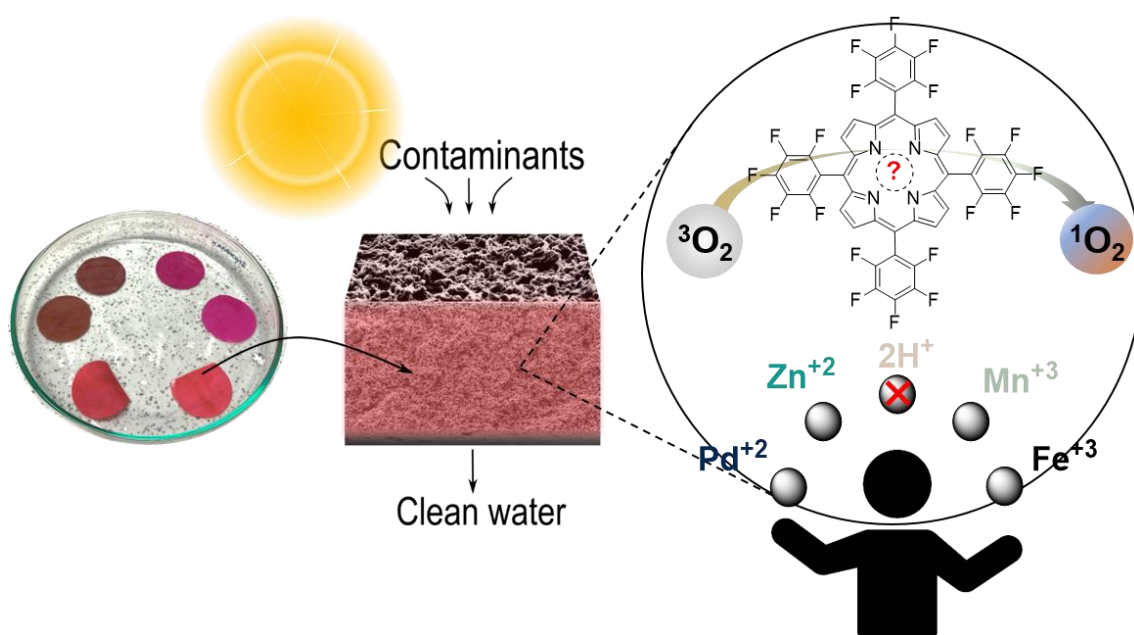
quantify the residual estrogenicity of the permeate collected after photocatalytic treatment, a series of toxicity assays should be performed.<sup>379</sup>

## 5.4 Summary

This chapter has established that significant removal of estrone and 17 $\beta$ -estradiol micropollutants (at environmental relevant concentrations) can be achieved in a single pass using the PdTFPP-PVDF membranes and white LED illumination. The limited removal of testosterone and progesterone however suggests their low reactivity with singlet oxygen. The degree of 17 $\beta$ -estradiol removal is strongly affected by the residence time, irradiance, molecule ionization and the membrane charge. These findings were corroborated by the photodegradation experiments conducted at different water flux and wLED light intensity, and feed solution pH. Remarkably, at water flux 60 L m<sup>-2</sup> h<sup>-1</sup> and light intensity of 10 mW cm<sup>-2</sup>, the 17 $\beta$ -estradiol concentration in the permeate can be reduced from 100 to 2 ng L<sup>-1</sup> – a value closely approaching the guideline value in the drinking water (1 ng L<sup>-1</sup>).

Although the palladium content in porphyrin-coated membranes is low (0.025% wt), the reliance on noble metals is not a sustainable long-term solution. Hence, it is necessary to look for an alternative for Pd-porphyrin, which will contain abundant elements and be able to withstand prolonged illumination.

# 6 Palladium- vs Noble-Metal-Free Porphyrin Complexes



The contents of this chapter have been published in the separate work. Figures and Tables have been adapted with permission from Lyubimenko, R. et al. (2022); Copyright 2022 Elsevier. The citations in the following text are omitted.

**Lyubimenko, R.;** Richards, B. S.; Schäfer, A. I.; Turshatov, A., Noble-metal-free photosensitizers for continuous-flow photochemical oxidation of steroid hormone micropollutants under sunlight. *J. Membr. Sci.*, 642 (2022) 119981.

## *Acknowledgments and Contributions*

The core experiments in this chapter were conceived by the author and Andrey Turshatov. Bryce S. Richards (IMT) and Andrea I. Schäfer (IAMT) assisted with realization of conceptualized ideas via careful planning. The author prepared the PCM samples and developed the methodology for their testing. Alessandra Imbrogno (IAMT) prepared the stock solutions of radiolabeled steroid hormones and helped with the radiotracer waste management. Dmitry Busko (IMT) is greatly acknowledged for the steady-state and time-resolved photoluminescence measurements, including the studies of singlet oxygen phosphorescence. The streak camera measurements for the singlet and triplet lifetimes of porphyrins in solution were performed by Milian Kaiser (IMT). Data analysis was carried out by the author with the assistance of Andrey Turshatov, Bryce S. Richards, and Andrea I. Schäfer.

## 6.1 Introduction

The enhanced mass transport of reactants within photocatalytic membranes makes them a promising photoreactor architecture for achieving abatement of steroid hormone micropollutants. Until now, a single type of porphyrin (Pd-TFPP) loaded onto the PVDF membrane has been studied. However, the noble-metal containing catalysts are not ultimately sustainable due to the finite natural supply (for example, of palladium). As the choice of central metal ion in metalloporphyrins has strong implications on their photocatalytic activity, this chapter dives into the steroid hormone degradation performance using the PVDF membranes coated with porphyrin with and without noble-metal cation.

### Objectives

To address the question, the following objectives are set out:

- Fabricate and investigate the photocatalytic activity of four membrane-immobilized PS (see Figure 6.1) towards the steroid hormone micropollutants using simulated terrestrial sunlight;
- Identify limiting factors for the use of noble metal-free porphyrins in studies of 17 $\beta$ -estradiol degradation under strong illumination and oxygen-deficient conditions;
- Gauge the photostability of selected PSs after immobilization on PVDF membranes by photobleaching studies conducted under accelerated aging with ultraviolet–violet (UV–violet) light.

A short summary with key results concludes the chapter.

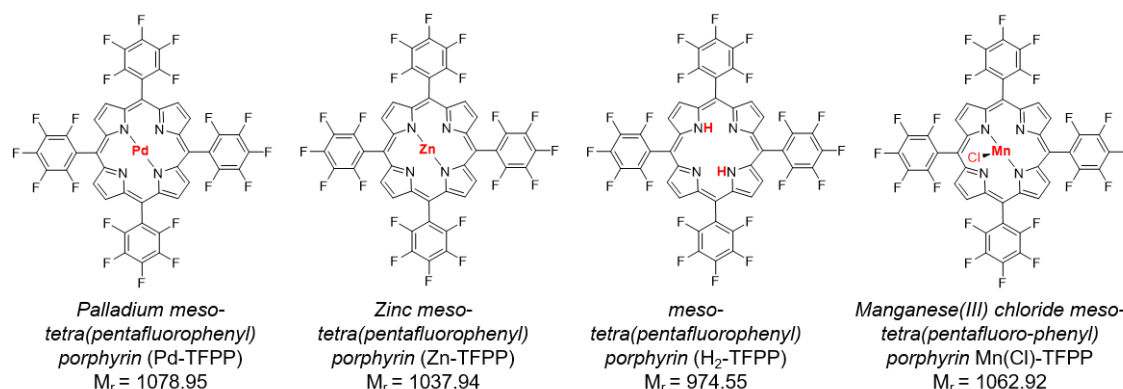


Figure 6.1: The chemical structures of porphyrins investigated in this chapter. The central metal ion, or lack thereof, is highlighted.

### Modification of the Experimental Filtration System

The photocatalytic filtration set-up was integrated with the solar simulator (SolSim) used as a light source in the degradation experiments (see Figure 3.4a). The experimental protocol remained unchanged from the previous chapter (see also Table 3.7), except for the manual activation of the SolSim light. The information on technical characteristics and height of the SolSim is provided in Materials and Methods (Section 3.3.2).



## 6.2 Characterization of Noble-Metal-Free PCM

The FT-IR spectra prove that the chemical structure of porphyrins is unchanged after adsorption on the membranes (Figure 6.2a). The  $\nu_{C=C}$ ,  $\delta_{C-H}$  bands are specific to noble-metal-free porphyrins as well. All four types of porphyrin-coated membranes exhibit the pyrrole and phenyl ring bending bands between 1500 and 1520  $\text{cm}^{-1}$  ( $\nu_{C=C}$ ), in-plane ( $900\text{--}1050\text{ cm}^{-1}$ ) and out-of-plane stretching bands ( $700\text{--}730\text{ cm}^{-1}$ ). The position and intensity of the bands correlate with the earlier investigated Pd-TFPP (see Figure 4.4a). The appearance of new  $\delta_{N-H}$  band at  $3319\text{ cm}^{-1}$  exclusively for  $\text{H}_2$ -TFPP marks its free-base nature (lack of a central ion).

The nature of ion occupying the central cavity in porphyrin molecules (see Figure 6.1) changes the position and intensity of absorption bands. Figure 6.2b depicts the absorbance spectra of PCM with and without noble metal ions. Conventionally, porphyrins absorb light in two wavelength regions: Soret ( $350\text{--}450\text{ nm}$ ) and Q-bands ( $500\text{--}700\text{ nm}$ ). Unlike metalloporphyrins, free-base porphyrin-coated membrane exhibit four peaks (at 504, 538, 580, 634 nm) in the Q-band region. The spectra of PCM using Mn(III)Cl-porphyrin show pronounced near-infrared light absorption ( $\lambda = 770\text{ nm}$ ), which is inconsistent with the absorption spectra of similar  $\text{Mn}^{+3}$ -porphyrin in solution published elsewhere.<sup>189</sup> The appearance of this absorption band may be due to the presence of Mn(II)-bacteriochlorin impurities in commercial porphyrin.<sup>380</sup> Also, the light scattering of a pristine PVDF membrane (measured without corrections) causes the apparent absorption at wavelengths  $\lambda > 900\text{ nm}$ .

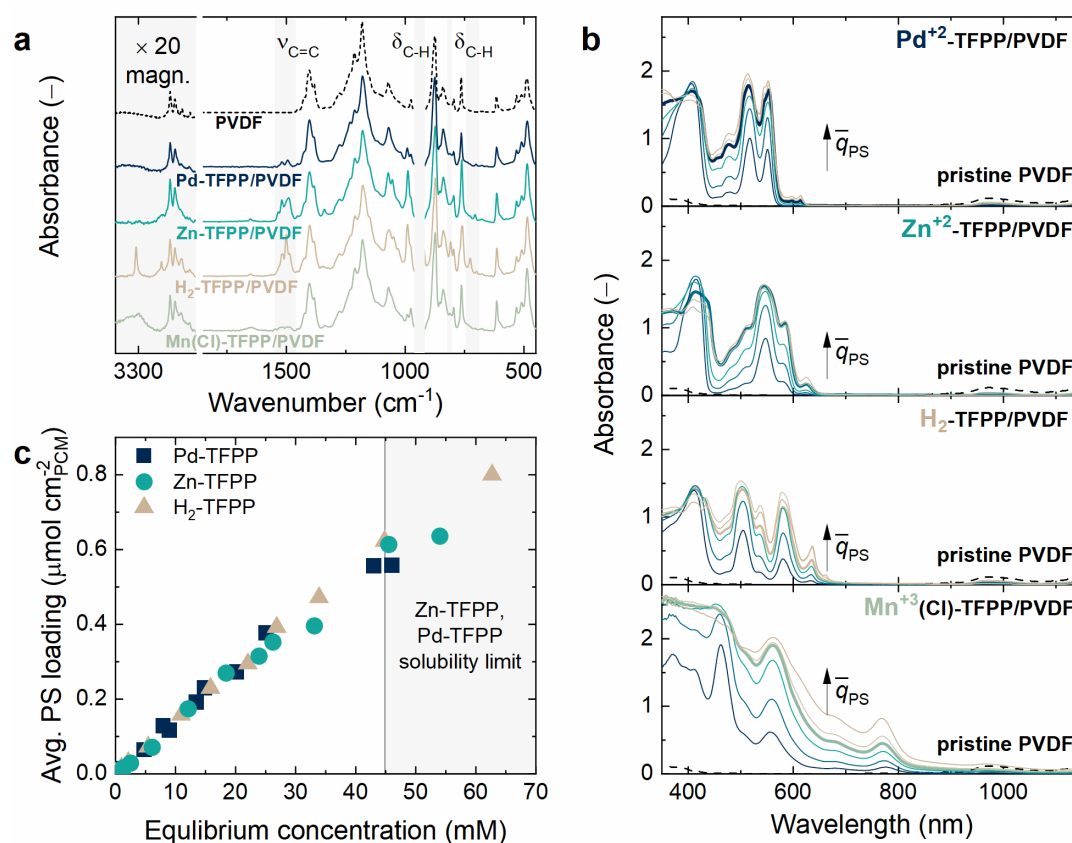


Figure 6.2: **a** The FT-IR spectra at  $\bar{q}_{PS} = (0.23 \pm 0.02)\ \mu\text{mol cm}^{-2}$ , and **b** The UV-vis absorbance spectra of the four types of PS/PVDF membranes recorded in a water-filled cuvette inside an integrating sphere at various loading (solid lines),  $\bar{q}_{PS} = 0.03\text{--}0.41\ \mu\text{mol cm}^{-2}$ , plotted against a pristine uncoated one (dashed line). **c** the PS adsorption isotherms ( $t = 4\text{ h}$ , temperature of  $(23 \pm 1)\text{ }^\circ\text{C}$ ). The absorption spectra of PCM with the reference PS loading,  $\bar{q}_{PS} = (0.23 \pm 0.02)\ \mu\text{mol cm}^{-2}$ , were marked as bold lines.

Overall, the integrated absorbance (at wavelengths 350–1150 nm) rises with the porphyrin loading ( $\bar{q}_{PS}$ ) in the following order:  $H_2$ -TFPP < Zn-TFPP < Pd-TFPP << Mn(Cl)-TFPP. Notably, the PS loading directly correlates with porphyrin concentration in solution as seen from adsorption isotherms in Figure 6.2c. Yet, at high concentrations (>45 mM), Zn- and Pd-porphyrins precipitate on the membrane surface as the solubility limit is reached. Note that increasing the amount of adsorbed porphyrin does not cause a spectral shift of the absorption (shown in Figure 6.2b) or PL peak positions (see Figure 6.3). When the porphyrin loading increases, the position of PL peak is not altered. This result provides evidence for the lack of PS molecular aggregates (via  $\pi$ - $\pi$  stacking) known to distort absorption spectra and decrease the  $^1O_2$  generation.<sup>381, 382</sup> The change in PL intensity for Zn-TFPP (at 588 nm) and  $H_2$ -TFPP (at 639 nm) was attributed to the effects of reabsorption of the emitted light.

The ability of investigated porphyrins to generate  $^1O_2$  can be quantified via infrared phosphorescence measurement (see Figure 6.4). All investigated PS demonstrate the specific emission peak at 1271 nm, which is attributed to  $^1O_2$  phosphorescence. However, due to the weak PL signal from the water-immersed PCM is weak (Figure 6.4a), measurement was not possible.

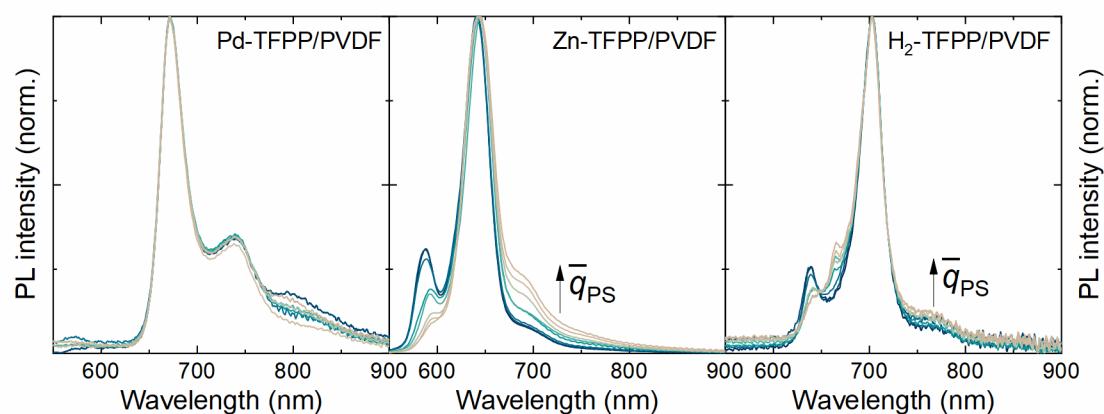


Figure 6.3: PL spectra of different Pd-TFPP-, Zn-TFPP-,  $H_2$ -TFPP/PVDF membranes recorded in Milli-Q water. PS loading varied: 0.02–0.55  $\mu\text{mol cm}^{-2}$ . The spectra were normalized to the strongest PL peak.

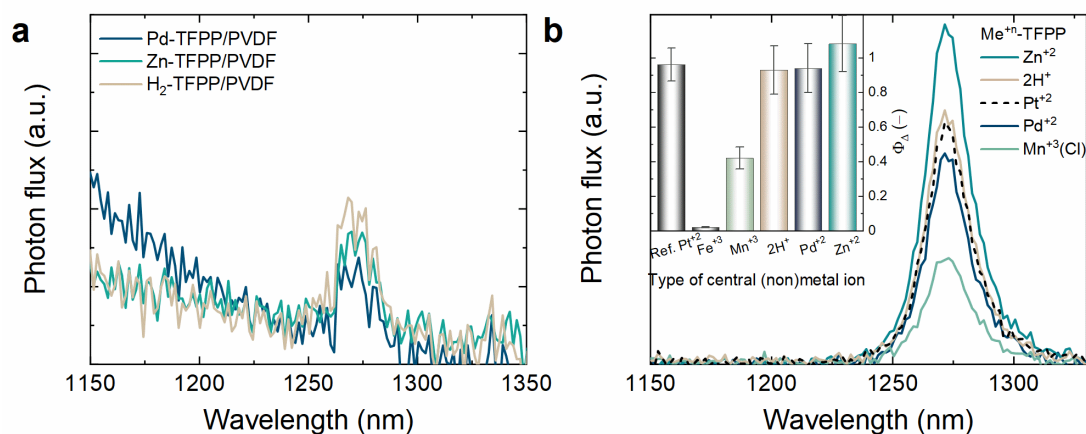


Figure 6.4: The infrared PL spectra of **a** PCMs and **b** porphyrin solutions in air-saturated ethanol. The inset: the determined values of  $^1O_2$  quantum yield generation, including that of the reference Pt-TFPP.

Instead, the PL measurements were performed in solution, as demonstrated in Figure 6.4b. The resulted spectra can be used to determine the  $^1\text{O}_2$  output of noble-metal-free PS (quantum yield) after correlation with the PL signal of the reference PS (Pt-TFPP,  $\Phi_\Delta = 0.96$  in ethanol). Zn-TFPP, H<sub>2</sub>-TFPP and Pd-containing PS demonstrate the similarly high quantum yield ( $\Phi_\Delta > 0.9$ ), whereas the quantum yield of Mn(Cl)-TFPP is substantially lower ( $\Phi_\Delta = 0.4 \pm 0.15$ ). The results of efficient  $^1\text{O}_2$  generation by noble-metal-free porphyrins suggest that the novel kinds of PS can be as effective as Pd-TFPP for SH oxidation.

## 6.3 Effect of Central Metal Ion on Photocatalytic Degradation of SH Micropollutants

### 6.3.1 Effect on Porphyrin Loading on Photocatalytic Removal of 17 $\beta$ -estradiol

To test the assumption that noble metal-free PS are comparable to their Pd-based counterparts in photocatalytic activity, the results of photocatalytic degradation of SH can be addressed. A fair comparison of intrinsic activity of different photocatalytic systems is possible when the number of photons absorbed is relatively the same. For example, at unified  $\varphi_{abs}^{ref} = 1.19 \cdot 10^{20} \text{ s}^{-1} \text{ m}^{-2}$ , the previously used (gLED, wLED) light sources and SolSim can effectively excite PCM (Figure 3.7b) and achieve the similar values of 17 $\beta$ -estradiol removal (see Figure 6.5):  $R = (73 \pm 6)\%$  using gLED,  $R = (85 \pm 5)\%$  using wLED, and  $R = (89 \pm 4)\%$  using SolSim. By following the similar procedure (described in detail in Section 3.3.2), one can compensate the difference in absorption spectra of PCM (see also Figure 6.2b).

The intensity of a broad-band light source (SolSim) has been adjusted such that  $\varphi_{abs}^{ref} = 1.19 \cdot 10^{20} \text{ s}^{-1} \text{ m}^{-2}$  ( $I_{inc}$  values presented in Table 3.5). According to the experimental protocol (Table 3.7), each photocatalytic experiment starts with a dark phase ( $V_p = 100 \text{ mL}$ ) to achieve the adsorption-desorption equilibrium (Figure 6.6a). When a mounted PCM is excited with SolSim, the concentration of 17 $\beta$ -estradiol in the permeate is drastically reduced, reaching a steady state at  $c_{p,ss}/c_f = 0.18$  for Pd-TFPP,  $c_{p,ss}/c_f = 0.64$ ,  $c_{p,ss}/c_f = 0.78$ . In contrast, the Mn(Cl)-TFPP-coated membranes do not decrease 17 $\beta$ -estradiol concentration ( $c_{p,ss}/c_f = 1.00$ ).

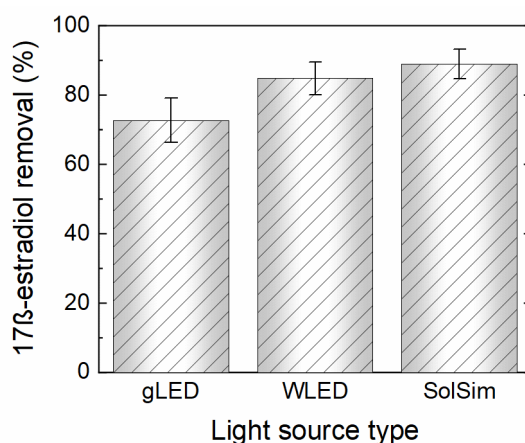


Figure 6.5: Comparison of the three different light sources ( $I_{inc}$  values reported in Figure 3.7b) in experiments on photocatalytic degradation of 17 $\beta$ -estradiol using Pd-TFPP/PVDF membranes at  $J_w = 600 \text{ L m}^{-2} \text{ h}^{-1}$ , feed solution pH  $8.2 \pm 0.2$ ,  $\bar{q}_{PS} = (0.23 \pm 0.02) \mu\text{mol cm}^{-2}$  of membrane

Note that at reference PS loading of  $\bar{q}_{PS} = (0.22 \pm 0.01) \mu\text{mol cm}^{-2}$  previously optimized for Pd-TFPP,<sup>276</sup> the Pd-porphyrin ensures the lower 17 $\beta$ -estradiol concentration in the permeate and hence the superior removal (highlighted in Figure 6.6a).

To gain further insight into the photocatalytic activity of PCM, the effect of porphyrin loading on 17 $\beta$ -removal can be examined. The full graphs showing the evolution of 17 $\beta$ -estradiol concentration in the permeate using four types of porphyrin-coated membranes can be found in Figure A.3 (Appendix). Figure 6.6b depicts the results of 17 $\beta$ -estradiol removal, which increases with the porphyrin loading and reaches at  $\bar{q}_{PS} = (0.40 \pm 0.02) \mu\text{mol cm}^{-2}$  the profound degradation results:  $R = (77 \pm 4)\%$ ,  $(52 \pm 10)\%$ ,  $(53 \pm 9)\%$  for Pd-TFPP, Zn-TFPP and H<sub>2</sub>-TFPP/PVDF, respectively. Mn(Cl)-TFPP/PVDF membranes do not reduce the concentration of 17 $\beta$ -estradiol at any porphyrin loading ( $R \approx 0\%$ ). Remarkably, the 17 $\beta$ -estradiol removal using Pd-TFPP/PVDF membranes levels off at  $\bar{q}_{PS} = 0.17 \mu\text{mol cm}^{-2}$ , which is consistent with the results shown in Chapter 5 ( $R = 79\% \pm 4\%$  for wLED excitation,  $I_{inc} = 10.0 \text{ mW cm}^{-2}$ ,  $J_w = 600 \text{ L m}^{-2} \text{ h}^{-1}$ ).

When increasing the Zn-TFPP loading from 0.41 to 0.62  $\mu\text{mol cm}^{-2}$ , the 17 $\beta$ -estradiol removal achieved with PCM drops from 52% to  $\sim 15\%$ . This dramatic (and reproducible) decrease in 17 $\beta$ -estradiol degradation can be ascribed to concentration quenching of triplet states occurring due to the high coverage of the PVDF membrane by Zn-TFPP molecules. This hypothesis agrees with the reduced triplet state lifetime observed in the work using Mg- and Pt-porphyrin films.<sup>383</sup> When the number of photons absorbed by the studied PCM is relatively close ( $\varphi_{abs}^{ref} = 1.19 \cdot 10^{20} \text{ s}^{-1} \text{ m}^{-2}$ ), the H<sub>2</sub>-TFPP and Zn-TFPP-impregnated membranes provide 1.5–3 times less 17 $\beta$ -estradiol removal compared to the membranes coated with noble metal porphyrin. Still, the membranes coated with noble-metal-free porphyrins (Zn-TFPP and H<sub>2</sub>-TFPP) exhibit the accelerated kinetics of 17 $\beta$ -estradiol oxidation<sup>384</sup> as to the benchmark PVDF-TiO<sub>2</sub> membrane<sup>372</sup> or other TiO<sub>2</sub>-decorated systems.<sup>240, 385</sup> Table 6.1 summarizes the results of work on 17 $\beta$ -estradiol degradation using TiO<sub>2</sub>- and porphyrin-coated materials.

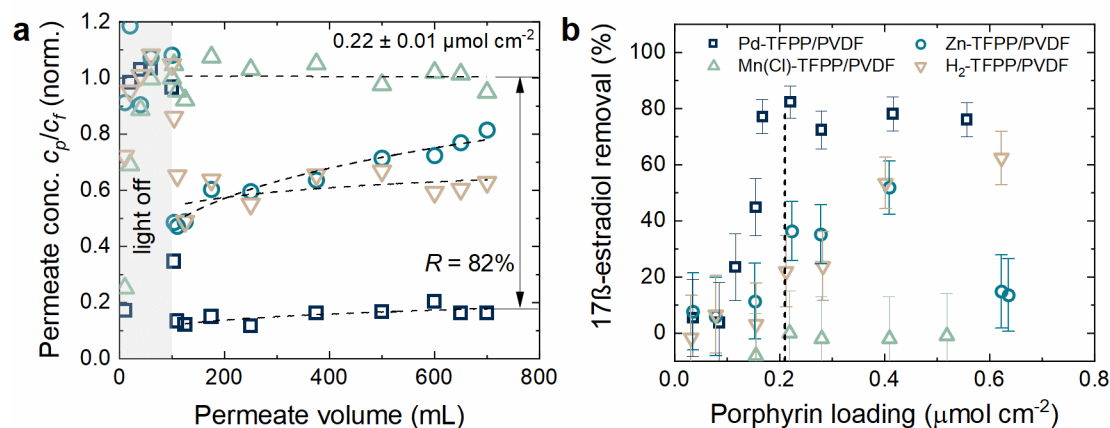


Figure 6.6: Influence of porphyrin loading on the process of 17 $\beta$ -estradiol photocatalytic degradation. **a** Evolution of normalized 17 $\beta$ -estradiol concentration in the permeate as a function of permeate volume using PCM at reference PS loading,  $\bar{q}_{PS} = (0.22 \pm 0.01) \mu\text{mol cm}^{-2}$ ; **b** 17 $\beta$ -estradiol removal versus porphyrin loading. Conditions:  $c_f = 100 \pm 10 \text{ ng L}^{-1}$ , in 1 mM NaHCO<sub>3</sub>, 10 mM NaCl solution (pH =  $8.3 \pm 0.2$ ),  $c_{rO_2} = (8.5 \pm 0.4) \text{ mg L}^{-1}$ ,  $J_w = 600 \text{ L m}^{-2} \text{ h}^{-1}$ ,  $I_{inc}$  of SolSim was adjusted to the PS type as given in Table 3.5.

Table 6.1: The summary of the results of 17 $\beta$ -estradiol degradation by TiO<sub>2</sub>- and porphyrin-decorated materials

Photocatalytic material/membrane	Light conditions (light type, $\lambda_{exc}$ , power or $I_{inc}$ )	$c_r$ , $\mu\text{g L}^{-1}$	Regime, reactor type (volume)	Observed rate constant $k_{obs}$ , $\text{min}^{-1}$	Reference
TiO <sub>2</sub> /PTFE mesh	Black FL-lamp, 8x15 W, 1.2 mW $\text{cm}^{-2}$	250	Batch, stirred tank (5000 mL)	0.16–0.2 (at 10–30 °C)	Nakashima <i>et al.</i> , 2003 <sup>385</sup>
TiO <sub>2</sub> /quartz coil	Hg-lamp, 0.27–2.51 W	817	Continuous-flow, plug-flow reactor (3.14 mL)	0.174–0.500 (0.134–0.400)	Coleman <i>et al.</i> , 2005 <sup>384</sup>
TiO <sub>2</sub> /PVDF membrane	UV lamp, 365 nm, 100W, 2.5 mW $\text{cm}^{-2}$	10	Continuous-flow, membrane reactor recirculation (feed)	0.016	Wang <i>et al.</i> , 2016 <sup>372</sup>
TiO <sub>2</sub> (P25)/porous Ti sheet	UV-LED, 365 nm 0.13 mW $\text{cm}^{-2}$	4	Batch, stirred tank (300 mL)	0.003	Arlos <i>et al.</i> , 2016 <sup>386</sup>
H <sub>2</sub> -TFPP	13x18W FL lamps, 380–700 nm, 4 mW $\text{cm}^{-2}$	5000	Continuous-flow, plug-flow reactor (~ 2 mL)	0.192	Fernández <i>et al.</i> , 2017 <sup>306</sup>
H <sub>2</sub> -TFPP/Fe <sub>3</sub> O <sub>4</sub> /SiO <sub>2</sub> nanoparticles				0.021	
TiO <sub>2</sub> /PES membrane	UV-LED, 365 nm, 10 mW $\text{cm}^{-2}$	0.1	Continuous-flow, membrane reactor (void vol. 0.022 mL)	48.0 $\pm$ 0.6 (0.80 $\pm$ 0.01 s <sup>-1</sup> )	Lotfi <i>et al.</i> , 2021 <sup>340</sup>
Pd-TFPP/PVDF membrane	White-light LED, 400–700 nm, 10 mW $\text{cm}^{-2}$	0.02–1	Continuous-flow, membrane reactor (void vol. 0.018 mL)	87.0 $\pm$ 3.5 (1.45 $\pm$ 0.06 s <sup>-1</sup> )	Lyubimenko <i>et al.</i> , 2021 <sup>341</sup>
Zn-TFPP/PVDF membrane	Solar simulator, 350–1150 nm, 80.5 mW $\text{cm}^{-2}$	0.1	Continuous-flow, membrane reactor (void vol. 0.018 mL)	38–55 (0.64–0.91) <sup>a,b</sup>	Lyubimenko <i>et al.</i> , 2022 <sup>184</sup>
H <sub>2</sub> -TFPP/PVDF membrane				23–66 (0.34–1.10) <sup>a,b</sup>	

<sup>a</sup> calculated using  $k_{obs}$  for PdTFPP as a reference value (assuming the linearity of kinetic rate law for both PS)

<sup>b</sup> determined at loadings 0.21–0.62  $\mu\text{mol cm}^{-2}$

### 6.3.2 Photocatalytic Degradation of Steroid Hormones

It has been demonstrated in Chapter 5 that Pd-TFPP/PVDF membranes efficiently remove estrone and 17 $\beta$ -estradiol, yet do not decrease the concentration of testosterone and progesterone in the permeate. The limited reactivity with singlet oxygen may be related to the chemical structure of steroid hormones: the presence of absence of phenolic moiety (Table 2.3). Whether this hypothesis is valid for selected noble-metal-free porphyrins (Zn-TFPP and H<sub>2</sub>-TFPP producing almost exclusively <sup>1</sup>O<sub>2</sub>) is investigated in the photodegradation experiments. Note that Mn(Cl)-TFPP/PVDF membranes is excluded from the study. Figure 6.7a depicts the removal of four steroid hormones by Pd-, Zn- and free-base-coated PVDF membranes. Similar to 17 $\beta$ -estradiol, high removal of estrone can be achieved with all three PCM types:  $R = (90 \pm 4)\%$  using Pd-porphyrin,  $R = (40 \pm 13)\%$  using Zn-porphyrin, and  $R = (64 \pm 7)\%$  using free-base porphyrin. When Pd/TFPP and Zn-TFPP-coated membranes are used, the poorly reproducible removal of progesterone (0–72%) is observed. Testosterone does not undergo removal by any of the three PCM studied.

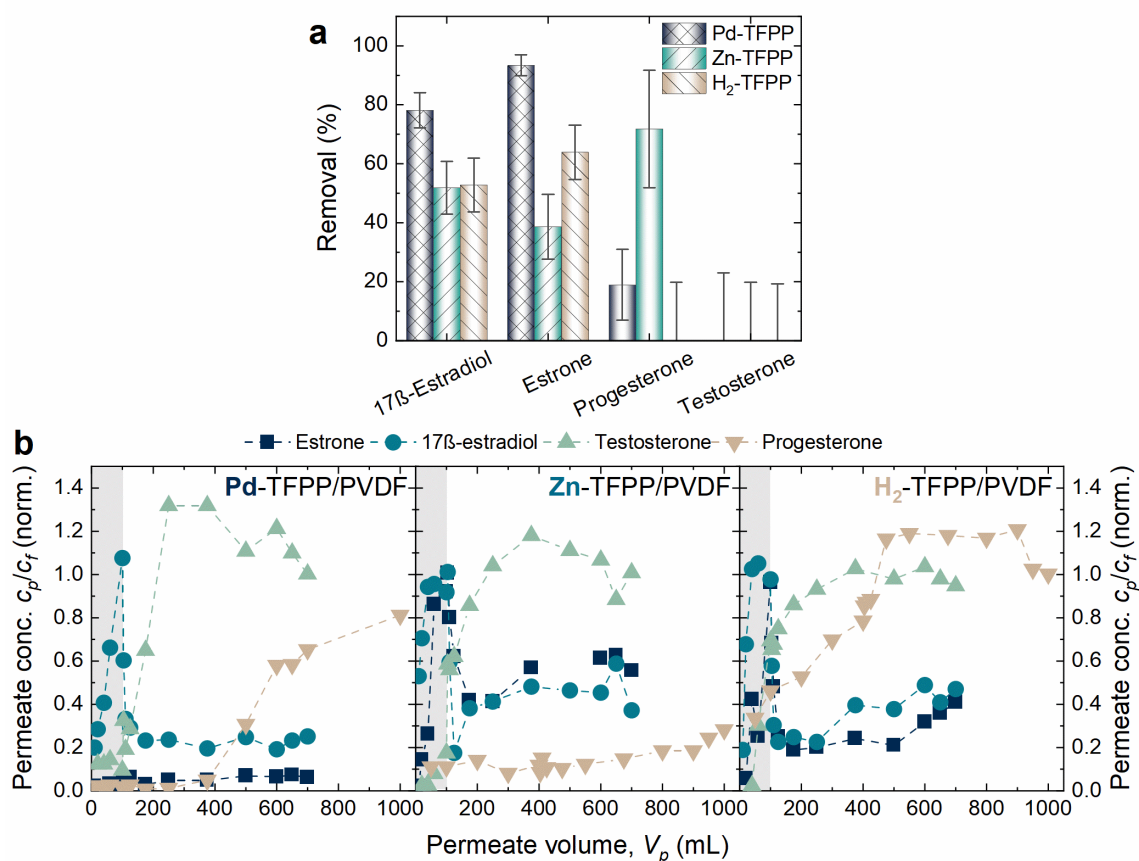


Figure 6.7: **a** Removal of SHs (estrone, 17 $\beta$ -estradiol, testosterone, progesterone). Absence of crosshatch filling of the graph bars indicates removal solely by adsorption. **b** Evolution of SH normalized concentration in the permeate as a function of permeate volume using Pd-TFPP-, Zn-TFPP-, H<sub>2</sub>-TFPP/PVDF membranes.  $\bar{q}_{PS} = (0.40 \pm 0.02) \mu\text{mol cm}^{-2}$ ,  $c_f = (100 \pm 10) \text{ ng L}^{-1}$ , background solution of 1 mM NaHCO<sub>3</sub>, 10 mM NaCl, pH =  $8.2 \pm 0.2$ ,  $c_f(\text{O}_2) = (8.5 \pm 0.4) \text{ mg L}^{-1}$ ,  $J_w = 600 \text{ L m}^{-2} \text{ h}^{-1}$ ,  $h_{nc}$  (SolSim) as given in Table 3.5.

When examining the evolution of steroid hormone concentration in the permeate (Figure 6.7b), it is seen that the concentration of progesterone and testosterone does not reach the steady-state values by the end of

the dark phase. Note that the dark phase in experiments with progesterone is longer ( $V_p = 400$  mL to compensate for the high uptake by the PVDF membranes) than that using testosterone ( $V_p = 100$  mL). Furthermore, the concentration of either of these steroid hormones in the permeate keeps rising even when SolSim is switched on. In contrast, the concentration of estrone or  $17\beta$ -estradiol in the permeate is significantly reduced upon illumination of PCM, thus indicating effective photocatalytic degradation. Overall, the duration of the dark phase has no effect on reactivity of progesterone bound to PCM with produced ROS.

Notably, both estrone and  $17\beta$ -estradiol molecules have phenolic groups (highlighted in SH chemical structures, see Table 2.3), which function as electron donors and thus promote the reaction with electron acceptors, such as singlet oxygen or other ROS.<sup>318, 320, 387</sup> Oppositely, the cyclohexanone moiety of progesterone and testosterone is electron-deficient and prone to react with electron-rich species. This observation suggests that the oxidation rate of progesterone and testosterone molecules by certain ROS ( $^1O_2$ ,  $\cdot OH$ ) can be hindered. The reaction kinetics of  $17\beta$ -estradiol oxidation is further accelerated when phenolic groups are deprotonated<sup>320</sup> (see  $pK_a$  values in Table 2.3), whereas the ketone functional groups can only be protonated ( $pK_a > 20$ ). As a future outlook, novel photosensitizers producing different types of ROS could provide the degradation of recalcitrant contaminants, such as testosterone and progesterone.

## 6.4 Limiting Factors of Photocatalytic Oxidation using Noble-Metal Free PS

### 6.4.1 Generation of $^1O_2$ as a Limiting Factor of Noble-Metal-Free Porphyrins

An important underlying assumption is that noble-metal-free porphyrin similar to Pd-porphyrin produce selective oxidizing agent, namely singlet oxygen, which actively partakes in the degradation mechanism. The hypothesis of  $^1O_2$ -mediated oxidation of SHs is supported by the following observations:

- (1) With the exception of Mn(Cl)-TFPP, the studied porphyrins highly efficiently generate the singlet oxygen in solution ( $\Phi_\Delta = 0.9-1.0$ ) as also shown in Figure 6.4, Table 6.2;
- (2) Non-selective hydroxyl radical can react with testosterone or progesterone molecules as observed in other works,<sup>388</sup> even though the degradation efficiency is 1–2 orders lower than that for estrone or  $17\beta$ -estradiol;<sup>50, 389</sup>
- (3) Hydroxyl radical involvement in oxidation can be excluded as there is no effect of methanol as a strong radical scavenger (see Figure 3.18);
- (4) The collision of PS excited state and pollutant molecule is unlikely at  $ng\ L^{-1}$  concentrations.<sup>317</sup> The formation of transient species (cation- and anion-radicals) acting as ROS can be hence ruled out;
- (5) The electron transfer to molecular oxygen ( $E^0(O_{2(aq)}/O_2^{\cdot-}) = -0.16V$ )<sup>390</sup> is excluded due to the low thermodynamic probability of superoxide anion formation (see the results of Gibbs energy calculation for photoinduced electron transfer in Table 6.3).

The first sign of limited electron transfer to molecular oxygen is seen in the small difference in redox potentials ( $< 0.2$  V). When calculated using Rehm-Weller equation (see Equation 3.16), the Gibbs energy values for photoinduced electron transfer are low ( $< -5.1$  kcal  $mol^{-1}$ ), indicating that electron-deficient porphyrins are unlikely to transfer an electron to molecular oxygen.<sup>391</sup>

Table 6.2: The summary of the photophysical properties of the porphyrins with and without noble metals

Photo-sensitizer	$\epsilon \cdot 10^3 (\lambda_{\max}),$ $M^{-1}cm^{-1}$ (nm) in DMF	$\tau_T^0, \mu s$		$\tau_S^0, ns$ measured (literature )	$\Phi_{\Delta}$ in solution, measured (literature)
		water-soaked PCM	THF		
Pd-TFPP	22.9 (517)	1145	64.6	n/a	0.95±0.14
H <sub>2</sub> -TFPP	21.8 (504)	195	n/a	14.9 (10–11) <small>204, 392</small>	0.90±0.14 (0.6–0.8) <sup>393</sup>
Zn-TFPP	25.4 (550)	18700	n/a	1.6 (1.4) <sup>394</sup>	1.05±0.15
Mn(Cl)-TFPP	8.8 (560)	n/d	n/a	12.7	0.4±0.06

Table 6.3: Summary of electrochemical parameters of the selected photosensitizers

Photo-sensitizer	First oxidation potential, V (vs. NHE) <sup>a</sup>	Excited state energy (wavelength) of the first triplet state, eV (nm)	Excited state potential $E_{ox}^{T*}$ , V (vs. NHE)	Gibbs energy for electron transfer $\Delta G_{PET}$ , kcal mol <sup>-1</sup>
Pd-TFPP	1.47 <sup>206</sup>	1.85 (671)	-0.38	-5.1
Zn-TFPP	1.56 <sup>395</sup>	1.77 (700)	-0.21	-1.2
H <sub>2</sub> -TFPP	1.73 <sup>396</sup>	1.65 (750)	+0.08	+5.5

<sup>a</sup> The conversion between different electrode potentials was realized using:  $E_{Ag/AgNO_3} = +0.27$  V vs. normal hydrogen electrode (NHE).

The final evidence for <sup>1</sup>O<sub>2</sub>-mediated process is obtained from experiments conducted in oxygen-depleted conditions. The concentration of dissolved oxygen in the feed can be reduced to trace level ( $c_{f,O_2} = 0.005$  mg L<sup>-1</sup>) by spiking the feed solution with 15 mM sodium sulfite (scavenger of dissolved oxygen).<sup>397</sup> Figure 6.8 depicts that the addition of sulfite ion excess substantially suppresses the oxidation of 17 $\beta$ -estradiol both for porphyrin with (from 78% to 6% using Pd-TFPP) and without noble metals (from 52% to 0% using Zn-porphyrin, from 53% to 22% using free-base porphyrin). These results confirm the crucial role of molecular oxygen-based ROS in 17 $\beta$ -degradation for all three porphyrin types. As the O<sub>2</sub><sup>-</sup> generation is unlikely (see above), <sup>1</sup>O<sub>2</sub> is presumably the dominant driver of photocatalytic degradation among other potentially produced ROS. Only in this case can the different results of estrone or 17 $\beta$ -estradiol removal with selected porphyrins (see Figure 6.7) be explained by uneven  $\Phi_{\Delta}$  values.

The different removal of 17 $\beta$ -estradiol achieved in experiments with the number of absorbed photons adjusted to one value ( $\phi_{abs}^{ref} = 1.19 \cdot 10^{20}$  s<sup>-1</sup> m<sup>-2</sup>) indicates the discrepancy between the  $\Phi_{\Delta}$  measurements in solution and in solid state. Hence, it is assumed that the measured quantum yield of PS in ethanol ( $\Phi_{\Delta} = 0.9-1.0$ ) does not match that after PS immobilization on a membrane. Note that the <sup>1</sup>O<sub>2</sub> phosphorescence signal of water-immersed PCM is too weak for reliable measurements. Two types of tests can lend additional support to the above given hypothesis: i) perform the photocatalytic experiments under elevated irradiance approaching to that of terrestrial sunlight (80.5 mW cm<sup>-2</sup>); ii) compare the photophysical characteristics of porphyrins in solution and in solid state.



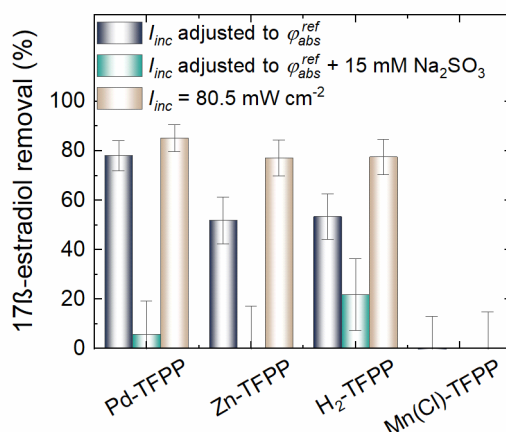


Figure 6.8: Photocatalytic oxidation of 17 $\beta$ -estradiol using Pd-TFPP-, Zn-TFPP-, H<sub>2</sub>-TFPP/PVDF membranes: under standard SolSim settings ( $I_{inc}$  adjusted to  $\phi_{abs}^{ref}$ ) and elevated illumination ( $I_{inc} = 80.5 \text{ mW cm}^{-2}$ ). At standard illumination, two types of experiments were conducted: with 15 mM Na<sub>2</sub>SO<sub>3</sub>,  $c_r(\text{O}_2) = 0.005 \text{ mg L}^{-1}$ , and without oxygen scavenger,  $c_r(\text{O}_2) = 8.5\text{--}8.9 \text{ mg L}^{-1}$ .

The first approach aims to maximize the output of <sup>1</sup>O<sub>2</sub> by simply providing more light. As displayed in Figure 6.8, H<sub>2</sub>-TFPP and Zn-TFPP-coated membranes perform by 50% better under elevated  $I_{inc}$ , whereas the 17 $\beta$ -estradiol removal ( $R = 77\text{--}78\%$ ) approaches to that of membranes with noble-metal porphyrin. Notably, the photocatalytic activity of Pd-TFPP-coated membranes barely improves (from  $R = 78\%$  to  $R = 85\%$ ), and Mn(Cl)-TFPP – tested additionally at high irradiance – is still not reactive. The results of the 17 $\beta$ -estradiol degradation studies indicate that H<sub>2</sub>-TFPP and Zn-TFPP immobilized on PVDF membranes produce less singlet oxygen than their noble-metal counterpart per quanta. This observation contrasts with the measurements of  $\Phi_{\Delta}$  in solution, where the ability to generate <sup>1</sup>O<sub>2</sub> by all three PSs was almost the same (Figure 6.4). This discrepancy may indicate a change in the photophysical properties of porphyrin in solution and after immobilization on PVDF membranes.

#### 6.4.2 Photophysical Studies of Porphyrins with and without Noble Metals

Changes in photophysical properties of the studied PS are revealed by measurements of the steady-state and time-resolved PL. Here, two parameters characterizing the photocatalytic activity of a PS can be examined: excited state lifetime and the rate of intersystem crossing (ISC). Figure 6.9a,b exhibits the considerable PL signal in porphyrin solution and upon their immobilization on PVDF membranes. In both states, Zn-TFPP, Pd-TFPP, H<sub>2</sub>-TFPP and Mn(Cl)-TFPP exhibit only one emissive state with maxima at 645, 671, 703 and 712 nm, respectively. Although Mn(Cl)-TFPP in solution showed the distinct PL and the ability to generate singlet oxygen ( $\Phi_{\Delta} = 0.45$ , Figure 6.4) its immobilized form was weakly luminescent (Figure 6.9b) and not photocatalytically active (Figure 6.6). This finding excluded the collection of time-resolved PL signal for Mn(Cl)-TFPP/PVDF membrane. Time-resolved PL spectroscopy analysis (Figure 6.9c,d) revealed that the lifetime of the excited triplet state of Pd-TFPP on PCM was significantly extended: from  $\tau_T = 65 \text{ ms}$  (in degassed THF) to  $\tau_T = 1145 \mu\text{s}$  (for PCM in deoxygenated water). Although the long-lived signal of phosphorescence (emission from triplet state) was not detected for Zn-TFPP and H<sub>2</sub>-TFPP in solution, their immobilized forms demonstrated long ( $\approx 200 \mu\text{s}$ , H<sub>2</sub>-TFPP) and ultra-long ( $\approx 18700 \mu\text{s}$ , Zn-TFPP) phosphorescence as shown in Figure 6.9d.

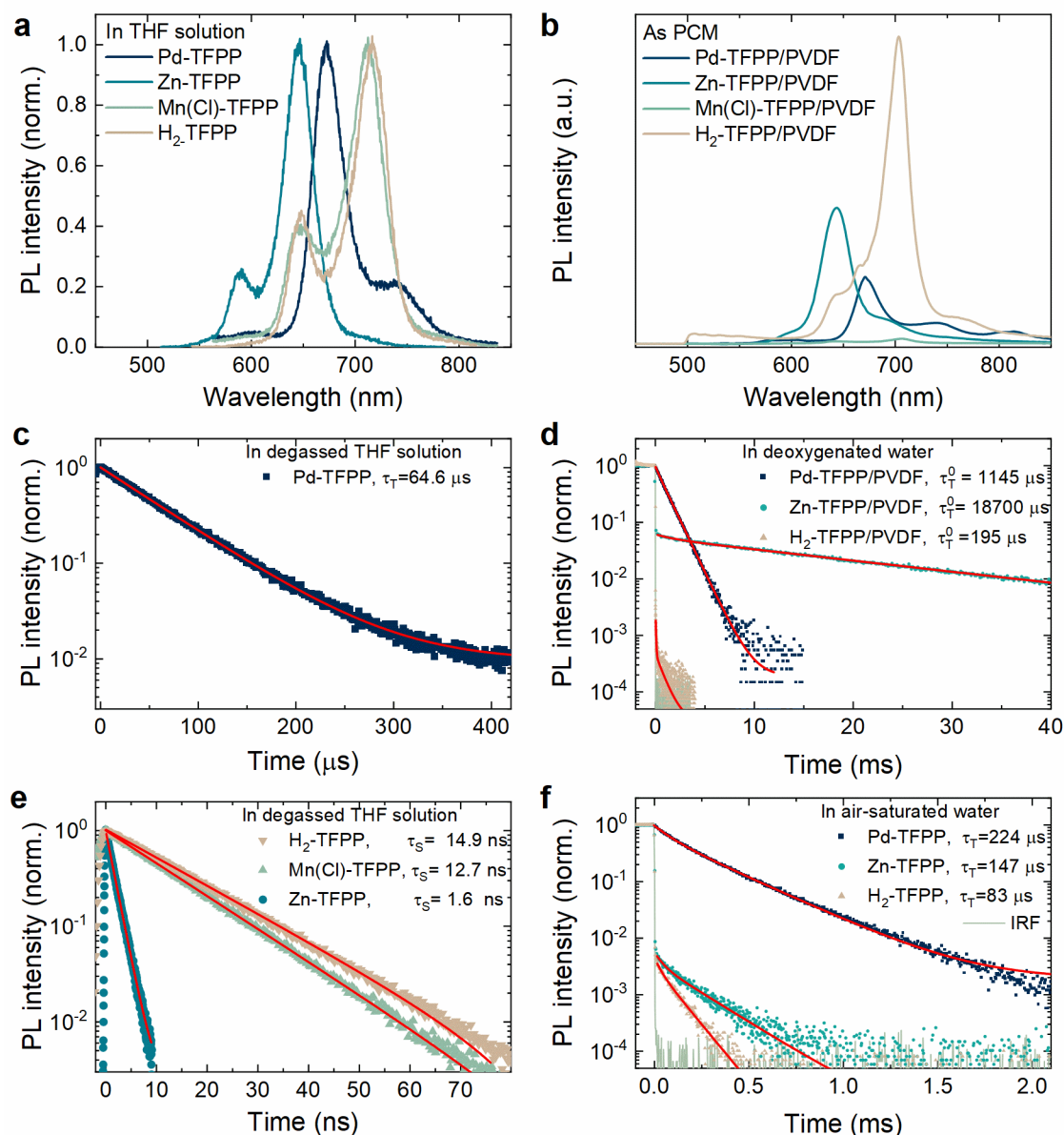


Figure 6.9: Photophysical characterization of porphyrin- and porphyrin-coated membranes with and without noble metal ion. **a, b** Steady-state and **c-f** time resolved PL studies using PCM immersed in **d** deoxygenated and **f** air-saturated water. **c, e** Results of streak camera measurements using degassed solutions of porphyrin in tetrahydrofuran. Instrument response function (IRF) depicts how the emissive components with extremely short lifetime are seen by the detector.

Note also that the PL signal for Zn-TFPP and H<sub>2</sub>-TFPP significantly dropped upon closing the laser shutter (by about 90 and 99.9%) that indicates the presence of short-lived PL components. Indeed, the streak-camera measurements confirmed it by recording the nanosecond fluorescence signal for Zn- and free-base porphyrins (Figure 6.9e). The detection of fluorescence also hints at emission from the singlet excited state of porphyrins and reduced probability of triplet state generation (low intersystem crossing, ISC). For noble-metal holding porphyrins, the ISC approaches to unity that ensures high population of porphyrin triplet states and low fluorescence. Remarkably, both ISC and triplet state affect the efficiency of <sup>1</sup>O<sub>2</sub> generation (evaluated via  $\Phi_{\Delta}$ ), which can be approximated with Equation 6.1:

$$\Phi_{\Delta} \approx \Phi_T P_T^{O_2} f_{T,\Delta}^{O_2} \quad (6.1)$$

where  $\Phi_T$  is the quantum yield of excited triplet state generation (defined largely by an ISC rate);  $P_T^{O_2}$  is the probability of quenching by dissolved oxygen molecules ( $P_T^{O_2} = 1 - \frac{\tau_T}{\tau_T^0}$ );  $f_{T,\Delta}^{O_2}$  is the ratio of the quenched porphyrin triplet states to the produced  $^1O_2$  molecules (assumed to be equal).

The time-resolved PL studies performed in air-saturated water (Figure 6.9f) revealed the significantly reduced triplet state lifetime for all three porphyrin types, thereby confirming efficient quenching by dissolved oxygen molecules. Notably, the  $P_T^{O_2}$  (a metric of quenching efficiency of PS by molecular oxygen) increased in the order: H<sub>2</sub>-TFPP (0.57) < Pd-TFPP (0.80) < Zn-TFPP (0.99). Among the studied porphyrins, the difference in  $P_T^{O_2}$  is less than a factor of two, while the triplet state population (assessed via ISC) of Zn-TFPP is orders of magnitude lower than that of Pd-porphyrin. Thus, when it comes to efficiency of  $^1O_2$  generation (estimated by  $\Phi_{\Delta}$ ), the superior  $\Phi_{ISC}$  attributed to noble-metal porphyrins prevails over the long excited-state lifetime ( $\tau_T$ ), as in Zn-porphyrin. Hence, superior photocatalytic activity of Pd-TFPP is ascribed to the efficient ISC (close to 1) compared to its noble-metal-free counterparts (reduced probability of  $^3PS^*$  formation,  $\Phi_T < 1$ ).

Together, these results imply that the light intensity is a limiting factor in the typical experiment using noble-metal-free porphyrins at  $I_{inc} = 11\text{--}14 \text{ mW cm}^{-2}$  (*reaction rate*  $\propto I_{inc}$ ). For Pd-TFPP with highly efficient ISC, the reaction kinetics remains in the reaction-limited regime at much lower irradiance,  $I_{inc} < 4 \text{ mW cm}^{-2}$  (see also Section 5.2.5) and enters the mass-transfer controlled zone at standard irradiance level. When mass transfer of one of the reactants is the limiting step, the rate of  $^1O_2$  generation is no longer affected by light intensity. Conversely, the immobilized noble-metal-free porphyrins exhibit the lower  $\Phi_{\Delta}$ , hence the reaction-controlled regime for them can expand to the standard level of SolSim illumination ( $11\text{--}14 \text{ mW cm}^{-2}$ ) and higher. Amplifying the intensity to sunlight levels provides an increase in singlet oxygen production, which is then observed as a significant improvement in 17 $\beta$ -estradiol removal using Zn- or free-base porphyrins. Thus, the conclusion of comparable photocatalytic activity of noble-metal-free and Pd-porphyrin holds true at illumination levels approaching to that contained in full terrestrial sunlight ( $80.3 \text{ mW cm}^{-2}$  within 350–1150 nm). Prolonged illumination with intense UV-visible light can have implications on the PCM stability, which is examined in the next section.

## 6.5 Changes Caused by Accelerated Aging of PCM

As pointed out in Chapter 4, stability of PS-based photocatalytic membranes is a crucial criterion for long-term solar-driven water treatment applications. In this section, photostability of novel PCM is probed after accelerated photobleaching of porphyrins with and without noble metal. The aging and treatment of collected membranes is described in the protocol for photostability experiments (see Table 3.10). Figure 6.10 portrays the visual changes of the benchmark Pd-TFPP/PVDF membrane after various periods of UV-violet light exposure. After 250 h illumination in the UV-violet-LED chamber, the membrane is completely bleached and exhibits only the residual dark-green color from the transformation products. The pristine PVDF membrane is not subject to light-induced changes and still retains its white color. The detailed information of porphyrin transformation can be obtained from the UV-Vis absorption spectra. To avoid the possible artefacts from the measurement of solid samples in the integrating sphere, the PCM are solubilized in DMF solvent. Figure 6.11a exhibits the absorption spectra normalized to the optical density at the peak wavelength of the Q-band transition.

With increasing exposure time in the UV-Violet-LED chamber up to 125 h, absorbance decreases steadily in the entire spectrum of all three porphyrins. Minor peaks appear in the region of  $\lambda = 600 \text{ nm}$  for Pd-

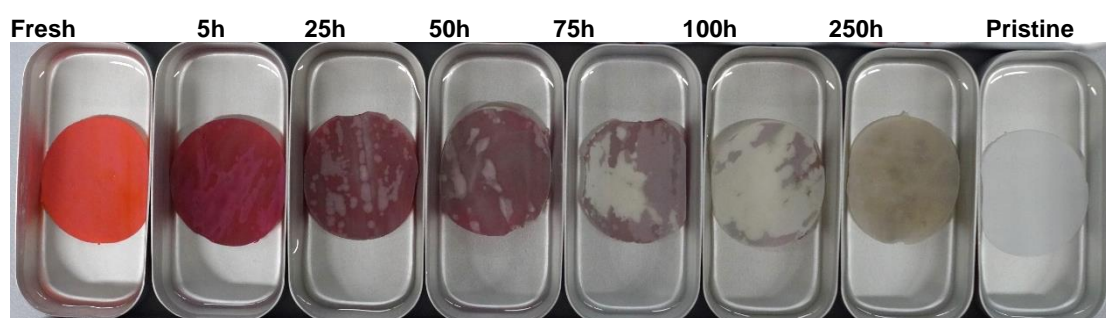


Figure 6.10: Photographs of Pd-TFPP/PVDF membranes after different time of UV-violet light exposure (365 + 405 nm,  $I_{inc} = 222 \text{ mW cm}^{-2}$ ) in the light soaking chamber (see Figure 3.10a). Note the right-hand sample showing a pristine PVDF membrane exposed to 250 h irradiation

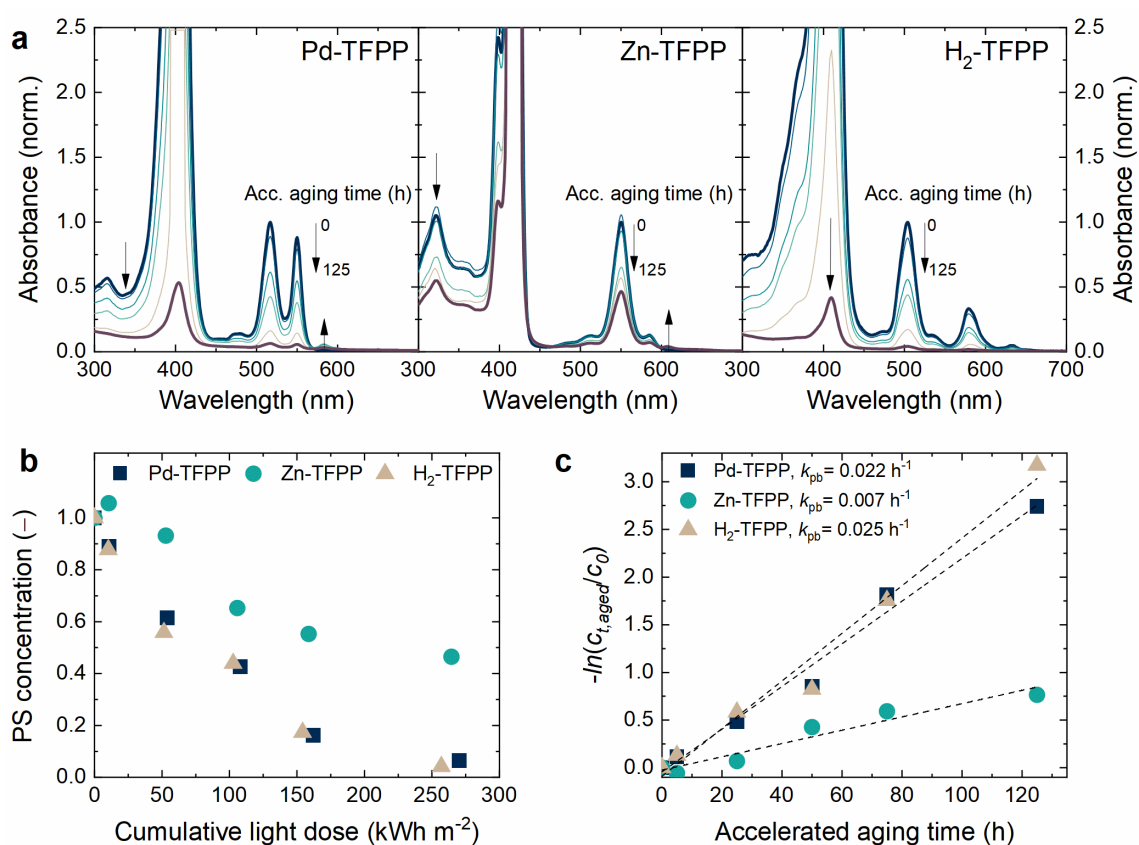


Figure 6.11: The UV-vis absorbance spectra of dissolved (in dimethylformamide) Pd-TFPP-, Zn-TFPP-, H<sub>2</sub>-TFPP/PVDF membranes after accelerated aging ( $t = 0$ –125 h). The spectra were normalized to the absorbance of a fresh membrane at  $\lambda = 518 \text{ nm}$ . **b** Effect of cumulative dose of absorbed light radiation on the remaining concentration of porphyrin on the photocatalytic membrane and **c** linear regression analysis on the logarithm of porphyrin concentration at aging time  $t$  ( $C_{t,aged}$ ) versus the value of a fresh membrane ( $C_0$ ). Conditions:  $\bar{q}_{PS} = (0.40 \pm 0.02) \mu\text{mol cm}^{-2}$ ,  $I_{inc}$  (UV-violet-LED chamber) =  $222 \text{ mW cm}^{-2}$ .

and Zn-porphyrin and start disappear after 75 h exposure time. This finding suggests the conversion of PS to other photoactive (possibly porphyrinoid) products, which also undergo further transformation. Hence, irreversible photodecomposition of immobilized porphyrins can be concluded.

Using the extinction coefficient derived from the calibration curves (see also Table 6.2), the measured absorbance is easily converted to PS concentration. Figure 6.11b displays the changes of normalized PS concentration with cumulative light dose, which is used for compensation of different absorption spectra. The concentration of porphyrins gradually decreases with cumulative light dose. Once the light dose reaches 257–270 kWh m<sup>-2</sup> (equivalent to 125 h of accelerated aging), Pd- and free-base porphyrin turn out to be completely photobleached. Notably, up to 40% of Zn-TFPP porphyrin loaded onto PVDF membrane remains intact at this exposure time. The amount of absorbed light radiation (257–270 kWh m<sup>-2</sup>) corresponds to 84–88 days of continuous illumination (considering 3.06 kWh m<sup>-2</sup> equivalent daily dose of AM1.5g solar illumination in the 350–1150 nm).<sup>357</sup>

The kinetics of PS photobleaching can be described with the pseudo-first-order model (see Figure 6.11c). The change in the natural logarithm of the normalized PS concentration varies linearly with aging time. The slope of the linear fit yields the photobleaching rate constant ( $k_{pb}$ ), which can be used as a photostability metric. For example, Zn-TFPP undergoes the degradation 3–4 times slower ( $k_{pb} = 0.007 \text{ h}^{-1}$ ) than more active Pd-TFPP ( $k_{pb} = 0.022 \text{ h}^{-1}$ ) or less active H<sub>2</sub>-TFPP ( $k_{pb} = 0.025 \text{ h}^{-1}$ ). Surprisingly, the photobleaching rates of Pd-TFPP and H<sub>2</sub>-TFPP are similar, although these PS exhibit different photocatalytic activities.

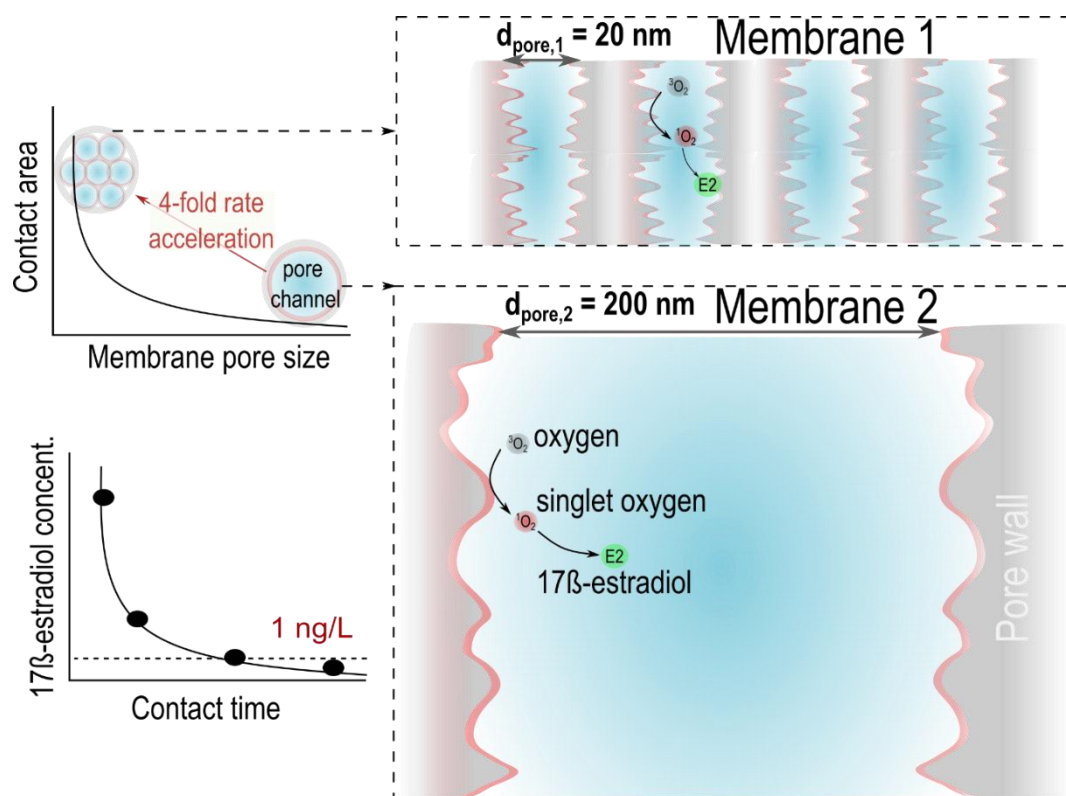
To be fit for outdoor application, photocatalytic membranes must be stable for several months in sunlight. Hence, the comparison between accelerated and outdoor photobleaching may be useful (considering only the spectral characteristics of light). As a threshold of PS photobleaching, the half-life period ( $t_{1/2,eq}$ ) can be used based on the daily average effective duration of AM1.5g illumination (3.1 h)<sup>357</sup> as described fully in . The equivalent number of days corresponding to degradation of the half of loaded PS molecules follows the order (in days): 56 (H<sub>2</sub>-TFPP) < 81 (Pd-TFPP) < 222 (Zn-TFPP). The calculated half-life of the porphyrins under study can be used as a re-coating interval for the PCM. The duration and frequency of the recoating procedure is close to those of membrane chemical cleaning (hour-long, 4 times a year) organized at water treatment plants.<sup>398</sup> As expected membrane longevity is measured in years (5–10 years for an ultrafiltration membrane)<sup>26</sup>, tens of recoating cycles would be required to get close to the lifetime acceptable for industrial applications of PCM. The current study conducted at the accelerated aging conditions (high light intensity and the high porphyrin loading) does not cover all factors governing the photobleaching rate: i) light irradiance,<sup>195</sup> ii) surface coverage by PS molecules,<sup>196</sup> iii) material of the membrane host,<sup>197</sup> iv) oxygen concentration.<sup>195</sup> Thus, it is difficult to judge the exact reason for the augmented photostability of Zn-TFPP. It is assumed that the difference lies in the combination of photophysical ( $\tau_T$ ,  $\Phi_A$ , see Table 6.2) and electrochemical (redox potential, Table 6.3) characteristics.

## 6.6 Summary

This chapter sets out that porphyrins of the similar molecular structure (H<sub>2</sub>-TFPP) exhibit different light absorption and photocatalytic activity depending on the complex with metal ions. Photodegradation experiments corroborate that Zn- and free-base porphyrins can remove 17 $\beta$ -estradiol as effectively as their noble-metal counterpart (Pd-porphyrin) under illumination corresponding to terrestrial sunlight (80.5 mW cm<sup>-2</sup>). When the light intensity is reduced (while fixing the number of absorbed photon), Pd-porphyrin outperforms the noble-metal free porphyrins: up to 64% and 62% removal for Zn- and free-base porphyrin, and the non-photocatalytically active manganese(III)-porphyrin. All observations are consistent with the <sup>1</sup>O<sub>2</sub>-mediated degradation process, thus supporting the hypothesis that light intensity is a limiting factor in typical experiments ( $I_{inc} = 11\text{--}12 \text{ mW cm}^{-2}$ ) using noble-metal free porphyrins.

In contrast to other tested porphyrins, around 40% of the Zn-porphyrin molecules in the PVDF membrane retain after 125 h of accelerated aging. This increase in stability can compensate for the high loading and strong illumination required to achieve 17 $\beta$ -estradiol removal comparable to that using Pd-TFPP. Overall, the expected lifespan of the porphyrins studied (several months), gives confidence in the possibility of outdoor application of PCM based on porphyrin complex containing earth-abundant elements.

# 7 Implications of Reactant-Porphyrin Contact in PCMs



The contents of this chapter have been published in the separate work. Figures and Tables have been adapted with permission from Lyubimenko, R. et al. (2022);<sup>251</sup> Copyright 2022 Elsevier. The citations to the original work in the following text are omitted.

**Lyubimenko, R.;** Turshatov, A.; Welle, A.; Weidler, P. G.; Richards, B. S.; Schäfer, A. I. (2022). Enhanced photocatalytic efficiency via improved contact in a solar-driven membrane reactor for steroid hormone removal. *Chem. Eng. J.*, 451, 138449.

## *Acknowledgments and Contributions*

The core experiments were designed by the author, Andrey Turshatov (IMT), Bryce S. Richards (IMT), and Andrea I. Schäfer (IAMT). The argon adsorption/desorption isotherms of pristine PVDF membranes were recorded by Dr. Peter G. Weidler (IFG). The ToF-SIMS analysis of Pd-porphyrin-coated membranes was conducted by Dr. Alexander Welle (IFG). The measurements of porosity (helium pycnometry, mercury intrusion method) and pore size distribution (mercury intrusion method) were carried out by Margarete Offermann (IAM) under the guidance of Dr. Joachim Binder (IAM). Data analysis was performed by the author with the support of Andrey Turshatov, Bryce S. Richards, and Andrea I. Schäfer.

## 7.1 Introduction

Fast heterogeneous reactions are controlled by the rate of mass transfer of reactants to the catalyst surface. In Chapter 5, it was concluded that the mass transfer of reagents to and from the PCM surface is efficient due to the high rate constant of 17 $\beta$ -estradiol oxidation ( $k_{\text{obs}} = 1.45 \text{ s}^{-1}$ ). The findings also presented in Chapter 5 revealed that the rate of 17 $\beta$ -estradiol degradation is likely heterogeneous and controlled by diffusion at low-to-medium water flux values and high irradiance levels. It is hence anticipated that improving the contact between reactants and the PS-coated membrane surface can boost the photocatalytic activity.

In PCM, the contact between water-borne reactants and immobilized porphyrin molecules is determined by i) the contact area; and ii) the contact time available for production and reaction with the  $^1\text{O}_2$  formed in situ. The contact area of a PCM – estimated by active surface area-to-volume ratio – depends on the choice of a pristine membrane. Choosing membranes with small pore sizes can provide a larger surface area. In addition, the diffusion distance in narrow membrane pore channels is reduced, which reduces mixing time and improves contact. To ensure almost complete SH removal and to bring the 17 $\beta$ -estradiol concentration to the regulatory value of  $1 \text{ ng L}^{-1}$ , the contact time need to be increased according to the membrane type.

### Objectives

To test the hypothesis of whether the improved contact achieved by greater contact area and longer contact time in PCM will contribute to the SH degradation process, this chapter pursues the following scientific objectives:

- i. Investigate the role of contact area in the 17 $\beta$ -estradiol degradation (removal and disappearance rates) using photocatalytic membranes with different pore sizes;
- ii. Demonstrate the effect of longer contact time in the stack of small-pore PCMs on the photocatalytic degradation of 17 $\beta$ -estradiol;
- iii. Determine the degradation of other SHs using the PCM with large surface area and small pore size.

A short summary with key results concludes the chapter.

### Modification of the Experimental Filtration System

The photocatalytic filtration set-up remained largely unchanged from the previous chapter. A low-range pressure sensor (0.4 bar) was installed in the feed line for testing permeability and photocatalytic degradation of microfiltration membranes, while a high-range pressure sensor was used for UF-based PCMs. The experimental protocol to be followed was as given in Table 3.7.

## 7.2 Mass Transport Limitation in PCMs

The positive effect of water flux ( $J_w$ ) on the oxidation rate of 17 $\beta$ -estradiol using Pd-TFPP-coated PVDF membranes (MP200,  $\bar{d}_{\text{por}} = 200 \text{ nm}$ ) has been outlined for  $I_{\text{inc}} = 10.0 \text{ mW cm}^{-2}$  (wLED) in Figure 5.2 (Chapter 5). As water flux is directly related to the velocity in the pore channels, one can obtain the insights into the rate-controlling step of 17 $\beta$ -estradiol oxidation at different irradiance levels.



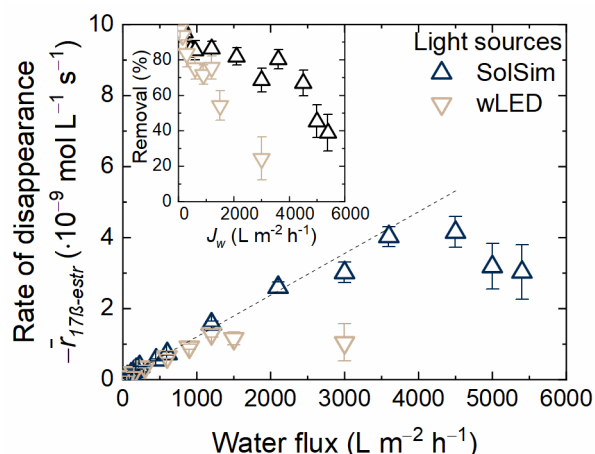


Figure 7.1: Evolution of the rate of 17 $\beta$ -estradiol disappearance as a function of water flux using the reference MP200 membrane,  $\bar{q}_{pS} = (0.22 \pm 0.02) \mu\text{mol cm}^{-2}$  illuminated by one of the light sources: wLED at  $I_{inc} = (10 \pm 0.1) \text{ mW cm}^{-2}$  and SolSim at  $I_{inc} = (81.0 \pm 0.6) \text{ mW cm}^{-2}$ . The inset: the change of 17 $\beta$ -estradiol removal with  $J_w$ .

Figure 7.1 depicts the evolution of  $\bar{r}_{17\beta\text{-estr}}$  as a function of the  $J_w$  through the reference MP200 membrane under standard wLED illumination and under abundance of light using SolSim. The SolSim was operated at intensities close to sunlight in the 350–1150 nm wavelength region  $I_{inc} = (81.0 \pm 0.6) \text{ mW cm}^{-2}$ . The  $\bar{r}_{17\beta\text{-estr}}$  gradually increases with the water flux with either of the two light sources. At high water flux the  $\bar{r}_{17\beta\text{-estr}}$  levels out and reaches plateau at  $J_w > 1200 \text{ L m}^{-2} \text{ h}^{-1}$  (wLED) and at  $J_w > 3600 \text{ L m}^{-2} \text{ h}^{-1}$  (SolSim). While high water flux in the PCM promotes the process of 17 $\beta$ -estradiol degradation, the higher  $J_w$  reduces contact time and thus impairs the achieved removal (see the inset of Figure 7.1). For instance, the 17 $\beta$ -estradiol removal drops i) from 86% to 67% ( $J_w$  increasing from 1200 to 4500  $\text{L m}^{-2} \text{ h}^{-1}$ ) for the SolSim; and ii) from 76% to 24% ( $J_w$  increasing from 1200 to 3000  $\text{L m}^{-2} \text{ h}^{-1}$ ) for the wLED.

The improvement in  $\bar{r}_{17\beta\text{-estr}}$  at higher water flux indicates that the rate of 17 $\beta$ -estradiol degradation is limited by external mass transfer, that is, contact between the reactants and the immobilized porphyrin. The appearance of a plateau for  $\bar{r}_{17\beta\text{-estr}}$  marks the transition of the overall reaction rate from the mass-transfer control to the reaction-rate control. The water flux corresponding to the change of the rate-limiting step depends on the irradiance of the light source, indicating that the higher irradiance level corresponds to the higher value of limiting  $\bar{r}_{17\beta\text{-estr}}$ . Consequently, an increase in the irradiance level should be accompanied by the establishment of a higher water flux through the PCM. Thus, the photocatalytic process is free from the limitation of mass transfer steps.<sup>218</sup> Other studies on the decomposition of methylene blue, salicylic acid in a continuous-flow mode also report two operating regimes: a linear and nonlinear increase in reaction rate by changing  $J_w$ .<sup>399-401</sup>

The real-scale process is likely to maintain a low to medium water flux ( $J_w < 1200 \text{ L m}^{-2} \text{ h}^{-1}$ ) through the PCM for the following reasons: i) moderate transmembrane pressure (directly related to energy costs), and ii) the tendency to almost completely eliminate SH in one pass. Further efforts to enhance the degradation kinetics without changing  $J_w$  should be aimed at facilitating the mass transfer steps via improved contact inside the PCM. Reagent contact with the active phase (porphyrin) can be improved in reactors characterized by a large surface area per unit volume ( $a'_V$ ,  $\text{m}^2 \text{ m}^{-3}$ ). In photoreactors such as PCMs,  $a'_V$  is determined by the choice of membrane type.

## 7.3 Influence of Membrane Type on PCM Characteristics

### 7.3.1 Small-Pore Size Membranes Provide the Large Surface Area

The hypothesis that narrowing the pore channels can contribute to an increase in surface area was tested by selecting six PVDF membranes with different mean pore sizes. Figure 7.2a exhibits the SEM images revealing the top surface morphology of the PVDF membranes. The top surface of the ultrafiltration (NM20) membranes has the smallest pores compared to other microfiltration membranes ( $\bar{d}_{por} = 0.1\text{--}0.45\ \mu\text{m}$ ). This observation is in compliance with the  $\bar{d}_{por}$  values provided in Table 3.3 except for the top surface of HW650 membrane showing low porosity, with pores on the same scale as the NM20 membrane. Noteworthy, HW650 is a multilayer membrane consisting of a thin (5–10  $\mu\text{m}$ ), low-porosity PVDF film casted onto a microfiber mesh (Figure 7.2b). The thickness of HW650 (mesh and PVDF layers) and other symmetrical PVDF membranes was determined from the low-magnification SEM images of membrane cross-section (Figure 7.2c) and summarized in Table 3.3. All the examined membranes are thick (90–130  $\mu\text{m}$ ) compared to the NM20 ultrafiltration membranes (25–30  $\mu\text{m}$ ).

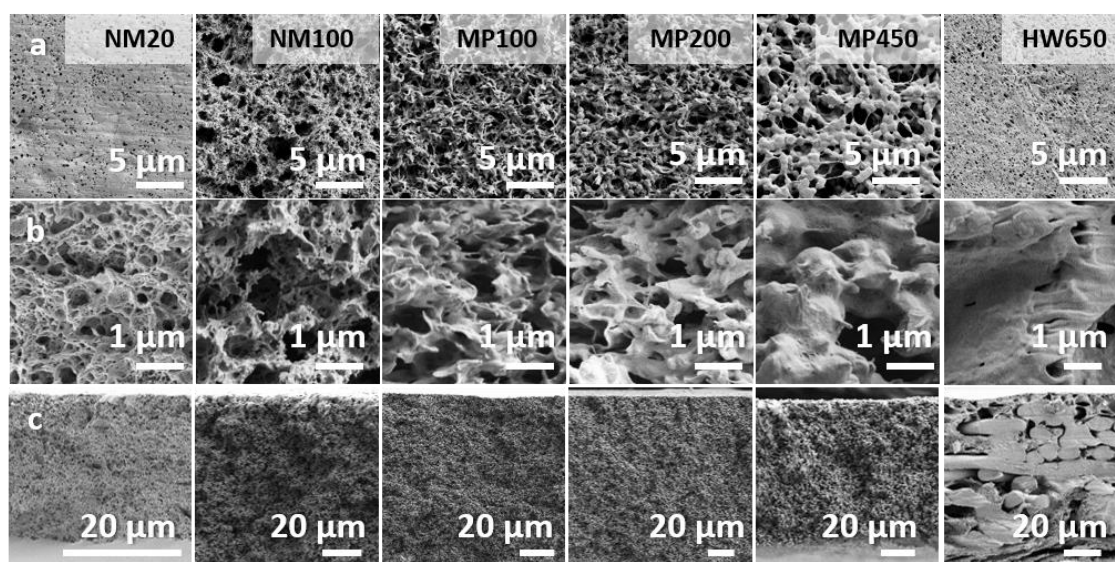


Figure 7.2: **a** Top view and **b, c** cross-sectional (high and low magnification) SEM images of examined pristine PVDF membranes.

The morphology parameters affecting  $a'_V$  (surface area, pore size, porosity) are inextricably linked in porous materials, such as adsorbents or membranes<sup>402</sup>. Small-pore size PVDF membranes offer the large contact area, provided that the membrane porosity remains unaffected. To check whether this is true for the selected membranes, the median pore size and the specific surface area ( $a_s$ ) of pristine PVDF membranes were correlated. The median pore size was determined experimentally from mercury porosimetry, whereas the specific surface area was derived from argon adsorption-desorption isotherms using both the BET ( $a_{s,BET}$ ) and DFT ( $a_{s,DFT}$ ) models. The  $a_{s,BET}$  values are on average 22% greater than the  $a_{s,DFT}$  values. The argon adsorption/desorption isotherms were recorded to estimate the specific surface area of pristine PVDF membranes (Figure 7.3a). The pore size distribution of these membranes was obtained by mercury intrusion porosimetry and demonstrated in Figure 7.3b. Additionally, the median pore diameter of the membranes was calculated using the porometer software that was used in the analysis below.

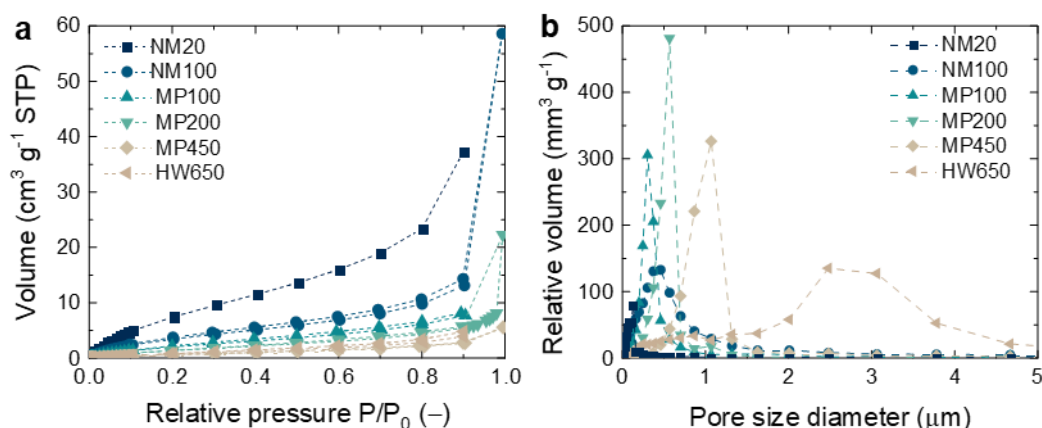


Figure 7.3: **a** The argon adsorption/desorption isotherms at 87K for the six types of pristine PVDF membranes after 24 h degassing at 95 °C. The number in the membrane label indicates the mean pore size (in nm) provided by the manufacturer; and **b** Pore size distribution of all six types of PVDF membranes obtained by mercury intrusion porosimetry.

Figure 7.4a outlines that the surface area and the pore size of pristine PVDF membranes are conversely related to each other. Furthermore, ultrafiltration (NM20) membrane provides 2–10 times more surface area than microfiltration membranes. The pore volume related to mesoporosity of NM20 membranes ( $V_{\text{por}, < 25\text{nm}} = 0.045 \text{ cm}^3 \text{ g}^{-1}$ ) is almost by an order of magnitude higher than of other microfiltration membranes ( $V_{\text{por}, < 25\text{nm}} < 0.007 \text{ cm}^3 \text{ g}^{-1}$ ). These findings indicate that the greater  $a_s$  of ultrafiltration NM20 membranes is due to the larger volume of mesopores rather than to differences in membrane porosity, as evidenced by the relatively narrow range of porosity values ( $\psi_m = 40\text{--}60\%$ ) shown in Figure 7.4b. The data obtained by the methods of helium pycnometry and mercury intrusion porosimetry are consistent with the manufacturer's data even for thin NM20 ultrafiltration membranes.

The surface area available for the adsorption of PS molecules can affect the porphyrin loading into the membrane. All six types of PVDF membranes impregnated with Pd-TFPP using low, middle, and high concentration solutions demonstrate three recurring trends of relative porphyrin loading ( $q_{\text{PS}}$ , wt%) shown in Figure 7.4c. When increasing Pd-TFPP solution concentration from 5 to 30 mM, the porphyrin loading increases by 4–5 times. It is noteworthy that twice as dense porphyrin loading can be achieved on NM20 ultrafiltration membranes, which also exhibit the higher  $a_s$ .

The filtration characteristics of PVDF membranes with different mean pore size were evaluated by measuring the water permeability of pristine and PS-coated membranes. Compared to other membrane types, NM20 membranes are subject to the lower water permeability ( $L_p = 75\text{--}110 \text{ L m}^{-2} \text{ h}^{-1} \text{ bar}^{-1}$ , see Figure 7.4d), which corresponds to the ultrafiltration process.<sup>403</sup> Likewise, the range of  $\Delta P$  in pressure-flux plots (Figure 7.5) also indicates that NM20 membrane (0–8 bar) requires the much higher pressure compared to MF-membrane counterparts (0–0.5 bar). The measured permeability of the tested membranes is directly related to the median pore size shown in Figure 7.4a. At higher PS loading the measured water permeability decreased for all membranes other than the MP450 membrane.

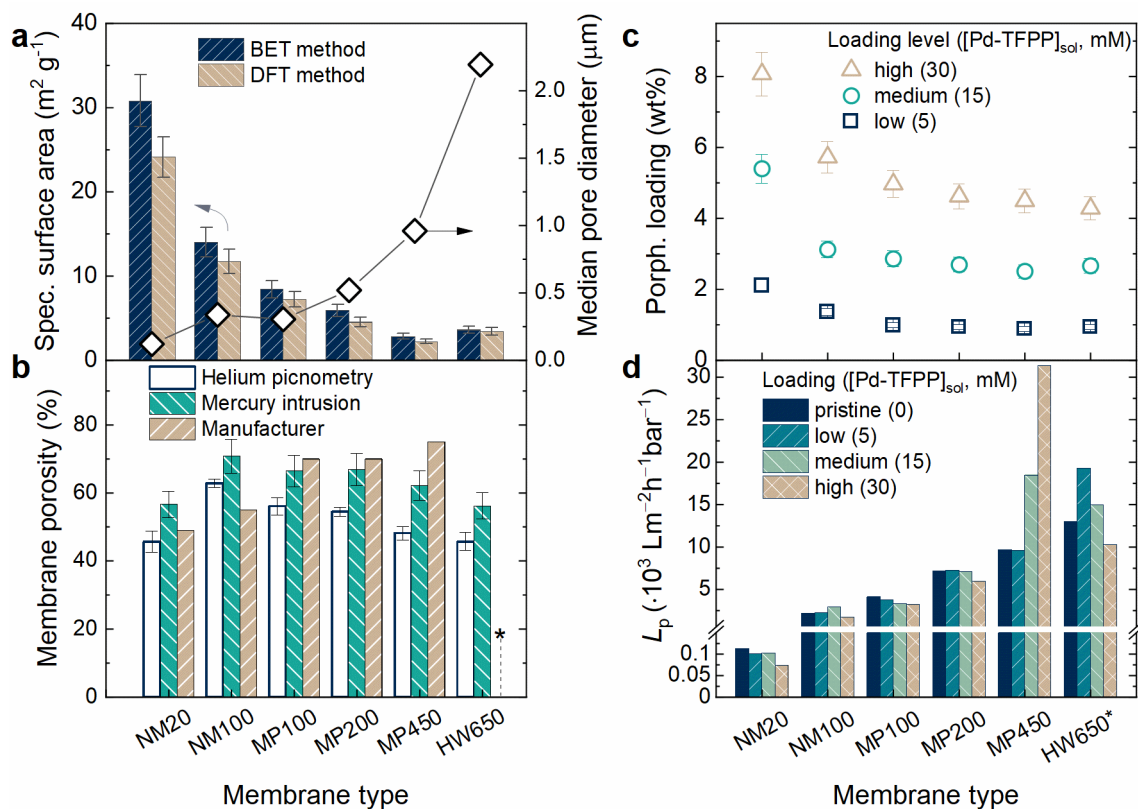


Figure 7.4: **a** Specific surface area of pristine PVDF membranes obtained from BET/DFT analysis and plotted as a function of the median pore size; **b** Membrane porosity (experimental and provided by manufacturer) of pristine PVDF membranes; **c** Porphyrin loading (in wt%); and **d** pure water permeability of PCM prepared from low (5 mM), medium (15 mM) and high (30 mM) Pd-TFPP solutions.

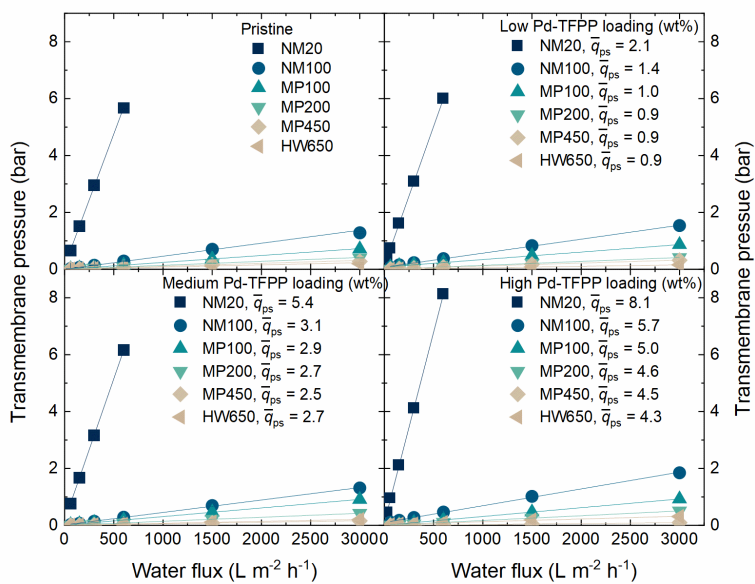


Figure 7.5: The pressure-water flux graphs obtained from the filtration experiment (dead-end mode) for evaluation of permeability for pristine and porphyrin-coated membranes (at three levels of PS loading).

The degree of light penetration through the PCM is characterized by the UV-Vis spectra recorded in transmission mode (Figure 7.6a). Increasing porphyrin loading diminishes the transmittance in the whole measurement range (350–1150 nm) that is attributed to absorption, reflection and scattering effects. Among the examined types of PVDF membranes, the thickest MP200 is the least transparent (<2% at the highest loading). Despite the twice higher  $q_{PS}$ , NM20 membranes transmit light the most (up to 17% at the highest loading) in the excitation region of Pd-TFPP (350–600 nm). In the regions without light absorption by Pd-TFPP (above 600 nm), there is a loss of transmittance due to strong scattering and reflection of light. The fraction of light available for ROS generation is presented in Figure 7.6b as transmittance ( $\bar{T}$ , %), which is spectral transmittance integrated in the 350–600 nm wavelength region (see the integrated and spectral definitions defined in Table 2.9). The  $\bar{T}$  decreases with the porphyrin loading and is conversely proportional to the membrane thickness: NM20 > NM100 > MP450 > MP100  $\approx$  HW650 > MP200. If neglecting the light scattering of porphyrin, the corresponding integral of absorbance ( $\bar{\alpha}$ ) can be determined. An example of  $\bar{\alpha}$  for NM20 membrane is shown Figure 7.6b.

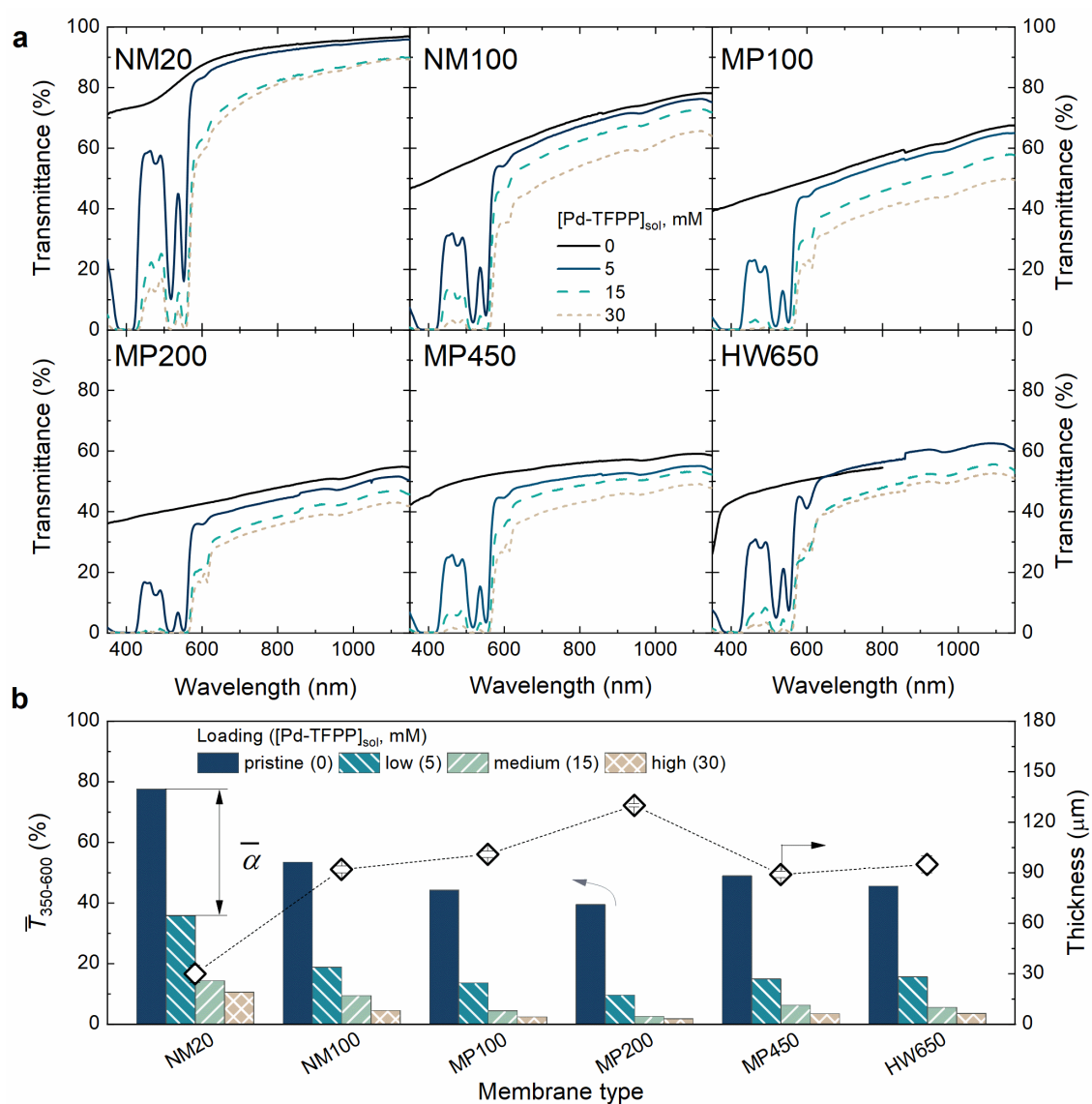


Figure 7.6: **a** UV-Vis transmittance spectra; and **b** the integral of transmittance for the wavelength region of 350–600 nm ( $\bar{T}_{350-600}$ ) of pristine and Pd-TFPP-coated PVDF membranes. The determined light absorbance (%) is shown exemplary for the NM20 membrane ( $\bar{\alpha}=42\%$ ).

Figure 7.7 provides the full data of  $\bar{\alpha}$  values, which serve as an estimate of light utilized for ROS generation. The value of  $\bar{\alpha}$  was calculated by subtracting the transmittance of the pristine PVDF membrane in the 350–600 nm wavelength region from the corresponding PCM. The significant rise of absorbance is observed when increasing the Pd-TFPP concentration from 5 to 15 mM: ranging from 1.2-fold (MP200) to 1.5-fold (NM20). Further increasing the Pd-TFPP concentration leads to slight improvement in absorbance (by 1–5%).

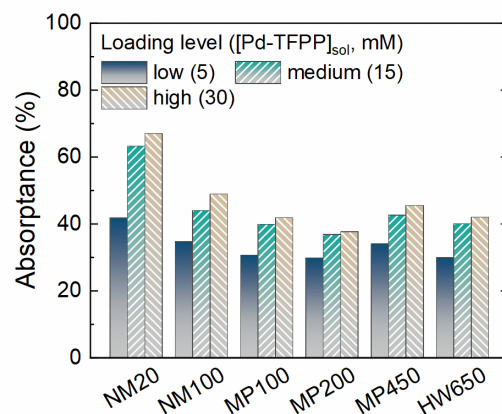


Figure 7.7: Integral of absorbance ( $\bar{\alpha}$ , %) in the excitation region (350–600 nm) of porphyrin-coated PVDF membranes prepared from 5, 15, 30 mM solutions of Pd-TFPP.

### 7.3.2 Impact of the Membrane Type on 17 $\beta$ -estradiol Degradation

The examined PVDF membranes exhibiting the various  $a_S$  can affect the contact area and thus promote the contact between the reagents and the immobilized photosensitizer. Single-pass photocatalytic experiments using six different Pd-TFPP/PVDF membranes may provide evidence for the proposed hypothesis. Similar to the studies conducted in the previous chapters, degree of removal and rate of disappearance determined after collecting 700 mL permeate serve as important metrics of effectiveness and efficiency of degradation process (Figure 7.8). For these studies, 17 $\beta$ -estradiol was chosen as the type of SH micropollutant with the highest estrogenic potency. To better understand the role of membrane type in the degradation process, each membrane type was tested at three loading levels (low, medium, and high) corresponding to 5, 15, 30 mM Pd-TFPP solutions and at the standard  $J_w = 600 \text{ L m}^{-2} \text{ h}^{-1}$  ( $\bar{t}_{con} < 1 \text{ s}$ ).

Figure 7.8a reveals that all PCMs except HW650 provide significant removal of 17 $\beta$ -estradiol ( $R_{17\beta\text{-estr}} = 70\text{--}90\%$ ) at loading level denoted as high (30 mM Pd-TFPP solution). At loading level denoted as medium (15 mM solution), the membranes with larger pores (MP450, HW650) and NM100 exhibit the lower removal ( $R_{17\beta\text{-estr}} = 40\text{--}60\%$ ) compared to other membranes (73–85%). The application of PCMs made from microfiltration membranes soaked in 5 mM Pd-TFPP solutions (low loading level) achieves by far the lowest 17 $\beta$ -estradiol removal ranging from 9% to 27%. Irrespective of porphyrin loading, NM20 ultrafiltration membranes provide high degree of 17 $\beta$ -estradiol removal ( $R_{17\beta\text{-estr}} = 78\text{--}83\%$ ). NM20 membranes at all three loading levels exhibit four times higher  $\bar{t}_{17\beta\text{-estr}}$  than other microfiltration membranes ( $\bar{d}_{por} = 0.1\text{--}0.65 \mu\text{m}$ ).



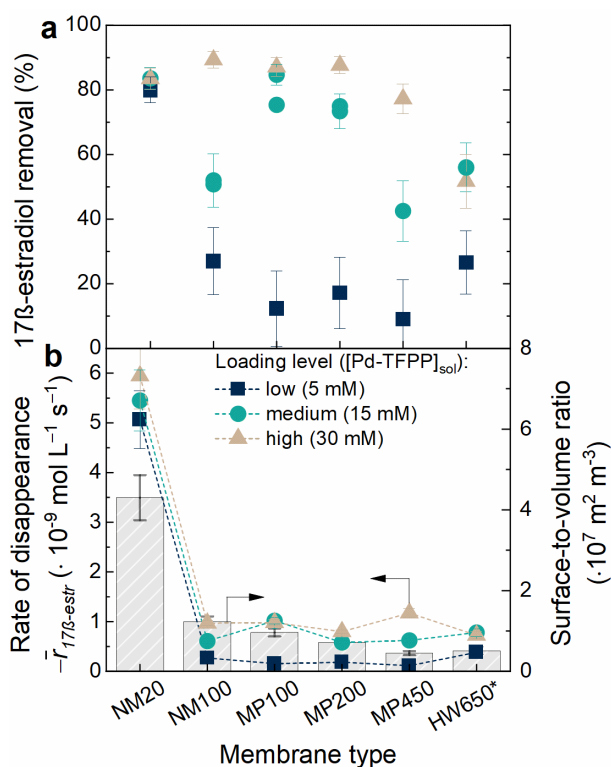


Figure 7.8: Photocatalytic activity of Pd-TFPP/PVDF membranes at low, medium, and high PS loading prepared from 5, 15, and 30 mM porphyrin solution, respectively. **a** Removal, and **b** the corresponding disappearance rate of 17 $\beta$ -estradiol ( $\bar{r}_{17\beta\text{-estr}}$ ) plotted against the surface-to-volume ratio of membranes.  $J_w = 600 \text{ L m}^{-2} \text{ h}^{-1}$ ,  $I_{inc} = (14.5 \pm 0.5) \text{ mW cm}^{-2}$ ,  $C_f = (105 \pm 10) \text{ ng L}^{-1}$ ,  $\text{pH} = 8.2 \pm 0.2$ .

Since the degraded amount of 17 $\beta$ -estradiol is normalized to the contact time (adopted as hydraulic residence time), the exhibited  $\bar{r}_{17\beta\text{-estr}}$  values are decoupled from the difference in thickness or porosity of the membranes used. A conceivable explanation for the superior  $\bar{r}_{17\beta\text{-estr}}$  using NM20 membranes is the greater surface-to-volume ratio ( $a'_V = 4.5 \cdot 10^7 \text{ m}^2 \text{ m}^{-3}$ ) compared to other PVDF membranes ( $a'_V = 0.5\text{--}1.2 \cdot 10^7 \text{ m}^2 \text{ m}^{-3}$ ) – all values shown in Figure 7.8b. The parameters used for calculation of  $a'_V$  and the corresponding errors are summarized in Table 3.9. The above findings indicate that PCMs made from NM20 membranes differ greatly from other PVDF membranes with respect to photocatalytic activity.

## 7.4 Role of Contact Time in the 17 $\beta$ -estradiol Degradation

### 7.4.1 Porphyrin Depth Distribution in Single and Stacked PCMs

Complete elimination of 17 $\beta$ -estradiol requires a longer contact time, which must correlate with the PCM thickness. The reference MP200 membrane employed in the studies presented in Chapters 5–7 is by far the thickest (Figure 7.2c), and it has a porphyrin-depleted central region of 100–120  $\mu\text{m}$  (see also Figure 4.3). It can be hence assumed that the distribution of porphyrin across the PCM may be bound to the improved photocatalytic activity of NM20 membranes. Considering the higher relative PS loading ( $q_{ps}$ ) in NM20-based PCMs, it is necessary to explore the depth profile of Pd-TFPP in PCMs.

Figure 7.9a shows the chemical mapping of Pd<sup>+</sup> ions in MP200 and NM20 membranes obtained from ToF-SIMS analysis of PCM cross section. Since the lighter color attributes to the higher Pd<sup>+</sup> signal (note the logarithmic scale in Figure 7.9a), a more uniform change in Pd<sup>+</sup> signal intensity is observed across the thickness of the NM20 membrane (in the *z*-direction). As Pd<sup>+</sup> signal corresponds to that of the intact Pd-TFPP molecules, the evolution of Pd<sup>+</sup> signal intensity in the *z*-direction can be converted to the porphyrin depth distribution. Figure 7.9b outlines the Pd-TFPP depth distribution ( $\bar{q}_{PS,z}$ , nmol cm<sup>-2</sup> μm<sup>-1</sup>) corresponding to the porphyrin loading. The procedure for conversion of the Pd<sup>+</sup> ion signal intensity into the depth profile of porphyrin is described in Materials and Methods (Section 3.5.2). The highest amount of PS is located in the top surface 10–15 μm regions of the NM20 membrane ( $\bar{q}_{PS,z} = 3\text{--}5$  nmol cm<sup>-2</sup> μm<sup>-1</sup>) and the MP200 membrane ( $\bar{q}_{PS,z} = 1\text{--}3$  nmol cm<sup>-2</sup> μm<sup>-1</sup>). The middle and the bottom regions of MP200 membranes are relatively depleted with porphyrin, ( $1.4 \pm 0.8$ ) nmol cm<sup>-2</sup> μm<sup>-1</sup>.

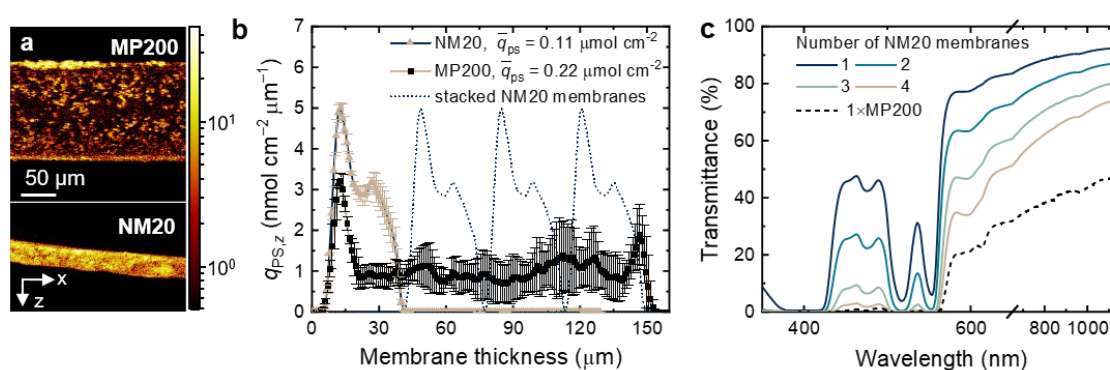


Figure 7.9: **a** Chemical mapping images and **b** the Pd-TFPP depth distribution of NM20 ( $\bar{q}_{PS} = 0.11$  μmol cm<sup>-2</sup>) and MP200 ( $\bar{q}_{PS} = 0.22$  μmol cm<sup>-2</sup>) membranes using ToF-SIMS analysis. A lighter color is for a stronger signal intensity. Note: the dotted lines copy the Pd<sup>+</sup> distribution profile in the first NM20 membrane. **c** Transmission spectra of the Pd-TFPP-coated NM20 stacks and single MP200 membranes.

Unlike the MP200 membranes, thin NM20 membranes demonstrate the narrower Pd-TFPP depth distribution. To compensate for the small thickness, several thin NM20 membranes can be stacked on top of each other (see dashed lines in Figure 7.9b). Thus, there is a more uniform PS distribution across the membrane thickness, comparable to the MP200. The presence of porphyrin-depleted regions can be also mitigated. In addition, the stacking approach may incrementally prolong the contact time and allow for the lower concentration of 17β-estradiol in the permeate. The recorded UV-Vis transmission spectra indicate that there is enough light coming through the NM20 membrane stacks compared to MP200 membrane (Figure 7.9c). However, it is unclear whether the fraction of light transmitted in the Pd-TFPP excitation region (350–600 nm) is sufficient to further reduce 17β-estradiol concentration. This question will be revealed in the next section.

#### 7.4.2 Extended Contact Time in Stacked PCMs for 17β-estradiol Elimination

The elimination of SH using PCMs occurs while the pollutant molecules are in contact with ROS produced in situ. When the Pd-TFPP molecules loaded over the entire PCM volume are fully illuminated, the contact time approaches the residence time, which varies with water flux (for the dead-end regime) and membrane thickness (see also Figure 3.19a). Stacking identical NM20 membranes ( $\bar{q}_{PS} = 0.11$  μmol cm<sup>-2</sup>) on top of each other is an attractive model system to i) study the role of contact time in photocatalytic water treatment; and ii) avoid changing the water flux and hence the reaction kinetics.



Figure 7.10 demonstrates the results of the photocatalytic experiments conducted under the optimized conditions (low water flux, high irradiance) using the stacked NM20 and single MP200 membranes. Figure 7.10a outlines that using either of the configurations allows to reduce the concentration of 17 $\beta$ -estradiol to an instrument detection limit of 0.7 ng L<sup>-1</sup> (see the LOD and LOQ levels in Figure 3.16). The 17 $\beta$ -estradiol concentration declines from (4.0  $\pm$  0.9) ng L<sup>-1</sup> to (1.3  $\pm$  0.5) ng L<sup>-1</sup> as the number of stacked NM20 membranes increases from one to four. When mounting the single MP200 membranes, the permeate concentration can be reduced to  $c_p = (0.7 \pm 0.7)$  ng L<sup>-1</sup> at  $J_w = 150$  L m<sup>-2</sup> h<sup>-1</sup>. Note that the contact time is half as long ( $t_{con} = 1.7$  s) compared to the results shown in Chapter 5 ( $c_p = (2 \pm 1)$  ng L<sup>-1</sup>,  $t_{con} = 4.3$  s,  $I_{inc} = 10.0$  mW cm<sup>-2</sup>). Hence, the enhancement effect is likely due to the higher irradiance. Remarkably, the 17 $\beta$ -estradiol concentration in the permeate at  $I_{inc} = (81.0 \pm 0.6)$  mW cm<sup>-2</sup> is eliminated below the regulatory value for 17 $\beta$ -estradiol in drinking water (1 ng L<sup>-1</sup>) proposed by the European Commission. Overall, the findings indicate that using multiple stacked PCM (subject to low water permeability, see Figure 3.19b) is not a prerequisite for the complete elimination of 17 $\beta$ -estradiol.

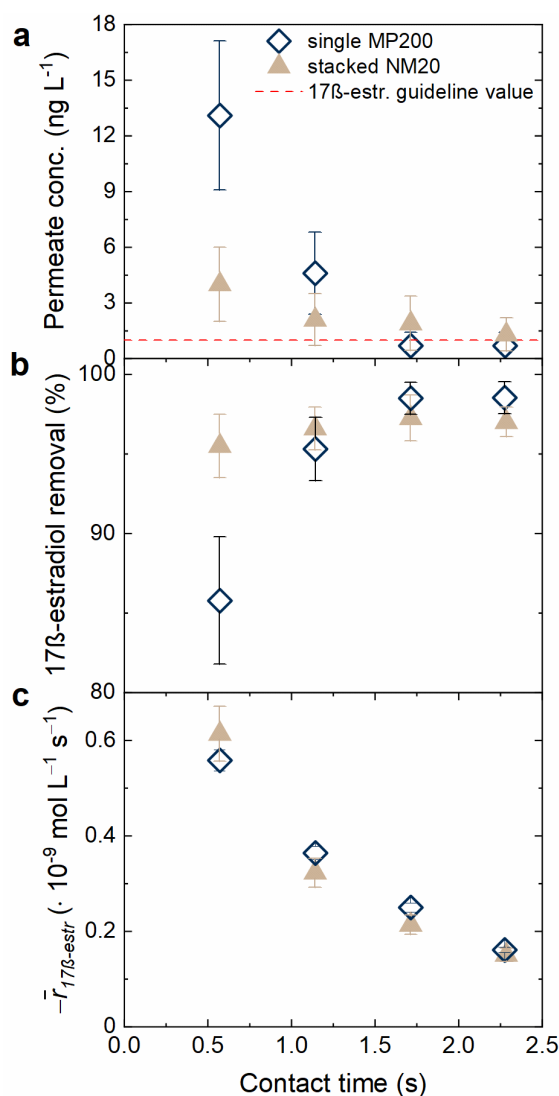


Figure 7.10: **a** Concentration in the permeate, **b** removal, and **c** the rate of disappearance of 17 $\beta$ -estradiol as a function of contact time in the NM20 stack ( $n_m = 1-4$ ,  $J_w = 60$  L m<sup>-2</sup> h<sup>-1</sup>,  $\bar{q}_{pS} = 0.11$   $\mu$ mol cm<sup>-2</sup>) and single MP200 membranes ( $J_w = 113-450$  L m<sup>-2</sup> h<sup>-1</sup>,  $\bar{q}_{pS} = 0.25$   $\mu$ mol cm<sup>-2</sup>).  $I_{inc} = (81.7 \pm 1)$  mW cm<sup>-2</sup>, pH =  $8.2 \pm 0.2$ .

When increasing the contact time from 0.57 to 1.71 s, the growth of 17 $\beta$ -estradiol removal is higher for a single MP200 membrane (from 86 to 99%) than via increase in number of NM20 membranes (from 95 to 98%) (Figure 7.10b). Within the short contact time (0.57 s), porphyrin-coated NM20 membranes achieve both higher removal and the higher disappearance rate of 17 $\beta$ -estradiol. However, the latter steadily decreases at higher contact time (Figure 7.10c). As the  $\bar{r}_{17\beta\text{-estr}}$  represent the integrated values per membrane, the vanishing of  $\bar{r}_{17\beta\text{-estr}}$  (and slight improvement of  $R_{17\beta\text{-estr}}$ ) after stacking more NM20 membranes is probably due to an (exponential) decrease in i) concentration of pollutants and ii) light intensity in the second and subsequent membranes.<sup>404</sup>

Under continuous illumination,  $^{ss}c_{O_2}$  linearly changes with the number of absorbed photons<sup>309</sup> (more details in Section 5.2.4, Equation 5.2). Assuming that  $\alpha_\lambda$  (%)  $\approx 1 - T_\lambda$  and neglecting the residual reflection and light scattering – the spectra of incident and absorbed photon flux ( $\varphi_{\text{abs},\lambda}$ ) for the stacked NM20 membranes can be estimated from the transmittance spectra (see Figure 7.9c). Figure 7.11a depicts that the spectral photon flux  $\varphi_{\text{abs},\lambda}$  (using the incident photon flux of the SolSim light source) reduces when passing through one, two, three and four stacked NM20 membranes. The integration of the  $\varphi_{\text{abs},\lambda}$  in the wavelength region of 350–700 nm for the stacked NM20 membranes yields the  $\varphi'_{\text{abs}}$  values (Figure 7.11b).

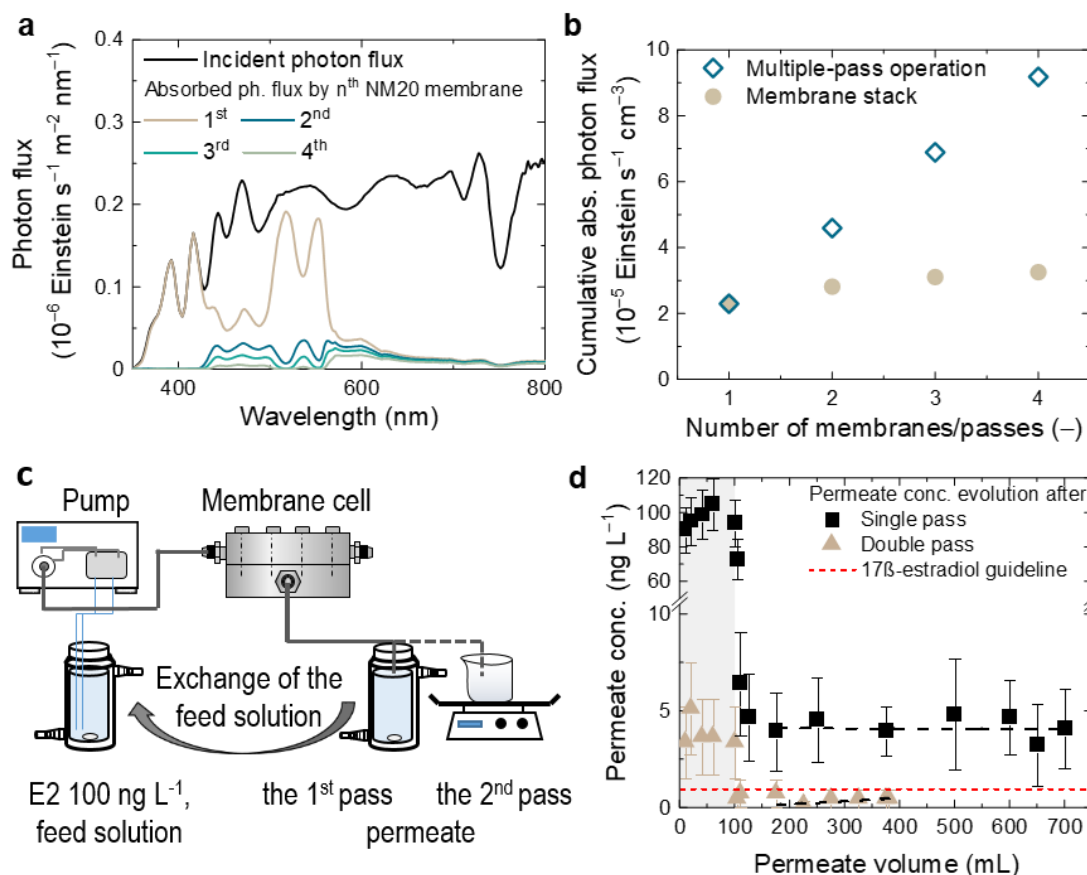


Figure 7.11: **a** Spectra of incident and absorbed photon fluxes of each NM20 membrane in a stacked configuration. **b** The change of absorbed photon flux as a function of the number of stacked NM20 membranes or the number of passes through a single PM. **c** Simplified schematic representation of the experimental set-up for multiple-pass operation (permeate collected after the 1<sup>st</sup> pass is reused in the next experiment); **d** Change in 17 $\beta$ -estradiol concentration in the permeate as a function of permeate volume using NM20 membranes ( $\bar{q}_{PS} = 0.11 \mu\text{mol cm}^{-2}$ ,  $J_w = 60 \text{ L m}^{-2} \text{ h}^{-1}$ ,  $I_{\text{inc}} = 80.3 \text{ mW cm}^{-2}$ ) after the several passes.

The rise of  $\phi'_{abs}$  in membrane stack experiments levels off with a number of stacked membranes. Consequently, the amount of  $^1O_2$  produced in the second, third or fourth stacked PCM is not enough to reach the guideline value for  $17\beta$ -estradiol in drinking water in a single pass through the PMR. An alternative approach is to treat the collected permeate using PCM in several runs (Figure 7.11c). Thus, strong attenuation of light through the PMR is mitigated (Figure 7.11b). Figure 7.11d exhibits that  $17\beta$ -estradiol in the permeate after the first and second pass drops to  $(4 \pm 2)$  ng L $^{-1}$  and below LOD level ( $0.7$  ng L $^{-1}$ ), respectively. The contact time of  $1.2$  s in a single NM20 membrane is hence sufficient to reach the target concentration for E2 in drinking water. This strategy allows to overcome strong light attenuation observed in a membrane stack by mimicking the concept of numbering-up for the PM-based photoreactors. The practical application of a multi-pass mode or membrane stack is questionable because of the increased energy demand due to the pressure increase. In summary, tuning the contact time can ensure almost complete  $17\beta$ -estradiol degradation. This knowledge can help in eliminating other SH micropollutants.

## 7.5 Studies of NM20 Membranes under Optimized Conditions for SH Elimination

Achieving the guideline value for  $17\beta$ -estradiol in drinking water has motivated the studies on degradation of other SH micropollutants. Namely, estrone, testosterone, progesterone – all possess distinct characteristics, which lead to differences in their photocatalytic decomposition.<sup>341</sup> The question arises whether improved contact in PCM based on ultrafiltration membranes (NM20) may help in the degradation of recalcitrant testosterone and progesterone. To achieve the best degradation outcomes, it is imperative to apply the most favorable conditions: long contact time (at low water flux), high irradiance (1-Sun equivalent) and high Pd-TFPP loading,  $\bar{q}_{PS} = (0.41 \pm 0.02)$   $\mu\text{mol cm}^{-2}$ . The water flux through NM20 membranes adjusted to  $60$  L m $^{-2}$  h $^{-1}$  at  $\Delta P = 3.5$ – $6.2$  bar is close to the filtration performance of nanofiltration membranes ( $J_w = 50$  L m $^{-2}$  h $^{-1}$ , 6–10 bar).<sup>371</sup>

Figure 7.12 presents the results obtained from the SH degradation experiments. Similar to the experiments with  $17\beta$ -estradiol, the degradation experiments began with the breakthrough curves. In this region (marked as a grey area in Figure 7.12a), the concentration of SH in the permeate rose.

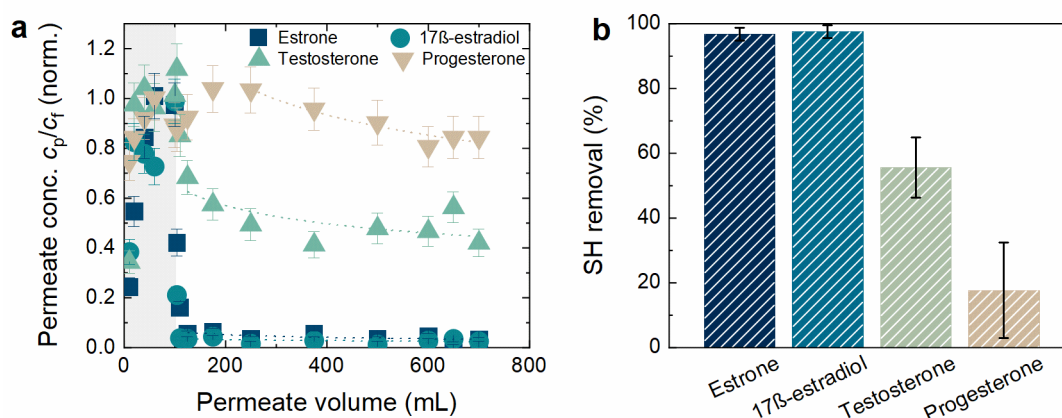


Figure 7.12: **a** Evolution of SH concentration in the permeate; and **b** the corresponding removal using single Pd-TFPP coated NM20 membranes:  $\bar{q}_{PS} = (0.41 \pm 0.02)$   $\mu\text{mol cm}^{-2}$ ,  $J_w = 60$  L m $^{-2}$  h $^{-1}$  ( $Q_f = 0.2$  mL min $^{-1}$ ),  $c_{f,SH} = (100 \pm 10)$  ng L $^{-1}$ , feed solution pH  $8.2 \pm 0.2$ , light intensity  $I_{inc} = (81.5 \pm 0.6)$  mW cm $^{-2}$ .

When PMs are illuminated at  $V_p = 100$  mL, the concentration of estrone and  $17\beta$ -estradiol drops sharply, unlike the concentrations of testosterone and progesterone, which decrease gradually. The steady-state value of  $c_p/c_f$  recorded at  $V_p = 700$  mL result in the removal values depicted in Figure 7.12b. Estrone,  $R = (97 \pm 1)\%$ , and  $17\beta$ -estradiol,  $R = (98 \pm 1)\%$ , undergo the highest degradation using the PCMs based on NM20 membranes. A completely different pattern of degradation is observed for testosterone,  $R = (54 \pm 9)\%$ , and progesterone,  $R = (18 \pm 15)\%$ . Thus, the effectiveness of photocatalytic oxidation using porphyrin-coated NM20 membranes varies among all four chosen SH, which is consistent with the experiments performed using MP200 membranes (see Chapters 5 and 6).

The reason of facile elimination of estrone and  $17\beta$ -estradiol in contrast to the testosterone and progesterone lies in reaction kinetics. As explained in Chapter 6, the rate constant of oxidation reaction with electrophilic  $^1\text{O}_2$  depends largely on the presence of electron-donating (for example, amine, methoxy, phenol) groups. These particular “activating” substituents are missing in the structure of testosterone and progesterone that accounts for the low reaction rates. For example, the reactivity of testosterone derivative (17-hydroxy-4-methyl-*androst-3-one*) with  $^1\text{O}_2$  is by 3–4 orders of magnitude lower (the reactivity index of  $200 \text{ mol L}^{-1}$ )<sup>309</sup> than that of  $17\beta$ -estradiol derivative (the reactivity index of  $0.033 \text{ mol L}^{-1}$ ).<sup>373</sup>

Notably, testosterone undergoes considerable oxidation after transport through the NM20 membrane coated with Pd-TFPP in contrast to the previous results ( $R < 11\%$ , see Figure 5.10, Figure 6.7). Thus, the reaction rates between estrogenic SH and testosterone are within one order of magnitude, when using porphyrin-coated NM20 membranes. This finding suggests that the slow reactions can be accelerated by improving the contact between the contaminant and the ROS molecules formed *in situ* inside the nanometer pore channels. It can be assumed that the geometry of ultrafiltration NM20 membranes renders the local increase in  $^1\text{O}_2$  concentration due to the spatial confinement of porphyrin molecules in nanoscale pores. Similar observation of enhanced kinetics under nanoconfinement was reported in a series of studies on catalytic membranes by Shuo Zhang, Menachem Elimelech, Jae-Hong Kim *et al.*<sup>248, 405, 406</sup> The hypothesis above warrants a detailed elucidation of the mechanism that lies beyond the scope of this dissertation.

## 7.6 Summary

This chapter discusses the role of reactant contact within PCM in the process of photocatalytic degradation. The choice of a PVDF membrane has great implications on the contact area as evidenced by the results of the specific surface area of six PVDF membranes with mean pore size ranging from 650 to 20 nm.

Pristine PVDF membranes with smaller pore sizes provide a larger specific surface area, whereas water permeability is a trade-off parameter that decreases non-linearly with mean pore size. Enlarging the surface area of PCM increases the relative porphyrin loading (per membrane weight), which contributes to an increase in the contact area as evidenced by surface-to-volume ratio. NM20 ultrafiltration membranes ( $\bar{d}_{por} = 0.02 \mu\text{m}$ ) with the highest surface-to-volume ratio ( $a'_V = 4.5 \cdot 10^7 \text{ m}^2 \text{ m}^{-3}$ ) exhibit 4–5 times higher rate of  $17\beta$ -estradiol disappearance than other microfiltration membranes ( $\bar{d}_{por} = 0.1\text{--}0.45 \mu\text{m}$ ).

Comparative experiments with the PCM made from either NM20 or reference MP200 ( $\bar{d}_{pore} = 0.2 \mu\text{m}$ ) membranes demonstrate that the  $17\beta$ -estradiol concentration in the permeate can be reduced to the guideline value for drinking water ( $1 \text{ ng L}^{-1}$ ). Adjusting the contact time by water flux allows even the large-pore MP200 membranes to be competitive. Experiments carried out with NM20 membranes under optimized conditions (long contact time, high irradiance, high porphyrin loading) provide high removal of estrone with  $R = (97 \pm 2)\%$ ,  $17\beta$ -estradiol with  $R = (98 \pm 2)\%$ , and previously resistant to treatment testosterone with  $R = (56 \pm 9)\%$ .

# 8

## Conclusion

This thesis sets out that the elimination of steroid hormone micropollutants using porphyrin-assisted photocatalytic membranes (PCMs) is an emerging technology that shows encouraging results and thus heralds their practical application. A special focus is put on the studies of operating parameters to accelerate the degradation reaction rate and collect the insights into the photostability of PCMs (membrane and photosensitizer). A brief outlook to the future suggests avenues for the further development of porphyrin-coated PVDF membranes in the field of water purification. The implications of this thesis will be also relevant to other hybrid technologies for water treatment, which combine advanced oxidation processes with membrane filtration.

### 8.1 Summary and Discussion

The main achievements of this thesis are packed into three key results, which are summarized and discussed below.

#### *Porphyrin-Coated Membranes Remove Efficiently Steroid Hormones and Organic Dyes*

The photocatalytic membranes are easily prepared via adsorption of Pd-porphyrin on hydrophobic PVDF membranes. The time-resolved photoluminescence studies corroborate that the immobilized Pd-porphyrin molecules retain their photophysical properties (long excited state lifetime, intersystem crossing close to unity, efficient quenching by molecular oxygen) along with strong absorption in the wavelength region of visible spectrum. The Pd<sup>2+</sup>, Zn<sup>2+</sup>, and free-base porphyrins exhibit the high efficiency of singlet oxygen generation as confirmed by high quantum yield in solution ( $\Phi_{\Delta} = 0.9\text{--}1.0$ ). These results have been attributed to the combination of an effective intersystem crossing and a long lifetime of the triplet state.

Excellent ability for generation of singlet oxygen is reflected in the high degree of model pollutant degradation (e.g., methylene blue or uric acid), thus confirming the high photocatalytic activity of PCMs. By reducing the water flux and hence increasing the residence time, up to 80% MB could be removed in a single pass. The rate of MB degradation using Pd-TFPP/PVDF membranes is an order of magnitude higher (based on the reaction rate constant) than the process using a pristine PVDF membrane (photolysis). Even within the short contact time (1–10 s), the contribution of photolysis – the degradation in absence of photocatalyst – to the total MB removal can be significant, reaching 14% depending on residence time. Strong photolysis is beneficial to the overall degradation in the real process organized in water treatment plants. However, in order to develop new technologies for water purification – for example, photocatalytic oxidation with PCM – photocatalytic degradation must surpass non-catalytic ways of pollutant elimination.

The effective removal of organic dyes laid the ground work for eliminating the real pollutants present in water bodies in trace concentrations, namely steroid hormones micropollutants. An analytical method based on liquid chromatography and flow scintillation analysis was preliminarily developed to separate the degradation by-products and quantify radiolabeled steroid hormones at environmentally relevant levels (nanograms per liter). This method allows the concentration of steroid hormones to be analyzed at a limit-of-detection 1.5–2.4 ng L<sup>-1</sup> in small-volume samples (1.5 mL) without prior extraction.

The developed analytical method – without any sample enrichment steps – allows for the direct evaluation of removal and degradation kinetics. For example, almost complete removal of 17 $\beta$ -estradiol to the level corresponding to the guideline value for drinking water (1 ng L<sup>-1</sup>) is achieved after initial optimization of the process parameters (e.g., water flux of 60 L m<sup>-2</sup> h<sup>-1</sup>, light intensity of 10 mW cm<sup>-2</sup>) using Pd-porphyrin-coated membranes. In addition, the degradation reaction proceeds more efficiently at higher water flux and high concentrations of contaminants, as evidenced by the increased disappearance rate of 17 $\beta$ -estradiol in the corresponding studies. Estrone has a strong reactivity with produced singlet oxygen and degrades to the same extent as 17 $\beta$ -estradiol. The non-estrogenic SH (testosterone and progesterone) do not possess a phenolic group in their molecular structure and hence lack the electron-rich structure required for fast reaction with singlet oxygen. Therefore, these two types of hormones do not undergo degradation in studies using porphyrin-coated membranes with or without the noble metal.

Nevertheless, porphyrins without noble metals (zinc and free base) can achieve a comparable rate of 17 $\beta$ -estradiol degradation, when exposed to higher levels of irradiation (close to the intensity of sunlight,  $\approx$ 81 mW cm<sup>-2</sup>). Increased light intensity is necessary to compensate for the lower quantum yield of singlet oxygen of zinc- and free-base porphyrins, as evidenced by the time-resolved PL studies. Photocatalytic studies using PCM based on porphyrins with other earth-abundant transition metals (Mn<sup>+3</sup>-, Fe<sup>+3</sup>-porphyrins) do not yield considerable degradation. The incomplete *d* sub-shell in the electronic structure of manganese or iron ions contributes to the rapid deactivation of excited states of porphyrin and low intersystem crossing.

Using the mass spectra of the collected permeate samples, the irreversible oxidation of MB or 17 $\beta$ -estradiol to multiple by-products was revealed. Although the underlying degradation mechanism was not detailed, the finding above is crucial for the prospects of pollutant decomposition, ultimately leading to organic acids, carbon dioxide and water. At the current development stage, it is not yet possible to claim mineralization when using porphyrin-coated membranes. Given the lack of work on photosensitizer-coated membranes for oxidative removal of micropollutants, these results may contribute to the pollutant abatement using porphyrin molecules as a viable type of solar-driven organic photocatalyst.

#### *Porphyrin and PVDF Membrane Materials Exhibit Sufficient Photostability to Withstand Prolonged Sunlight Exposure*

Similar to other organic photosensitizers, porphyrins undergo transformation upon prolonged illumination. The mass spectra revealed that the products of Pd-porphyrin photodegradation after 14 h green light exposure, (532  $\pm$  18) nm, are likely to have chlorin or bacteriochlorin nature. This conclusion is supported by appearance of specific red-shifted peaks in the UV-Vis absorption spectra (between 600 and 700 nm) and the new infrared absorption peaks corresponding to vibration of carbon-oxygen bonds ( $\nu_{C=O}$ ).

Extended illumination leads to photobleaching accompanied by a decrease in light absorption of porphyrins at characteristic peaks in the UV and visible range. This observation was confirmed in accelerated aging tests of PCMs prepared from Pd-, Zn-, and free-base porphyrins. The lifespan of Zn-porphyrin was 3 to 4 times longer than PCM with free-base or Pd-porphyrin. If one considers the average daily effective illumination of 3.1 h in the Karlsruhe region, the half of Zn-porphyrin molecules loaded to the membrane can survive 222 days of outdoor exposure (in contrast to 56 and 81 days for free-base and Pd-porphyrin). Overall, the nature of central metal ion in porphyrins affects both the photocatalytic activity and photostability.

The membrane material plays a crucial role in the photostability of the whole PCM. The porphyrin-loaded membranes are made of the PVDF polymer, which is a robust material not changing even after 250 h of accelerated aging under UV-violet radiation. UV-Vis and infrared absorption spectra, as well as electron

microscopy images did not reveal the considerable differences compared to the pristine membranes, nor total organic carbon in water, where the membrane was kept during the irradiation.

*When Light is Abundant, the Reaction Kinetics is Limited by the Contact between the Reagents the Immobilized Porphyrin*

The change in the type of pollutant (Chapter 5), the light source (Chapters 5,6), or the nature of coordinated metal in porphyrins (Chapter 6) was accompanied by the optimization of the process parameters and protocol amendments for higher removal and degradation rates. The implications of the porphyrin loading, water flux, irradiance and solution chemistry (pH, presence of background electrolyte, dissolved oxygen) on removal and oxidation kinetics of MB and 17 $\beta$ -estradiol were considered.

The reaction rate of a photocatalytic reaction was shown to be governed by i) flux of absorbed photons ( $\varphi_{\text{abs}}$ , reaction dominance) given by Equation (8.1); ii) mass transfer of reactants to the fixed photocatalyst (mass-transfer dominance) given by Equation (8.2):

$$r_i = k_i \epsilon \varphi_{\text{abs},V}^{\beta}, \text{ at low irradiance} \quad (8.1)$$

$$r_i = k_m a'_V c_f, \text{ at high irradiance } (c_s \approx 0) \quad (8.2)$$

where  $k_i$  is the intrinsic reaction rate constant ( $\text{mol L}^{-1} \text{s}^{-1}$ ),  $\epsilon$  is the constant of proportionality ( $\text{mol L}^{-1} \text{s}$ );  $\beta$  is the exponent showing the relationship to irradiance (-);  $\varphi_{\text{abs},V}$  is the volumetric flux of absorbed photons (mols of photons  $\text{L}^{-1} \text{s}^{-1}$ );  $k_m$  is the mass transfer coefficient ( $\text{m s}^{-1}$ );  $c_f$  is the feed concentration ( $\text{mol L}^{-1}$ ).

The mass-transfer dominance ( $\beta \rightarrow 0$ ) implies that the overall reaction rate is no longer controlled by the irradiance level, but by the rate of external mass transfer (represented by  $k_m a'_V$ ). In Chapter 7, the external mass transfer was accelerated by increasing the contact area and contact time – hence the enhanced contact the reagents and the porphyrin-coated surface of a PCM.

The specific surface area is higher in small-pore PVDF membranes, thus allowing them to adsorb more porphyrin. The surface area increases as the mean pore size of membranes decreases, while their porosity remains unchanged. The ratio of surface area to pore volume (surface-to-volume ratio) – used as an estimate of contact area – affects strongly the degradation kinetics at low and middle porphyrin loadings. At high porphyrin loading, degradation is determined by the contact time in the PCM, as evidenced by the relative stable removal of 17 $\beta$ -estradiol for all six tested membrane types. Based on data of the rate of disappearance, the PCM prepared from ultrafiltration membrane ( $\bar{d}_{\text{por}} = 20 \text{ nm}$ ) demonstrated the superior (4-fold higher) oxidation rates compared to other microfiltration membranes ( $\bar{d}_{\text{por}}$  from 100 to 650 nm).

As a result of parameter optimization, it was found that PCM prepared from both microfiltration ( $\bar{d}_{\text{por}} = 200 \text{ nm}$ ) and ultrafiltration ( $\bar{d}_{\text{por}} = 20 \text{ nm}$ ) membranes provided a 17 $\beta$ -estradiol concentration, which corresponds to the guideline value for drinking water proposed by the European Union ( $1 \text{ ng L}^{-1}$ ). The culmination of the studies on contact enhancement was that testosterone – subject to limited removal by Pd-TFPP/PVDF microfiltration membranes ( $\bar{d}_{\text{por}} = 200 \text{ nm}$ ) – was degraded using the PCM made from an ultrafiltration membrane under the most favorable conditions.

## 8.2 Future Outlook

In the current form, photocatalytic membranes prepared via adsorption of Pd-porphyrin on PVDF membranes are limited to the laboratory scale. For successful application of porphyrin-coated membranes in a real water- or wastewater treatment process, additional work will be needed.

### 8.2.1 Degradation Performance

Despite the nearly complete elimination of 17 $\beta$ -estradiol (down to 1 ng L<sup>-1</sup>), no information is available regarding the degradation pathway or toxicity of produced permeate. The main obstacle to integrating advanced oxidation processes, such as photocatalytic oxidation, into existing water treatment plants will be a negative change, or lack thereof, in the toxicity levels of treated water. Among the tests gauging the toxicity of steroid hormones, there are those for estrogen and androgen potency.<sup>379, 407</sup> Here, the challenge would be to combine methodologies of water treatment and ecotoxicology into one.

Furthermore, the real surface water contains not only one type of pollutants with salt background, but tens to hundreds of other micropollutants along with dissolved organic matter. The photocatalytic activity of PCM using steroid hormones spiked into real waters was not part of this dissertation. Hence, two types of studies will provide a better understanding of the effect of wastewater matrix on the PCM performance.

Firstly, the effect of dissolved organic matter can be investigated by adding humic substances (humic and fulvic acids), ubiquitous in surface waters, to the feed solution. The humic substances absorb light in the blue wavelength region that can impair the light absorption ability of porphyrin-coated membranes. Also, they are known to produce different types of ROS, including singlet oxygen, thereby contributing to the pollutant degradation.

Secondly, the versatility of porphyrin-coated membranes must be established by testing multiple contaminants in single- and multi-component mixtures. The pesticides and per- and polyfluoroalkyl substances could be selected as the prominent classes of micropollutants. Similar to the work described in this thesis, the analytical methods for each type of pollutant will have to be developed and validated.

### 8.2.2 Photosensitizer Stability

Slowing down the degradation of the immobilized organic photocatalyst is another major bottleneck of the practical application of PCM in water treatment, and hence it is an essential direction for future research. Although pentafluorinated porphyrins have shown promising results in mitigating self-degradation, they are still far from being industrial appealing in terms of photostability. There would be needed such porphyrin-like compounds that can withstand longer illumination (on the scale of months) without losing the ability to generate singlet oxygen or other reactive oxygen species.

Meeting both requirements – exceptional photocatalytic activity and photostability – is a challenging, yet not impossible task. Here, the compromise must be found between the diminished generation of ROS and the prolonged lifespan of the organic photocatalyst. A promising direction would be using phthalocyanines or BODIPY dyes – an emerging class of photostable photosensitizers.

Additionally, the immobilization of porphyrin by physical adsorption is not permanent. Thus, a novel fabrication procedure for PCM is needed to avoid the washout of immobilized photosensitizers or their by-products formed during the extended illumination. Anchoring the photosensitizer molecules to the



membrane surface by grafting or electrostatic interaction methods could provide better stability of PCM in the long term.

### 8.2.3 Reaction Modelling and PCM Optimization

In this dissertation, the absorbed photon flux was calculated from absorption spectra of photocatalytic membranes. This procedure is associated with several assumptions, such as neglecting photon scattering. Future research should always i) conduct measurements of absorbed photons via actinometry agents, and ii) assess the amount of produced singlet oxygen per pass *via* trap molecule experiments (for example, furfuryl alcohol,  $k_t = (1.1-1.2) \cdot 10^8 \text{ M}^{-1} \text{ s}^{-1}$ ). These tests will reveal the ratio of singlet oxygen generated to that, which is readily available for reaction. The obtained value is close to the quantum yield of the photochemical reaction – an indicator of the efficiency of the photocatalytic process – which is also a decisive criterion for the practical application of PCM.

In addition, the question of whether the depletion of dissolved oxygen inside the PCM occurs requires experimental confirmation. The in-line oxygen sensor installed in the permeate side would provide an answer to the question above. If the depletion of dissolved oxygen indeed takes place, then the full study of the effect of dissolved oxygen might be valuable. These results will provide the basis for solving the problem of dissolved oxygen deficiency by additional aeration or by redesigning the PCM reactor.

Limited singlet oxygen-induced oxidation kinetics for effective degradation of recalcitrant pollutants (testosterone, progesterone) prevents porphyrin-coated membrane to achieve their full potential and even practical applications. An inspiring example of successful oxidation of testosterone using ultrafiltration membranes ( $\bar{d}_{por} = 20 \text{ nm}$ ) indicates the rate acceleration inside the nanoscale membrane pore channels. Consequently, it is necessary to understand the degree of reaction rate acceleration achieved with other ultrafiltration ( $\bar{d}_{por} = 5-20 \text{ nm}$ ) or even nanofiltration ( $\bar{d}_{por} = 1-2 \text{ nm}$ ) membranes. This finding will help oxidize other persistent pollutants, for instance, progesterone.

# Appendix: Supporting Graphs

## A.1 Process Parameters in Methylene Blue Degradation Experiments

Process parameters in photocatalytic experiments using MB as a model pollutant were continuously monitored and stored using LabView software. Figure A.1 exhibits the readings of the pressure sensors and temperature in the feed and permeate lines recorded during the experiments carried out at different water flux ( $J_w = 30\text{--}300\text{ L m}^{-2}\text{ h}^{-1}$ ). The data interval was every 30 seconds and plotted without averaging. These results confirm that the feed pressure and temperature in the feed and permeate remained stable within the experiments.

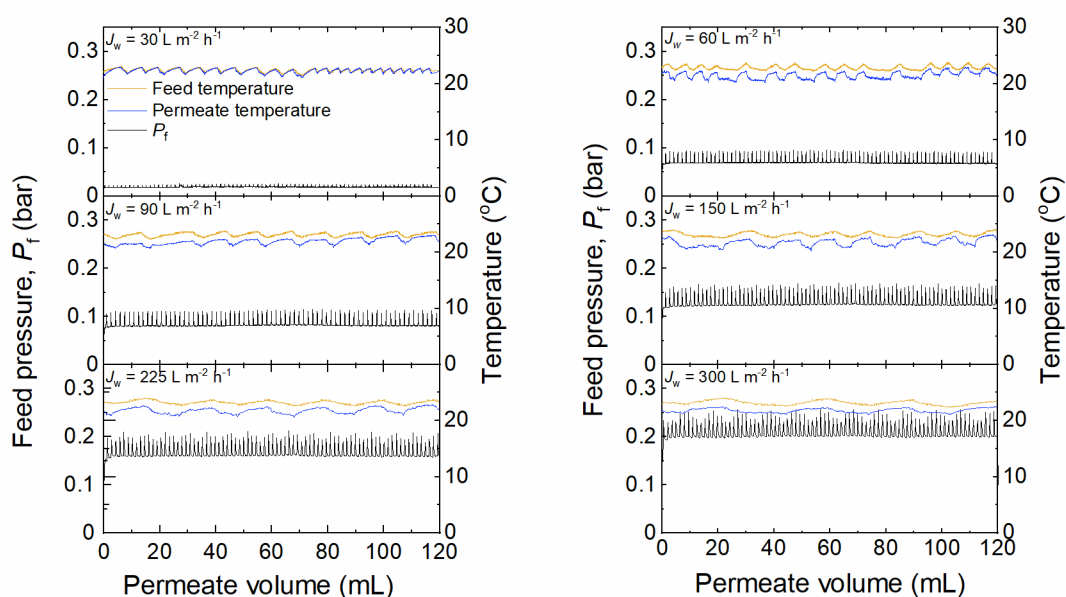


Figure A.1: The changes of feed pressure, feed and permeate temperature in single-pass continuous-flow photocatalytic experiments with MB as a model pollutant (gLED excitation  $\lambda_{exc} = (528 \pm 20)\text{ nm}$ ,  $J_w = 30\text{--}300\text{ L m}^{-2}\text{ h}^{-1}$ ,  $I_{inc} = 21\text{ mW cm}^{-2}$ ,  $[\text{MB}] = 1\text{ mg L}^{-1}$ ;  $\bar{q}_{PS} = (0.21 \pm 0.02)\text{ }\mu\text{mol cm}^{-2}$ ).

## A.2 Process Parameters in 17 $\beta$ -estradiol Degradation Experiments

Figure A.2 summarizes the process parameters (feed solution pH, pressure, temperature, dissolved oxygen) monitored during the typical photodegradation experiment using 17 $\beta$ -estradiol (see conditions in the main part, Table 3.5). The change of feed solution pH  $8.2 \pm 0.1$  and dissolved oxygen,  $c_f = (8.57 \pm 0.02)$  within one experiment was negligible. The higher initial pH of the feed solution ( $8.6 \pm 0.4$ ) were due to the prolonged storage of stock sodium bicarbonate solution. During the experiment the transmembrane pressure (pressure difference before and after the membrane increased by 14%: from  $\Delta P = (0.125 \pm 0.005)$  bar at  $V_p = 0$  mL to  $\Delta P = (0.143 \pm 0.005)$  bar at  $V_p = 700$  mL).

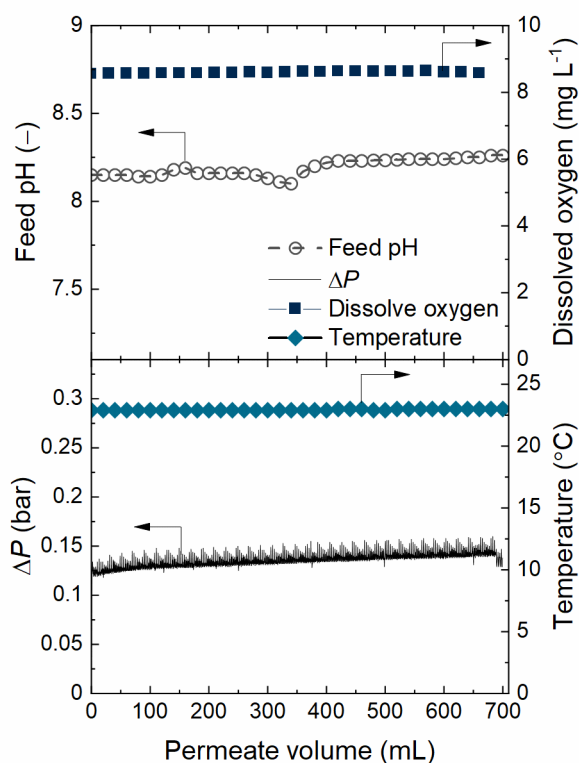


Figure A.2: The typical changes of pH, dissolved oxygen, feed temperature and transmembrane pressure in single-pass continuous-flow photocatalytic experiments with 17 $\beta$ -estradiol micropollutant in experiments ( $J_w = 600 \text{ L m}^{-2} \text{ h}^{-1}$ ,  $J_{inc} = 10 \text{ mW cm}^{-2}$ ,  $c_f(17\beta\text{-estradiol}) = 100 \text{ ng L}^{-1}$ ; in background solution 1 mM NaHCO<sub>3</sub>, 10 mM NaCl). Feed temperature was controlled with a chiller at 23°C.

### A.3. Effect of the Porphyrin Type on 17 $\beta$ -estradiol Degradation

Figure A.3 depicts the evolution of the normalized permeate concentration with the permeate volume collected during the degradation of 17 $\beta$ -estradiol using PCM made with four porphyrin types at various loadings ( $\bar{q}_{PS}$ =0.04–0.64  $\mu\text{mol cm}^{-2}$ ). After evaluating  $c_{p,ss}/c_f$  at a permeate volume of  $V_p = 700$  mL, the data was converted to the graphs of removal and shown in the main part (Figure 6.6). Overall, an increase in PS loading leads to improved 17 $\beta$ -estradiol degradation, as evidenced by a decrease in normalized 17 $\beta$ -estradiol concentration at the end of the experiment ( $V_p = 700$  mL).

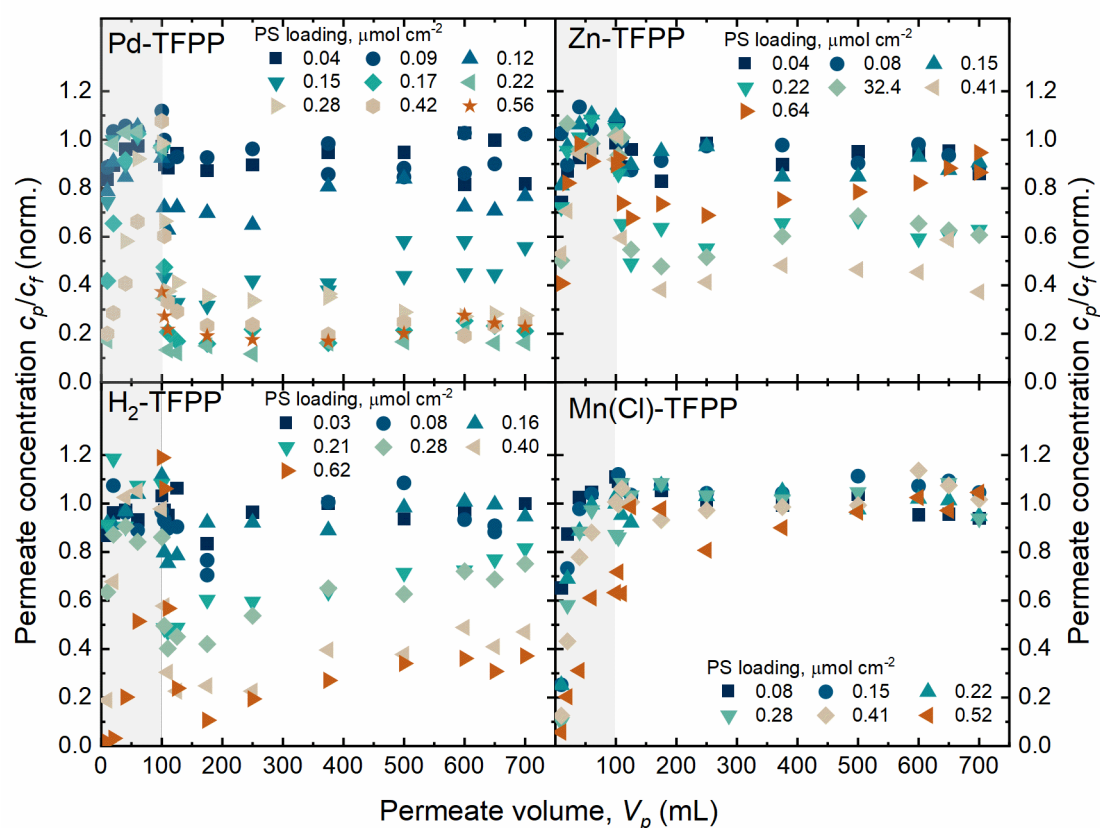


Figure A.3: The evolution of the 17 $\beta$ -estradiol concentration in the permeate as a function of the permeate volume. Conditions:  $J_w = 600$  L  $\text{m}^{-2}$   $\text{h}^{-1}$ ,  $i_{inc}$  of SolSim: (13.9  $\pm$  0.2) mW  $\text{cm}^{-2}$  using Pd-TFPP, (11.4  $\pm$  0.3) mW  $\text{cm}^{-2}$  using H<sub>2</sub>-TFPP, (12.2  $\pm$  0.2) mW  $\text{cm}^{-2}$  using Zn-TFPP, (6.3  $\pm$  0.2) mW  $\text{cm}^{-2}$  using Mn(Cl)-TFPP;  $c_f$ (17 $\beta$ -estradiol) = (100  $\pm$  11) ng  $\text{L}^{-1}$  in background solution (1 mM NaHCO<sub>3</sub>, 10 mM NaCl, pH 8.2  $\pm$  0.2).

#### A.4 Effect of the Membrane Type on 17 $\beta$ -estradiol Degradation

The permeate samples containing 17 $\beta$ -estradiol were collected throughout the experiment and subjected to the UHPLC-FSA analysis. The resulted  $c_p$  values were normalized by the 17 $\beta$ -estradiol concentration in the feed, and plotted in Figure A.4 as a function of the permeate volume. All experiments were performed in the dark for the first 100 mL of the collected permeate (marked as grey areas in Figure A.4). The contribution of adsorption to the 17 $\beta$ -estradiol removal was thus minimized. Effectiveness of treatment was determined at the last point of the fitting curve in the interval of  $V_p = 125\text{--}700$  mL and converted to removal ( $R$ ) shown in the main text (Figure 7.8). All types of PVDF membranes significantly reduced the 17 $\beta$ -estradiol concentration in the permeate after impregnation of membrane with Pd-TFPP at medium (15 mM) and high (30 mM) concentrations.

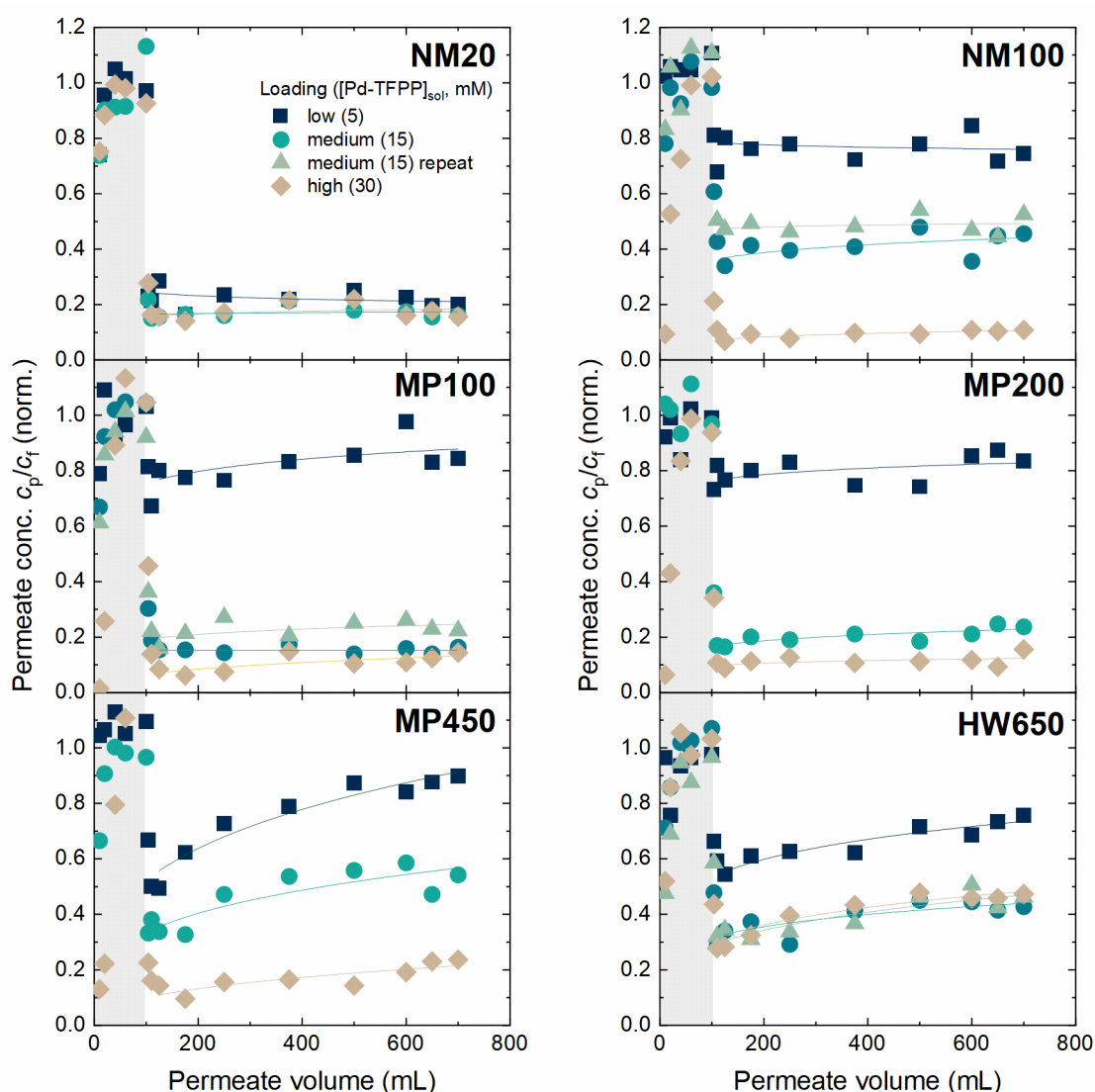


Figure A.4: The evolution of the 17 $\beta$ -estradiol concentration in the permeate as a function of the permeate volume using the different Pd-TFPP/PVDF membranes at three different PS loading.  $J_w = 600$  L m $^{-2}$  h $^{-1}$ ,  $I_{inc}$  of SolSim:  $(14.5 \pm 0.5)$  mW cm $^{-2}$ ,  $c_r(\text{SH}) = 100$  ng L $^{-1}$  in 1 mM NaHCO $_3$ , 10 mM NaCl solution (pH  $8.2 \pm 0.2$ ).

# Bibliography

1. UNESCO World Water Assessment Programme. (2018). The United Nations World Water Development Report 2018 (United Nations Educational); New York, United States. Available online: [www.unwater.org/publications/world-water-development-report-2018/](http://www.unwater.org/publications/world-water-development-report-2018/). (accessed 18 June 2022).
2. World Health Organization (WHO). 2022. Water-related diseases: information sheets. Available online: <https://www.who.int/news-room/fact-sheets/detail/sanitation>. (accessed 18 June 2022).
3. United Nations (UN) Inter-agency Group for Child Mortality Estimation. (2020). Levels & Trends in Child Mortality. Available online: <https://www.unicef.org/media/79371/file/UN-IGME-child-mortality-report-2020.pdf>. (accessed 07 June 2022).
4. Boretti, A.; Rosa, L. (2019). Reassessing the projections of the World Water Development Report. *npj Clean Water*, 2 (1), 15. DOI: 10.1038/s41545-019-0039-9.
5. Flammini, A.; Puri, M.; Pluschke, L.; Dubois, O. (2014). Walking the Nexus Talk: Assessing the Water-Energy-Food Nexus in the Context of the Sustainable Energy for All Initiative; *Climate, Energy and Tenure Division (NRC), Food and Agriculture Organization of the United Nation*: Rome, Italy. Available online: <https://www.fao.org/3/i3959e/i3959e.pdf>. (accessed 07 June 2022).
6. Global Water Intelligence. (2020). The Global Water Tariff Survey 2020; Global Water Intelligence: Oxford, UK. Available online: <https://www.globalwaterintel.com/products-and-services/market-research-reports/tariff-survey-2020>. (accessed 7 June 2022).
7. McDonald, R. I.; Green, P.; Balk, D.; Fekete, B. M.; Revenga, C.; Todd, M.; Montgomery, M. (2011). Urban growth, climate change, and freshwater availability. *Proceedings of the National Academy of Sciences*, 108 (15), 6312-6317. DOI: 10.1073/pnas.1011615108.
8. Schwarzenbach, R. P.; Escher, B. I.; Fenner, K.; Hofstetter, T. B.; Johnson, C. A.; Von Gunten, U.; Wehrli, B. (2006). The challenge of micropollutants in aquatic systems. *Science*, 313 (5790), 1072-1077. DOI: 10.1126/science.1127291.
9. Barbosa, M. O.; Moreira, N. F.; Ribeiro, A. R.; Pereira, M. F.; Silva, A. M. (2016). Occurrence and removal of organic micropollutants: an overview of the watch list of EU Decision 2015/495. *Water Res.*, 94, 257-279. DOI: 10.1016/j.watres.2016.02.047.
10. Sanderson, J. T. (2006). The steroid hormone biosynthesis pathway as a target for endocrine-disrupting chemicals. *Toxicol. Sci.*, 94 (1), 3-21. DOI: 10.1093/toxsci/kfl051.
11. Mills, L. J.; Chichester, C. (2005). Review of evidence: Are endocrine-disrupting chemicals in the aquatic environment impacting fish populations? *Sci. Total Environ.*, 343 (1), 1-34. DOI: 10.1016/j.scitotenv.2004.12.070.
12. Adeel, M.; Song, X.; Wang, Y.; Francis, D.; Yang, Y. (2017). Environmental impact of estrogens on human, animal and plant life: A critical review. *Environ. Int.*, 99, 107-119. DOI: 10.1016/j.envint.2016.12.010.
13. Luo, Y.; Guo, W.; Ngo, H. H.; Nghiem, L. D.; Hai, F. I.; Zhang, J.; Liang, S.; Wang, X. C. (2014). A review on the occurrence of micropollutants in the aquatic environment and their fate and removal during wastewater treatment. *Sci. Total Environ.*, 473-474, 619-641. DOI: 10.1016/j.scitotenv.2013.12.065.
14. Liu, Z.-h.; Lu, G.-n.; Yin, H.; Dang, Z.; Rittmann, B. (2015). Removal of Natural Estrogens and Their Conjugates in Municipal Wastewater Treatment Plants: A Critical Review. *Environ. Sci. Technol.*, 49 (9), 5288-5300. DOI: 10.1021/acs.est.5b00399.
15. European Commission. (2020). Directive (EU) 2020/2184 of the European Parliament and of the Council of 16 December 2020 on the quality of water intended for human consumption (recast) Off. J. Eur. Union Vol. L 435, 1-62.

16. Environmental and Water Resources Institute (EWRI) (2009). Contaminants of Emerging Environmental Concern. (Bhandari, A.; Surampalli, R. Y.; Adams, C. D.; Champagne, P.; Ong, S. K.; Tyagi, R. D.; Zhang, T. Eds.) p. 490. Reston, Virginia, USA: *American Society of Civil Engineers*.
17. Yang, Y.; Ok, Y. S.; Kim, K.-H.; Kwon, E. E.; Tsang, Y. F. (2017). Occurrences and removal of pharmaceuticals and personal care products (PPCPs) in drinking water and water/sewage treatment plants: A review. *Sci. Total Environ.*, 596-597, 303-320. DOI: 10.1016/j.scitotenv.2017.04.102.
18. Margot, J. (2015). Micropollutant removal from municipal wastewater: from conventional treatments to advanced biological processes. École polytechnique fédérale de Lausanne (EPFL). Lausanne, Switzerland.
19. Hodges, B. C.; Cates, E. L.; Kim, J.-H. (2018). Challenges and prospects of advanced oxidation water treatment processes using catalytic nanomaterials. *Nat. Nanotechnol.*, 13 (8), 642-650. DOI: 10.1038/s41565-018-0216-x.
20. Sudhakaran, S.; Maeng, S. K.; Amy, G. (2013). Hybridization of natural systems with advanced treatment processes for organic micropollutant removals: New concepts in multi-barrier treatment. *Chemosphere*, 92 (6), 731-737. DOI: 10.1016/j.chemosphere.2013.04.021.
21. McArdell, C. S. (2015). The first full-scale advanced ozonation plant in the Dübendorf WWTP running; the new Swiss water protection act approved. *Norman Bulletin*, 36-37. Available online: [http://www.norman-network.net/sites/default/files/files/bulletins/NORMAN%20Bulletin\\_n4March2015\\_vfinal.pdf](http://www.norman-network.net/sites/default/files/files/bulletins/NORMAN%20Bulletin_n4March2015_vfinal.pdf). (accessed 18 June 2022).
22. M. Athing, F. B., A. Duffek, I. Ebert, A. Eckhardt, E. Hassold, M. Helmecke, I. Kirst, B. Krause, P. Lepom, S. Leuthold, C. Mathan, V. Mohaupt, J. F. Moltmann, A. Müller, I. Nöh, C. Pickl, U. Pirntke, K. Pohl, J. Rechenberg, M. Suhr, C. Thierbach, L. Tietjen, P. Von der Ohe, C. Winde. (2018). Recommendations for reducing micropollutants in waters; *Umweltbundesamt: Dessau-Roßlau, Germany*. p 60. Available online: [https://www.umweltbundesamt.de/sites/default/files/medien/1410/publikationen/180709\\_uba\\_pos\\_mikroverunreinigung\\_en\\_bf.pdf](https://www.umweltbundesamt.de/sites/default/files/medien/1410/publikationen/180709_uba_pos_mikroverunreinigung_en_bf.pdf). (accessed 07 June 2022).
23. Johnson, A. C.; Sumpter, J. P. (2015). Improving the Quality of Wastewater To Tackle Trace Organic Contaminants: Think before You Act! *Environ. Sci. Technol.*, 49 (7), 3999-4000. DOI: 10.1021/acs.est.5b00916.
24. Baker, R. W. (2012). Membrane technology and applications. 3rd ed. Weinheim: *Wiley-VCH*.
25. Schäfer, I. A. (2001). Natural organics removal using membranes: principles, performance, and cost. Boca Raton, U.S.A: *CRC Press*.
26. Asano, T. (2007). Water reuse : issues, technologies, and applications. 1st ed. New York, USA: *McGraw-Hill*.
27. Kim, S. D.; Cho, J.; Kim, I. S.; Vanderford, B. J.; Snyder, S. A. (2007). Occurrence and removal of pharmaceuticals and endocrine disruptors in South Korean surface, drinking, and waste waters. *Water Res.*, 41 (5), 1013–1021. DOI: 10.1016/j.watres.2006.06.034.
28. Imbrogno, A.; Boussouga, Y.-A.; Nghiem, L. D. S., A. I. (2021). Trace Contaminant Removal by Nanofiltration. In *Nanofiltration: Principles, Applications, and New Materials*, 2nd ed.; (Schäfer, A. I.; Fane, A. G. Eds.), 805-887. Weinheim, Germany: *Wiley-VCH Verlag*.
29. Judd, S. (2011). The MBR book: principles and applications of membrane bioreactors for water and wastewater treatment. 2nd ed., (Judd, S.; Judd, C. Eds.). *Elsevier*.
30. Grandclément, C.; Seyssiecq, I.; Piram, A.; Wong-Wah-Chung, P.; Vanot, G.; Tiliacos, N.; Roche, N.; Doumenq, P. (2017). From the conventional biological wastewater treatment to hybrid processes, the evaluation of organic micropollutant removal: A review. *Water Res.*, 111, 297-317. DOI: 10.1016/j.watres.2017.01.005.

31. Besha, A. T.; Gebreyohannes, A. Y.; Tufa, R. A.; Bekele, D. N.; Curcio, E.; Giorno, L. (2017). Removal of emerging micropollutants by activated sludge process and membrane bioreactors and the effects of micropollutants on membrane fouling: A review. *Journal of Environmental Chemical Engineering*, 5 (3), 2395-2414. DOI: 10.1016/j.jece.2017.04.027.
32. Tagliavini, M.; Weidler, P. G.; Njel, C.; Pohl, J.; Richter, D.; Böhringer, B.; Schäfer, A. I. (2020). Polymer-based spherical activated carbon – ultrafiltration (UF-PBSAC) for the adsorption of steroid hormones from water: Material characteristics and process configuration. *Water Res.*, 185, 116249. DOI: 10.1016/j.watres.2020.116249.
33. Margot, J.; Kienle, C.; Magnet, A.; Weil, M.; Rossi, L.; de Alencastro, L. F.; Abegglen, C.; Thonney, D.; Chèvre, N.; Schärer, M.; Barry, D. A. (2013). Treatment of micropollutants in municipal wastewater: Ozone or powdered activated carbon? *Sci. Total Environ.*, 461-462, 480-498. DOI: 10.1016/j.scitotenv.2013.05.034.
34. Snyder, S. A.; Adham, S.; Redding, A. M.; Cannon, F. S.; DeCarolis, J.; Oppenheimer, J.; Wert, E. C.; Yoon, Y. (2007). Role of membranes and activated carbon in the removal of endocrine disruptors and pharmaceuticals. *Desalination*, 202 (1), 156–181. DOI: 10.1016/j.desal.2005.12.052.
35. Shannon, M. A.; Bohn, P. W.; Elimelech, M.; Georgiadis, J. G.; Marinas, B. J.; Mayes, A. M. (2008). Science and technology for water purification in the coming decades. *Nature*, 452, 301–310. DOI: 10.1038/nature06599.
36. Alvarez, P. J. J.; Chan, C. K.; Elimelech, M.; Halas, N. J.; Villagrán, D. (2018). Emerging opportunities for nanotechnology to enhance water security. *Nat. Nanotechnol.*, 13 (8), 634-641. DOI: 10.1038/s41565-018-0203-2.
37. von Gunten, U. (2018). Oxidation Processes in Water Treatment: Are We on Track? *Environ. Sci. Technol.*, 52 (9), 5062-5075. DOI: 10.1021/acs.est.8b00586.
38. von Gunten, U. (2003). Ozonation of drinking water: Part II. Disinfection and by-product formation in presence of bromide, iodide or chlorine. *Water Res.*, 37 (7), 1469–1487. DOI: 10.1016/S0043–1354(02)00458-X.
39. Merle, T.; Pronk, W.; von Gunten, U. (2017). MEMBRO3X, a Novel Combination of a Membrane Contactor with Advanced Oxidation (O<sub>3</sub>/H<sub>2</sub>O<sub>2</sub>) for Simultaneous Micropollutant Abatement and Bromate Minimization. *Environmental Science & Technology Letters*, 4 (5), 180–185. DOI: 10.1021/acs.estlett.7b00061.
40. Bein, E.; Zucker, I.; Drewes, J. E.; Hübner, U. (2020). Ozone membrane contactors for water and wastewater treatment: A critical review on materials selection, mass transfer and process design. *Chem. Eng. J.*, 127393. DOI: 10.1016/j.cej.2020.127393.
41. Gassie, L. W.; Englehardt, J. D. (2017). Advanced oxidation and disinfection processes for onsite net-zero greywater reuse: A review. *Water Res.*, 125, 384-399. DOI: 10.1016/j.watres.2017.08.062.
42. Snyder, S. A.; Wert, E. C.; Rexing, D. J.; Zegers, R. E.; Drury, D. D. (2006). Ozone Oxidation of Endocrine Disruptors and Pharmaceuticals in Surface Water and Wastewater. *Ozone: Science & Engineering*, 28 (6), 445-460. DOI: 10.1080/01919510601039726.
43. Torres, N. H.; Santos, G. d. O. S.; Romanholo Ferreira, L. F.; Américo-Pinheiro, J. H. P.; Eguiluz, K. I. B.; Salazar-Banda, G. R. (2021). Environmental aspects of hormones estriol, 17 $\beta$ -estradiol and 17 $\alpha$ -ethinylestradiol: Electrochemical processes as next-generation technologies for their removal in water matrices. *Chemosphere*, 267, 128888. DOI: 10.1016/j.chemosphere.2020.128888.
44. Chong, M. N.; Jin, B.; Chow, C. W.; Saint, C. (2010). Recent developments in photocatalytic water treatment technology: a review. *Water Res.*, 44 (10), 2997-3027. DOI: 10.1016/j.watres.2010.02.039.



45. Mushtaq, F.; Chen, X.; Torlakcik, H.; Steuer, C.; Hoop, M.; Siringil, E. C.; Marti, X.; Limburg, G.; Stipp, P.; Nelson, B. J.; Pané, S. (2019). Magnetoelectrically Driven Catalytic Degradation of Organics. *Adv. Mater.*, 31 (28), 1901378. DOI: 10.1002/adma.201901378.
46. Liang, Z.; Yan, C.-F.; Rtimi, S.; Bandara, J. (2019). Piezoelectric materials for catalytic/photocatalytic removal of pollutants: Recent advances and outlook. *Appl. Catal. B: Environ.*, 241, 256-269. DOI: 10.1016/j.apcatb.2018.09.028.
47. Mauter, M. S.; Zucker, I.; Perreault, F.; Werber, J. R.; Kim, J.-H.; Elimelech, M. (2018). The role of nanotechnology in tackling global water challenges. *Nature Sustainability*, 1 (4), 166–175. DOI: 10.1038/s41893-018-0046-8.
48. Dincer, I. (2000). Renewable energy and sustainable development: a crucial review. *Renewable Sustainable Energy Rev.*, 4 (2), 157–175. DOI: 10.1016/S1364-0321(99)00011-8.
49. Cates, E. L. (2017). Photocatalytic water treatment: so where are we going with this? *Environ. Sci. Technol.*, 51 (2), 757-758. DOI: 10.1021/acs.est.6b06035.
50. Benotti, M. J.; Stanford, B. D.; Wert, E. C.; Snyder, S. A. (2009). Evaluation of a photocatalytic reactor membrane pilot system for the removal of pharmaceuticals and endocrine disrupting compounds from water. *Water Res.*, 43 (6), 1513–1522. DOI: 10.1016/j.watres.2008.12.049.
51. Ganiyu, S. O.; van Hullebusch, E. D.; Cretin, M.; Esposito, G.; Oturan, M. A. (2015). Coupling of membrane filtration and advanced oxidation processes for removal of pharmaceutical residues: A critical review. *Sep. Purif. Technol.*, 156, 891-914. DOI: 10.1016/j.seppur.2015.09.059.
52. Reif, M.; Dittmeyer, R. (2003). Porous, catalytically active ceramic membranes for gas–liquid reactions: a comparison between catalytic diffuser and forced through flow concept. *Catal. Today*, 82 (1), 3–14. DOI: 10.1016/S0920-5861(03)00197-4.
53. Loeb, S. K.; Alvarez, P. J. J.; Brame, J. A.; Cates, E. L.; Choi, W.; Crittenden, J.; Dionysiou, D. D.; Li, Q.; Li-Puma, G.; Quan, X.; Sedlak, D. L.; David Waite, T.; Westerhoff, P.; Kim, J.-H. (2019). The technology horizon for photocatalytic water treatment: sunrise or sunset? *Environ. Sci. Technol.*, 53 (6), 2937-2947. DOI: 10.1021/acs.est.8b05041.
54. Shi, Y.; Huang, J.; Zeng, G.; Cheng, W.; Hu, J. (2019). Photocatalytic membrane in water purification: is it stepping closer to be driven by visible light? *J. Membr. Sci.*, 584, 364-392. DOI: 10.1016/j.memsci.2019.04.078.
55. Seitzinger, S.; Harrison, J. A.; Böhlke, J. K.; Bouwman, A. F.; Lowrance, R.; Peterson, B.; Tobias, C.; Drecht, G. V. (2006). Denitrification across landscapes and waterscapes: a synthesis. *Ecol. Appl.*, 16 (6), 2064-2090. DOI: 10.1890/1051-0761(2006)016[2064:DALAWA]2.0.CO;2.
56. Jackson, R. B.; Carpenter, S. R.; Dahm, C. N.; McKnight, D. M.; Naiman, R. J.; Postel, S. L.; Running, S. W. (2001). Water in a changing world. *Ecol. Appl.*, 11 (4), 1027–1045. DOI: 10.1890/1051-0761(2001)011[1027:WIACW]2.0.CO;2.
57. Escher, B. I.; Stapleton, H. M.; Schymanski, E. L. (2020). Tracking complex mixtures of chemicals in our changing environment. *Science*, 367 (6476), 388-392. DOI: 10.1126/science.aay6636.
58. Johnson, A. C.; Jin, X.; Nakada, N.; Sumpter, J. P. (2020). Learning from the past and considering the future of chemicals in the environment. *Science*, 367 (6476), 384-387. DOI: 10.1016/j.scitotenv.2021.150025.
59. Loos, R.; Carvalho, R.; António, D. C.; Comero, S.; Locoro, G.; Tavazzi, S.; Paracchini, B.; Ghiani, M.; Lettieri, T.; Blaha, L.; Jarosova, B.; Voorspoels, S.; Servaes, K.; Haglund, P.; Fick, J.; Lindberg, R. H.; Schwesig, D.; Gawlik, B. M. (2013). EU-wide monitoring survey on emerging polar organic contaminants in wastewater treatment plant effluents. *Water Res.*, 47 (17), 6475-6487. DOI: 10.1016/j.watres.2013.08.024.
60. Terzić, S.; Senta, I.; Ahel, M.; Gros, M.; Petrović, M.; Barcelo, D.; Müller, J.; Knepper, T.; Martí, I.; Ventura, F.; Jovančić, P.; Jabučar, D. (2008). Occurrence and fate of emerging wastewater

- contaminants in Western Balkan Region. *Sci. Total Environ.*, 399 (1), 66-77. DOI: 10.1016/j.scitotenv.2008.03.003.
61. Patel, M.; Kumar, R.; Kishor, K.; Mlsna, T.; Pittman, C. U.; Mohan, D. (2019). Pharmaceuticals of Emerging Concern in Aquatic Systems: Chemistry, Occurrence, Effects, and Removal Methods. *Chem. Rev.*, 119 (6), 3510-3673. DOI: 10.1021/acs.chemrev.8b00299.
62. Colborn, T.; Saal, F. S. v.; Soto, A. M. (1993). Developmental effects of endocrine-disrupting chemicals in wildlife and humans. *Environ. Health Perspect.*, 101 (5), 378-384. DOI: 10.1289/ehp.93101378.
63. Richardson, S. D.; Plewa, M. J.; Wagner, E. D.; Schoeny, R.; DeMarini, D. M. (2007). Occurrence, genotoxicity, and carcinogenicity of regulated and emerging disinfection by-products in drinking water: A review and roadmap for research. *Mutation Research/Reviews in Mutation Research*, 636 (1), 178-242. DOI: 10.1016/j.mrrev.2007.09.001.
64. Lösel, R.; Wehling, M. (2003). Nongenomic actions of steroid hormones. *Nature Reviews Molecular Cell Biology*, 4 (1), 46-55. DOI: 10.1038/nrm1009.
65. Aemig, Q.; Hélias, A.; Patureau, D. (2021). Impact assessment of a large panel of organic and inorganic micropollutants released by wastewater treatment plants at the scale of France. *Water Res.*, 188, 116524. DOI: 10.1016/j.watres.2020.116524.
66. Gadd, J. B.; Tremblay, L. A.; Northcott, G. L. (2010). Steroid estrogens, conjugated estrogens and estrogenic activity in farm dairy shed effluents. *Environ. Pollut.*, 158 (3), 730-736. DOI: 10.1016/j.envpol.2009.10.015.
67. Ray, P.; Zhao, Z.; Knowlton, K. (2013). Emerging contaminants in livestock manure: hormones, antibiotics and antibiotic resistance genes. In Sustainable animal agriculture, (Kebreab, E. Ed.) 268-283. Boston, USA: CAB International.
68. Laurenson, J. P.; Bloom, R. A.; Page, S.; Sadrieh, N. (2014). Ethinyl Estradiol and Other Human Pharmaceutical Estrogens in the Aquatic Environment: A Review of Recent Risk Assessment Data. *The AAPS Journal*, 16 (2), 299-310. DOI: 10.1208/s12248-014-9561-3.
69. Kostich, M.; Flick, R.; Martinson, J. (2013). Comparing predicted estrogen concentrations with measurements in US waters. *Environ. Pollut.*, 178, 271-277. DOI: 10.1016/j.envpol.2013.03.024.
70. Kuch, H. M.; Ballschmiter, K. (2001). Determination of Endocrine-Disrupting Phenolic Compounds and Estrogens in Surface and Drinking Water by HRGC-(NCI)-MS in the Picogram per Liter Range. *Environ. Sci. Technol.*, 35 (15), 3201-3206. DOI: 10.1021/es010034m.
71. Fan, Z.; Hu, J.; An, W.; Yang, M. (2013). Detection and Occurrence of Chlorinated Byproducts of Bisphenol A, Nonylphenol, and Estrogens in Drinking Water of China: Comparison to the Parent Compounds. *Environ. Sci. Technol.*, 47 (19), 10841-10850. DOI: 10.1021/es401504a.
72. Vulliet, E.; Cren-Olivé, C.; Grenier-Loustalot, M.-F. (2011). Occurrence of pharmaceuticals and hormones in drinking water treated from surface waters. *Environ. Chem. Lett.*, 9 (1), 103-114. DOI: 10.1007/s10311-009-0253-7.
73. Houtman, C. J. (2010). Emerging contaminants in surface waters and their relevance for the production of drinking water in Europe. *Journal of Integrative Environmental Sciences*, 7 (4), 271-295. DOI: 10.1080/1943815X.2010.511648.
74. Ho, S.-M.; Tang, W.-Y.; Belmonte de Frausto, J.; Prins, G. S. (2006). Developmental exposure to estradiol and bisphenol A increases susceptibility to prostate carcinogenesis and epigenetically regulates phosphodiesterase type 4 variant 4. *Cancer Res.*, 66 (11), 5624-5632. DOI: 10.1158/0008-5472.Can-06-0516.
75. Li, X.; Li, H.; Jia, L.; Li, X.; Rahman, N. (2015). Oestrogen action and male fertility: experimental and clinical findings. *Cell. Mol. Life Sci.*, 72 (20), 3915-3930. DOI: 10.1007/s00018-015-1981-4.

76. Giwercman, A.; Rylander, L.; Giwercman, Y. L. (2007). Influence of endocrine disruptors on human male fertility. *Reprod. Biomed. Online*, 15 (6), 633-642. DOI: 10.1016/S1472-6483(10)60530-5.
77. Manickum, T.; John, W. (2014). Occurrence, fate and environmental risk assessment of endocrine disrupting compounds at the wastewater treatment works in Pietermaritzburg (South Africa). *Sci. Total Environ.*, 468-469, 584-597. DOI: 10.1016/j.scitotenv.2013.08.041.
78. Zhong, R.; Zou, H.; Gao, J.; Wang, T.; Bu, Q.; Wang, Z.-L.; Hu, M.; Wang, Z. (2021). A critical review on the distribution and ecological risk assessment of steroid hormones in the environment in China. *Sci. Total Environ.*, 786, 147452. DOI: 10.1016/j.scitotenv.2021.147452.
79. Sousa, J. C. G.; Ribeiro, A. R.; Barbosa, M. O.; Pereira, M. F. R.; Silva, A. M. T. (2018). A review on environmental monitoring of water organic pollutants identified by EU guidelines. *J. Hazard. Mater.*, 344, 146-162. DOI: 10.1016/j.jhazmat.2017.09.058.
80. Tang, Z.; Liu, Z.-h.; Wang, H.; Dang, Z.; Liu, Y. (2021). Occurrence and removal of 17 $\alpha$ -ethynylestradiol (EE2) in municipal wastewater treatment plants: Current status and challenges. *Chemosphere*, 271, 129551. DOI: 10.1016/j.chemosphere.2021.129551.
81. Torres, N. H.; Aguiar, M. M.; Ferreira, L. F. R.; Américo, J. H. P.; Machado, Â. M.; Cavalcanti, E. B.; Tornisielo, V. L. (2015). Detection of hormones in surface and drinking water in Brazil by LC-ESI-MS/MS and ecotoxicological assessment with *Daphnia magna*. *Environ. Monit. Assess.*, 187 (6), 379. DOI: 10.1007/s10661-015-4626-z.
82. Zhang, J.-N.; Ying, G.-G.; Yang, Y.-Y.; Liu, W.-R.; Liu, S.-S.; Chen, J.; Liu, Y.-S.; Zhao, J.-L.; Zhang, Q.-Q. (2018). Occurrence, fate and risk assessment of androgens in ten wastewater treatment plants and receiving rivers of South China. *Chemosphere*, 201, 644-654. DOI: 10.1016/j.chemosphere.2018.02.144.
83. Fan, Z.; Wu, S.; Chang, H.; Hu, J. (2011). Behaviors of Glucocorticoids, Androgens and Progestogens in a Municipal Sewage Treatment Plant: Comparison to Estrogens. *Environ. Sci. Technol.*, 45 (7), 2725-2733. DOI: 10.1021/es103429c.
84. Havens, S. M.; Hedman, C. J.; Hemming, J. D. C.; Mieritz, M. G.; Shafer, M. M.; Schauer, J. J. (2020). Occurrence of estrogens, androgens and progestogens and estrogenic activity in surface water runoff from beef and dairy manure amended crop fields. *Sci. Total Environ.*, 710, 136247. DOI: 10.1016/j.scitotenv.2019.136247.
85. Zhang, K.; Zhao, Y.; Fent, K. (2017). Occurrence and Ecotoxicological Effects of Free, Conjugated, and Halogenated Steroids Including 17 $\alpha$ -Hydroxypregnanolone and Pregnenediol in Swiss Wastewater and Surface Water. *Environ. Sci. Technol.*, 51 (11), 6498-6506. DOI: 10.1021/acs.est.7b01231.
86. Guyón, N. F.; Roggio, M. A.; Amé, M. V.; Hued, A. C.; Valdés, M. E.; Giojalas, L. C.; Wunderlin, D. A.; Bistoni, M. A. (2012). Impairments in aromatase expression, reproductive behavior, and sperm quality of male fish exposed to 17 $\beta$ -estradiol. *Environ. Toxicol. Chem.*, 31 (5), 935-940. DOI: 10.1002/etc.1790.
87. Gioiosa, L.; Fissore, E.; Ghirardelli, G.; Parmigiani, S.; Palanza, P. (2007). Developmental exposure to low-dose estrogenic endocrine disruptors alters sex differences in exploration and emotional responses in mice. *Horm. Behav.*, 52 (3), 307-316. DOI: 10.1016/j.yhbeh.2007.05.006.
88. Van Donk, E.; Peacor, S.; Grosser, K.; De Senerpont Domis, L. N.; Lüring, M. (2016). Pharmaceuticals May Disrupt Natural Chemical Information Flows and Species Interactions in Aquatic Systems: Ideas and Perspectives on a Hidden Global Change. In *Rev. Environ. Contam. Toxicol.*, (de Voogt, P.; Gunther, F. A. Eds.), 91-105. Cham: Springer International Publishing.
89. Clotfelter, E. D.; Bell, A. M.; Levering, K. R. (2004). The role of animal behaviour in the study of endocrine-disrupting chemicals. *Anim. Behav.*, 68 (4), 665-676. DOI: 10.1016/j.anbehav.2004.05.004.

90. Kidd, K. A.; Blanchfield, P. J.; Mills, K. H.; Palace, V. P.; Evans, R. E.; Lazorchak, J. M.; Flick, R. W. (2007). Collapse of a fish population after exposure to a synthetic estrogen. *Proceedings of the National Academy of Sciences*, 104 (21), 8897-8901. DOI:
91. Blanchfield, P. J.; Kidd, K. A.; Docker, M. F.; Palace, V. P.; Park, B. J.; Postma, L. D. (2015). Recovery of a Wild Fish Population from Whole-Lake Additions of a Synthetic Estrogen. *Environ. Sci. Technol.*, 49 (5), 3136-3144. DOI: 10.1021/es5060513.
92. Schubert, S.; Peter, A.; Burki, R.; Schönenberger, R.; Suter, M. J. F.; Segner, H.; Burkhardt-Holm, P. (2008). Sensitivity of brown trout reproduction to long-term estrogenic exposure. *Aquat. Toxicol.*, 90 (1), 65-72. DOI: 10.1016/j.aquatox.2008.08.002.
93. Yamamoto, H.; Liljestrand, H. M. (2004). Partitioning of selected estrogenic compounds between synthetic membrane vesicles and water: effects of lipid components. *Environ. Sci. Technol.*, 38 (4), 1139–1147. DOI:
94. Hurwitz, A.; Liu, S., T. (1977). Determination of aqueous solubility and pKa values of estrogens. *J. Pharm. Sci.*, 66 (5), 624-627. DOI: 10.1002/jps.2600660504.
95. Barry, B. W.; Eini, D. I. D. E. (1976). Solubilization of hydrocortisone, dexamethasone, testosterone and progesterone by long - chain polyoxyethylene surfactants. *J. Pharm. Pharmacol.*, 28 (3), 210-218. DOI: 10.1111/j.2042-7158.1976.tb04133.x.
96. Lundberg, B.; Lövgren, T.; Heikius, B. (1979). Simultaneous solubilization of steroid hormones II: androgens and estrogens. *J. Pharm. Sci.*, 68 (5), 542-545. DOI: 10.1002/jps.2600680506.
97. Fulford, M.; Slonek, J.; Groves, M. (1986). A note on the solubility of progesterone in aqueous polyethylene glycol 400. *Drug Dev. Ind. Pharm.*, 12 (4), 631-635. DOI:
98. Ruchelman, M. W.; Haines, P. (1967). Solubility studies of estradiol in organic Solvents using gas-liquid chromatography. *J. Chromatogr. Sci.*, 5 (6), 290-296. DOI: 10.1093/chromsci/5.6.290.
99. Ruchelman, M. W. (1967). Solubility studies of estrone in organic solvents using gas-liquid chromatography. *Anal. Biochem.*, 19 (1), 98–108. DOI: 10.1016/0003-2697(67)90139-X.
100. Ruchelman, M. W. (1971). Solubility studies of testosterone in organic solvents using gas chromatography. *J. Chromatogr. Sci.*, 9 (4), 235-240. DOI: 10.1093/chromsci/9.4.235.
101. Sieminska, L.; Ferguson, M.; Zerda, T. W.; Couch, E. (1997). Diffusion of steroids in porous sol-gel glass: application in slow drug delivery. *J. Sol-Gel Sci. Technol.*, 8 (1), 1105–1109. DOI: 10.1007/BF02436991.
102. Brion, F.; Le Page, Y.; Piccini, B.; Cardoso, O.; Tong, S. K.; Chung, B. C.; Kah, O. (2012). Screening estrogenic activities of chemicals or mixtures in vivo using transgenic (*cyp19a1b*-GFP) zebrafish embryos. *PLoS One*, 7 (5), e36069. DOI: 10.1371/journal.pone.0036069.
103. Yost, E. E.; Meyer, M. T.; Dietze, J. E.; Meissner, B. M.; Worley-Davis, L.; Williams, C. M.; Lee, B.; Kullman, S. W. (2013). Comprehensive assessment of hormones, phytoestrogens, and estrogenic activity in an anaerobic swine waste lagoon. *Environ. Sci. Technol.*, 47 (23), 13781–13790. DOI: 10.1021/es4026408.
104. Perrin, D. D.; Dempsey, B.; Serjeant, E. P. (1981). pKa prediction for organic acids and bases. *Springer Netherlands*.
105. Lewis, K.; Archer, R. (1979). pKa values of estrone, 17 $\beta$ -estradiol and 2-methoxyestrone. *Steroids*, 34 (5), 485-499. DOI: 10.1016/S0039-128X(79)80011-2.
106. Perkin Elmer. 2022. Technical data sheet. Estradiol, [2,4,6,7-3H(N)]-. Product Number: NET317. Available online: <https://www.perkinelmer.com/resources>. (accessed 07 June 2022).
107. Perkin Elmer. 2022. Technical data sheet. Estrone, [2,4,6,7-3H(N)]-. Product Number: NET319. Available online: <https://www.perkinelmer.com/resources>. (accessed 07 June 2022).
108. Perkin Elmer. 2022. Technical data sheet. Testosterone, [1,2,6,7-3H(N)]-. Product Number: NET370. Available online: <https://www.perkinelmer.com/resources>. (accessed 07 June 2022).

109. Perkin Elmer. 2022. Technical data sheet. Progesterone, [1,2,6,7-3H(N)]-. Product Number: NET381. Available online: <https://www.perkinelmer.com/resources>. (accessed 07 June 2022).
110. SCHER (Scientific Committee on Health and Environmental Risks). (30 March 2011). Chemicals and the water framework directive: draft environmental quality standards–17 $\beta$ -estradiol (E2). Available online: [https://ec.europa.eu/health/scientific\\_committees/environmental\\_risks/docs/scher\\_o\\_131.pdf](https://ec.europa.eu/health/scientific_committees/environmental_risks/docs/scher_o_131.pdf). (accessed 07 June 2022).
111. US EPA. (2012). Revisions to the Unregulated Contaminant Monitoring Regulation (UCMR 3) for Public Water Systems; *US Environmental Protection Agency: Federal Register*. pp 26072-26101. Available online: <https://www.govinfo.gov/app/details/FR-2012-05-02/2012-9978>. (accessed 18 June 2022).
112. Wu, J.; Hariri, S.; Qin, F.; Hang, K. P.; Cai, C. (2019). Analysis of low part per trillion levels of estrogens in serum without derivatization using QSight 420 UHPLC/MS/MS System (Application note); PerkinElmer, Inc. Available online: <https://www.perkinelmer.com/lab-solutions/resources/docs/APP-Estrogen-in-Serum-17139.pdf>. (accessed 18 June 2022).
113. Glineur, A.; Barbera, B.; Nott, K.; Carbonnelle, P.; Ronkart, S.; Lognay, G.; Tyteca, E. (2018). Trace analysis of estrogenic compounds in surface and groundwater by ultra high performance liquid chromatography-tandem mass spectrometry as pyridine-3-sulfonyl derivatives. *J. Chromatogr. A*, 1534, 43-54. DOI: 10.1016/j.chroma.2017.12.042.
114. He, P.; Aga, D. S. (2019). Comparison of GC-MS/MS and LC-MS/MS for the analysis of hormones and pesticides in surface waters: advantages and pitfalls. *Analytical Methods*, 11 (11), 1436–1448. DOI: 10.1039/C8AY02774A.
115. Matějčiček, D.; Kubáň, V. (2008). Enhancing sensitivity of liquid chromatographic/ion-trap tandem mass spectrometric determination of estrogens by on-line pre-column derivatization. *J. Chromatogr. A*, 1192 (2), 248-253. DOI: 10.1016/j.chroma.2008.03.061.
116. Miège, C.; Bados, P.; Brosse, C.; Coquery, M. (2009). Method validation for the analysis of estrogens (including conjugated compounds) in aqueous matrices. *TrAC, Trends Anal. Chem.*, 28 (2), 237-244. DOI: 10.1016/j.trac.2008.11.005.
117. Lv, X.; Xiao, S.; Zhang, G.; Jiang, P.; Tang, F. (2016). Occurrence and removal of phenolic endocrine disrupting chemicals in the water treatment processes. 6 (1), 22860. DOI: 10.1038/srep22860.
118. Shackleton, C.; Pozo, O. J.; Marcos, J. (2018). GC/MS in recent years has defined the normal and clinically disordered steroidome: will it soon be surpassed by LC/Tandem MS in this role? *J. Endocr. Soc.*, 2 (8), 974-996. DOI: 10.1210/js.2018-00135.
119. Marcos, J.; Pozo, O. J. (2015). Derivatization of steroids in biological samples for GC–MS and LC–MS analyses. *Bioanalysis*, 7 (19), 2515-2536. DOI: 10.4155/bio.15.176.
120. Raben, M. S.; Bloembergen, N. (1951). Determination of radioactivity by solution in a liquid scintillator. *Science*, 114 (2962), 363-364. DOI: 10.1126/science.114.2962.363.
121. Gabet, V.; Miège, C.; Bados, P.; Coquery, M. (2007). Analysis of estrogens in environmental matrices. *TrAC, Trends Anal. Chem.*, 26 (11), 1113–1131. DOI: 10.1016/j.trac.2007.10.003.
122. Bridle, H. L.; Heringa, M. B.; Schafer, A. I. (2016). Solid-phase microextraction to determine micropollutant-macromolecule partition coefficients. *Nat. Protoc.*, 11 (8), 1328-44. DOI: 10.1038/nprot.2016.068.
123. Lyubimenko, R.; Richards, B. S.; Turshatov, A.; Schäfer, A. I. (2020). Separation and degradation detection of nanogram-per-litre concentrations of radiolabelled steroid hormones using combined liquid chromatography and flow scintillation analysis. *Sci. Rep.*, 10 (1), 7095. DOI: 10.1038/s41598-020-63697-y.
124. Penner, N.; Klunk, L. J.; Prakash, C. (2009). Human radiolabeled mass balance studies: objectives, utilities and limitations. *Biopharm. Drug Disposition*, 30 (4), 185-203. DOI: 10.1002/bdd.661.

125. L'Annunziata, M. F. (2012). Flow-Cell Analysis. In Handbook of radioactivity analysis, Third ed.; (L'Annunziata, M. F. Ed.) 1117–1178. Amsterdam: *Elsevier*.
126. Tykva, R.; Wimmer, Z.; Vlasáková, V.; Novák, J.; Havlíček, L. (2005). Biodegradation of juvenoid diastereoisomers: Radio-HPLC and MS analysis. *Chemosphere*, 60 (9), 1197–1202. DOI: 10.1016/j.chemosphere.2005.02.012.
127. Abdel-Khalik, J.; Björklund, E.; Nielsen, F. K.; Hansen, M. (2017). Incorporation of <sup>14</sup>C-cholesterol in human adrenal corticocarcinoma H295R cell line and online-radiodetection of produced <sup>14</sup>C-steroid hormone metabolites. *J. Pharm. Biomed. Anal.*, 145, 569-575. DOI: 10.1016/j.jpba.2017.06.058.
128. Pettersson, H.; Lundqvist, J.; Oliw, E.; Norlin, M. (2009). CYP7B1-mediated metabolism of 5 $\alpha$ -androstane-3 $\alpha$ , 17 $\beta$ -diol (3 $\alpha$ -Adiol): A novel pathway for potential regulation of the cellular levels of androgens and neurosteroids. *Biochim. Biophys. Acta, Mol. Cell Biol. Lipids*, 1791 (12), 1206–1215. DOI: 10.1016/j.bbalip.2009.08.010.
129. Plumb, R.; Castro-Perez, J.; Granger, J.; Beattie, I.; Joncour, K.; Wright, A. (2004). Ultra-performance liquid chromatography coupled to quadrupole-orthogonal time-of-flight mass spectrometry. *Rapid Commun. Mass Spectrom.*, 18 (19), 2331-2337. DOI: 10.1002/rcm.1627.
130. Dear, G. J.; Patel, N.; Kelly, P. J.; Webber, L.; Yung, M. (2006). TopCount coupled to ultra-performance liquid chromatography for the profiling of radiolabeled drug metabolites in complex biological samples. *J. Chromatogr. B*, 844 (1), 96–103. DOI: 10.1016/j.jchromb.2006.07.041.
131. Glaze, W. H.; Kang, J.-W.; Chapin, D. H. (1987). The Chemistry of Water Treatment Processes Involving Ozone, Hydrogen Peroxide and Ultraviolet Radiation. *Ozone: Science & Engineering*, 9 (4), 335-352. DOI: 10.1080/01919518708552148.
132. Bennedsen, L. R. (2014). Chapter 2 - In situ Chemical Oxidation: The Mechanisms and Applications of Chemical Oxidants for Remediation Purposes. In Chemistry of Advanced Environmental Purification Processes of Water, (Søgaard, E. G. Ed.) 13-74. Amsterdam: *Elsevier*.
133. Oh, W.-D.; Dong, Z.; Lim, T.-T. (2016). Generation of sulfate radical through heterogeneous catalysis for organic contaminants removal: Current development, challenges and prospects. *Appl. Catal. B: Environ.*, 194, 169-201. DOI: 10.1016/j.apcatb.2016.04.003.
134. Buettner, G. R. (1993). The Pecking Order of Free Radicals and Antioxidants: Lipid Peroxidation,  $\alpha$ -Tocopherol, and Ascorbate. *Arch. Biochem. Biophys.*, 300 (2), 535-543. DOI: 10.1006/abbi.1993.1074.
135. Buxton, G. V.; Greenstock, C. L.; Helman, W. P.; Ross, A. B. (1988). Critical Review of rate constants for reactions of hydrated electrons, hydrogen atoms and hydroxyl radicals ( $\cdot$ OH/ $\cdot$ O $^-$ ) in Aqueous Solution. *J. Phys. Chem. Ref. Data*, 17 (2), 513-886. DOI: 10.1063/1.555805.
136. von Gunten, U. (2003). Ozonation of drinking water: Part I. Oxidation kinetics and product formation. *Water Res.*, 37 (7), 1443–1467. DOI: 10.1016/S0043–1354(02)00457-8.
137. Burns, J. M.; Cooper, W. J.; Ferry, J. L.; King, D. W.; DiMento, B. P.; McNeill, K.; Miller, C. J.; Miller, W. L.; Peake, B. M.; Rusak, S. A.; Rose, A. L.; Waite, T. D. (2012). Methods for reactive oxygen species (ROS) detection in aqueous environments. *Aquat. Sci.*, 74 (4), 683-734. DOI: 10.1007/s00027-012-0251-x.
138. Nonell, S.; Flors, C. (2016). Steady-State and Time-Resolved Singlet Oxygen Phosphorescence Detection in the Near-IR. In Singlet Oxygen: Applications in Biosciences and Nanosciences, Volume 2, (Nonell, S.; Flors, C. Eds.), Vol. 2,7-26. Cambridge, UK: *The Royal Society of Chemistry*.
139. Markham, S. C. (1955). Photocatalytic properties of oxides. *J. Chem. Educ.*, 32 (10), 540. DOI: 10.1021/ed032p540.
140. Fujishima, A.; Honda, K. (1972). Electrochemical photolysis of water at a semiconductor electrode. *Nature*, 238 (5358), 37-38. DOI: 10.1038/238037a0.

141. Fujishima, A.; Zhang, X.; Tryk, D. A. (2008). TiO<sub>2</sub> photocatalysis and related surface phenomena. *Surf. Sci. Rep.*, 63 (12), 515-582. DOI: 10.1016/j.surfrep.2008.10.001.
142. Fagan, R.; McCormack, D. E.; Dionysiou, D. D.; Pillai, S. C. (2016). A review of solar and visible light active TiO<sub>2</sub> photocatalysis for treating bacteria, cyanotoxins and contaminants of emerging concern. *Mater. Sci. Semicond. Process.*, 42, 2–14. DOI: 10.1016/j.mssp.2015.07.052.
143. Serrà, A.; Philippe, L.; Perreault, F.; Garcia-Segura, S. (2020). Photocatalytic treatment of natural waters. Reality or hype? The case of cyanotoxins remediation. *Water Res.*, 116543. DOI: 10.1016/j.watres.2020.116543.
144. Puralytics. 2021. Available online: <https://puralytics.com/>. (accessed 18 June 2022).
145. Brightwater Environmental. 2021. BrightWater Titanium Advanced Oxidation Process (AOP). Available online: <http://www.brightwaterenvironmental.co.uk/aop/titanium-aop/titanium-aop-page/>. (accessed 18 June 2022).
146. Iervolino, G.; Zammit, I.; Vaiano, V.; Rizzo, L. (2020). Limitations and Prospects for Wastewater Treatment by UV and Visible-Light-Active Heterogeneous Photocatalysis: A Critical Review. *Top Curr Chem (Z)*, 225-264. DOI: 10.1007/978-3-030-49492-6\_7.
147. Dong, H.; Zeng, G.; Tang, L.; Fan, C.; Zhang, C.; He, X.; He, Y. (2015). An overview on limitations of TiO<sub>2</sub>-based particles for photocatalytic degradation of organic pollutants and the corresponding countermeasures. *Water Res.*, 79, 128–146. DOI: 10.1016/j.watres.2015.04.038.
148. Asahi, R.; Morikawa, T.; Ohwaki, T.; Aoki, K.; Taga, Y. (2001). Visible-Light Photocatalysis in Nitrogen-Doped Titanium Oxides. *Science*, 293 (5528), 269-271. DOI: 10.1126/science.1061051.
149. In, S.; Orlov, A.; Berg, R.; García, F.; Pedrosa-Jimenez, S.; Tikhov, M. S.; Wright, D. S.; Lambert, R. M. (2007). Effective Visible Light-Activated B-Doped and B,N-Codoped TiO<sub>2</sub> Photocatalysts. *J. Am. Chem. Soc.*, 129 (45), 13790–13791. DOI: 10.1021/ja0749237.
150. Kemacheevakul, P.; Chuangchote, S. (2021). Photocatalytic Remediation of Organic Pollutants in Water. In *Water Pollution and Remediation: Photocatalysis*, (Inamuddin; Ahamed, M. I.; Lichtfouse, E. Eds.), 1-51. Cham, Switzerland: *Springer International Publishing*.
151. Low, J.; Yu, J.; Jaroniec, M.; Wageh, S.; Al-Ghamdi, A. A. (2017). Heterojunction Photocatalysts. *Adv. Mater.*, 29 (20), 1601694. DOI: 10.1002/adma.201601694.
152. Dong, P.; Hou, G.; Xi, X.; Shao, R.; Dong, F. (2017). WO<sub>3</sub>-based photocatalysts: morphology control, activity enhancement and multifunctional applications. *Environmental Science: Nano*, 4 (3), 539-557. DOI: 10.1039/C6EN00478D.
153. Zargazi, M.; Chahkandi, M. (2021). Bismuth-Based Compounds as Visible Light Photocatalyst for Remediation and Water Splitting. In *Water Pollution and Remediation: Photocatalysis*, (Inamuddin; Ahamed, M. I.; Lichtfouse, E. Eds.), 321-358. Cham: *Springer International Publishing*.
154. Banerjee, S.; Pillai, S. C.; Falaras, P.; O’Shea, K. E.; Byrne, J. A.; Dionysiou, D. D. (2014). New Insights into the Mechanism of Visible Light Photocatalysis. *The Journal of Physical Chemistry Letters*, 5 (15), 2543-2554. DOI: 10.1021/jz501030x.
155. Afzal, S.; Daoud, W. A.; Langford, S. J. (2013). Photostable Self-Cleaning Cotton by a Copper(II) Porphyrin/TiO<sub>2</sub> Visible-Light Photocatalytic System. *ACS Applied Materials & Interfaces*, 5 (11), 4753-4759. DOI: 10.1021/am400002k.
156. Zhang, Z.; Bai, L.; Li, Z.; Qu, Y.; Jing, L. (2019). Review of strategies for the fabrication of heterojunctional nanocomposites as efficient visible-light catalysts by modulating excited electrons with appropriate thermodynamic energy. *Journal of Materials Chemistry A*, 7 (18), 10879–10897. DOI: 10.1039/C9TA02373A.
157. Díez-Mato, E.; Cortezón-Tamarit, F. C.; Bogialli, S.; García-Fresnadillo, D.; Marazuela, M. D. (2014). Phototransformation of model micropollutants in water samples by photocatalytic singlet

- oxygen production in heterogeneous medium. *Appl. Catal. B: Environ.*, 160–161, 445-455. DOI: 10.1016/j.apcatb.2014.05.050.
158. Liu, C.; Liu, K.; Wang, C.; Liu, H.; Wang, H.; Su, H.; Li, X.; Chen, B.; Jiang, J. (2020). Elucidating heterogeneous photocatalytic superiority of microporous porphyrin organic cage. *Nat. Commun.*, 11 (1), 1047. DOI: 10.1038/s41467-020-14831-x.
159. Silvestri, S.; Fajardo, A. R.; Iglesias, B. A. (2021). Supported porphyrins for the photocatalytic degradation of organic contaminants in water: a review. *Environ. Chem. Lett.* DOI: 10.1007/s10311-021-01344-2.
160. Piccirillo, G.; Aroso, R. T.; Rodrigues, F.; Carrilho, R.; Pinto, S.; Calvete, M. J.; Pereira, M. M. (2021). Oxidative Degradation of Pharmaceuticals: The Role of Tetrapyrrole-Based Catalysts. *Catalysts*, 11 (11), 1335. DOI: 10.3390/catal11111335.
161. Daniell, M. D.; Hill, J. S. (1991). A history of photodynamic therapy. *Aust. N. Z. J. Surg.*, 61 (5), 340-348. DOI: 10.1111/j.1445-2197.1991.tb00230.x.
162. O'Regan, B.; Grätzel, M. (1991). A low-cost, high-efficiency solar cell based on dye-sensitized colloidal TiO<sub>2</sub> films. *Nature*, 353 (6346), 737-740. DOI: 10.1038/353737a0.
163. Zhou, J.; Liu, Q.; Feng, W.; Sun, Y.; Li, F. (2015). Upconversion Luminescent Materials: Advances and Applications. *Chem. Rev.*, 115 (1), 395-465. DOI: 10.1021/cr400478f.
164. Romero, N. A.; Nicewicz, D. A. (2016). Organic Photoredox Catalysis. *Chem. Rev.*, 116 (17), 10075–10166. DOI: 10.1021/acs.chemrev.6b00057.
165. Kampouri, S.; Stylianou, K. C. (2019). Dual-functional photocatalysis for simultaneous hydrogen production and oxidation of organic substances. *ACS Catal.*, 9 (5), 4247-4270. DOI: 10.1021/acscatal.9b00332.
166. Miranda, M. A.; Galindo, F.; Amat, A. M.; Arques, A. (2001). Pyrylium salt-photosensitised degradation of phenolic contaminants present in olive oil wastewaters with solar light: Part II. Benzoic acid derivatives. *Appl. Catal. B: Environ.*, 30 (3), 437-444. DOI: 10.1016/S0926-3373(00)00259-9.
167. Gmurek, M.; Olak-Kucharczyk, M.; Ledakowicz, S. (2017). Photochemical decomposition of endocrine disrupting compounds – A review. *Chem. Eng. J.*, 310, 437-456. DOI: 10.1016/j.cej.2016.05.014.
168. Lacombe, S.; Pigot, T. (2016). Materials for selective photo-oxygenation vs. photocatalysis: preparation, properties and applications in environmental and health fields. *Catal. Sci. Technol.*, 6 (6), 1571–1592. DOI:
169. DeRosa, M. C.; Crutchley, R. J. (2002). Photosensitized singlet oxygen and its applications. *Coord. Chem. Rev.*, 233-234, 351-371. DOI: 10.1016/S0010-8545(02)00034-6.
170. Brame, J.; Long, M.; Li, Q.; Alvarez, P. (2014). Trading oxidation power for efficiency: differential inhibition of photo-generated hydroxyl radicals versus singlet oxygen. *Water Res.*, 60, 259-66. DOI: 10.1016/j.watres.2014.05.005.
171. Kim, H.; Kim, W.; Mackeyev, Y.; Lee, G.-S.; Kim, H.-J.; Tachikawa, T.; Hong, S.; Lee, S.; Kim, J.; Wilson, L. J.; Majima, T.; Alvarez, P. J. J.; Choi, W.; Lee, J. (2012). Selective oxidative degradation of organic pollutants by singlet oxygen-mediated photosensitization: tin porphyrin versus C<sub>60</sub> aminofullerene systems. *Environ. Sci. Technol.*, 46 (17), 9606-9613. DOI: 10.1021/es301775k.
172. Brzozowski, A. M.; Pike, A. C.; Dauter, Z.; Hubbard, R. E.; Bonn, T.; Engström, O.; Öhman, L.; Greene, G. L.; Gustafsson, J.-Å.; Carlquist, M. (1997). Molecular basis of agonism and antagonism in the oestrogen receptor. *Nature*, 389 (6652), 753-758. DOI: 10.1038/39645.
173. Nosaka, Y.; Nosaka, A. Y. (2017). Generation and Detection of Reactive Oxygen Species in Photocatalysis. *Chem. Rev.*, 117 (17), 11302–11336. DOI: 10.1021/acs.chemrev.7b00161.



174. Marin, M. L.; Santos-Juanes, L.; Arques, A.; Amat, A. M.; Miranda, M. A. (2012). Organic photocatalysts for the oxidation of pollutants and model compounds. *Chem. Rev.*, 112 (3), 1710–1750. DOI: 10.1021/cr2000543.
175. Di Mascio, P.; Martinez, G. R.; Miyamoto, S.; Ronsein, G. E.; Medeiros, M. H.; Cadet, J. (2019). Singlet molecular oxygen reactions with nucleic acids, lipids, and proteins. *Chem. Rev.*, 119 (3), 2043–2086. DOI: 10.1021/acs.chemrev.8b00554.
176. Taniguchi, M.; Du, H.; Lindsey, J. S. (2018). PhotochemCAD 3: Diverse Modules for Photophysical Calculations with Multiple Spectral Databases. *Photochem. Photobiol.*, 94 (2), 277–289. DOI: 10.1111/php.12862.
177. Nichiporovich, I.; Kochubeeva, N.; Kruk, N.; Kuz'mitskii, V. (2004). Bacteriochlorin e6 as a sensitizer for photodynamic therapy. *J. Appl. Spectrosc.*, 71 (6), 814–817. DOI: 10.1007/s10812-005-0007-7.
178. Gouterman, M.; Wagnière, G. H.; Snyder, L. C. (1963). Spectra of porphyrins: Part II. Four orbital model. *J. Mol. Spectrosc.*, 11 (1), 108–127. DOI: 10.1016/0022-2852(63)90011-0.
179. Auwärter, W.; Ćija, D.; Klappenberger, F.; Barth, J. V. (2015). Porphyrins at interfaces. *Nat. Chem.*, 7 (2), 105–120. DOI: 10.1038/nchem.2159.
180. Guldi, D. M.; Mody, T. D.; Gerasimchuk, N. N.; Magda, D.; Sessler, J. L. (2000). Influence of large metal cations on the photophysical properties of texaphyrin, a rigid aromatic chromophore. *J. Am. Chem. Soc.*, 122 (34), 8289–8298. DOI: 10.1021/ja001578b.
181. Arnaut, L. G. (2011). Chapter 5 - Design of porphyrin-based photosensitizers for photodynamic therapy. In *Adv. Inorg. Chem.*, (Eldik, R. v.; Stochel, G. Eds.), Vol. 63, 187–233. Academic Press.
182. Dąbrowski, J. M.; Pucelik, B.; Regiel-Futyra, A.; Brindell, M.; Mazuryk, O.; Kyzioł, A.; Stochel, G.; Macyk, W.; Arnaut, L. G. (2016). Engineering of relevant photodynamic processes through structural modifications of metallotetrapyrrolic photosensitizers. *Coord. Chem. Rev.*, 325, 67–101. DOI: 10.1016/j.ccr.2016.06.007.
183. Lakowicz, J. R. (2006). Introduction to Fluorescence. In *Principles of Fluorescence Spectroscopy*, (Lakowicz, J. R. Ed.) 1–26. Boston, MA: Springer US.
184. Lyubimenko, R.; Richards, B. S.; Schäfer, A. I.; Turshatov, A. (2022). Noble-metal-free photosensitizers for continuous-flow photochemical oxidation of steroid hormone micropollutants under sunlight. *J. Membr. Sci.*, 642, 119981. DOI: 10.1016/j.memsci.2021.119981.
185. Shi-Kang, W.; Hou-Chen, Z.; Guo-Zhu, C.; Da-Nian, X.; Hui-Jun, X. (1985). A study on the ability of some phthalocyanine compounds for photogenerating singlet oxygen. *Acta Chim. Sin. (Engl. Ed.)*, 3 (1), 21–25. DOI: 10.1002/cjoc.19850030105.
186. Koren, K.; Borisov, S. M.; Klimant, I. (2012). Stable optical oxygen sensing materials based on click-coupling of fluorinated platinum(II) and palladium(II) porphyrins—A convenient way to eliminate dye migration and leaching. *Sensors Actuators B: Chem.*, 169, 173–181. DOI: 10.1016/j.snb.2012.04.062.
187. Önal, E.; Saß, S.; Hurpin, J.; Ertekin, K.; Topal, S. Z.; Kumke, M. U.; Hirel, C. (2017). Lifetime-based oxygen sensing properties of palladium(II) and platinum(II) meso-tetrakis(4-phenylethynyl)phenylporphyrin. *J. Fluoresc.*, 27 (3), 861–868. DOI: 10.1007/s10895-016-2022-x.
188. Kee, H. L.; Bhaumik, J.; Diers, J. R.; Mroz, P.; Hamblin, M. R.; Bocian, D. F.; Lindsey, J. S.; Holten, D. (2008). Photophysical characterization of imidazolium-substituted Pd(II), In(III), and Zn(II) porphyrins as photosensitizers for photodynamic therapy. *J. Photochem. Photobiol. A*, 200 (2), 346–355. DOI: 10.1016/j.jphotochem.2008.08.006.
189. Jung, J.; Ohkubo, K.; Goldberg, D. P.; Fukuzumi, S. (2014). Photocatalytic oxygenation of 10-methyl-9, 10-dihydroacridine by O<sub>2</sub> with manganese porphyrins. *J. Phys. Chem. A*, 118 (32), 6223–6229. DOI: 10.1021/jp505860f.

190. Monteiro, C. J. P.; Pereira, M. M.; Azenha, M. E.; Burrows, H. D.; Serpa, C.; Arnaut, L. G.; Tapia, M. J.; Sarakha, M.; Wong-Wah-Chung, P.; Navaratnam, S. (2005). A comparative study of water soluble 5,10,15,20-tetrakis(2,6-dichloro-3-sulfophenyl)porphyrin and its metal complexes as efficient sensitizers for photodegradation of phenols. *Photochemical & Photobiological Sciences*, 4 (8), 617-624. DOI: 10.1039/B507597A.
191. Aulin, Y. V.; van Seville, M.; Moes, M.; Grozema, F. C. (2015). Photochemical upconversion in metal-based octaethyl porphyrin–diphenylanthracene systems. *RSC Adv.*, 5 (130), 107896–107903. DOI: 10.1039/C5RA20602B.
192. Azenha, E. I. G.; Serra, A. C.; Pineiro, M.; Pereira, M. M.; Seixas de Melo, J.; Arnaut, L. G.; Formosinho, S. J.; Rocha Gonsalves, A. M. d. A. (2002). Heavy-atom effects on metalloporphyrins and polyhalogenated porphyrins. *Chem. Phys.*, 280 (1), 177–190. DOI: 10.1016/S0301-0104(02)00485-8.
193. Yang, E.; Diers, J. R.; Huang, Y.-Y.; Hamblin, M. R.; Lindsey, J. S.; Bocian, D. F.; Holten, D. (2013). Molecular Electronic Tuning of Photosensitizers to Enhance Photodynamic Therapy: Synthetic Dicyanobacteriochlorins as a Case Study. *Photochem. Photobiol.*, 89 (3), 605-618. DOI: 10.1111/php.12021.
194. Bonnett, R.; Martinez, G. (2001). Photobleaching of sensitizers used in photodynamic therapy. *Tetrahedron*, 57 (47), 9513-9547. DOI: 10.1016/S0040-4020(01)00952-8.
195. Finlay, J. C.; Mitra, S.; Patterson, M. S.; Foster, T. H. (2004). Photobleaching kinetics of Photofrin in vivo and in multicell tumour spheroids indicate two simultaneous bleaching mechanisms. *Phys. Med. Biol.*, 49 (21), 4837-4860. DOI: 10.1088/0031-9155/49/21/001.
196. Presley, K. F.; Stang, M. A.; Cheong, S.; Marjo, C. E.; Spiegler, E. N.; Lannutti, J. J. (2019). Photostability of oxygen-sensitive core-shell nanofibers. *Sensors Actuators B: Chem.*, 283, 269-277. DOI: 10.1016/j.snb.2018.12.015.
197. Enko, B.; Borisov, S. M.; Regensburger, J.; Bäumlner, W.; Gescheidt, G.; Klimant, I. (2013). Singlet oxygen-induced photodegradation of the polymers and dyes in optical sensing materials and the effect of stabilizers on these processes. *J. Phys. Chem. A*, 117 (36), 8873-8882. DOI: 10.1021/jp4046462.
198. Jemli, M.; Alouini, Z.; Sabbahi, S.; Gueddari, M. (2002). Destruction of fecal bacteria in wastewater by three photosensitizers. *J. Environ. Monit.*, 4 (4), 511-516. DOI: 10.1039/B204637G.
199. Merchat, M.; Spikes, J. D.; Bertoloni, G.; Jori, G. (1996). Studies on the mechanism of bacteria photosensitization by meso-substituted cationic porphyrins. *J. Photochem. Photobiol. B: Biol.*, 35 (3), 149–157. DOI: 10.1016/S1011-1344(96)07321-6.
200. Nyokong, T. (2007). Effects of substituents on the photochemical and photophysical properties of main group metal phthalocyanines. *Coord. Chem. Rev.*, 251 (13), 1707–1722. DOI: 10.1016/j.ccr.2006.11.011.
201. Demchenko, A. P. (2020). Photobleaching of organic fluorophores: quantitative characterization, mechanisms, protection. *Methods and Applications in Fluorescence*, 8 (2), 022001. DOI: 10.1088/2050-6120/ab7365.
202. Yang, W.; Feng, S.; Zhang, X.; Wang, Y.; Li, C.; Zhang, L.; Zhao, J.; Gurzadyan, G. G.; Tao, S. (2021). Bodipy-Containing Porous Microcapsules for Flow Heterogeneous Photocatalysis. *ACS Applied Materials & Interfaces*, 13 (32), 38722-38731. DOI: 10.1021/acsami.1c10807.
203. Mula, S.; Ray, A. K.; Banerjee, M.; Chaudhuri, T.; Dasgupta, K.; Chattopadhyay, S. (2008). Design and Development of a New Pyrromethene Dye with Improved Photostability and Lasing Efficiency: Theoretical Rationalization of Photophysical and Photochemical Properties. *The Journal of Organic Chemistry*, 73 (6), 2146-2154. DOI: 10.1021/jo702346s.
204. Yang, S. I.; Seth, J.; Strachan, J.-P.; Gentemann, S.; Kim, D.; Holten, D.; Lindsey, J. S.; Bocian, D. F. (1999). Ground and excited state electronic properties of halogenated tetraarylporphyrins.

- Tuning the building blocks for porphyrin-based photonic devices. *J. Porphyrins Phthalocyanines*, 3 (2), 117–147. DOI: 10.1002/(SICI)1099-1409(199902)3:2<117::AID-JPP110>3.0.CO;2-X.
205. Wang, X.-d.; Wolfbeis, O. S. (2014). Optical methods for sensing and imaging oxygen: materials, spectroscopies and applications. *Chem. Soc. Rev.*, 43 (10), 3666-3761. DOI: 10.1039/C4CS00039K.
206. To, W. P.; Liu, Y.; Lau, T. C.; Che, C. M. (2013). A robust palladium(II)-porphyrin complex as catalyst for visible light induced oxidative C–H functionalization. *Chem. - Eur. J.*, 19 (18), 5654–64. DOI: 10.1002/chem.201203774.
207. Goslinski, T.; Piskorz, J. (2011). Fluorinated porphyrinoids and their biomedical applications. *J. Photochem. Photobiol. C*, 12 (4), 304-321. DOI: 10.1016/j.jphotochemrev.2011.09.005.
208. Lee, S.-K.; Okura, I. (1997). Photostable Optical Oxygen Sensing Material: Platinum Tetrakis(pentafluorophenyl)porphyrin Immobilized in Polystyrene. *Anal. Commun.*, 34 (6), 185–188. DOI: 10.1039/a701130j.
209. Wu, M.; Liu, Z.; Zhang, W. (2021). An ultra-stable bio-inspired bacteriochlorin analogue for hypoxia-tolerant photodynamic therapy. *Chemical Science*, 12 (4), 1295–1301. DOI: 10.1039/D0SC05525E.
210. Grabenhorst, L.; Trofymchuk, K.; Steiner, F.; Glembockyte, V.; Tinnefeld, P. (2020). Fluorophore photostability and saturation in the hotspot of DNA origami nanoantennas. *Methods and Applications in Fluorescence*, 8 (2), 024003. DOI: 10.1088/2050-6120/ab6ac8.
211. Zheng, Q.; Juette, M. F.; Jockusch, S.; Wasserman, M. R.; Zhou, Z.; Altman, R. B.; Blanchard, S. C. (2014). Ultra-stable organic fluorophores for single-molecule research. *Chem. Soc. Rev.*, 43 (4), 1044–1056. DOI: 10.1039/c3cs60237k.
212. Ostapko, J.; Gorski, A.; Buczyńska, J.; Golec, B.; Nawara, K.; Kharchenko, A.; Listkowski, A.; Ceborska, M.; Pietrzak, M.; Waluk, J. (2020). Towards more photostable, brighter, and less phototoxic chromophores: Synthesis and properties of porphyrins functionalized with cyclooctatetraene. *Chemistry—A European Journal*, 26 (70), 16666–16675. DOI: 10.1002/chem.202001804.
213. Dubois, A.; Canva, M.; Brun, A.; Chaput, F.; Boilot, J.-P. (1996). Photostability of dye molecules trapped in solid matrices. *Appl. Opt.*, 35 (18), 3193-3199. DOI: 10.1364/AO.35.003193.
214. Swoboda, M.; Henig, J.; Cheng, H.-M.; Brugger, D.; Haltrich, D.; Plumeré, N.; Schlierf, M. (2012). Enzymatic Oxygen Scavenging for Photostability without pH Drop in Single-Molecule Experiments. *ACS Nano*, 6 (7), 6364-6369. DOI: 10.1021/nn301895c.
215. Bhupathiraju, N. D. K.; Rizvi, W.; Batteas, J. D.; Drain, C. M. (2016). Fluorinated porphyrinoids as efficient platforms for new photonic materials, sensors, and therapeutics. *Org. Biomol. Chem.*, 14 (2), 389-408. DOI: 10.1039/C5OB01839K.
216. Song, F.; Peng, X.; Lu, E.; Zhang, R.; Chen, X.; Song, B. (2004). Syntheses, spectral properties and photostabilities of novel water-soluble near-infrared cyanine dyes. *J. Photochem. Photobiol. A*, 168 (1), 53-57. DOI: 10.1016/j.jphotochem.2004.05.012.
217. Visan, A.; van Ommen, J. R.; Kreutzer, M. T.; Lammertink, R. G. H. (2019). Photocatalytic Reactor Design: Guidelines for Kinetic Investigation. *Ind. Eng. Chem. Res.*, 58 (14), 5349-5357. DOI: 10.1021/acs.iecr.9b00381.
218. Ollis, D. (2013). Photocatalytic treatment of water: irradiance influences. In *Photocatalysis and water purification: from fundamentals to recent applications*, (Pichat, P. Ed.) 311-333. Weinheim, Germany: Wiley - VCH Verlag GmbH & Co. KGaA
219. Gaya, U. I. (2014). *Heterogeneous photocatalysis using inorganic semiconductor solids*. 1st ed. Dordrecht, Netherlands: Springer Science.
220. Choi, Y.; Ye, Y.; Mackeyev, Y.; Cho, M.; Lee, S.; Wilson, L. J.; Lee, J.; Alvarez, P. J. J.; Choi, W.; Lee, J. (2014). C60 aminofullerene-magnetite nanocomposite designed for efficient visible

- light photocatalysis and magnetic recovery. *Carbon*, 69, 92–100. DOI: 10.1016/j.carbon.2013.11.065.
221. Fernández, L.; Esteves, V. I.; Cunha, Â.; Schneider, R. J.; Tomé, J. P. C. (2016). Photodegradation of organic pollutants in water by immobilized porphyrins and phthalocyanines. *J. Porphyrins Phthalocyanines*, 20 (01n04), 150–166. DOI: 10.1142/s108842461630007x.
222. Chatterjee, D. K.; Fong, L. S.; Zhang, Y. (2008). Nanoparticles in photodynamic therapy: An emerging paradigm. *Adv. Drug Del. Rev.*, 60 (15), 1627–1637. DOI: 10.1016/j.addr.2008.08.003.
223. Akkerman, I.; Janssen, M.; Rocha, J.; Wijffels, R. H. (2002). Photobiological hydrogen production: photochemical efficiency and bioreactor design. *Int. J. Hydrogen Energy*, 27 (11), 1195–1208. DOI: 10.1016/S0360-3199(02)00071-X.
224. Malato, S.; Fernández-Ibáñez, P.; Maldonado, M. I.; Oller, I.; Polo-López, M. I. (2013). Solar Photocatalytic Pilot Plants: Commercially Available Reactors. In *Photocatalysis and Water Purification: From Fundamentals to Recent Applications*, (Pichat, P. Ed.) 377-397. Wiley - VCH Verlag GmbH & Co. KGaA.
225. Cambié, D.; Bottecchia, C.; Straathof, N. J. W.; Hessel, V.; Noël, T. (2016). Applications of Continuous-Flow Photochemistry in Organic Synthesis, Material Science, and Water Treatment. *Chem. Rev.*, 116 (17), 10276–10341. DOI: 10.1021/acs.chemrev.5b00707.
226. James F. Shackelford, W. A. E. (2000). *CRC Materials Science and Engineering Handbook* (3rd ed.). Boca Raton: CRC Press.
227. Lei, L.; Wang, N.; Zhang, X. M.; Tai, Q.; Tsai, D. P.; Chan, H. L. W. (2010). Optofluidic planar reactors for photocatalytic water treatment using solar energy. *Biomicrofluidics*, 4 (4), 043004. DOI: 10.1063/1.3491471.
228. Schweitzer, C.; Schmidt, R. (2003). Physical Mechanisms of Generation and Deactivation of Singlet Oxygen. *Chem. Rev.*, 103 (5), 1685–1758. DOI: 10.1021/cr010371d.
229. Wang, N.; Zhang, X.; Chen, B.; Song, W.; Chan, N. Y.; Chan, H. L. W. (2012). Microfluidic photoelectrocatalytic reactors for water purification with an integrated visible-light source. *Lab Chip*, 12 (20), 3983-3990. DOI: 10.1039/C2LC40428A.
230. Mozia, S. (2010). Photocatalytic membrane reactors (PMRs) in water and wastewater treatment. A review. *Sep. Purif. Technol.*, 73 (2), 71-91. DOI: 10.1016/j.seppur.2010.03.021.
231. Zheng, X.; Shen, Z.-P.; Shi, L.; Cheng, R.; Yuan, D.-H. (2017). Photocatalytic Membrane Reactors (PMRs) in Water Treatment: Configurations and Influencing Factors. *Catalysts*, 7 (8), 224. DOI: 10.3390/catal7080224.
232. Rani, C. N.; Karthikeyan, S.; Prince Arockia Doss, S. (2021). Photocatalytic ultrafiltration membrane reactors in water and wastewater treatment - A review. *Chemical Engineering and Processing - Process Intensification*, 165, 108445. DOI: 10.1016/j.cep.2021.108445.
233. Kusworo, T. D.; Budiyo; Kumoro, A. C.; Utomo, D. P. (2022). Photocatalytic nanohybrid membranes for highly efficient wastewater treatment: A comprehensive review. *J. Environ. Manage.*, 317, 115357. DOI: 10.1016/j.jenvman.2022.115357.
234. Ochuma, I. J.; Fishwick, R. P.; Wood, J.; Winterbottom, J. M. (2007). Optimisation of degradation conditions of 1,8-diazabicyclo[5.4.0]undec-7-ene in water and reaction kinetics analysis using a cocurrent downflow contactor photocatalytic reactor. *Appl. Catal. B: Environ.*, 73 (3), 259-268. DOI: 10.1016/j.apcatb.2006.12.008.
235. Merabet, S.; Bouzaza, A.; Wolbert, D. (2009). Photocatalytic degradation of indole in a circulating upflow reactor by UV/TiO<sub>2</sub> process—Influence of some operating parameters. *J. Hazard. Mater.*, 166 (2), 1244–1249. DOI: 10.1016/j.jhazmat.2008.12.047.
236. Chen, D.; Ray, A. K. (1998). Photodegradation kinetics of 4-nitrophenol in TiO<sub>2</sub> suspension. *Water Res.*, 32 (11), 3223-3234. DOI: 10.1016/S0043-1354(98)00118-3.

237. Liu, T.; Wang, L.; Liu, X.; Sun, C.; Lv, Y.; Miao, R.; Wang, X. (2020). Dynamic photocatalytic membrane coated with ZnIn<sub>2</sub>S<sub>4</sub> for enhanced photocatalytic performance and antifouling property. *Chem. Eng. J.*, 379, 122379. DOI: 10.1016/j.cej.2019.122379.
238. Zhang, Q.; Chen, S.; Fan, X.; Zhang, H.; Yu, H.; Quan, X. (2018). A multifunctional graphene-based nanofiltration membrane under photo-assistance for enhanced water treatment based on layer-by-layer sieving. *Appl. Catal. B: Environ.*, 224, 204-213. DOI: 10.1016/j.apcatb.2017.10.016.
239. Zhang, X.; Du, A. J.; Lee, P.; Sun, D. D.; Leckie, J. O. (2008). TiO<sub>2</sub> nanowire membrane for concurrent filtration and photocatalytic oxidation of humic acid in water. *J. Membr. Sci.*, 313 (1), 44-51. DOI: 10.1016/j.memsci.2007.12.045.
240. Dittmeyer, R.; Caro, J. (2008). Catalytic membrane reactors. In Handbook of heterogeneous catalysis, (Ertl, G.; Knözinger, H., H, S; Weitkamp, J. Eds.), 2198-2248. Weinheim, Germany: Wiley-VCH Verlag GmbH & Co. KGaA.
241. Horovitz, I.; Avisar, D.; Baker, M. A.; Grilli, R.; Lozzi, L.; Di Camillo, D.; Mamane, H. (2016). Carbamazepine degradation using a N-doped TiO<sub>2</sub> coated photocatalytic membrane reactor: Influence of physical parameters. *J. Hazard. Mater.*, 310, 98–107. DOI: 10.1016/j.jhazmat.2016.02.008.
242. Wang, W.-Y.; Irawan, A.; Ku, Y. (2008). Photocatalytic degradation of Acid Red 4 using a titanium dioxide membrane supported on a porous ceramic tube. *Water Res.*, 42 (19), 4725-4732. DOI: 10.1016/j.watres.2008.08.021.
243. Regmi, C.; Lotfi, S.; Espíndola, J. C.; Fischer, K.; Schulze, A.; Schäfer, A. I. (2020). Comparison of photocatalytic membrane reactor types for the degradation of an organic molecule by TiO<sub>2</sub>-coated PES membrane. *Catalysts*, 10 (7), 725. DOI: 10.3390/catal10070725.
244. Su, C.-Y.; Yang, T.-H.; Gurylev, V.; Huang, S.-H.; Wu, J.-M.; Perng, T.-P. (2015). Extremely high efficient nanoreactor with Au@ZnO catalyst for photocatalysis. *Nanotechnology*, 26 (39), 394001. DOI: 10.1088/0957-4484/26/39/394001.
245. Visan, A.; Rafieian, D.; Ogieglo, W.; Lammertink, R. G. H. (2014). Modeling intrinsic kinetics in immobilized photocatalytic microreactors. *Appl. Catal. B: Environ.*, 150–151, 93–100. DOI: 10.1016/j.apcatb.2013.12.003.
246. Kiwi-Minsker, L.; Renken, A. (2008). Microstructured reactors. In Handbook of Heterogeneous Catalysis, (Ertl, G.; Knözinger, H., H, S; Weitkamp, J. Eds.), 2248-2264. Weinheim, Germany: Wiley-VCH Verlag GmbH & Co. KGaA.
247. Wang, N.; Zhang, X.; Wang, Y.; Yu, W.; Chan, H. L. W. (2014). Microfluidic reactors for photocatalytic water purification. *Lab Chip*, 14 (6), 1074–1082. DOI: 10.1039/C3LC51233A.
248. Zhang, S.; Sun, M.; Hedtke, T.; Deshmukh, A.; Zhou, X.; Weon, S.; Elimelech, M.; Kim, J.-H. (2020). Mechanism of Heterogeneous Fenton Reaction Kinetics Enhancement under Nanoscale Spatial Confinement. *Environ. Sci. Technol.*, 54 (17), 10868–10875. DOI: 10.1021/acs.est.0c02192.
249. Levenspiel, O. (1998). Chemical reaction engineering, 3rd ed. New York: John Wiley & Sons Inc.
250. Hsieh, H. P. (1996). Inorganic membranes for separation and reaction. first ed., Vol. 3 Elsevier.
251. Lyubimenko, R.; Turshatov, A.; Welle, A.; Weidler, P. G.; Richards, B. S.; Schäfer, A. I. (2022). Enhanced photocatalytic efficiency via improved contact in a solar-driven membrane reactor for steroid hormone removal. *Chem. Eng. J.*, 451, 138449. DOI: 10.1016/j.cej.2022.138449
252. Chin, S. S.; Chiang, K.; Fane, A. G. (2006). The stability of polymeric membranes in a TiO<sub>2</sub> photocatalysis process. *J. Membr. Sci.*, 275 (1-2), 202-211. DOI: 10.1016/j.memsci.2005.09.033.
253. Luo, Y.-R. (2007). Comprehensive handbook of chemical bond energies. CRC press.

254. Loginova, N.; Madorskaya, L. Y.; Podlesskaya, N. (1983). Relations between the thermal stability of partially fluorinated polymers and their structure. *Polymer Science USSR*, 25 (12), 2995-3000. DOI: 10.1016/0032-3950(83)90052-7.
255. Giannetti, E. (2005). Thermal stability and bond dissociation energy of fluorinated polymers: a critical evaluation. *J. Fluorine Chem.*, 126 (4), 623-630. DOI: 10.1016/j.jfluchem.2005.01.008.
256. Rabek, J. F. (1995). Polymer Photodegradation. 1st ed. London, UJ: *Springer Science & Business Media*.
257. Amao, Y. (2003). Probes and polymers for optical sensing of oxygen. *Microchimica Acta*, 143 (1), 1–12. DOI: 10.1007/s00604-003-0037-x.
258. Zhao, J.; Liao, C.; Liu, J.; Shen, X.; Tong, H. (2016). Development of mesoporous titanium dioxide hybrid poly(vinylidene fluoride) ultrafiltration membranes with photocatalytic properties. *J. Appl. Polym. Sci.*, 133 (19). DOI: 10.1002/app.43427.
259. Dzinun, H.; Othman, M. H. D.; Ismail, A. F.; Matsuura, T.; Puteh, M. H.; Rahman, M. A.; Jaafar, J. (2018). Stability study of extruded dual layer hollow fibre membranes in a long operation photocatalysis process. *Polym. Test.*, 68, 53-60. DOI: 10.1016/j.polymertesting.2018.03.048.
260. Lee, M. J.; Ong, C. S.; Lau, W. J.; Ng, B. C.; Ismail, A. F.; Lai, S. O. (2016). Degradation of PVDF-based composite membrane and its impacts on membrane intrinsic and separation properties. *J. Polym. Eng.*, 36 (3), 261-268. DOI: 10.1515/polyeng-2015-0064.
261. Rabek, J. F.; Rånby, B. (1978). The Role of Singlet Oxygen in the Photooxidation of Polymers. *Photochem. Photobiol.*, 28 (4-5), 557-569. DOI: 10.1111/j.1751-1097.1978.tb06969.x.
262. Basile, A.; Mozia, S.; Molinari, R. (2018). Current Trends and Future Developments on (Bio-) Membranes: Photocatalytic Membranes and Photocatalytic Membrane Reactors. 1st ed. Amsterdam, Netherlands: *Elsevier*.
263. So, M. C.; Jin, S.; Son, H.-J.; Wiederrecht, G. P.; Farha, O. K.; Hupp, J. T. (2013). Layer-by-Layer Fabrication of Oriented Porous Thin Films Based on Porphyrin-Containing Metal–Organic Frameworks. *J. Am. Chem. Soc.*, 135 (42), 15698–15701. DOI: 10.1021/ja4078705.
264. Xia, Z.; Zhao, Y.; Darling, S. B. (2021). Covalent Organic Frameworks for Water Treatment. *Advanced Materials Interfaces*, 8 (1), 2001507. DOI: 10.1002/admi.202001507.
265. Chakraborty, S.; Loutatidou, S.; Palmisano, G.; Kujawa, J.; Mavukkandy, M. O.; Al-Gharabli, S.; Curcio, E.; Arafat, H. A. (2017). Photocatalytic hollow fiber membranes for the degradation of pharmaceutical compounds in wastewater. *Journal of Environmental Chemical Engineering*, 5 (5), 5014-5024. DOI: 10.1016/j.jece.2017.09.038.
266. Yu, S.; Wang, Y.; Sun, F.; Wang, R.; Zhou, Y. (2018). Novel mpg-C3N4/TiO2 nanocomposite photocatalytic membrane reactor for sulfamethoxazole photodegradation. *Chem. Eng. J.*, 337, 183–192. DOI: 10.1016/j.cej.2017.12.093.
267. Leong, S.; Razmjou, A.; Wang, K.; Hapgood, K.; Zhang, X.; Wang, H. (2014). TiO<sub>2</sub> based photocatalytic membranes: A review. *J. Membr. Sci.*, 472, 167–184. DOI: 10.1016/j.memsci.2014.08.016.
268. Zhang, M.; Yang, Y.; An, X.; Hou, L.-a. (2021). A critical review of g-C3N4-based photocatalytic membrane for water purification. *Chem. Eng. J.*, 412, 128663. DOI: 10.1016/j.cej.2021.128663.
269. Fang, H.; Wang, M.; Yi, H.; Zhang, Y.; Li, X.; Yan, F.; Zhang, L. (2020). Electrostatic Assembly of Porphyrin-Functionalized Porous Membrane toward Biomimetic Photocatalytic Degradation Dyes. *ACS Omega*, 5 (15), 8707-8720. DOI: 10.1021/acsomega.0c00135.
270. Wang, M.; Zhang, Y.; Yu, G.; Zhao, J.; Chen, X.; Yan, F.; Li, J.; Yin, Z.; He, B. (2020). Monolayer porphyrin assembled SPSf/PES membrane reactor for degradation of dyes under visible light irradiation coupling with continuous filtration. *Journal of the Taiwan Institute of Chemical Engineers*, 109, 62-70. DOI: 10.1016/j.jtice.2020.02.013.

271. Becker-Jahn, J.; Griebel, J.; Glaß, S.; Langowski, P.; Nieß, S.; Schulze, A. (2021). Photoactive polymer membranes for degradation of pharmaceuticals from water. *Catal. Today*, 364, 256-262. DOI: 10.1016/j.cattod.2020.05.017.
272. Zhang, L.; Zhao, Y.-H.; Bai, R. (2011). Development of a multifunctional membrane for chromatic warning and enhanced adsorptive removal of heavy metal ions: Application to cadmium. *J. Membr. Sci.*, 379 (1-2), 69-79. DOI: 10.1016/j.memsci.2011.05.044.
273. Bonnett, R.; Krysteva, M. A.; Lalov, I. G.; Artarsky, S. V. (2006). Water disinfection using photosensitizers immobilized on chitosan. *Water Res.*, 40 (6), 1269-75. DOI: 10.1016/j.watres.2006.01.014.
274. Li, J.; Yin, L.; Qiu, G.; Li, X.; Liu, Q.; Xie, J. (2015). A photo-bactericidal thin film composite membrane for forward osmosis. *Journal of Materials Chemistry A*, 3 (13), 6781-6786. DOI: 10.1039/c5ta00430f.
275. Zhu, J.; Sun, G. (2012). Preparation and photo-oxidative functions of poly(ethylene-co-methacrylic acid) (PE-co-MAA) nanofibrous membrane supported porphyrins. *J. Mater. Chem.*, 22 (21), 10581. DOI: 10.1039/c2jm16703d.
276. Lyubimenko, R.; Busko, D.; Schäfer, A. I.; Richards, B. S.; Turshatov, A. (2019). Efficient photocatalytic removal of methylene blue using a metalloporphyrin-poly(vinylidene fluoride) hybrid membrane in a flow-through reactor. *ACS Appl. Mater. Interfaces*, 11 (35), 31763-31776. DOI: 10.1021/acsami.9b04601.
277. Bolton, J. R.; Bircher, K. G.; Tumas, W.; Tolman, C. A. (2001). Figures-of-merit for the technical development and application of advanced oxidation technologies for both electric- and solar-driven systems (IUPAC Technical Report). *Pure Appl. Chem.*, 73 (4), 627-637. DOI: 10.1351/pac200173040627.
278. Abegglen, C. S., H. (2012). Micropollutants dans les eaux usées urbaines. Etapes de traitement supplémentaire dans les stations d'épuration; *Swiss Federal Office for the Environment: Connaissance de l'environnement 1214*. p 87. Available online: [https://www.bafu.admin.ch/dam/bafu/fr/dokumente/wasser/uw-umwelt-wissen/mikroverunreinigungenauskommunalemabwasser.pdf.download.pdf/micropolluants\\_dansleseauxuseesurbaines.pdf](https://www.bafu.admin.ch/dam/bafu/fr/dokumente/wasser/uw-umwelt-wissen/mikroverunreinigungenauskommunalemabwasser.pdf.download.pdf/micropolluants_dansleseauxuseesurbaines.pdf). (accessed 17 June 2022).
279. Miklos, D. B.; Remy, C.; Jekel, M.; Linden, K. G.; Drewes, J. E.; Hübner, U. (2018). Evaluation of advanced oxidation processes for water and wastewater treatment – A critical review. *Water Res.*, 139, 118–131. DOI: 10.1016/j.watres.2018.03.042.
280. Spasiano, D.; Marotta, R.; Malato, S.; Fernandez-Ibañez, P.; Di Somma, I. (2015). Solar photocatalysis: Materials, reactors, some commercial, and pre-industrialized applications. A comprehensive approach. *Appl. Catal. B: Environ.*, 170–171, 90–123. DOI: 10.1016/j.apcatb.2014.12.050.
281. Eurostat Energy (EU). 2021. Electricity prices for non-household consumers - bi-annual data (from 2007 onwards). Available online: [https://ec.europa.eu/eurostat/databrowser/view/nrg\\_pc\\_205/default/table?lang=en](https://ec.europa.eu/eurostat/databrowser/view/nrg_pc_205/default/table?lang=en). (accessed 17 June 2022).
282. Büeler, A.; Wunderlin, P. M., Ernst, A. (2018). Energieeffizienz in Anlagen zur MV-Elimination. 42-48. Available online: [https://www.aquaetgas.ch/de/energie/effizienz/20181112\\_ag11\\_energieeffizienz-in-anlagen-zur-mv-elimination/](https://www.aquaetgas.ch/de/energie/effizienz/20181112_ag11_energieeffizienz-in-anlagen-zur-mv-elimination/) (accessed 17 June 2022).
283. Fachhochschule Nordwestschweiz (FHNW). (2020). Innovative Solutions in the Process Industry for next generation Resource Efficient Water management. Report on evaluation of technologies at the CLARIANT site. Available online: <https://cordis.europa.eu/project/id/723702/results/de>. (accessed 17 June 2022).
284. Pérez, G.; Gómez, P.; Ortiz, I.; Urriaga, A. (2022). Techno-economic assessment of a membrane-based wastewater reclamation process. *Desalination*, 522, 115409. DOI: 10.1016/j.desal.2021.115409.

285. Meda, A. (2010). Untersuchung der Randbedingungen für die Wasserwiederverwendung und Kernprojektkoordinierung Verbundprojekt: Exportorientierte Forschung und Entwicklung auf dem Gebiet der Wasserver- und -entsorgung, Kernprojekt B Hygienisierung und Wasserwiederverwendung, Teilprojekt B0 ; Abschlussbericht. (Müller, K.; Cornel, P. Eds.). *TU, Inst. IWAR, FG Abwassertechnik*.
286. Bellona, C.; Heil, D.; Yu, C.; Fu, P.; Drewes, J. E. (2012). The pros and cons of using nanofiltration in lieu of reverse osmosis for indirect potable reuse applications. *Sep. Purif. Technol.*, 85, 69-76. DOI: 10.1016/j.seppur.2011.09.046.
287. Waqas, S.; Bilal, M. R.; Aqsha, A.; Yub Harun, N.; Ayoub, M.; Wirzal, M. D. H.; Jaafar, J.; Mulyati, S.; Elma, M. (2021). Effect of membrane properties in a membrane rotating biological contactor for wastewater treatment. *Journal of Environmental Chemical Engineering*, 9 (1), 104869. DOI: 10.1016/j.jece.2020.104869.
288. Böhler, M.; Hernandez, A.; McArdeall, C. S.; Siegrist, H., Joss, A., & Baggenstos, M. (2020). Elimination von Spurenstoffen durch granuliert Aktivkohle-Filtration (GAK). Grosstechnische Untersuchungen auf der ARA Furt, Bülach. Schlussbericht. ; EAWAG. Available online: <https://www.dora.lib4ri.ch/eawag/islandora/object/eawag:21845>. (accessed 17 June 2022).
289. Schäfer, A. I.; Akanyeti, I.; Semião, A. J. C. (2011). Micropollutant sorption to membrane polymers: A review of mechanisms for estrogens. *Adv. Colloid Interface Sci.*, 164 (1), 100–117. DOI: 10.1016/j.cis.2010.09.006.
290. Dharupaneedi, S. P.; Nataraj, S. K.; Nadagouda, M.; Reddy, K. R.; Shukla, S. S.; Aminabhavi, T. M. (2019). Membrane-based separation of potential emerging pollutants. *Sep. Purif. Technol.*, 210, 850-866. DOI: 10.1016/j.seppur.2018.09.003.
291. van Rijn, C. J. (2004). Nano and micro engineered membrane technology. *Elsevier*.
292. Chang, S.; Waite, T. D.; Schäfer, A. I.; Fane, A. G. (2003). Adsorption of the Endocrine-Active Compound Estrone on Microfiltration Hollow Fiber Membranes. *Environ. Sci. Technol.*, 37 (14), 3158-3163. DOI: 10.1021/es0261574.
293. Yoon, Y.; Westerhoff, P.; Snyder, S. A.; Wert, E. C. (2006). Nanofiltration and ultrafiltration of endocrine disrupting compounds, pharmaceuticals and personal care products. *J. Membr. Sci.*, 270 (1), 88–100. DOI: 10.1016/j.memsci.2005.06.045.
294. Heredia Deba, S. A.; Wols, B. A.; Yntema, D. R.; Lammertink, R. G. H. (2022). Transport and surface reaction model of a photocatalytic membrane during the radical filtration of methylene blue. *Chem. Eng. Sci.*, 254, 117617. DOI: 10.1016/j.ces.2022.117617.
295. Gu, Y.; Bacchin, P.; Lahitte, J.-F.; Remigy, J.-C.; Favier, I.; Gómez, M.; Gin, D. L.; Noble, R. D. (2017). Catalytic membrane reactor for Suzuki-Miyaura C–C cross-coupling: Explanation for its high efficiency via modeling. *AIChE J.*, 63 (2), 698-704. DOI: 10.1002/aic.15379.
296. Berberidou, C.; Poullos, I.; Xekoukoulotakis, N. P.; Mantzavinos, D. (2007). Sonolytic, photocatalytic and sonophotocatalytic degradation of malachite green in aqueous solutions. *Appl. Catal. B: Environ.*, 74 (1), 63-72. DOI: 10.1016/j.apcatb.2007.01.013.
297. Mboula, V. M.; Héquet, V.; Andrès, Y.; Gru, Y.; Colin, R.; Doña-Rodríguez, J. M.; Pastrana-Martínez, L. M.; Silva, A. M. T.; Leleu, M.; Tindall, A. J.; Mateos, S.; Falaras, P. (2015). Photocatalytic degradation of estradiol under simulated solar light and assessment of estrogenic activity. *Appl. Catal. B: Environ.*, 162, 437-444. DOI: 10.1016/j.apcatb.2014.05.026.
298. Friedmann, D.; Mendive, C.; Bahnemann, D. (2010). TiO<sub>2</sub> for water treatment: Parameters affecting the kinetics and mechanisms of photocatalysis. *Appl. Catal. B: Environ.*, 99 (3), 398-406. DOI: 10.1016/j.apcatb.2010.05.014.
299. Herrmann, J.-M. (2010). Photocatalysis fundamentals revisited to avoid several misconceptions. *Appl. Catal. B: Environ.*, 99 (3-4), 461-468. DOI: 10.1016/j.apcatb.2010.05.012.
300. Amat, A. M.; Arques, A.; Bossmann, S. H.; Braun, A. M.; Göb, S.; Miranda, M. A.; Oliveros, E. (2004). Oxidative degradation of 2,4-xylydine by photosensitization with 2,4,6-triphenylpyrylium:



- homogeneous and heterogeneous catalysis. *Chemosphere*, 57 (9), 1123–1130. DOI: 10.1016/j.chemosphere.2004.08.029.
301. Li Puma, G.; Puddu, V.; Tsang, H. K.; Gora, A.; Toepfer, B. (2010). Photocatalytic oxidation of multicomponent mixtures of estrogens (estrone (E1), 17 $\beta$ -estradiol (E2), 17 $\alpha$ -ethynylestradiol (EE2) and estriol (E3)) under UVA and UVC radiation: Photon absorption, quantum yields and rate constants independent of photon absorption. *Appl. Catal. B: Environ.*, 99 (3), 388-397. DOI: 10.1016/j.apcatb.2010.05.015.
302. Fogler, H. S. (2016). Elements of chemical reaction engineering. Fifth ed. Boston, United States of America: *Prentice Hall*.
303. Bloh, J. Z. (2019). A Holistic Approach to Model the Kinetics of Photocatalytic Reactions. *Frontiers in Chemistry*, 7 (128). DOI: 10.3389/fchem.2019.00128.
304. Vezzoli, M.; Martens, W. N.; Bell, J. M. (2011). Investigation of phenol degradation: True reaction kinetics on fixed film titanium dioxide photocatalyst. *Appl. Catal., A*, 404 (1), 155–163. DOI: 10.1016/j.apcata.2011.07.025.
305. Yu, H.; Zhang, K.; Rossi, C. (2007). Theoretical study on photocatalytic oxidation of VOCs using nano-TiO<sub>2</sub> photocatalyst. *J. Photochem. Photobiol. A*, 188 (1), 65-73. DOI: 10.1016/j.jphotochem.2006.11.021.
306. Fernández, L.; Borzecka, W.; Lin, Z.; Schneider, R.; Huvaere, K.; Esteves, V.; Cunha, Â.; Tomé, J. (2017). Nanomagnet-photosensitizer hybrid materials for the degradation of 17 $\beta$ -estradiol in batch and flow modes. *Dyes Pigm.*, 142, 535-543. DOI: 10.1016/j.dyepig.2017.04.010.
307. Berger, T. E.; Regmi, C.; Schäfer, A. I.; Richards, B. S. (2020). Photocatalytic degradation of organic dye via atomic layer deposited TiO<sub>2</sub> on ceramic membranes in single-pass flow-through operation. *J. Membr. Sci.*, 604, 118015. DOI: 10.1016/j.memsci.2020.118015.
308. Su, Y.; Straathof, N. J.; Hessel, V.; Noel, T. (2014). Photochemical transformations accelerated in continuous-flow reactors: basic concepts and applications. *Chem. - Eur. J.*, 20 (34), 10562-89. DOI: 10.1002/chem.201400283.
309. Wilkinson, F.; Helman, W. P.; Ross, A. B. (1995). Rate constants for the decay and reactions of the lowest electronically excited singlet state of molecular oxygen in solution. An expanded and revised compilation. *J. Phys. Chem. Ref. Data*, 24 (2), 663–1021. DOI: 10.1063/1.555965.
310. Malato, S.; Fernández-Ibáñez, P.; Maldonado, M. I.; Blanco, J.; Gernjak, W. (2009). Decontamination and disinfection of water by solar photocatalysis: Recent overview and trends. *Catal. Today*, 147 (1), 1-59. DOI: 10.1016/j.cattod.2009.06.018.
311. Ravelli, D.; Dondi, D.; Fagnoni, M.; Albini, A. (2009). Photocatalysis. A multi-faceted concept for green chemistry. *Chem. Soc. Rev.*, 38 (7), 1999-2011. DOI: 10.1039/B714786B.
312. Ollis, D. F. (2018). Kinetics of Photocatalyzed Reactions: Five Lessons Learned. *Frontiers in Chemistry*, 6 (378). DOI: 10.3389/fchem.2018.00378.
313. Choo, K.-H. (2018). Modeling Photocatalytic Membrane Reactors. In Current Trends and Future Developments on (Bio-) Membranes, (Basile, A.; Spazzafumo, G. Eds.), 297-316. *Elsevier*.
314. Saquib, M.; Muneer, M. (2003). TiO<sub>2</sub>-mediated photocatalytic degradation of a triphenylmethane dye (gentian violet), in aqueous suspensions. *Dyes Pigm.*, 56 (1), 37-49. DOI: 10.1016/S0143-7208(02)00101-8.
315. Adeel, M.; Saeed, M.; Khan, I.; Muneer, M.; Akram, N. (2021). Synthesis and Characterization of Co-ZnO and Evaluation of Its Photocatalytic Activity for Photodegradation of Methyl Orange. *ACS Omega*, 6 (2), 1426–1435. DOI: 10.1021/acsomega.0c05092.
316. Scully, F. E.; Hoigné, J. (1987). Rate constants for reactions of singlet oxygen with phenols and other compounds in water. *Chemosphere*, 16 (4), 681-694. DOI: 10.1016/0045-6535(87)90004-X.
317. Martinez-Haya, R.; Gomis, J.; Arques, A.; Marin, M. L.; Amat, A. M.; Miranda, M. A. (2017). Time-resolved kinetic assessment of the role of singlet and triplet excited states in the

- photocatalytic treatment of pollutants at different concentrations. *Appl. Catal. B: Environ.*, 203, 381-388. DOI: 10.1016/j.apcatb.2016.10.042.
318. Díaz, M.; Luiz, M.; Alegretti, P.; Furlong, J.; Amat-Guerri, F.; Massad, W.; Criado, S.; García, N. A. (2009). Visible-light-mediated photodegradation of 17 $\beta$ -estradiol: Kinetics, mechanism and photoproducts. *J. Photochem. Photobiol. A*, 202 (2), 221-227. DOI: 10.1016/j.jphotochem.2008.12.008.
319. Miller, J. S. (2005). Rose bengal-sensitized photooxidation of 2-chlorophenol in water using solar simulated light. *Water Res.*, 39 (2), 412-422. DOI: 10.1016/j.watres.2004.09.019.
320. García, N. A. (1994). New trends in photobiology: Singlet-molecular-oxygen-mediated photodegradation of aquatic phenolic pollutants. A kinetic and mechanistic overview. *J. Photochem. Photobiol. B: Biol.*, 22 (3), 185-196. DOI: 10.1016/1011-1344(93)06932-S.
321. Gmurek, M.; Miller, J. S.; Ledakowicz, S. (2012). Kinetics of the photosensitized degradation of benzyl 4-hydroxybenzoate in homogeneous aqueous solution under visible-light irradiation. *Chem. Eng. J.*, 210, 417-424. DOI: 10.1016/j.cej.2012.08.097.
322. Błędzka, D.; Gmurek, M.; Gryglik, M.; Olak, M.; Miller, J.; Ledakowicz, S. (2010). Photodegradation and advanced oxidation of endocrine disruptors in aqueous solutions. *Catal. Today*, 151 (1-2), 125-130. DOI: 10.1016/j.cattod.2010.03.040.
323. Mota, H. P.; Quadrado, R. F.; Iglesias, B. A.; Fajardo, A. R. (2020). Enhanced photocatalytic degradation of organic pollutants mediated by Zn(II)-porphyrin/poly(acrylic acid) hybrid microparticles. *Appl. Catal. B: Environ.*, 119208. DOI: 10.1016/j.apcatb.2020.119208.
324. Gmurek, M.; Bizukojć, M.; Mosinger, J.; Ledakowicz, S. (2015). Application of photoactive electrospun nanofiber materials with immobilized meso-tetraphenylporphyrin for parabens photodegradation. *Catal. Today*, 240, 160-167. DOI: 10.1016/j.cattod.2014.06.015.
325. Lado Ribeiro, A. R.; Moreira, N. F. F.; Li Puma, G.; Silva, A. M. T. (2019). Impact of water matrix on the removal of micropollutants by advanced oxidation technologies. *Chem. Eng. J.*, 363, 155-173. DOI: 10.1016/j.cej.2019.01.080.
326. Lee, Y.; von Gunten, U. (2010). Oxidative transformation of micropollutants during municipal wastewater treatment: Comparison of kinetic aspects of selective (chlorine, chlorine dioxide, ferrate<sup>VI</sup>, and ozone) and non-selective oxidants (hydroxyl radical). *Water Res.*, 44 (2), 555-566. DOI: 10.1016/j.watres.2009.11.045.
327. Brame, J.; Long, M.; Li, Q.; Alvarez, P. (2015). Inhibitory effect of natural organic matter or other background constituents on photocatalytic advanced oxidation processes: Mechanistic model development and validation. *Water Res.*, 84, 362-371. DOI: 10.1016/j.watres.2015.07.044.
328. Uyguner-Demirel, C. S.; Birben, N. C.; Bekbolet, M. (2017). Elucidation of background organic matter matrix effect on photocatalytic treatment of contaminants using TiO<sub>2</sub>: A review. *Catal. Today*, 284, 202-214. DOI: 10.1016/j.cattod.2016.12.030.
329. Mopper, K.; Zhou, X. (1990). Hydroxyl Radical Photoproduction in the Sea and Its Potential Impact on Marine Processes. *Science*, 250 (4981), 661-664. DOI: 10.1126/science.250.4981.661.
330. Cory, R. M.; Cotner, J. B.; McNeill, K. (2009). Quantifying Interactions between Singlet Oxygen and Aquatic Fulvic Acids. *Environ. Sci. Technol.*, 43 (3), 718-723. DOI: 10.1021/es801847g.
331. Liu, Q.-T.; Cumming, R. I.; Sharpe, A. D. (2009). Photo-induced environmental depletion processes of  $\beta$ -blockers in river waters. *Photochemical & Photobiological Sciences*, 8 (6), 768-777. DOI: 10.1039/B817890A.
332. Keane, P. M.; Kelly, J. M. (2011). Triplet-state dynamics of a metalloporphyrin photosensitiser (PtTMPyP4) in the presence of halides and purine mononucleotides. *Photochemical & Photobiological Sciences*, 10 (10), 1578-1586. DOI: 10.1039/C1PP05125C.

333. Valeur, B.; Berberan-Santos, M. N. (2012). Effects of Intermolecular Photophysical Processes on Fluorescence Emission. In *Molecular Fluorescence: Principles and Applications*, 2nd ed.; (Valeur, B. B.-S., M.N. Ed.) 141–179. Weinheim, Germany: Wiley - VCH Verlag
334. Neves, C. M. B.; Filipe, O. M. S.; Mota, N.; Santos, S. A. O.; Silvestre, A. J. D.; Santos, E. B. H.; Neves, M. G. P. M. S.; Simões, M. M. Q. (2019). Photodegradation of metoprolol using a porphyrin as photosensitizer under homogeneous and heterogeneous conditions. *J. Hazard. Mater.*, 370, 13-23. DOI: 10.1016/j.jhazmat.2018.11.055.
335. Merck Millipore. 2022. Durapore® Membrane Filter, 0.22 µm. Overview, Physicochemical Information. Available online: [https://www.merckmillipore.com/DE/en/product/Durapore-Membrane-Filter-0.22m,MM\\_NF-GVWP00010](https://www.merckmillipore.com/DE/en/product/Durapore-Membrane-Filter-0.22m,MM_NF-GVWP00010). (accessed 18 June 2022).
336. Personal communication. (2021). Theoretical porosity of PVDF20, PVDF100 membranes. K. Zeiter, Ed. Novamem AG, <https://novamem.com/>: Switzerland.
337. Merck Millipore. 2022. Durapore® Membrane Filter, 0.1 µm. Overview, Physicochemical Information. Available online: [https://www.merckmillipore.com/DE/en/product/Durapore-Membrane-Filter-0.1m,MM\\_NF-VVHP04700](https://www.merckmillipore.com/DE/en/product/Durapore-Membrane-Filter-0.1m,MM_NF-VVHP04700). (accessed 18 June 2022).
338. Merck Millipore. 2022. Durapore® Membrane Filter, 0.45 µm. Overview, Physicochemical Information. Available online: [https://www.merckmillipore.com/DE/en/product/Durapore-Membrane-Filter-0.45m,MM\\_NF-HVHP02500](https://www.merckmillipore.com/DE/en/product/Durapore-Membrane-Filter-0.45m,MM_NF-HVHP02500). (accessed 18 June 2022).
339. Imbrogno, A.; Schäfer, A. I. (2019). Comparative study of nanofiltration membrane characterization devices of different dimension and configuration (cross flow and dead end). *J. Membr. Sci.*, 585, 67-80. DOI: 10.1016/j.memsci.2019.04.035.
340. Lotfi, S.; Fischer, K.; Schulze, A.; Schäfer, A. I. (2022). Photocatalytic degradation of steroid hormone micropollutants by TiO<sub>2</sub>-coated polyethersulfone membranes in a continuous flow-through process. *Nat. Nanotechnol.*, 17 (4), 417-423. DOI: 10.1038/s41565-022-01074-8.
341. Lyubimenko, R.; Gutierrez Cardenas, O. I.; Richards, B. S.; Turshatov, A.; Schäfer, A. I. (2021). Photodegradation of steroid-hormone micropollutants in a flow-through membrane reactor coated with Pd(II)-porphyrin. *Appl. Catal. B: Environ.*, 291, 120097. DOI: 10.1016/j.apcatb.2021.120097.
342. ASTM G173-03(2012). Standard tables for reference solar spectral Irradiances: direct normal and hemispherical on 37° tilted surface. *ASTM International*: West Conshohocken, PA, 2012
343. Bregnhøj, M.; Dichmann, L.; McLoughlin, C. K.; Westberg, M.; Ogilby, P. R. (2018). Uric Acid: A Less-than-Perfect Probe for Singlet Oxygen. *Photochem. Photobiol.* DOI: 10.1111/php.12971.
344. (USP), U. S. P. (2007). Chapter <621> Chromatography/system suitability. In *United States Pharmacopeia 31 National Formulary 26 (USP 31–NF 26)*, (Pharmacopeia, U. S. Ed.) 508–520. Rockville, Maryland:
345. Validation of Chromatographic Methods. *Reviewer Guidance. Center for Drug Evaluation and Research (CDER)*: FDA, Rockville, MD, 1994
346. Hasebe, N.; Suzuki, K.; Horiuchi, H.; Suzuki, H.; Yoshihara, T.; Okutsu, T.; Tobita, S. (2015). Absolute phosphorescence quantum yields of singlet molecular oxygen in solution determined using an integrating sphere instrument. *Anal. Chem.*, 87 (4), 2360-2366. DOI: 10.1021/ac5042268.
347. Sreedhara, S. S.; Tata, N. R. (2013). A novel method for measurement of porosity in nanofiber mat using pycnometer in filtration. *Journal of Engineered Fibers and Fabrics*, 8 (4), 155892501300800408. DOI:
348. Smolders, K.; Franken, A. C. M. (1989). Terminology for Membrane Distillation. *Desalination*, 72 (3), 249-262. DOI: 10.1016/0011-9164(89)80010-4.
349. Eykens, L.; De Sitter, K.; Dotremont, C.; Pinoy, L.; Van der Bruggen, B. (2016). Characterization and performance evaluation of commercially available hydrophobic membranes for direct contact membrane distillation. *Desalination*, 392, 63-73. DOI: 10.1016/j.desal.2016.04.006.

350. Plötze, M.; Niemz, P. (2011). Porosity and pore size distribution of different wood types as determined by mercury intrusion porosimetry. *European journal of wood and wood products*, 69 (4), 649-657. DOI: 10.1007/s00107-010-0504-0.
351. Ellison, A. H.; Klemm, R. B.; Schwartz, A. M.; Grubb, L. S.; Petrash, D. A. (1967). Contact angles of mercury on various surfaces and the effect of temperature. *J. Chem. Eng. Data*, 12 (4), 607-609. DOI: 10.1021/je60035a037.
352. Shimizu, R. N.; Demarquette, N. R. (2000). Evaluation of surface energy of solid polymers using different models. *J. Appl. Polym. Sci.*, 76 (12), 1831-1845. DOI: 10.1002/(SICI)1097-4628(20000620)76:12<1831::AID-APP14>3.0.CO;2-Q.
353. Huisman, I. H.; Dutré, B.; Persson, K. M.; Trägårdh, G. (1997). Water permeability in ultrafiltration and microfiltration: Viscous and electroviscous effects. *Desalination*, 113 (1), 95-103. DOI: 10.1016/S0011-9164(97)00118-5.
354. L'Annunziata, M. F. (2012). Flow-Cell Analysis In Handbook of radioactivity analysis, 3rd ed.; (L'Annunziata, M. F. Ed.) 1117-1178. Amsterdam: *Academic Press*.
355. Malonda, A. G.; Carles, A. G. (2012). Radioactivity Counting Statistics. In Handbook of Radioactivity Analysis, (L'Annunziata, M. F. Ed.) 163-189. Amsterdam: *Academic Press*.
356. Shahmansouri, A.; Bellona, C. (2015). Nanofiltration technology in water treatment and reuse: applications and costs. *Water Sci. Technol.*, 71 (3), 309-319. DOI: 10.2166/wst.2015.015.
357. The European Commission's science and knowledge service. 2019. Photovoltaic geographical information system: monthly irradiation data. Available online: [https://re.jrc.ec.europa.eu/pvg\\_tools/en/#MR](https://re.jrc.ec.europa.eu/pvg_tools/en/#MR). (accessed 18 June 2022).
358. Verma, S.; Ghosh, H. N. (2012). Exciton Energy and Charge Transfer in Porphyrin Aggregate/Semiconductor (TiO<sub>2</sub>) Composites. *The Journal of Physical Chemistry Letters*, 3 (14), 1877-1884. DOI: 10.1021/jz300639q.
359. ISO 10678:2010 Fine ceramics (advanced ceramics, advanced technical ceramics) — Determination of photocatalytic activity of surfaces in an aqueous medium by degradation of methylene blue. *International Organization for Standardization (ISO)*: Geneva, 2010
360. Ruiz-Gonzalez, R.; Cortajarena, A. L.; Mejias, S. H.; Agut, M.; Nonell, S.; Flors, C. (2013). Singlet oxygen generation by the genetically encoded tag miniSOG. *J. Am. Chem. Soc.*, 135 (26), 9564-7. DOI: 10.1021/ja4020524.
361. Skovsen, E.; Snyder, J. W.; Lambert, J. D.; Ogilby, P. R. (2005). Lifetime and diffusion of singlet oxygen in a cell. *J. Phys. Chem. B*, 109 (18), 8570-3. DOI: 10.1021/jp051163i.
362. Yoneyama, H.; Toyoguchi, Y.; Tamura, H. (1972). Reduction of methylene blue on illuminated titanium dioxide in methanolic and aqueous solutions. *The Journal of Physical Chemistry*, 76 (23), 3460-3464. DOI: 10.1021/j100667a027.
363. Wang, W.; Ye, M.; He, L.; Yin, Y. (2014). Nanocrystalline TiO<sub>2</sub>-catalyzed photoreversible color switching. *Nano Lett.*, 14 (3), 1681-1686. DOI: 10.1021/nl500378k.
364. Hiroshi, O. (1961). Photoreduction of Methylene Blue by Visible Light in the Aqueous Solution Containing Certain Kinds of Inorganic Salts. II. Photobleached Product. *Bull. Chem. Soc. Jpn.*, 34 (8), 1057-1063. DOI: 10.1246/bcsj.34.1057.
365. Purchas, D.; Sutherland, K. (2002). Handbook of filter media. Oxford, UK: *Elsevier Science*.
366. Tsushima, M.; Tokuda, K.; Ohsaka, T. (1994). Use of Hydrodynamic Chronocoulometry for Simultaneous Determination of Diffusion Coefficients and Concentrations of Dioxygen in Various Media. *Anal. Chem.*, 66 (24), 4551-4556. DOI: 10.1021/ac00096a024.
367. Hori, T.; Kamon, N.; Kojima, H.; Rohner, R. M.; Zollinger, H. (1987). Structure correlation between diffusion coefficients of simple organic compounds and of anionic and cationic dyes in water. *J. Soc. Dyers Colour.*, 103 (7 - 8), 265-270. DOI: 10.1111/j.1478-4408.1987.tb01119.x.

368. Yu, Y.; Furuyama, T.; Tang, J.; Wu, Z.-Y.; Chen, J.-Z.; Kobayashi, N.; Zhang, J.-L. (2015). Stable iso-bacteriochlorin mimics from porpholactone: effect of a  $\beta$ -oxazolone moiety on the frontier  $\pi$ -molecular orbitals. *Inorg. Chem. Front.*, 2 (7), 671-677. DOI: 10.1039/c5qi00054h.
369. Ramasundaram, S.; Yoo, H. N.; Song, K. G.; Lee, J.; Choi, K. J.; Hong, S. W. (2013). Titanium dioxide nanofibers integrated stainless steel filter for photocatalytic degradation of pharmaceutical compounds. *J. Hazard. Mater.*, 258-259, 124-132. DOI: 10.1016/j.jhazmat.2013.04.047.
370. Aran, H. C.; Salamon, D.; Rijnaarts, T.; Mul, G.; Wessling, M.; Lammertink, R. G. H. (2011). Porous photocatalytic membrane microreactor (P2M2): a new reactor concept for photochemistry. *J. Photochem. Photobiol. A*, 225 (1), 36-41. DOI: 10.1016/j.jphotochem.2011.09.022.
371. Nghiem, L. D.; Schäfer, A. I.; Elimelech, M. (2004). Removal of natural hormones by nanofiltration membranes: measurement, modeling, and mechanisms. *Environ. Sci. Technol.*, 38 (6), 1888-1896. DOI: 10.1021/es034952r.
372. Wang, M.; Qu, F.; Jia, R.; Sun, S.; Li, G.; Liang, H. (2016). Preliminary study on the removal of steroidal estrogens using TiO<sub>2</sub>-doped PVDF ultrafiltration membranes. *Water*, 8 (4), 134. DOI: 10.3390/w8040134.
373. Planas, A.; Lupon, P.; Cascallo, M.; Bonet, J. J. (1989). Photo-oxygenation of styrenic estrogens: product characterization and kinetics of the dye-sensitized photo - oxygenation of 9,11-didehydroestrone derivatives. *Helv. Chim. Acta*, 72 (4), 715-724. DOI: 10.1002/hlca.19890720411.
374. Nguyen, M. N.; Weidler, P. G.; Schwaiger, R.; Schäfer, A. I. (2021). Interactions between carbon-based nanoparticles and steroid hormone micropollutants in water. *J. Hazard. Mater.*, 402, 122929. DOI: 10.1016/j.jhazmat.2020.122929.
375. Ogilby, P. R. (2010). Singlet oxygen: there is indeed something new under the sun. *Chem. Soc. Rev.*, 39 (8), 3181-209. DOI: 10.1039/b926014p.
376. Lin, A. Y.-C.; Reinhard, M. (2005). Photodegradation of common environmental pharmaceuticals and estrogens in river water. *Environ. Toxicol. Chem.*, 24 (6), 1303-1309. DOI: 10.1897/04-236r.1.
377. Irmak, S.; Erbatır, O.; Akgerman, A. (2005). Degradation of 17 $\beta$ -estradiol and bisphenol A in aqueous medium by using ozone and ozone/UV techniques. *J. Hazard. Mater.*, 126 (1), 54-62. DOI: 10.1016/j.jhazmat.2005.05.045.
378. Ohko, Y.; Iuchi, K.-i.; Niwa, C.; Tatsuma, T.; Nakashima, T.; Iguchi, T.; Kubota, Y.; Fujishima, A. (2002). 17 $\beta$ -Estradiol Degradation by TiO<sub>2</sub> Photocatalysis as a Means of Reducing Estrogenic Activity. *Environ. Sci. Technol.*, 36 (19), 4175-4181. DOI: 10.1021/es011500a.
379. Gómez, L.; Niegowska, M.; Navarro, A.; Amendola, L.; Arukwe, A.; Ait-Aissa, S.; Balzamo, S.; Barreca, S.; Belkin, S.; Bittner, M.; Blaha, L.; Buchinger, S.; Busetto, M.; Carere, M.; Colzani, L.; Dellavedova, P.; Denslow, N.; Escher, B. I.; Hogstrand, C.; Khan, E. A.; König, M.; Kroll, K. J.; Lacchetti, I.; Maillot-Marechal, E.; Moscovici, L.; Potalivo, M.; Sanseverino, I.; Santos, R.; Schifferli, A.; Schlichting, R.; Sforzini, S.; Simon, E.; Shpigel, E.; Sturzenbaum, S.; Vermeirssen, E.; Viarengo, A.; Werner, I.; Lettieri, T. (2021). Estrogenicity of chemical mixtures revealed by a panel of bioassays. *Sci. Total Environ.*, 785, 147284. DOI: 10.1016/j.scitotenv.2021.147284.
380. Schaberle, F. A.; Abreu, A. R.; Gonçalves, N. P. F.; Sá, G. F. F.; Pereira, M. M.; Arnaut, L. G. (2017). Ultrafast dynamics of manganese(III), manganese(II), and free-base bacteriochlorin: is there time for photochemistry? *Inorg. Chem.*, 56 (5), 2677-2689. DOI: 10.1021/acs.inorgchem.6b02871.
381. Bennett, L. E.; Ghiggino, K. P.; Henderson, R. W. (1989). Singlet oxygen formation in monomeric and aggregated porphyrin. *J. Photochem. Photobiol. B: Biol.*, 3 (1), 81-89. DOI: 10.1016/1011-1344(89)80022-3.
382. Pasternack, R. F.; Huber, P. R.; Boyd, P.; Engasser, G.; Francesconi, L.; Gibbs, E.; Fasella, P.; Cerio Venturo, G.; Hinds, L. d. (1972). Aggregation of meso-substituted water-soluble porphyrins. *J. Am. Chem. Soc.*, 94 (13), 4511-4517. DOI: 10.1021/ja00768a016.

383. Grenoble, S.; Gouterman, M.; Khalil, G.; Callis, J.; Dalton, L. (2005). Pressure-sensitive paint (PSP): concentration quenching of platinum and magnesium porphyrin dyes in polymeric films. *J. Lumin.*, 113 (1), 33-44. DOI: 10.1016/j.jlumin.2004.08.049.
384. Coleman, H. M.; Abdullah, M. I.; Eggins, B. R.; Palmer, F. L. (2005). Photocatalytic degradation of 17 $\beta$ -oestradiol, oestriol and 17 $\alpha$ -ethynyl-oestradiol in water monitored using fluorescence spectroscopy. *Appl. Catal. B: Environ.*, 55 (1), 23-30. DOI: 10.1016/j.apcatb.2004.07.004.
385. Nakashima, T.; Ohko, Y.; Kubota, Y.; Fujishima, A. (2003). Photocatalytic decomposition of estrogens in aquatic environment by reciprocating immersion of TiO<sub>2</sub>-modified polytetrafluoroethylene mesh sheets. *J. Photochem. Photobiol. A*, 160 (1), 115-120. DOI: 10.1016/S1010-6030(03)00229-6.
386. Arlos, M. J.; Liang, R.; Hatat-Fraile, M. M.; Bragg, L. M.; Zhou, N. Y.; Servos, M. R.; Andrews, S. A. (2016). Photocatalytic decomposition of selected estrogens and their estrogenic activity by UV-LED irradiated TiO<sub>2</sub> immobilized on porous titanium sheets via thermal-chemical oxidation. *J. Hazard. Mater.*, 318, 541-550. DOI: 10.1016/j.jhazmat.2016.07.048.
387. Raghavan, N. V.; Steenken, S. (1980). Electrophilic reaction of the hydroxyl radical with phenol. Determination of the distribution of isomeric dihydroxycyclohexadienyl radicals. *J. Am. Chem. Soc.*, 102 (10), 3495-3499. DOI: 10.1021/ja00530a031.
388. Rodríguez, E. M.; Fernández, G.; Alvarez, P. M.; Beltrán, F. J. (2012). TiO<sub>2</sub> and Fe (III) photocatalytic ozonation processes of a mixture of emergent contaminants of water. *Water Res.*, 46 (1), 152-166. DOI: 10.1016/j.watres.2011.10.038.
389. Rickman, K. A.; Mezyk, S. P. (2011). Removing estrogenic steroids from waters: the role of reducing hydrated electron reactions. *J. Adv. Oxid. Technol.*, 14 (1), 81-85. DOI: 10.1515/jaots-2011-0110.
390. Wood, P. M. (1988). The potential diagram for oxygen at pH 7. *Biochem. J.*, 253 (1), 287-289. DOI: 10.1042/bj2530287.
391. Miller, J. R.; Calcaterra, L.; Closs, G. (1984). Intramolecular long-distance electron transfer in radical anions. The effects of free energy and solvent on the reaction rates. *J. Am. Chem. Soc.*, 106 (10), 3047-3049. DOI: 10.1021/ja00322a058.
392. Kumar, P. H.; Venkatesh, Y.; Siva, D.; Ramakrishna, B.; Bangal, P. R. (2015). Ultrafast Relaxation Dynamics of 5,10,15,20-meso-Tetrakis Pentafluorophenyl Porphyrin Studied by Fluorescence Up-Conversion and Transient Absorption Spectroscopy. *J. Phys. Chem. A*, 119 (8), 1267-1278. DOI: 10.1021/jp512137a.
393. Cavaleiro, J. A. S.; Görner, H.; Lacerda, P. S. S.; MacDonald, J. G.; Mark, G.; Neves, M. G. P. M. S.; Nohr, R. S.; Schuchmann, H.-P.; von Sonntag, C.; Tomé, A. C. (2001). Singlet oxygen formation and photostability of meso-tetraarylporphyrin derivatives and their copper complexes. *J. Photochem. Photobiol. A*, 144 (2), 131-140. DOI: 10.1016/S1010-6030(01)00540-8.
394. Retsek, J. L.; Medforth, C. J.; Nurco, D. J.; Gentemann, S.; Chirvony, V. S.; Smith, K. M.; Holten, D. (2001). Conformational and electronic effects of phenyl-ring fluorination on the photophysical properties of nonplanar dodecaarylporphyrins. *The Journal of Physical Chemistry B*, 105 (27), 6396-6411. DOI: 10.1021/jp004556k.
395. Martini, L. A.; Moore, G. F.; Milot, R. L.; Cai, L. Z.; Sheehan, S. W.; Schmuttenmaer, C. A.; Brudvig, G. W.; Crabtree, R. H. (2013). Modular Assembly of High-Potential Zinc Porphyrin Photosensitizers Attached to TiO<sub>2</sub> with a Series of Anchoring Groups. *The Journal of Physical Chemistry C*, 117 (28), 14526-14533. DOI: 10.1021/jp4053456.
396. Jiang, J.; Swierk, J. R.; Materna, K. L.; Hedström, S.; Lee, S. H.; Crabtree, R. H.; Schmuttenmaer, C. A.; Batista, V. S.; Brudvig, G. W. (2016). High-Potential Porphyrins Supported on SnO<sub>2</sub> and TiO<sub>2</sub> Surfaces for Photoelectrochemical Applications. *The Journal of Physical Chemistry C*, 120 (51), 28971-28982. DOI: 10.1021/acs.jpcc.6b10350.

397. ANSI/ASCE 2-91 (1993). Measurement of Oxygen Transfer in Clean Water. New York, USA: *American Society of Civil Engineers*.
398. Porcelli, N.; Judd, S. (2010). Chemical cleaning of potable water membranes: A review. *Sep. Purif. Technol.*, 71 (2), 137–143. DOI: 10.1016/j.seppur.2009.12.007.
399. Phan, D. D.; Babick, F.; Nguyen, M. T.; Wessely, B.; Stintz, M. (2017). Modelling the influence of mass transfer on fixed-bed photocatalytic membrane reactors. *Chem. Eng. Sci.*, 173, 242-252. DOI: 10.1016/j.ces.2017.07.043.
400. Chen, D.; Li, F.; Ray, A. K. (2001). External and internal mass transfer effect on photocatalytic degradation. *Catal. Today*, 66 (2), 475-485. DOI: 10.1016/S0920-5861(01)00256-5.
401. Turchi, C. S.; Ollis, D. F. (1988). Photocatalytic reactor design: an example of mass-transfer limitations with an immobilized catalyst. *The Journal of Physical Chemistry*, 92 (23), 6852-6853. DOI: 10.1021/j100334a070.
402. Patel, H. A.; Byun, J.; Yavuz, C. T. (2017). Carbon Dioxide Capture Adsorbents: Chemistry and Methods. *ChemSusChem*, 10 (7), 1303–1317. DOI: 10.1002/cssc.201601545.
403. Mehta, A.; Zydney, A. L. (2005). Permeability and selectivity analysis for ultrafiltration membranes. *J. Membr. Sci.*, 249 (1-2), 245-249. DOI: 10.1016/j.memsci.2004.09.040.
404. Herz, R. K. (2004). Intrinsic kinetics of first-order reactions in photocatalytic membranes and layers. *Chem. Eng. J.*, 99 (3), 237-245. DOI: 10.1016/j.cej.2003.11.013.
405. Zhang, S.; Hedtke, T.; Zhu, Q.; Sun, M.; Weon, S.; Zhao, Y.; Stavitski, E.; Elimelech, M.; Kim, J.-H. (2021). Membrane-Confined Iron Oxide Nanocatalysts for Highly Efficient Heterogeneous Fenton Water Treatment. *Environ. Sci. Technol.*, 55 (13), 9266-9275. DOI: 10.1021/acs.est.1c01391.
406. Zhang, S.; Hedtke, T.; Wang, L.; Wang, X.; Cao, T.; Elimelech, M.; Kim, J.-H. (2021). Engineered Nanoconfinement Accelerating Spontaneous Manganese-Catalyzed Degradation of Organic Contaminants. *Environ. Sci. Technol.*, 55 (24), 16708–16715. DOI: 10.1021/acs.est.1c06551.
407. Sonneveld, E.; Jansen, H. J.; Riteco, J. A. C.; Brouwer, A.; van der Burg, B. (2004). Development of Androgen- and Estrogen-Responsive Bioassays, Members of a Panel of Human Cell Line-Based Highly Selective Steroid-Responsive Bioassays. *Toxicol. Sci.*, 83 (1), 136–148. DOI: 10.1093/toxsci/kfi005.